

2014

Removal of Sustained Casing Pressure by Gravity Displacement of Annular Fluid

Efecan Demirci

Louisiana State University and Agricultural and Mechanical College

Follow this and additional works at: https://digitalcommons.lsu.edu/gradschool_theses



Part of the [Petroleum Engineering Commons](#)

Recommended Citation

Demirci, Efecan, "Removal of Sustained Casing Pressure by Gravity Displacement of Annular Fluid" (2014). *LSU Master's Theses*. 3535.

https://digitalcommons.lsu.edu/gradschool_theses/3535

This Thesis is brought to you for free and open access by the Graduate School at LSU Digital Commons. It has been accepted for inclusion in LSU Master's Theses by an authorized graduate school editor of LSU Digital Commons. For more information, please contact gradetd@lsu.edu.

REMOVAL OF SUSTAINED CASING PRESSURE BY
GRAVITY DISPLACEMENT OF ANNULAR FLUID

A Thesis

Submitted to the Graduate Faculty of the
Louisiana State University and
Agricultural and Mechanical College
in partial fulfillment of the
requirements for the degree of
Master of Science in Petroleum Engineering

in

The Department of Petroleum Engineering

by

Efecan Demirci

B.S., Istanbul Technical University, 2010

May 2015

ACKNOWLEDGEMENTS

I am using this opportunity to express gratitude to my advisor, Dr. Andrew K. Wojtanowicz, who supported me throughout the course of this thesis. I am thankful for his inspiring guidance, invaluable constructive criticism and friendly advice during the work. I am also sincerely grateful to my committee members, Dr. Mayank Tyagi and Dr. Paulo Waltrich, for sharing their truthful and illuminating views about this work.

I would like to thank my country, Republic of Turkey, and Turkish Petroleum Corporation for giving me the opportunity and the funding to come to the United States.

I express my warm thanks to Joe O'day, Kristina Butler, Laura Beth Dong, Pritishma Lakhe, Wade Williams and Kevin Deville (Albemarle Corporation) who provided me the required and conducive conditions for the experiments. I would also like to thank Fenelon Nunes, Jeanette Wooden, Chris Carver, Dr. Wesley Williams, Randy Hughes and all other employees of LSU PERTT Lab. My appreciation goes also to Gregory Momen and Benjamin (from LSU Facility Resources), and my student colleagues Sultan Anbar, Imran Chaudhry, Jesse Lambert and Gorkem Aydin for their help throughout this work.

I am particularly grateful to my parents, Isin Alipaca and Gursel Demirci; without their successful cooperation, I would not have been here to complete this work. My special thanks go to Umran Serpen and Mustafa Onur, for teaching me about the engineering discipline in the first place. My gratitude goes also to my aunt, Nursel Kocamaz, for being my guarantor; and to my grandfather, Nefi Demirci, for keeping me dedicated. I am also thankful to my beloved friends, back home, and my girlfriend, Ebru Isidan, who I have insanely missed during my studies.

Lastly I would like to thank Yasin Demiralp, Cem Topaloglu, Ahmet Binselam, Koray Kinik, Darko Kupresan, Eric Thorson, Brian Piccolo, Paul van Els, Younes Alblooshi, Fatih Oz, Isil-Mert Akyuz, Bahadir-Elif Dursun, Volkan Kanat, and Kenan Gedik for their sincerity and stress relieving companionship during this period of my life. Also, I express my gratitude to Umut-Dilsad Meraler couple and their son, Can Efe, as well as Inga and Tarcin, for being my surrogate family in Baton Rouge.

TABLE OF CONTENTS

ACKNOWLEDGEMENTS	ii
LIST OF TABLES	vi
LIST OF FIGURES	viii
NOMENCLATURE.....	xv
ABSTRACT	xvi
CHAPTER 1: INTRODUCTION	1
1.1 Mechanism and Occurrence of Sustained Casing Pressure	1
1.2 SCP Remediation Efforts	2
1.3 Objective of this work.....	4
1.4 Methodology of this work.....	4
1.5 Literature Review on Gravity Displacement and Gravity Settling	5
CHAPTER 2: CHARACTERIZATION OF ANNULAR FLUID	11
2.1 Objective	11
2.2 Literature Review on Characterization of Annular Fluid	11
2.3 Determination of Annular Fluid Initial Properties	15
2.3.1 Generating Annular Fluid in Lab	16
2.3.2 Generalization of Annular Fluid Formula.....	17
2.4 Static Mud Column Experiments	18
2.4.1 Experimental Set-up, Matrix and Procedure	18
2.4.2 Results of Static Column Experiments	20
2.5 Mud Column Density Distribution vs. Time	21
2.6 Prediction of Barite Bed Height.....	23
2.7 Compaction Zone Porosity.....	25
CHAPTER 3: SELECTION OF KILL FLUID.....	28
3.1 Objective	28
3.2 Criteria and Desired Properties of Kill Fluid	28
3.3 Albemarle Brominated Organics	33
3.4 Compatibility Testing of Brominated Organics	34
3.4.1 Pilot Demo Test – 1	34
3.4.2 Pilot Demo Test – 2.....	35
3.4.3 Weighted Fluid Column Test	36
3.4.4 Bench-top Compatibility Tests	36
3.5 Summary	40

CHAPTER 4: VISUALIZATION OF GRAVITY DISPLACEMENT	41
4.1 Objective	41
4.2 Methodology	41
4.2.1 Physical Model Design and Fabrication	41
4.2.2 Fluids Properties.....	46
4.2.3 Experimental Procedure and Analysis	49
4.3 Results and discussion	49
4.3.1 Observations – Miscible Displacement.....	51
4.3.2 Observations – Immiscible Displacement.....	55
4.3.3 Relation to Field-Scale Applications	63
4.4 Maximum Injection Rate to Prevent Initial Dispersion	64
4.4.1 Side Injection	64
4.4.2 Top Injection	67
CHAPTER 5: PILOT SCALE EXPERIMENTS	72
5.1 Objective	72
5.2 Methodology	72
5.2.1 Physical Model Design and Fabrication	72
5.2.2 Experimental Procedure	75
5.2.3 Experimental Matrix	77
5.3 Results and Observations	81
5.4 Analysis of Pilot Testing Results	85
5.4.1 Process Performance Measures	85
5.4.2 Pressure Replacement Model.....	86
5.4.3 Algorithm of Analysis of Unfinished Runs	91
5.5 Empirical Correlations	92
5.5.1 Trend Analysis	92
5.5.2 Volume Displacement Ratio Correlation	94
5.5.3 Mixture zone Size Correlation	98
5.5.4 Use of Correlations for Design	100
5.6 Maximum Injection Rate for Buoyant Settling.....	103
CHAPTER 6: FULL SCALE TEST	110
6.1 Methodology	110
6.1.1 Well installation	110
6.1.2 Testing Procedure.....	113
6.1.3 Injection rate design	114
6.2 Results and Observations	116
6.2.1 Pressure data.....	117
6.2.2 Sampling	118
6.3 Analysis.....	120
6.4 Bridge-over of Buoyant Slippage	124
6.4.1 Effect of Pump Pulsation	124
6.4.2 Effect of Gas Flotation	126

CHAPTER 7: CONCLUSIONS	127
CHAPTER 8: RECOMMENDATIONS.....	129
REFERENCES.....	130
APPENDIX A: SELECTION OF KILL FLUID DERIVATION.....	137
APPENDIX B: PRESSURE REPLACEMENT MODEL DERIVATION	141
APPENDIX C: PILOT-SCALE MISCIBLE DISPLACEMENT RUN	147
APPENDIX D: SOFTWARE SCRIPTS.....	148
VITA	151

LIST OF TABLES

Table 2.1: Properties of drilling muds used in static column experiments.....	19
Table 2.2: Table of experimental porosity data for compaction zone density calculations.....	26
Table 3.1: Criteria and desired properties of kill fluid.....	32
Table 4.1: Table of hydraulic radiuses for various casings and annular areas (OC= Outer casing, IC= Inner casing, ID= Inner diameter, OD= Outer diameter, NW= nominal weight [lb/ft.], CS= Cross-Section, r_h = Hydraulic Radius)	44
Table 4.2: Statistical results of annulus hydraulic diameters.....	45
Table 4.3: Statistical properties of annulus hydraulic diameters	45
Table 4.4: Kill fluid properties used in slot experiments.....	47
Table 4.5: Prepared translucent fluid formulas for slot model experiments.....	48
Table 4.6: Properties of generated translucent fluids for slot experiments.....	48
Table 4.7: Table of results	50
Table 4.8: Fluid properties used in Figure 4.28 and Figure 4.29.....	70
Table 5.1: Table of annular fluids (AF) in pilot experiments	78
Table 5.2: Properties of annular fluids in pilot experiments.....	79
Table 5.3: Properties of kill fluids used in pilot experiments	79
Table 5.4: Experimental matrix of pilot-scale experiments.....	80
Table 5.5: Immiscible displacement test results and analysis.....	84
Table 5.6: Variables that might control displacement process	94
Table 5.7: Summary and parameter estimates of the fits.....	96
Table 5.8: Summary of fit for predicting exponential coefficient	99

Table 5.9: Parameter estimates calculated for predicting exponential coefficient	99
Table 5.10: Parameters used for upscaling example.....	102
Table 6.1: Properties of the kill and annular fluids.....	112
Table 6.2: Injection rate conversion from pilot-scale for full scale test	115
Table 6.3: Injection rate design based on different criterion	116
Table 6.4: Description of overflow samples	119
Table 6.5: Slopes of straight lines in Figure 6.14 and corresponding overflow densities	123

LIST OF FIGURES

Figure 1.1: Mechanism of sustained casing pressure ^[4]	1
Figure 1.2: Wells with SCP by age - outer continental shelf (OCS) ^[2]	2
Figure 1.3: Vertical well with spiral flow pattern in the rat-hole - miscible displacement of mud with cement slurry ^[11]	5
Figure 1.4: Schematic of heavy brine injection into lighter white oil - immiscible displacement experiment performed by Nishikawa ^[8] . Immediate dispersion and continuous settling of brine was reported.....	6
Figure 1.5: Primary fragmentation modes of a liquid jet ^[13] (Adopted from Reitz ^[14])	7
Figure 1.6: Schematics of flow patterns generated by an impinging jet (a) Gravity flow with draining flow width of W . (b) Rivulet flow with tail width of W_T . (c) Gravity flow with dry patch formation. R is the radius of the transition to a form of hydraulic jump, R_c is the radius of the corona at the level of the impingement to the film jump ^[23]	9
Figure 2.1: Hindered (left) and Boycott (right) settling kinetics under static conditions (V_0 is the particles settling velocity, H is the height, b is the width and α is the inclination angle) ^[46] .	13
Figure 2.2: Plot of measured and predicted density of centrifuged synthetic based weighted mud. Using unpublished empirical formulas ^[47]	14
Figure 2.3: A well interpretation combined with conventional logs and Isolation Scanner to determine cut-and-pull level ^[63]	16
Figure 2.4: Rheology of drilling mud, spacer and annular fluid mixtures.....	17
Figure 2.5: Picture of the mud/free water interface after 11 weeks of static settling	18
Figure 2.6: Picture of the 10-foot column.....	19
Figure 2.7: Density distribution of static mud experiments after certain times.....	20
Figure 2.8: Progressive gel strength vs time plot.....	21
Figure 2.9: Drop of stagnant mud column density in time	22
Figure 2.10: Porosity experiment. Weights and compaction volumes are measured.	25

Figure 2.11: Plot of compaction zone porosity experimental data and model.....	27
Figure 2.12: Change in compaction height with increasing mud density	27
Figure 3.1: Terminal velocity vs. size of fluid droplets ^[28]	30
Figure 3.2: Example plot of displacement time and droplet traveling time changing with the droplet size	32
Figure 3.3: Viscosity versus density of brominated organics blended with components A and B	34
Figure 3.4: Bench-top physical model for compatibility tests	37
Figure 3.5: Bench-top compatibility tests; (0.11, 0.28, 0.57 gpm) Flow patterns vary from Rayleigh to Atomization.	38
Figure 3.6: Snapshots of the tests when injection stopped. Mixture zone height increased with increasing injection rate.	38
Figure 3.7: Poured kill fluids into Non-Newtonian AF generate different flow patterns. Left: Low viscosity kill-fluid with Rayleigh mechanism. Middle: High viscosity kill-fluid with First-Induced break-up. Right: Second-Induced Break-up ^[14]	39
Figure 4.1: Well annulus (left) was cut from the red line; opened-up and converted into Slot model (right).	42
Figure 4.2: Dimensions plot for the slot model according to hydraulic radius theory	43
Figure 4.3: Statistical analysis of hydraulic radius of 40 intermediate casings	43
Figure 4.4: Slot model width vs. thickness plotted according to statistical results.....	45
Figure 4.5: Slot physical model schematics.....	46
Figure 4.6: Comparison of two translucent fluids and un-weighted bentonite muds	48
Figure 4.7: Injecting weighted mud KF2012 into water @~1 gpm (miscible displacement). Instant mixing occurs (Experiment #55).....	52

Figure 4.8: Injecting heavy mud KF2012 into Non-Newtonian TF0107 @~1 gpm (Experiment #53). Continuous rope transport and delayed mixing occur i.e. rope length = height of the model.....	52
Figure 4.9: Injecting heavy mud KF2014 into Non-Newtonian TF0107 @~2 gpm (Experiment #51). Rope of KF destabilizes before reaching the bottom due to higher injection rate.	53
Figure 4.10: Dimensionless plots of miscible displacement @1 gpm. Miscible kill fluids give poor displacement of water or water-based Bingham fluid.	54
Figure 4.11: KF3011 (brine - red) into 8.6 ppg un-weighted mud (brown) with 1 gpm flow rate (Experiment #57). A flocculated mud coating covered the brine stream as it went down and displaced the clean mud.	55
Figure 4.12: Mechanism of heavy brine slippage in mud.....	55
Figure 4.13: Heavy KF1701 displacing high-strength TF0107 (2 gpm) using side (left) and top (right) injection geometries.....	56
Figure 4.14: Top-injection of KF1203 into thin TF0101 at 5 gpm (Experiment #21). Fast injection “atomizes” KF into dispersed phase that eventually settles down with no stable mixture zone.....	57
Figure 4.15: Side injection of KF1203 into thin TF0101 at 5 gpm (Experiment #8). Impingement absorbs the injection rate energy. Fluid droplets settle down by buoyancy. No stable mixture zone is observed.	58
Figure 4.16: Dimensionless plots of immiscible displacement demonstrate beneficial effect of high density and detrimental effect of high injection rate on performance	58
Figure 4.17: Side injection of KF1701 into low viscosity TF0104 at 2 gpm (Experiment #33). There is a sharp TF/KF interface – negligible mixture zone formed.....	59
Figure 4.18: Side injection of KF1701 into high viscosity TF0102 at 2 gpm (Experiment #32). High strength of TF generated blurry AF/KF interface – mixture zone formed bottoms up.....	60
Figure 4.19: Top-injecting KF1701 into TF0107 at 1.5 gpm (Experiment #42). Despite low rate, dynamic jetting causes KF dispersion on its way downwards.....	60
Figure 4.20: Top injection of KF1203 into thin TF0101 at 0.75 gpm (Experiment #6). Relatively large KF droplets form and settle down by buoyancy. A sharp KF/AF interface is observed	61

Figure 4.21: Side injection of KF1701 into TF0107 at low 0.5 gpm rate (Experiment #36) w/o impingement. Despite high GS of TF, no mixture zone develops.....	62
Figure 4.22: Side injection of KF1701 into TF0107 at 2 gpm (Experiment #34). Higher flow rate creates a blurry interface between fluids.	62
Figure 4.23: Side-injection of KF1204 into TF0107 at 2 gpm (Experiment #30) with large impingement. Low viscosity kill fluid brakes into droplets that are carried upwards by ascending TF- gravity settling with dispersion.....	63
Figure 4.24: Impingement width actual vs prediction plot. Rivulet threshold is estimated as 2.2”	66
Figure 4.25: Fragmentation modes of a liquid jet in pressure atomization into an ambient fluid.	68
Figure 4.26: Matched flow pattern values for vertical injection.....	69
Figure 4.27: Rayleigh mechanism (left), transition (middle) and atomization modes (left) from experiments #20, #42 and #44 respectively	70
Figure 4.28: Critical injection (for atomization) can be increased several-fold with large nozzles.....	71
Figure 4.29: Critical injection rate (for atomization) can be increased for higher KF viscosities, and lower AF viscosities	71
Figure 5.1: Pilot model	73
Figure 5.2: Bottom of outer casing with pressure instruments	74
Figure 5.3: Gas injection installation below annular column’s bottom with inner pipe drain viewer.....	74
Figure 5.4: Top view down annular column showing spaced pressure transducers and KF side-injection port	75
Figure 5.5: Pilot model schematics.....	76
Figure 5.6: Bottom pressure change during experiment.....	77

Figure 5.7: Pressure vs. time plot of Batch 31 run; P_{max} = maximum final pressure, P_u = ultimate pressure (complete displacement).....	81
Figure 5.8: Pressure vs. time plots of Batch 6 and Batch 23 runs demonstrate unfinished displacements due shortage of KF	82
Figure 5.9: Depth of mixture zone above top of clean KF	83
Figure 5.10: Comparison plots of pressure buildup with (Batch 1 run) and without concurrent gas migration (Batch 35 run)	83
Figure 5.11: Fluid zones distribution in annulus: kill fluid (KF), mixture zone (MZ) and annular fluid (AF)	86
Figure 5.12: Exponential fit of mixture zone density with exponent (6) shows good match	87
Figure 5.13: Overflowing density change during Batch12 experimental data	88
Figure 5.14: Example plot for extrapolating measurements to estimate ultimate time	91
Figure 5.15: Extrapolation of pressure buildup for Batch 10 run	92
Figure 5.16: Extrapolation of pressure buildup for Batch 12 run	92
Figure 5.17: Change in dimensionless values and exponential coefficient with increasing annular fluid density. Batches 4, 31 and 15 runs show the effectiveness of the process when lighter and low structural strength AF is present	93
Figure 5.18: Change in dimensionless values and exponential coefficient with increasing flow rate. KF1204 injections into AF0903 with different rates (Batches 27, 28 and 29) show increasing mixture zone height and more losses to overflow with increasing rate	93
Figure 5.19: Scatter plot of experimental variables	95
Figure 5.20: Leverage plots of R_u residuals vs. all the variables	96
Figure 5.21: $\log R_u$ actual versus $\log R_u$ predicted with correlation in Equation 5.16 (Properties are shown in Table 5.7)	97
Figure 5.22: Profiler plot of variables	98
Figure 5.23: Prediction plot of mixture zone exponential coefficient	99

Figure 5.24: Mixture zone coefficient vs. flow rate for different AF viscosities for AF density 12 ppg.....	100
Figure 5.25: Example upscaled dimensionless displacement process at various flow rates. Increasing rate results in early deviation from 45 degree line.	103
Figure 5.26: Duration of displacement of three different critical rates for upscaling example ...	103
Figure 5.27: KF injection rate design plots ($\tau_0 = 2 \text{ lbf/100sqft}$, $\rho_{af} = 8.6 \text{ ppg}$, $\mu_{kf} = 8 \text{ cP}$, $\mu_{af} = 5 \text{ cP}$, $\sigma = 30 \text{ dyne/cm}$ and $A = 0.24 \text{ gal/ft}$)	109
Figure 6.1: Well#1 schematics.....	111
Figure 6.2: Full-scale test – well installation	112
Figure 6.3: Picture of well installation.....	113
Figure 6.4: Planned pressure change during test	114
Figure 6.5: Flip-flop test for injection design. KF is in black, Translucent Fluid is in light color.	115
Figure 6.6: Corresponding operation durations for injection rates based on Equation 5.46	116
Figure 6.7: Top and bottom pressure change.....	117
Figure 6.8: Change of hydrostatic pressure and KF injection rate	118
Figure 6.9: Taken samples during KF injection (Sample numbers are chronological). Kill fluid color is red. All samples, except S#3, show high KF content.	119
Figure 6.10: Overflow sample #3 taken after 2.5 hours of injection.	119
Figure 6.11: Samples taken during cleanup. Number 1 represent top of tubing and number 10 is the heavy displacing (cleaning) mud.....	120
Figure 6.12: Density change in top and bottom well sections	121
Figure 6.13: Actual and ideal change in E_p and SCP	122
Figure 6.14: Hydrostatic pressure buildup rate analysis	122

Figure 6.15: Pictures of samples from laboratory generated emulsion. #1 represents the highest and #4 represents the lowest portions of the mixture zone. No further separation occurred in 6 days (bottom samples).	123
Figure 6.16: Pump strokes per minute versus flow rate [Manual of Morgan Products Pump, Model 5500DS-TR2-SR2S].....	124
Figure 6.17: Feed pump pulsation after wellhead decompression brings injection rate above its limit.....	125
Figure C.1: Pressure plot of heavy mud kill fluid displacement. (Batch#34).....	147

NOMENCLATURE

KF	Kill fluid	AF	Annular fluid
μ_{kf}	Viscosity of KF [cP.]	μ_{af}	Viscosity of AF [cP.]
ρ_{kf}	Density of KF [ppg.]	ρ_{af}	Density of AF [ppg.]
d_n	Nozzle diameter [inches]	σ	Interfacial tension [dynes/cm]
Z	Modified Ohnesorge Number [-]	μ_p	Plastic viscosity [cP.]
W	Impingement width [inches]	\dot{m}	Mass flow rate [lb./s]
ϑ_A, ϑ_B	Droplet terminal velocities [feet/sec]	Ar	Archimedes number [-]
τ_0	Yield stress value of AF [lbf/100sqft]	ϑ_s	Particle slip velocity [feet/sec]
C_D	Drag coefficient [-]	ϑ_T	Transport velocity [feet/sec]
$\Delta\rho$	Density difference of fluids [ppg.]	d_{max}	Max stable droplet diameter [inches]
d_p	Droplet diameter for peak velocity	α, α_p	Velocity ratio and peak vel. Ratio [-]
m_p	Fit factor for peak velocity	α_{pm}	Mean peak velocity ratio [-]
t	Time	ρ_c	Compaction zone density [ppg.]
ϕ	Compaction zone porosity [-]	ρ_{um}	Un-weighted mud density [ppg.]
V_{um}	Volume of un-weighted mud [gal.]	V_a	Volume of annulus [gal.]
m_B	Mass of barite in mud [lb.]	ρ_{mud}	Mud density [ppg]
h_C	Height of compaction zone [feet]	h_a	Height of annulus [feet]
t_d	Displacement time	ϑ_d	Droplet velocity [feet/sec]
A_a	Annular cross-sectional area [sq.ft.]	V_d	Droplet volume
N, N_{max}	Droplet generation frequency [1/sec]	r_h	Hydraulic radius [inches]
P_{ba}	Bottom hydrostatic pressure [psi.]	E_v	Volumetric efficiency (1/R) [-]
E_p	Pressure replacement efficiency [-]	R	Volumetric Displacement ratio [-]
E_o	Eötvös Number [-]	Mo	Morton Number [-]
V_p	Volume of KF pumped [gal.]	P_o	Obtained bottom pressure [psi]
P_{af}	Initial bottom pressure [psi.]	R_L	End of linear Displacement ratio [-]
R_u	Ultimate Displacement ratio [-]	Re	Reynolds Number [-]
β_1, β_2	Dimensionless groups [-]	a	Exponential coefficient [feet]
P_u	Ultimate bottom pressure [psi.]	A	Annular capacity [gal/feet]

ABSTRACT

Sustained Casing Pressure (SCP) is the undesirable casing head pressure of a well annulus that rebuilds when bled-down. As the conventional methods for SCP removal using rigs are expensive, there is a need for improvement. Annular intervention for replacing the fluid above the leaking cement with a heavier fluid to stop gas migration is a solution for SCP removal; however, previous attempts failed due to miscibility of injected fluids. Using hydrophobic heavy fluids for the purpose is a newly proposed technique to the technology.

Potential of theoretically selected and produced immiscible heavy fluids are investigated in characterized annular fluids. A transparent laboratory scaled-down hydraulic analog of well's annulus provided visual evidence for displacement geometry and did the first stage testing of heavy fluid injection into clear synthetic-clay muds. A 20-foot physical model then tested the performance of the displacement process. Settling of various heavy fluids with densities from 11 to 23 ppg in drilling fluids with densities from 9 to 13 ppg provided quantitative bottom pressure data. Finally, a full-size test in 2750-foot well examined the viability of the technology.

Visualization experiments proved that the counter-current flow in annulus leads to up-lifting of heavy fluid droplets and must be minimized for a desirable displacement process. Selection of injection geometry and rate are also essential to maintain a controlled transport of heavy fluid downwards. Pilot experiments developed mathematical correlations relating the process performance to fluid properties and rate. Full-size test shows that hydrophobic heavy fluids are able to slip in long columns; however, bridge-over of buoyant settling may occur due to high injection rates and/or flotation effect of migrating gas that was entrapped in annular fluid.

The findings in this research present solid support to the viability of immiscible gravity displacement of annular fluid for remediating a well annulus affected with SCP. For given fluid properties and in confined annular space, injection rate is the key to a successful displacement. Finally, the research proved that the duration of a complete displacement process and required heavy fluid volume are inversely correlated. For any operation design; time and killing material restrictions must be considered.

CHAPTER 1: INTRODUCTION

1.1 Mechanism and Occurrence of Sustained Casing Pressure

Annular Casing Pressure (ACP) is defined as the accumulated pressure on the casing head; which may be the result of gas migration from tubing or cement leaks, thermal expansion of annular fluid, or may be deliberately applied for purposes such as gas lift or to reduce the pressure differential across a down-hole component. Ideally, pressure gauges on all the casing strings should read zero after bled-down, when the well is at steady-state flowing conditions. However, if the annular casing pressure returns after all valves are closed, then the casing annulus is said to be showing sustained casing pressure (SCP) ^[1]. SCP cannot be permanently bled off as it is caused by gas migration in the annular fluid column above the top of leaking cement (Figure 1.1) or tubing leaks. Statistical evidence shows that as the well ages, probability of SCP occurrence increases (Figure 1.2). Globally, +/- 35% of +/- 1.8 million well population has SCP^[2]. Problems resulting from SCP can be failure of casing head or casing shoe causing atmospheric emissions or underground blowouts, respectively. The leaking cement problem is widely spread as shown by statistics from GOM, Canada, Norway and other places where SCP has been regulated ^[1]. The US regulations (Bureau of Safety and Environment Enforcement, BSEE) require removal of severe SCP to continue operation and removal of any SCP prior to well's plugging and abandonment (P&A) operations^[3].

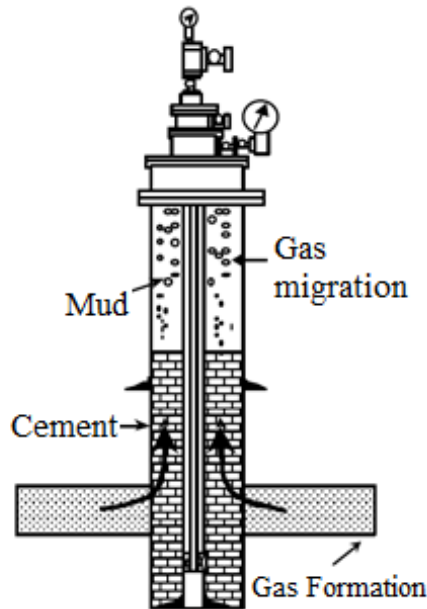


Figure 1.1: Mechanism of sustained casing pressure ^[4]

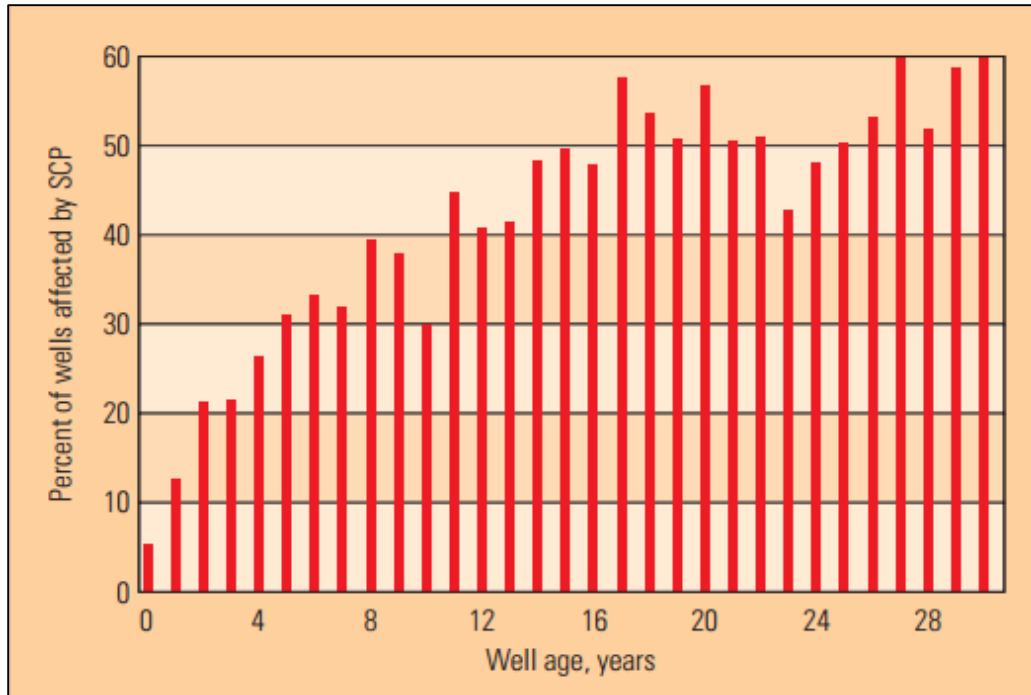


Figure 1.2: Wells with SCP by age - outer continental shelf (OCS) ^[2]

1.2 SCP Remediation Efforts

Tubing leaks, which are identified as the most dangerous cause of SCP, can easily be repaired with well work-over operations. However, remediations of flow through cement channels and cracks have been technically difficult. To date, industry has used few methods for solving the SCP problem by moving a rig to the well side. One of them involves termination of the inner casing string and placing cement plug. This method was reported as possible only where the cement sheath was absent behind the inner casing^[5]. Another rig method, section milling, involves milling a section of a casing and pumping cement to intercept gas flow. The main challenge for this method was stated as the difficulty of optimization of the milling tool size where the inner casing is eccentric in relation to the outer casing^[5].

Other methods – much less expensive than the rig methods – involve injecting “killing” material into the well’s annulus in order either to increase the hydrostatic pressure at the cement top and “kill” SCP, or plug the annulus with a sort of sealant to stop gas migration. The most challenging problem of these methods is the fact that the only possible access to the casing annulus is through the valve at the casing-head. Thereby, the killing material can either be

introduced with flexible tubing inserted to certain depth of the annulus (Casing Annulus Remediation System, CARS), or by direct injection to the top valve. Previous applications show that CARS can only reach to 1000 feet depth and was not promising to remediate SCP in deeper annuli ^[4]. Another study involved dropping down a low-melting-point alloy metal into the infected annulus, allowing to accumulate at the top of cement and melting it with an induction-heating tool to create a plug, that stops the fluid communication between the formation and the wellhead ^[6]. Full-scale testing of single-annulus laboratory models indicated that the method would work in the innermost annulus filled with water or synthetic-base muds. However, other-annulus model, which is more difficult to heat up with the induction tool, has never been tried. Even though the small-scale tests showed promising results on plugging the annular space this technology was never tried in a real well or commercialized, yet. Instead, another rig-less technique, bleed-and-lube method, had become popular due to its low price and practicality.

Bleed-and-lube method appears to be very simple and the least expensive of all the remediation methods. This method involves displacing annular fluid by consecutive cycles of pressure removal through bleeding followed with lubrication of small batches of heavy (kill) fluid. Few case histories reported some reduction in surface casing pressures and stated as partially successful when using Zinc Bromide as the kill fluid. However, pressure reduction was not enough to stop the gas migration ^[4]. Similarly, case histories of heavy mud lubrication showed that the technique was not capable of reducing SCP by a noticeable amount. In one such, prolonged lubricating an intermediate casing annulus did not remarkably reduce SCP and the annulus quit taking more heavy mud. Applying higher pump pressure to inject more mud resulted in creation of a new leak path from the intermediate casing into the production casing. Even though the intermediate casing pressure showed a slight reduction, existence of the new leak path confused the analysis and success of the technique could not be proven ^[1]. To date, the performance of the bleed-and-lube method using heavy brine or drilling mud has been rather poor.

Nishikawa et al. ^[7] discovered a strong relation between the bleed-and-lube method performance and the chemical interaction of heavy brines with fluids in the annulus. Their experiments in LSU showed that injection of heavy brine into water-base mud results in rapid flocculation of the mud. The flocculated mud creates a plug on top of the annulus and prevents

the brine from displacing the entire annular volume. Moreover, experiments involving water and brine showed no flocculation but complete displacement required very large number of injection cycles as the brine readily dissolved in the water [4, 7, 8]. The use of weighted mud as the killing fluid was also reported to be ineffective due to its mixing with annular fluid [8].

To date, field trials of SCP removal with heavy fluid displacement of annular fluid have been unsuccessful, however, laboratory experiments have shown that the gravity displacement method has merit if the two fluids are immiscible and the displacing fluid's density is sufficiently greater than that of the annular fluid^[8]. The immiscible gravity displacement technique may become viable and cheaper as compared to conventional SCP removal methods; thus, there is a need to study it further.

1.3 Objective of this work

The objective of this research was to investigate feasibility of hydrophobic heavy fluids for gravity displacement to remove SCP. In order to simulate field-like conditions, first step was to characterize mature annular fluid and generalize its structure and composition. The main objective was to develop a hydrophobic heavy fluid and to investigate its performance on displacing lighter annular fluids. Considering the visual incapability of annular geometry, a bench-top physical model was designed and fabricated to improve the understanding on the injection method limitations. Secondly, a pilot physical model would give quantitative data for the performance analysis of the displacement process. As the last piece of developing gravity displacement method, a full-scale experiment would give information about viability of the technology.

1.4 Methodology of this work

In this study, series of experiments have been designed and conducted with different physical models: bench-top, floor-top, pilot-size, and full-scale. The models are described in the following chapters. Experimental results have been, then, analyzed qualitatively and quantitatively. Qualitative work includes observation of trends and analysis of videotaped records. Quantitative analysis included development of empirical correlations to be used in formulation of analytical models of the gravity displacement process performance.

1.5 Literature Review on Gravity Displacement and Gravity Settling

Gravity displacement by using miscible heavy fluid is often used and discussed by the oil industry in cementing and setting of cement plug operations. The efficiency of the phenomena is mostly described as its dependency on the breaking of fluid-fluid interface that results in mixing of two fluids and slows down or prevents the down-movement of heavy fluid. Frigaard and Crawshaw^[9] experimentally studied two Bingham Plastic fluids in a closed-ended pipe that were separated with a single fluid-fluid interface; heavier fluid on top of lighter fluid. Their tests highlighted the behavior of the interface under different pipe inclinations, fluid rheology and densities. Their results stated that not only the interface yields easier compared to the horizontal pipe but also the presence of yield stresses maintains a statically stable interface. They also stated that yield stress prevents unstable movement of heavier fluid in the lighter fluid; high viscosity slows down the motion but do not stop it^[10]. Similar phenomenon was also observed in an annular geometry. During a cement plug setting experiment, the cement slurry unwound or roped from the bottom of the plug in a clockwise circular pattern^[11]. This movement would continue until the leading edge of the heavy cement slurry was at the bottom of the pipe (Figure 1.3).

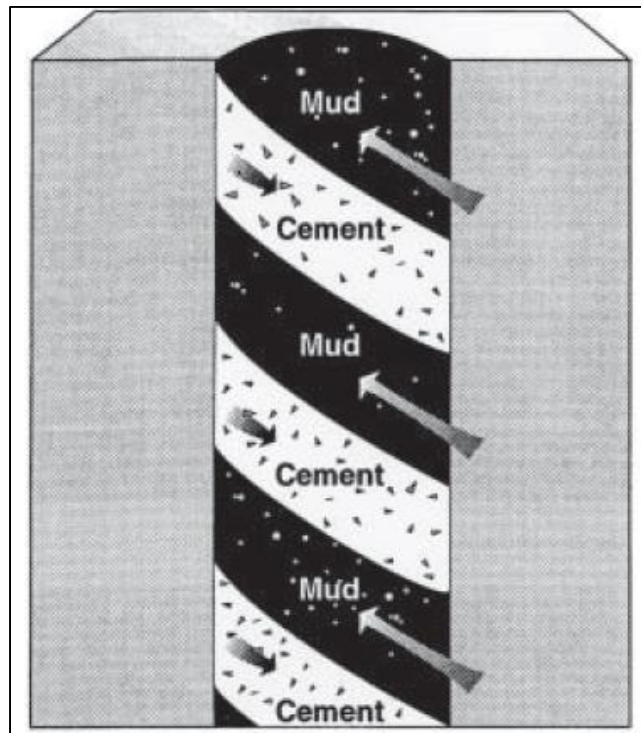


Figure 1.3: Vertical well with spiral flow pattern in the rat-hole - miscible displacement of mud with cement slurry^[11]

Displacement of a stagnant fluid begins with introducing the displacing body into the system. Immiscible displacement tests conducted, at LSU, involved injecting heavy brine or bentonite slurry into white oil through a vertical tubing ^[4]. It was reported that the heavy fluid parted immediately and dispersed into droplets just after entering the stagnant medium, white oil ^[4]. It was also observed that the large droplets settle faster than the small droplets (Figure 1.4). The reason for this is; after the injection forces applied by the positive jetting expire; drops of heavy fluid form and start moving only under buoyant forces. The displaced stagnant fluid moves upwards while heavy fluid is settling down in counter-current flow. The phenomenon is also called “gravity displacement”.

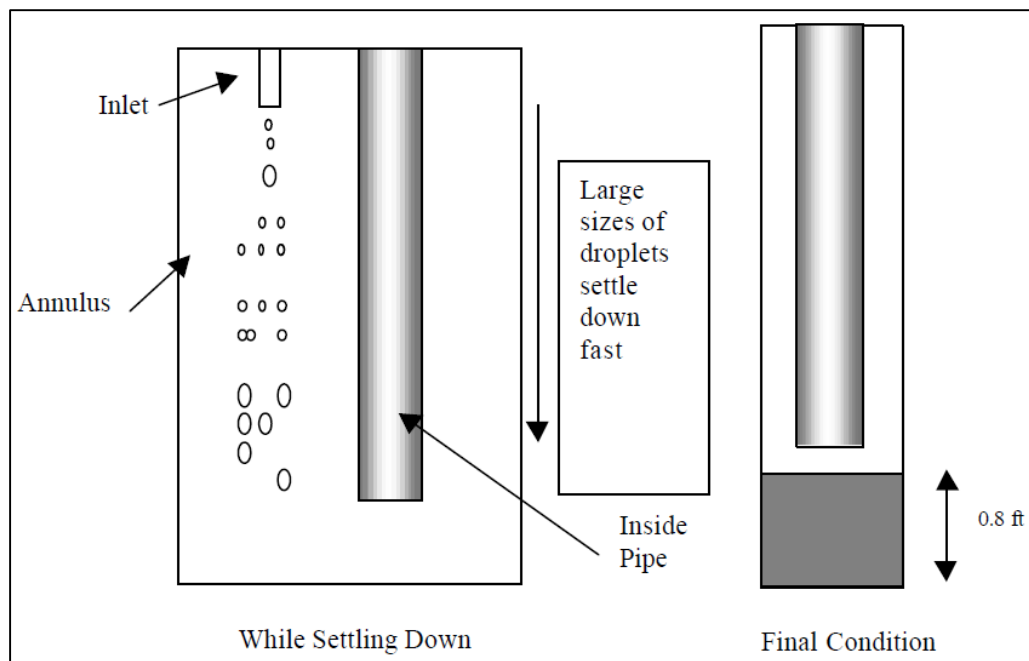


Figure 1.4: Schematic of heavy brine injection into lighter white oil - immiscible displacement experiment performed by Nishikawa ^[8]. Immediate dispersion and continuous settling of brine was reported.

Many researchers have studied fate of a vertical free liquid jet discharging into an ambient fluid. As a result of capillary instability, a liquid being injected into another immiscible fluid may break up into droplets either near the orifice or at the end of the jet. Experimental and analytical studies to date have revealed the effect of surface tensions on the fragmentation of heavier fluid when injected into a gaseous media. Ohnesorge ^[12] divided the breakup regimes of a circular liquid jet into three areas depending on the liquid Reynolds number and Ohnesorge

number, which is defined as a dimensionless number that relates the viscous forces to inertial and surface tension forces ($Oh = \sqrt{We}/Re = \mu/\sqrt{\rho\sigma d_n}$; $We = \rho u^2 d_n/\sigma$, μ = viscosity of the fluid, ρ = density of liquid, u = jet velocity, d_n = nozzle diameter, σ = liquid-air interfacial tension)^[13]. Reitz^[14] detailed the investigation and identified four main breakup regimes governed by Ohnesorge and Reynolds Numbers of the jet (qtd. in Multiphase Flow Handbook^[13]). As shown in Figure 1.5, Rayleigh mechanism generates a heavy fluid stream consisted of uniform heavy fluid droplets. As the flow rate increases, fragmentation mode transforms (to first and second wind induced regimes) and satellite droplets start occurring^[15]. As the Atomization type of jetting establishes droplets with various sizes form due to dispersion.

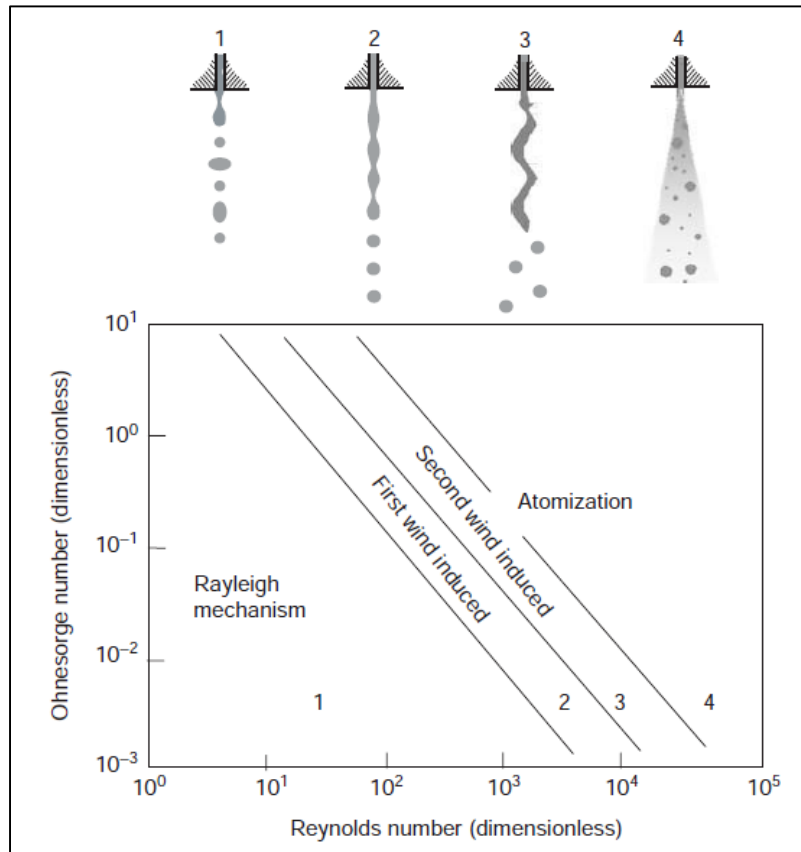


Figure 1.5: Primary fragmentation modes of a liquid jet^[13] (Adopted from Reitz^[14])

Size of droplets formed from the breakup of cylindrical liquid jets discharging into a gas was first analyzed by Tyler^[16] (qtd. in Teng et al.^[17]). By applying Rayleigh's instability theory for inviscid liquid jets vacuum and a mass balance at the end of the jet, he obtained a relationship

between the droplet diameter and the undisturbed jet diameter, without considering the ambient fluid properties. Teng et al. ^[17] developed a simple analytical equation to predict size of droplets formed during the breakup of cylindrical liquid jets while penetrating into another fluid. Their equation applies to low-velocity liquid-in-gas and liquid-in-liquid injections, and shows satisfactory match for both Newtonian and Non-Newtonian fluids. In order to include the ambient fluid properties, they modified the Ohnesorge number by considering the viscosities of both fluids.

Horizontal liquid jets impinging on a surface are used in many industrial applications such as cleaning and coating of surfaces, and paper and textile drying processes. Beside the horizontal free jets, confined jets are commonly referred to in the literature as submerged and free-surface jets. Submerged are defined as the jets issuing into a region containing the same liquid, and free-surface jets into ambient air (gas) ^[18]. Submerged jets can either be unconfined or confined by a plate attached to the nozzle and parallel to the impingement plane. Miranda and Campos ^[19] explained the laminar flow of a jet confined by a conical wall extending from the nozzle to an impingement plate in three regions: the impingement region, the wall region, and the expansion region. They indicated that the jet Reynolds number and the inlet velocity profile influences the entire flow strongly, while the distance between the nozzle and the plate only affects the expansion region. Numerical study of Storr and Behnia ^[20] also addresses free-surface jets - water jets impacting onto the pool of water. They stated that air entrainment occurs when a water jet falls under gravity through air headspace and separates from the flow as buoyancy overcomes the decreasing jet momentum.

To observe the cleaning capability of an unconfined impinging jet, Morison and Thorpe ^[21] conducted experiments by using a spray-ball that is often used as a cleaning material to wet a surface. They developed empirical equations for finding the width of the wetted area during impingement of the spray jet on the wall. Wilson et al. ^[22] defined and experimentally observed two impingement flow regions, gravity flow and rivulet flow, when water is jetting onto glass surfaces. As a result of their dimensional analysis, they highlighted the influence of Reynolds number and Eötvös number on impinging width ($Eo = \rho g W^2 / \sigma$, W = impinging width). Wang et al. ^[23] performed experiments using water but also three different aqueous solutions as the fluids impinging on glass and Perspex surfaces being injected from 1, 2 and 3 mm nozzles, and

identified one more flow pattern, gravity flow with dry patch (Figure 1.6). Their results showed that the impingement flow pattern is highly dependent on the wetting surface. In the experiments, Perspex surface mostly showed rivulet flow although the glass surfaces had more tendencies to generate gravity type of flow pattern. They also stated that the low contact angle and low viscosity promote a stable falling film after the impingement. This effect of viscosity was also showed by Nusselt ^[24] as a parameter that increases the thickness of the falling liquid film. According to his finding, increasing liquid viscosity generates a thicker film falling under the gravitational force (qtd. in Multiphase Flow Handbook^[13]).

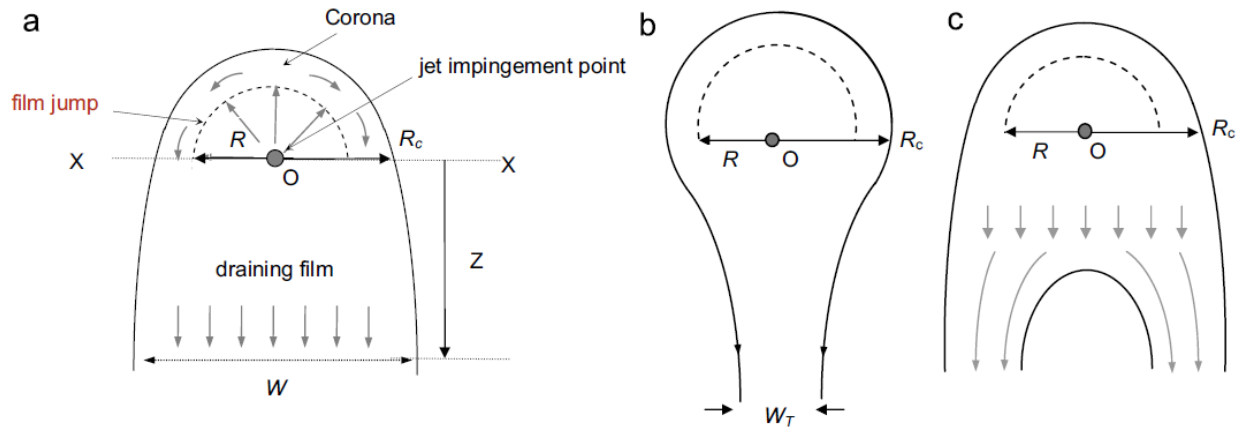


Figure 1.6: Schematics of flow patterns generated by an impinging jet (a) Gravity flow with draining flow width of W. (b) Rivulet flow with tail width of W_T. (c) Gravity flow with dry patch formation. R is the radius of the transition to a form of hydraulic jump, R_c is the radius of the corona at the level of the impingement to the film jump^[23].

Once the jetting forces acting on the liquid expire, dispersed heavy body starts moving in the stagnant fluid only under gravitational and buoyant forces. Archimedes law of buoyancy is the simplest approach for the gravity-based movement of a body in liquid. The dimensionless Archimedes number ($Ar = gL^3\rho_1(\rho - \rho_1)/\mu^2$, g = gravitational acceleration, L = characteristic length of body, ρ_1 = density of the fluid, ρ = density of the body and μ = dynamic viscosity of the fluid) has been generated to determine the motion of a body in a fluid due to density differences. When; $Ar \gg 1$, less dense bodies rise and denser bodies sink in the fluid. The highest Ar is possible with the maximum density difference and minimum fluid viscosity. The similar theory was employed by Stokes to analyze velocity of falling body in a liquid. In his work, slip velocity of a falling sphere in a Newtonian fluid was observed and explained by an

analytical formula ^[25]: $\vartheta_s = (\rho - \rho_f)gd^2/18\mu$ (ρ = Density of particle slipping in fluid, ρ_f = density of fluid, d = Diameter of sphere particle, μ = viscosity of fluid). Non-Newtonian fluids as the stagnant medium was studied by Dedegil ^[26]. He developed a particle velocity equation that involves the yield stress and the drag coefficient (C_D) generated by the ambient Non-Newtonian liquid. Drag coefficient of particles in structurally viscous fluids was considered as a function of particle Reynolds number, and functions based on experimental measurements were used ^[27].

Governing parameters of a particle slipping in fluid can be the density differential of the particle and the fluid, viscosity of the fluid and the particle diameter. However, the mechanism of heavy liquid droplets slipping in a stagnant medium is different. Krishna et al. ^[28] found a relationship between the terminal velocity and spherical diameter of immiscible droplets falling in fresh water ^[28]. They performed experiments with immiscible liquid drops with various densities, interfacial tensions and viscosities. As a result, they determined that viscosity of heavier fluids has no significant effect on terminal velocities of slipping droplets, and the velocity of a droplet starts decreasing after the droplet diameter exceeds certain (peak) value. Abdelouahab and Gatignol ^[29] generated analytical formulas that validate Krishna et al.'s experiments. They defined the limits of their model with the maximum stable droplet diameter proposed by Clift and Weber ^[30], which consisted of interfacial tension and density differential between fluids. Bozzano and Dente ^[31] also modeled droplet terminal velocity numerically, by relating the friction factor of the droplet to two dimensionless numbers: Eötvös number and Morton number. They developed expressions covering all droplet Reynolds numbers. Analytical formulas describing phenomena, discussed above, are provided in the following chapters.

In the light of previous studies, vertical and horizontal injection of a heavier fluid into an annulus filled with a lighter fluid follows different physics. Introducing heavy fluid through vertically placed tubing causes positive free jetting of the liquid and is not instantly affected by the annular boundaries. In contrast side-injection into annulus is instantly affected by the presence of the inner pipe wall boundary. It is a penetration of an axisymmetric positive impinging jet confined by the casing wall. Both scenarios of immiscible jetting may result in formation of droplets and these droplets that are supposed to settle at the bottom by traveling downwards in a counter-current flow of the annular fluid.

CHAPTER 2: CHARACTERIZATION OF ANNULAR FLUID

2.1 Objective

An annulus infected with SCP is expected to be full of the fluid (annular fluid) that remains after the cementing operation. Since the only access to any casing annulus is the top valve on the wellhead, taking samples of the fluids from inside has been extremely difficult. So, there is little information on properties and composition of these fluids. Properties of an aged annular fluid in the mature wells could only be predicted by long-term experiments simulating chronological process of the fluids aging from cementing operation to the time when migrating gas accumulates in the wellhead and the well reaches SCP equilibrium.

This chapter describes characterization of annular fluid (AF) by comparing a few published data with results of new experiments. The experiments with different annular fluids have been conducted over extended period of time.

2.2 Literature Review on Characterization of Annular Fluid

Cementing operation is the main component of drilling process for supporting the casing and protecting it from corrosion, and isolating different formations penetrated by the well^[32]. Typical cementing operation involves; running the casing down to the hole and creating an annulus, then pumping cement through inside of the casing by displacing the drilling fluid to the surface. During casing run, especially at extended reach wells, casing can be buckled and rotated for better axial force transfer. Rotation and/or buckling creates a different flow geometry than concentric or eccentric annuli ^[33] and should be considered during cementing. For cement to make a good bond with the formation and pipe, all the mud must be displaced by the cement ^[34]. Ideally cement should push out the entire initial fluid and reach to the surface; however, due to either calculation errors or economic reasons, the top of cement usually cannot make it to the well-head. Therefore, an annular fluid fills out the space between two casings above the top of cement. When the cement leaks gas, the aged annular fluid gets exposed to gas migration.

Drilling fluids, also known as the drilling muds, are mainly made with organic clays and weighting agents. A good cementing operation is possible by cleaning the well from mud and its cake efficiently, by also preventing the cement slurry from contamination. Though, contact between the drilling mud and cement slurry often results in the generation of a viscous mass at

the cement/mud interface ^[35]. This may lead to channeling of displacing fluid (cement slurry) through the initial fluid (mud); leaving patches of contaminated mud sticking to the walls of the casing and formation. So, in order to ensure complete removal of the mud; spacers and pre-flushes are commonly suggested and used ^[32]. Generally pre-flushes are fluids with low density and viscosity that act by thinning and dispersing the mud. Spacers are, on the other hand, carry weighting agents and fluid loss agents, and are generally characterized as a thickened composition which functions primarily as a fluid piston in displacing of mud in the well ^[36]. A better well cleaning can be achieved with turbulent flow in the annulus. It is important to accurately estimate the local stability of the fluid in the annulus, so that flow rate can be adjusted for the turbulent flow ^[37]. The content and pumping techniques of water-based spacers have been studied and tested to improve their compatibility with water-based drilling fluids for the most efficient displacement ^[38-40]. Based on experience from the previous cementing operations, 10 minute contact time between spacer and cement was recommended for minimum contamination of cement, and spacer to pre-flush ratio was suggested as four ^[35]. After the cementing operation; casing annulus is shut down and the remaining fluid, which is a combination of pre-flush, spacer and drilling mud is trapped between two casings, cement top and the well-head. As the time passes, fluid in the annulus transforms into a stagnant liquid column having thixotropic properties and stratified by gravity.

Gel strength is one of the significant properties of a drilling mud. During drilling operations, early (10 minutes) gel is considered an advantageous property, which acts to suspend drill cuttings and other solid additives such as the weighting agents within its structure when the mud is under static conditions^[41]. Experiments showed that the oil based muds build less gel strength than the water based muds^[42, 43]. Makinde et al. ^[44] studied the effects of temperature and aging time on properties of water-based drilling fluids. According to their experiments; plastic viscosities, yield point and gel strengths of water-based drilling fluids diminish with time and temperature. Erge ^[45] conducted a similar study on the temperature effect on the water-based fluids and observed similar results. With not enough gel strengths static settling of solids – particularly barite – in the fluid is expected to be much greater^[46].

Barite settling in stagnant drilling fluid (Barite Sag) is an undesirable problem in drilling operations ^[43] and causes density stratification in the mud column^[47]. In a drilling operation

barite sag can cause problems such as differential sticking of the drill string, formation of density gradient, wellbore instability, lost circulation, and may lead to serious well control issues^[48, 49]. The settling can occur in both vertical and inclined fluid columns. The vertical case is often called “Hindered settling” or “Free settling” with a compaction regime at the bottom, hindered settling regime above the compaction regime, and the top clarification regime free from solid particles (Figure 2.1)^[46]. Hindered settling is slower than free settling of a single particle due to changing concentrations and packing of the solid particles in a fluid^[50]. Experiments on corpuscles settlements conducted by Boycott^[51] showed that the sedimentation rate of the particles is a function of tubing inclination. Later, similar approach has been investigated by many researchers in barite sagging^[52, 53]. In horizontal and vertical wells the shorter distance to the lower side of the wall results in rapid generation of solids beds as compared to that in vertical wells^[54].

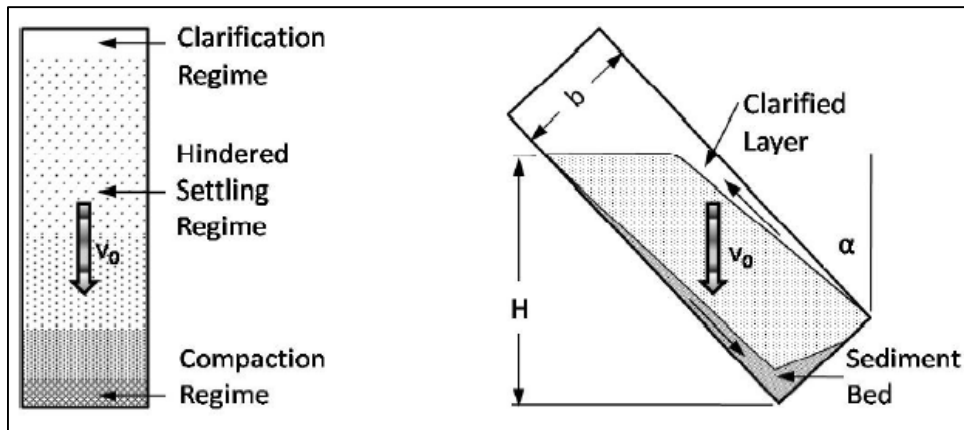


Figure 2.1: Hindered (left) and Boycott (right) settling kinetics under static conditions (V_0 is the particles settling velocity, H is the height, b is the width and α is the inclination angle)^[46].

Hanson et al.^[52] stated that the differences between the maximum and minimum mud weights after static sagging have been measured greater than 4 ppg. in the Gulf of Mexico^[52]. This difference was reported greater than 7 ppg. in oil base muds in the North Sea. In Atlantic Canada, the density recorded during the bottoms-up circulation of the 11.3-lb/gal SBM varied from 10.2 to 16.9 ppg.^[47]. In another study on cement spacers, it was stated that a good portion of barite in the spacer settled out in a short time when held under static conditions^[55].

In a gas-leaking well, gas bubbles are expected to migrate through the annular fluid column. Saasen et al.^[53] conducted experiments in a 2.13-meter pipe to evaluate and measure the effects

of fluid properties on barite sag. Two of their mud samples contained some small bubbles of residual air entrapped during mixing, and showed severe sag compared to the gas-cut samples. They reported that the migration of bubbles during the static period may induce barite sagging, but no further considerations were given^[53]. According to another study on drilling fluid reserve pits, as the depth in the pit increases; the density of the fluid gets heavier^[56]. A watery layer of light mud was observed at the top of drilling reserve pits that may have resulted from rainfalls. In addition to mud thinning due settling solids, a decanting column of free water develops on top of stagnant mud. Clay slurry dewatering experiments showed that calcium and magnesium-contaminated bentonite would release more water comparing to the pure sodium bentonite slurries^[57]. Bol ^[58] performed 24 hour free-water settling tests by using bentonite slurries with different concentrations and compositions. His experiments indicated that top-settling of water can occur from zero to 46 percent of the total slurry height. All the findings above support the three-zone stratification of an aged mud column shown in Figure 2.1. Many researchers have been trying to predict the height of these zones. In Figure 2.2, a centrifuge experiment conducted with weighted synthetic-based mud matched with an unpublished empirical model is shown. The plot measurements and the model indicate three zones – 20% compaction zone, %25 hindered settling zone and 55% clarification zone – similar to the discussion above ^[47].

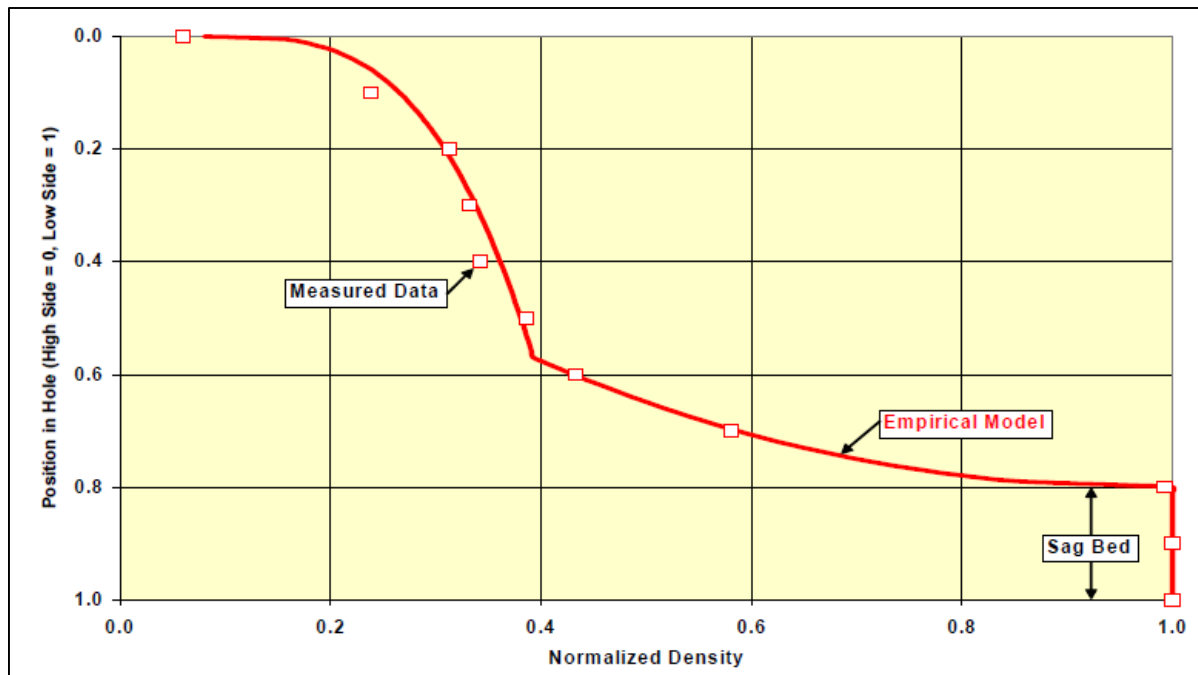


Figure 2.2: Plot of measured and predicted density of centrifuged synthetic based weighted mud. Using unpublished empirical formulas ^[47].

As discussed above, a compacted zone of settled barite is expected to deposit on the top of cement in the well is annulus. Size of this zone is important for well P&A operation using the cut-and-pull method that involves removing the inner casing and placing cement to maintain downhole integrity. One of the challenges of this method encountered by the industry was the incapability of production casing to be pulled up due to the compacted zone of settled Barite^[59]. Thus, the top of this zone should be estimated to perform a successful cut-and-pull operation. Conventional CBL (cement bond log) technology and invention of ultrasonic tools are still not accurate enough due of uncertainty of interpretation^[60]. Another relatively new logging technique called Third-Interface Echo (TIE) improves detection of the type of material in the entire annular volume^[61]. A combination of these measurements and known system parameters – such as the casing wall thickness and properties of annular fluid – provides definitive determination of zonal isolation^[60]. However, the improved technology would still not work with thick casings, light cements and heavy mud until a technique called the Isolation Scanner was introduced^[62]. The scanner is able to predict the materials behind the casing including the contaminated cements, heavy muds and annular solid sags^[63]. Consequently, the tool is capable to detect the top of compacted barite zone above the cement. Figure 2.3 shows a well interpretation consisted of various conventional logs and Isolation scanner to determine the level of cut-and-pull. As shown in the “Annulus Material” column of the figure, isolation scanner indicates an approximate 625-foot column of sagged barite on top of the cement. Furthermore, azimuthal evaluation shows the lightweight mud column above the barite section.

2.3 Determination of Annular Fluid Initial Properties

Annular fluid is a combination of three components: drilling mud, spacer and pre-flush. According to the definition, spacer should have the highest and pre-flush should have the lowest density among the components. Even though the properties of these fluids are theoretically known, companies sell spacers as commercial product and their composition is confidential. For this study, formulations of these fluids were taken from the patent of Griffin and Moran ^[36] and from the Well Cementing book of Nelson ^[35]. Then. The three components mixed together to create a typical annular fluid.

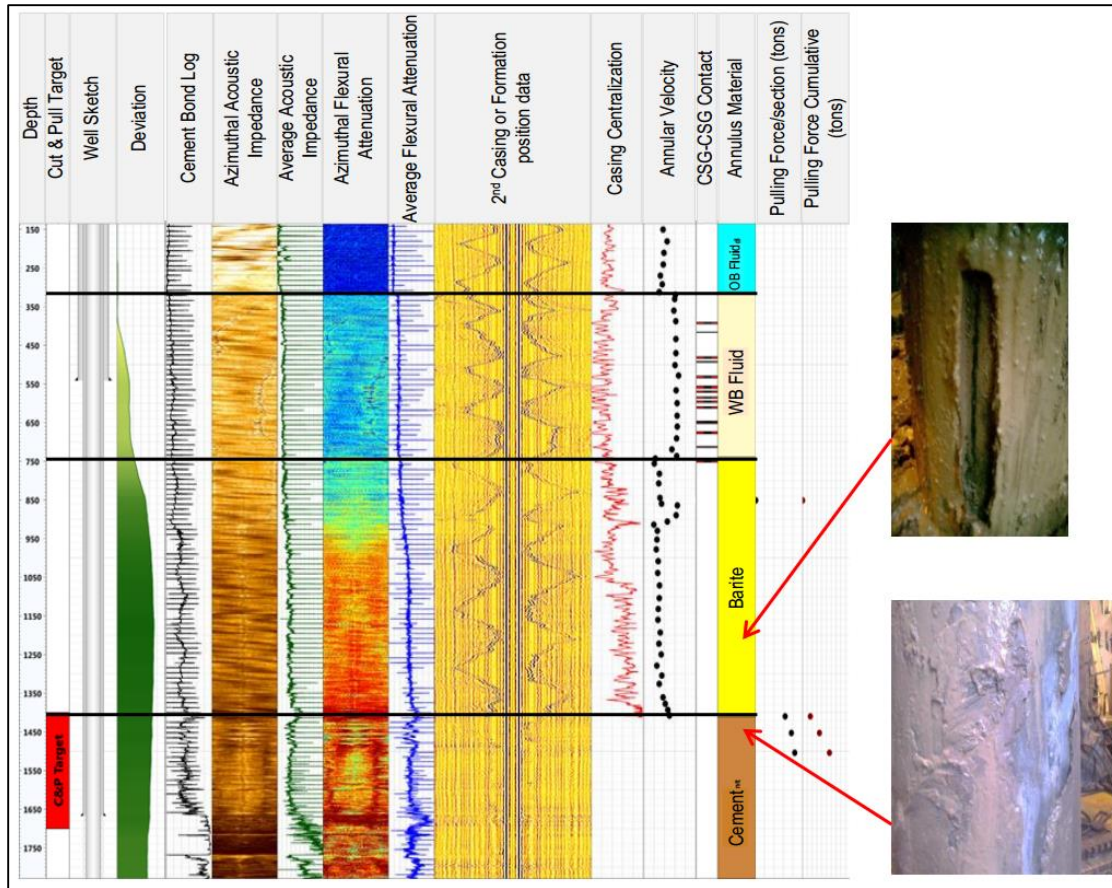


Figure 2.3: A well interpretation combined with conventional logs and Isolation Scanner to determine cut-and-pull level^[63].

2.3.1 Generating Annular Fluid in Lab

Firstly, 350 mL of a typical water-based drilling mud was mixed in the laboratory by adding 6% by weight (22 ppb) bentonite clay into 303 mL of water and weighting up to 12 ppg with 197 grams of barium sulfate.

The main duty of pre-flush is to decrease the density of the mud and to sweep for incoming spacer and cement slurry. This low density fluid is often water; thus, in some cases, to improve the dissolution of sticky mud cake on the casing wall, alcohol is mixed into water as well as various kinds of surfactants. To imitate the similar formula; a half and half mixture of 6.6 ppg isopropyl alcohol and tap water was used as the pre-flush.

Spacer is a complex mixture made mostly of water-soluble polymers, cellulose derivatives and organic clays. A spacer's density should be between the slurry and the mud, and also its viscosity should be as low as possible to allow turbulent flow at reasonable pumping rates for a

more efficient annular cleaning ^[35]. Accordingly, based on the patented formula^[36], a 13 ppg spacer was generated in the laboratory by adding 14.58 grams of bentonite, 7 grams of silica, 8 grams of calcium chloride, 3.5 grams of CMC and 250 grams of Barite into 350 mL of water. Rheology readings of both drilling mud and spacer were taken just after mixing.

Finally, three combinations of all these three components with different ratios; 80% Mud - 20% Pre-flush, 80% Mud - 20% Spacer, and 60% Mud - 20% Spacer - 20% Pre-flush were poured into one-liter beakers based on an order as it would be in an actual well: spacer at the bottom, pre-flush in the middle and drilling mud at the top. To overcome the chemical reactions and overtime mixing; all the beakers were isolated from the atmosphere and were stored in room temperature for 30 days before the necessary measurements.

2.3.2 Generalization of Annular Fluid Formula

As shown in Figure 2.4, all the fluid samples except the 80-20 percent mud-spacer mixture show similar rheology to that of a drilling mud. The reason of this high rheology was thought to be due to the high CMC concentration in the spacer. However, the mixture does not represent annular fluid because lack of preflush. When the spacer is mixed with the pre-flush together, its density the mixture becomes similar to the, as shown in Figure 2.4, initial mud properties.

In conclusion; although annular fluids in different wells may be different; they are expected to have similar density and rheological behavior to a typical drilling mud. Therefore, experiments on aging of annular fluid have been conducted with various water-based drilling muds.

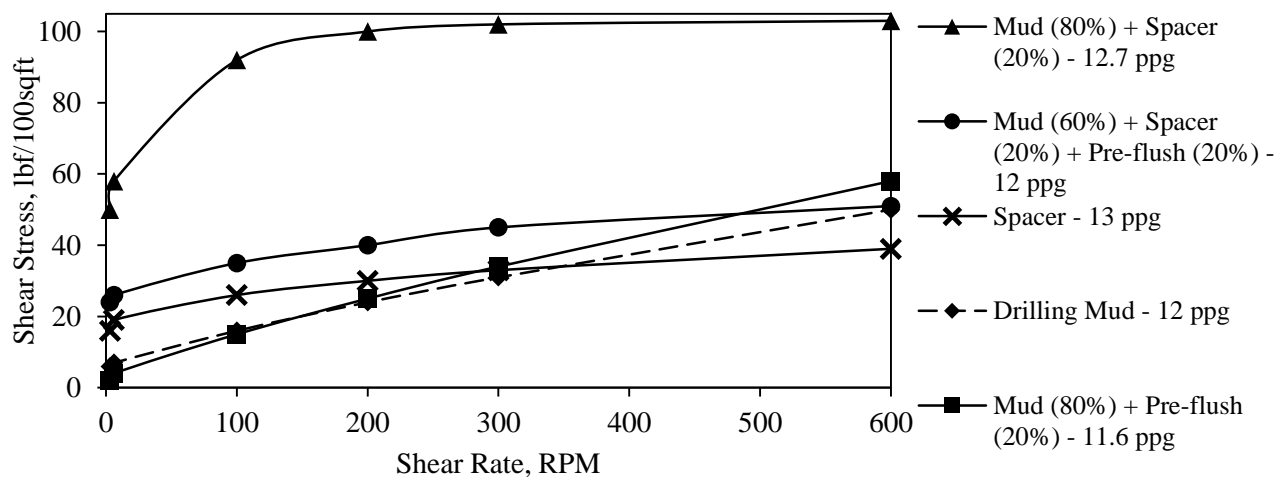


Figure 2.4: Rheology of drilling mud, spacer and annular fluid mixtures

2.4 Static Mud Column Experiments

Long-term gelation of stagnant drilling mud has been often discussed, and theoretically and experimentally studied by many researchers. However, previous field studies only considered the duration of static sagging at a maximum of 76 hours, due to the needs of drilling operators ^[47]. Lab studies also involved similar or less experimental durations. In a SCP-affected well, this time frame needs to be extended to months, or even years. In order to obtain a better prediction of an aged annular fluid, a series of pilot experiments have been carried out.

2.4.1 Experimental Set-up, Matrix and Procedure

A ten-foot column of the 4" PVC pipe was equipped with valves and pressure gauges spaced 18" apart 4" above the pipe bottom (Figure 2.6). For each test the column was filled with a water-based weighted drilling mud and initial hydrostatic pressure at each depth was measured. At the end of each test (3 to 11 weeks) final pressure values were measured (Figure 2.5). Then, samples of the mud were taken from each valve and their properties were measured. Initial properties of the muds are given in Table 2.1.



Figure 2.5: Picture of the mud/free water interface after 11 weeks of static settling



Figure 2.6: Picture of the 10-foot column.

Table 2.1: Properties of drilling muds used in static column experiments.

Static time, weeks	ρ (ppg)	μ_p (cP)	τ_0 (lbf/100sqft)	τ_{g10m} (lbf/100sqft)
3	12.5	10	4	5
4	12.5	9	3	4
7	13.6	20	9	9
11	14.5	30	30	16

2.4.2 Results of Static Column Experiments

Experiments showed density distribution with depth - Figure 2.7. In all tests there was a compaction zones at the bottom, free-water zone at the top, and a column of un-weighted mud in between. According to pressure readings taken from the gage installed on the bottom valve; compaction zone was still able to transmit the same hydrostatic pressure, (though gages were usually clogged due to bridged barite).

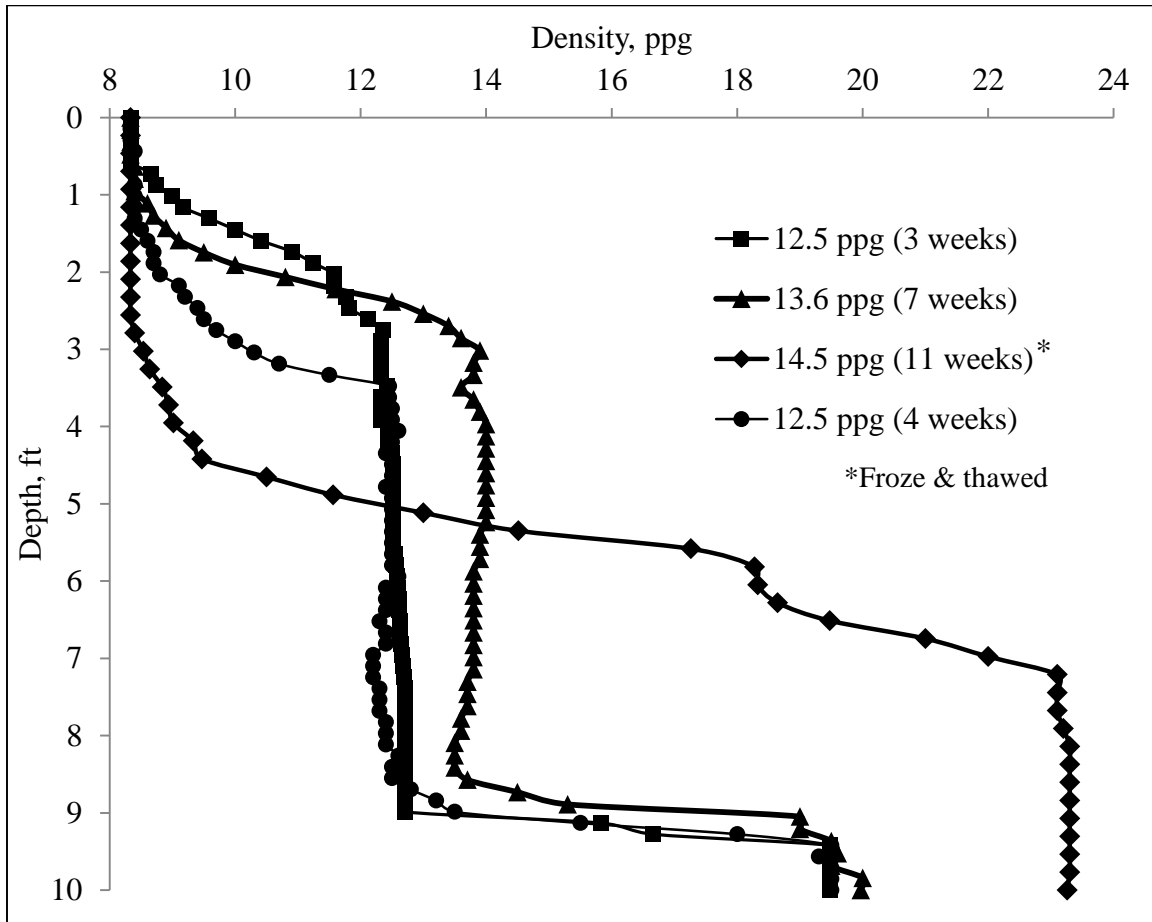


Figure 2.7: Density distribution of static mud experiments after certain times

The longest static time, 11 weeks, showed the tallest compaction zone and its density. However, during the experiment, outside temperature dropped under the freezing point for a few times. In the results, the mud froze and thawed occasionally during the experiment. Drop in temperature should increase gel strength in a water based drilling mud^[64]. However, dropping below the freeze point might have caused destabilization of hydrated clay structures^[65]. Considering this, more runs of the same mud were made.

Results of all experiments show density of the same compaction zone around 20 ppg. The top sections of the fluid columns were free-water underlain by un-weighted muds. The height of these sections and transitions between the heavy and light mud sections showed some differences. For example, 12.5 ppg mud with 4 weeks of static time had more un-weighted mud at the top compared to the one that stayed for 3 weeks. In addition, as the mud density went up; yield stress values in the mud sections were also increased.

2.5 Mud Column Density Distribution vs. Time

Another experiment was conducted to determine density change in a stagnant mud column over time. Particularly important was to find the effect of progressive gelation on Barite sag.

A twenty-foot pilot-scale physical model of 6” by 8” annulus was fabricated using steel pipes. Four pressure transducers were installed every 4 feet starting from 6” from the bottom of the annulus. More information about this model can be found in chapter 5.2.1 .

The column was filled with 13.2 ppg water-based bentonite mud, having plastic viscosity 65 cP, yield point of 20 lbf/100sqft, and progressive gel strength that would reach its maximum value of 80 lbf/100sqft in 8 to 15 hours as shown in Figure 2.8. Pressure values recorded every 30 seconds for 16 hours, were then converted to density of the mud column above each transducer.

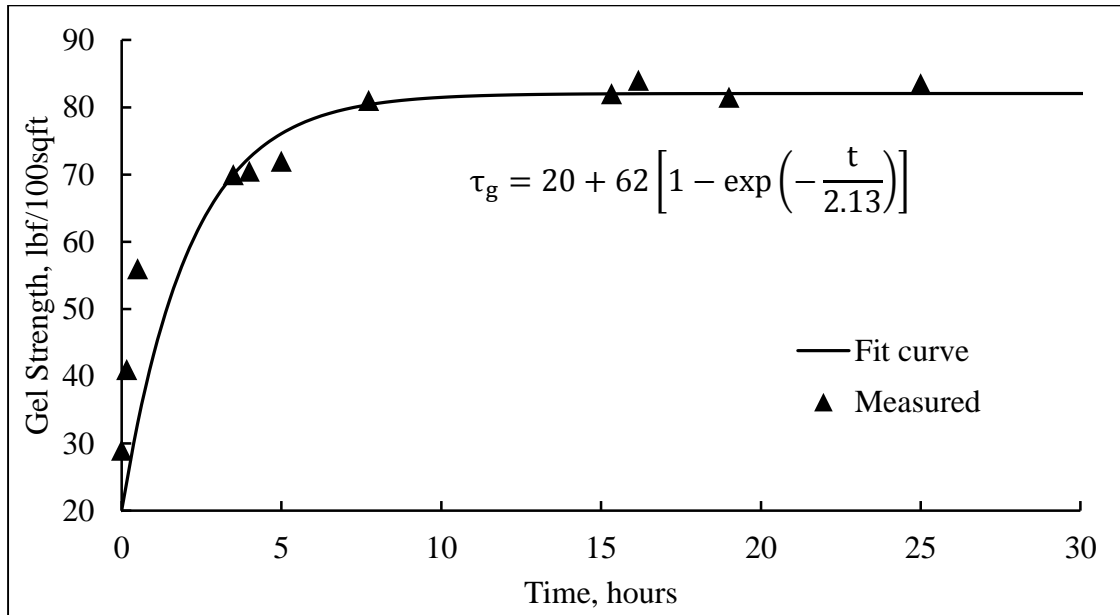


Figure 2.8: Progressive gel strength vs time plot

Four density plots are shown in Figure 2.9. All plots follow similar trends by they differ by density values. The initial increase is caused by the migration of air bubbles trapped in the mud during annulus fill-up. The reason for pressure (and density) drop in the 6th hour is the accidental activation of the safety valve. However, after the valve was closed, the pressure re-built to the same value in the 8th hour. After the 8th hour, there is a significant reduction of density (by 0.6-1 ppg) in all mud sections of the annulus despite the constant and high value of gel strength. The top mud section shows the highest reduction in density and the total mud column density drop is the smallest.

The results cannot be clearly explained – particularly the while mud column density drop. The upper mud sections lost density due barite settling despite high gel strength. Apparently gel strength was unable to prevent the settling or its actual value during Barite settling was smaller than that measured in viscometer and plotted in Figure 2.9.

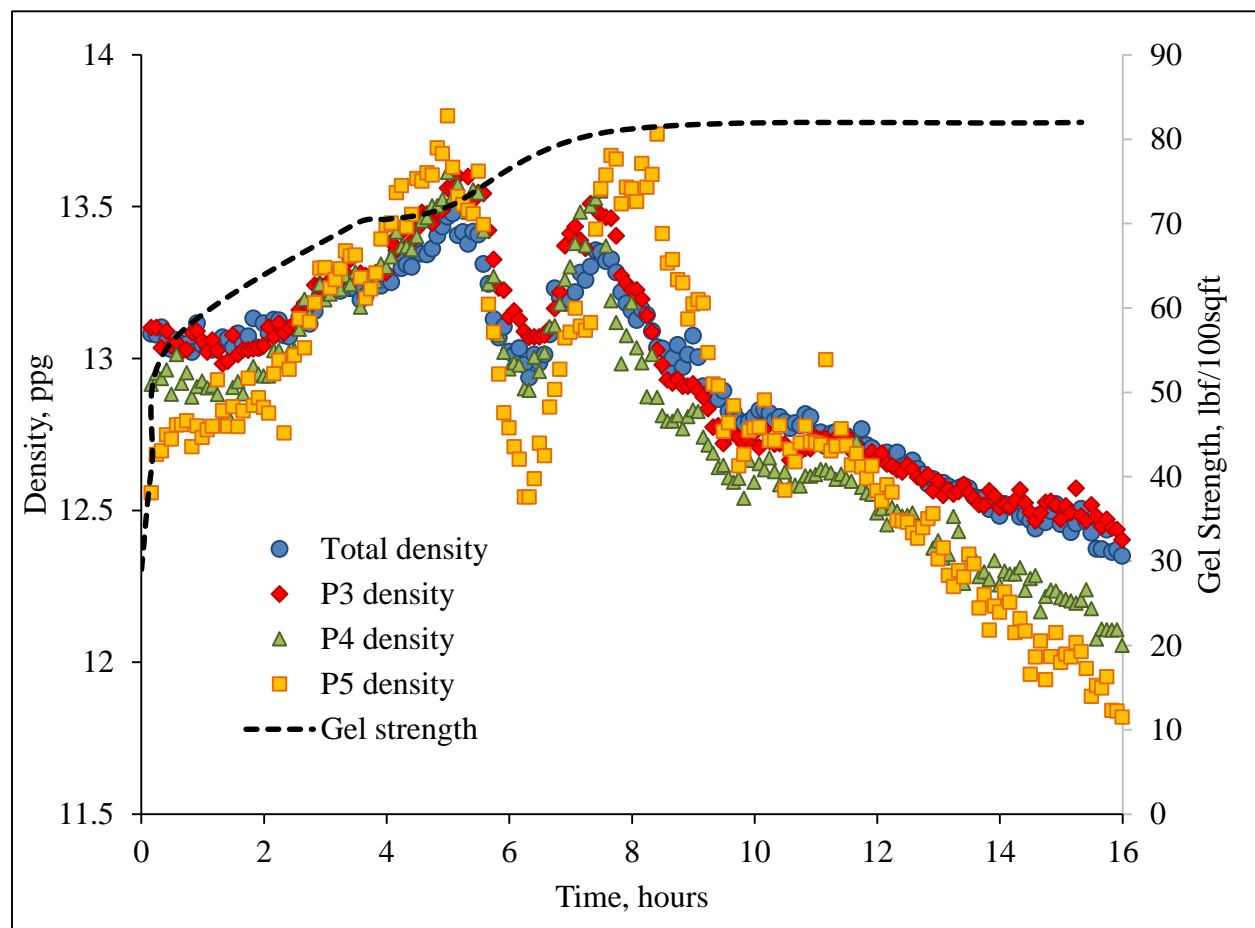


Figure 2.9: Drop of stagnant mud column density in time

Reduction in gel strength might be the cause or result of Barite settling as the two-phenomenon affect each other. Results of the mud aging study performed by Makinde et al. [44] showed gel strength reduction over time. However, testing of gel strength (Figure 2.8) disproves this finding. The reason of the contradiction may be the gel strength testing itself using viscometer. In the viscometer the mud sample is uniformly mixed before testing, so any settling of barite in the very small gap between the bob and cylinder is small or none. In the actual well, however, settling volume is not confined so the loss of Barite reduces the gel strength that in turn, enhances Barite sag. This seems to be the only way to explain formation of the free water section at the top of mud column.

In summary, the annular fluid characterization study shows that:

- Annular fluid and drilling mud are sufficiently similar so that the initial water-based drilling mud can represent the annular fluid after cementing.
- Over time weighted annular fluid undergoes the process of Barite sagging that cannot be prevented by progressive gelation.
- Final stratification of annular fluid includes free water top section and a bottom section of fluidized Barite bed (density ≈ 20 ppg) with an un-weighted mud section in between.

2.6 Prediction of Barite Bed Height

Height of the Barite bed can roughly be calculated by assuming that all the barite would settle down to the bottom over long time.

Then, density of the compacted section is,

$$\rho_c = \rho_B - \emptyset(\rho_B - \rho_{um}) \quad (2.1)$$

Where, \emptyset is estimated compaction zone porosity, ρ_B is the barite density (35 ppg), ρ_c is the compaction zone density (ppg), ρ_{um} is the un-weighted mud density (~ 8.6 ppg.)

Mud weighting formulas are,

$$V_{um} = V_a \frac{\rho_B - \rho_{mud}}{\rho_B - \rho_{um}} \quad (2.2)$$

$$m_B = (V_a - V_{um})\rho_B \quad (2.3)$$

so, the total mass of Barite is,

$$m_B = \left(\frac{\rho_{\text{mud}} - \rho_{\text{um}}}{\rho_B - \rho_{\text{um}}} \right) V_a * \rho_B \quad (2.4)$$

and the volume of compaction zone is,

$$V_c = \frac{m_B + V_c \emptyset \rho_{\text{um}}}{\rho_c}$$

Or,

$$V_c = \left(\frac{\rho_{\text{mud}} - \rho_{\text{um}}}{\rho_B - \rho_{\text{um}}} \right) \frac{V_a * \rho_B}{\rho_c} + \frac{V_c \emptyset \rho_{\text{um}}}{\rho_c} \quad (2.5)$$

Converting volume to annular height gives,

$$h_c = \left(\frac{\rho_{\text{mud}} - \rho_{\text{um}}}{\rho_B - \rho_{\text{um}}} \right) \frac{h_a * \rho_B}{\rho_c - \emptyset \rho_{\text{um}}} \quad (2.6)$$

and substituting Equation 2.1 gives,

$$h_c = \left(\frac{\rho_{\text{mud}} - \rho_{\text{um}}}{\rho_B - \rho_{\text{um}}} \right) \frac{h_a * \rho_B}{\rho_B - \emptyset(\rho_B - \rho_{\text{um}}) - \emptyset \rho_{\text{um}}}$$

or, finally,

$$h_c = \left(\frac{\rho_{\text{mud}} - \rho_{\text{um}}}{\rho_B - \rho_{\text{um}}} \right) \frac{h_a}{(1 - \emptyset)} \quad (2.7)$$

h_c – height of the compaction zone, feet

\emptyset – estimated compaction porosity

ρ_{mud} – initial mud density, ppg

h_a – height of annulus above cement, feet

ρ_{mud} – weighted mud density, ppg

V_a - volume of annulus above cement, gal

V_{um} – initial volume of un-weighted mud, gal

Practical use of Equation (2.7) requires value for the compaction zone porosity, \emptyset .

2.7 Compaction Zone Porosity

In order to estimate the compaction zone porosity, lab experiments were conducted in 100 mL graduated cylinders using mixture of water and barite (Figure 2.10). Empty (w_{empty}) and full (w_{full}) cylinder weights and compaction zone volumes are measured and used for calculating the compaction zone porosity.

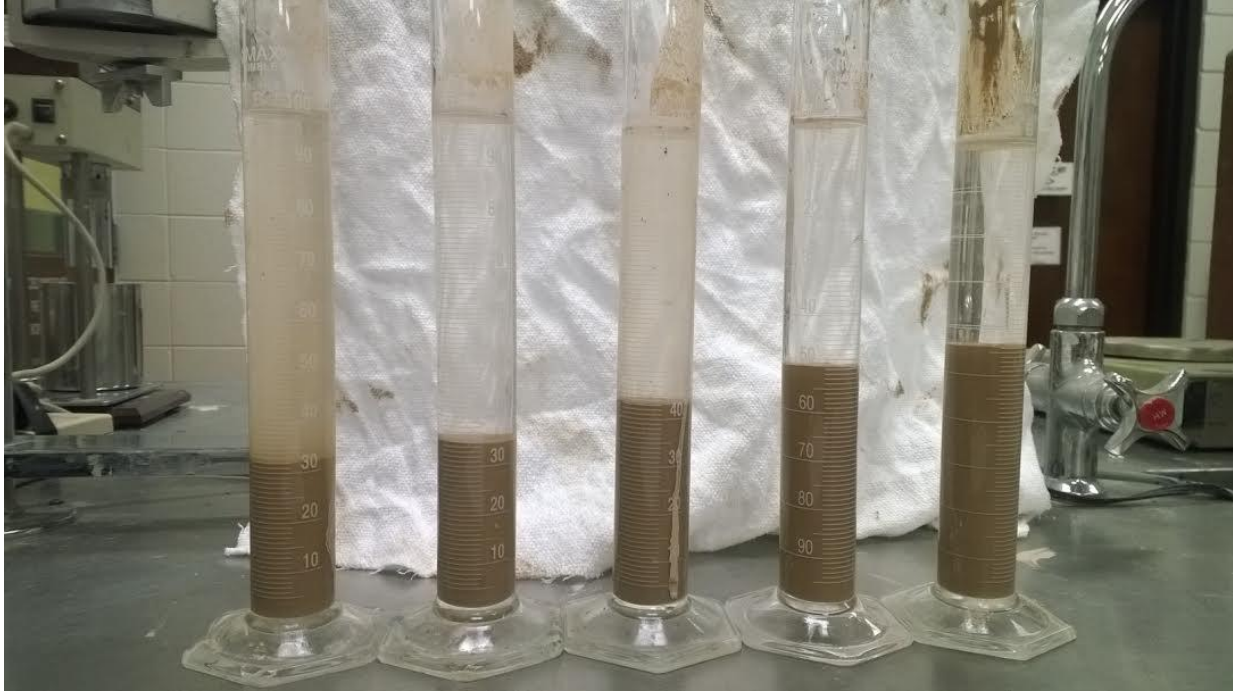


Figure 2.10: Porosity experiment. Weights and compaction volumes are measured.

For interpreting the experimental measurements equations below are used. The results are shown in Table 2.2.

Mixture density is calculated as,

$$\rho_{\text{mixture}} = (w_{\text{full}} - w_{\text{empty}})/100$$

After the settling is completed, sag density can be estimated as,

$$\rho_{\text{compaction}} = \frac{[w_{\text{full}} - w_{\text{empty}} - (100 - V_{\text{compaction}}) * \rho_{\text{water}}]}{V_{\text{compaction}}}$$

Remembering,

$$\rho_c = (1 - \emptyset) \rho_{\text{barite}} + \emptyset \rho_{\text{water}}$$

Porosity can be found by,

$$\emptyset = \frac{\rho_{\text{barite}} - \rho_{\text{compaction}}}{\rho_{\text{barite}} - \rho_{\text{water}}}$$

Table 2.2: Table of experimental porosity data for compaction zone density calculations

#	Empty cylinder wt. (gr)	Full cylinder wt. (gr)	Mixture density (g/cc)	Compaction volume (mL)	Compaction density (g/cc)	Estimated porosity
1	131.01	270	1.39	32	2.22	0.62
2	129.87	275	1.45	35	2.29	0.60
3	132.2	293	1.61	43.5	2.40	0.56
4	138.95	308	1.69	47	2.47	0.54
5	131.31	309	1.77	51.5	2.51	0.53

According to measurements, compaction zone porosities were lower for heavier mixtures of barite with water. The results are used for a compaction porosity model that would work for the muds that use barite as the weighting agent ($\rho_{\text{barite}} = 35$ ppg). The model fit is shown in Figure 2.11.

$$\emptyset(\rho_{\text{mud}}) = -0.026 \rho_{\text{mud}} + 0.909 \quad (2.8)$$

By employing Equations 2.7 and 2.8 an estimation of compaction zone height can be made. Experiments were conducted with a mixture of barite and water, thus, the model ignores the suspended barite in the mud structure and also ignores the cuttings remained from drilling. The model would roughly determine the displaceable annular fluid volume. Formulas can also provide help to cut and pull method; where the desired level of cutter should correspond to a barite-free region, to be able to pull the terminated casing.

For theoretical illustration, change in compaction height with increasing mud density is plotted in Figure 2.12. A 3000-foot annulus and un-weighted mud density of 8.6 ppg are used for the calculations.

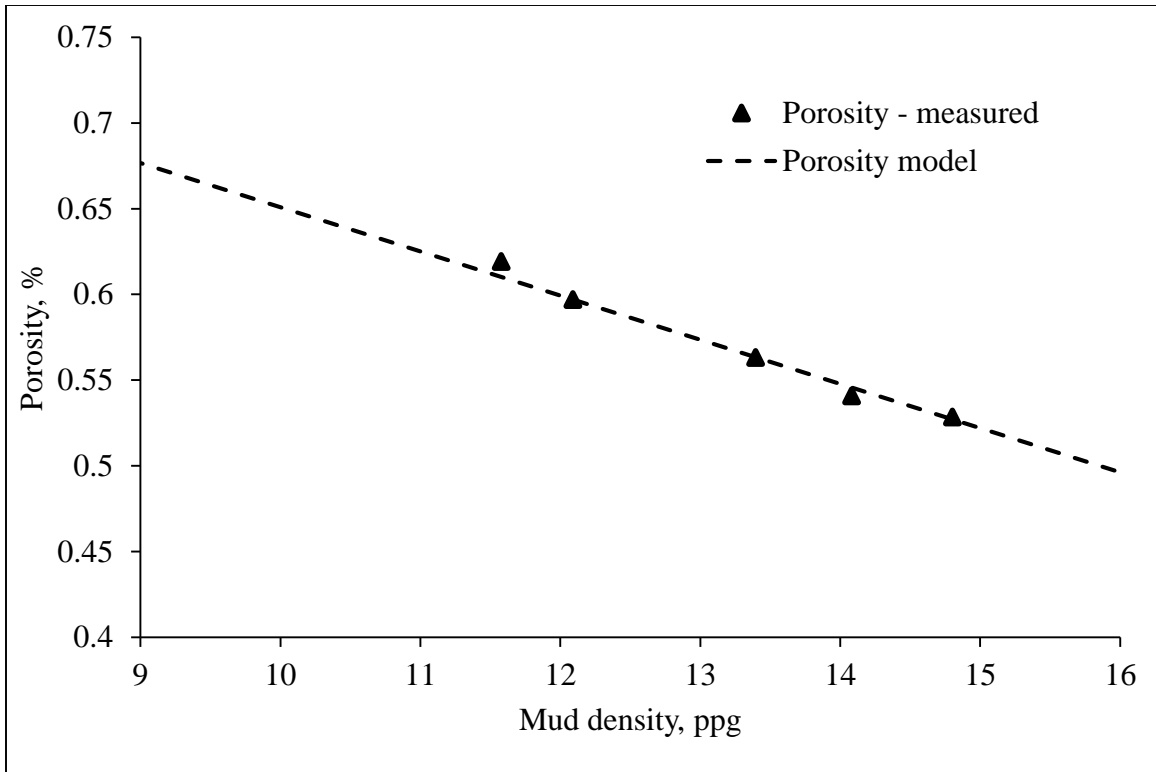


Figure 2.11: Plot of compaction zone porosity experimental data and model

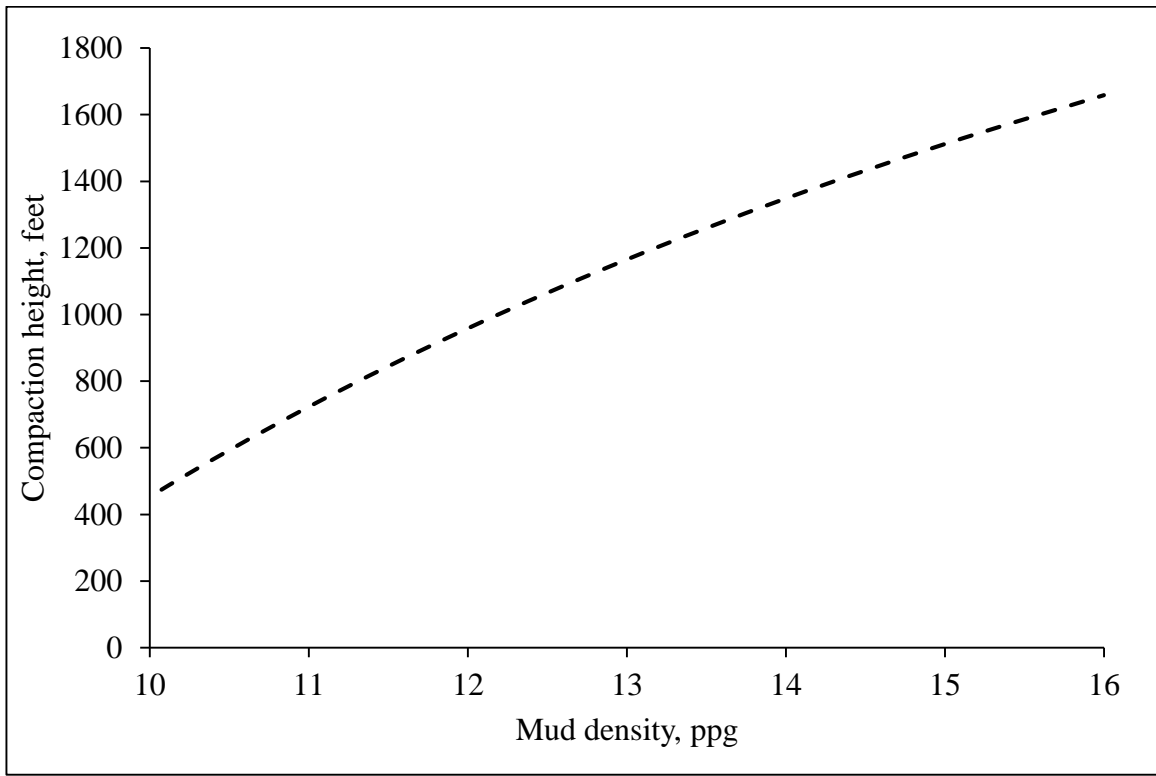


Figure 2.12: Change in compaction height with increasing mud density

CHAPTER 3: SELECTION OF KILL FLUID

3.1 Objective

As discussed above, past applications of the Bleed-and-Lube technique failed mostly because of the miscible kill fluid (KF) mixing with annular water-based fluid (AF).^[8] In this chapter, an immiscible kill fluid is defined theoretically, manufactured and evaluated in laboratory tests.

3.2 Criteria and Desired Properties of Kill Fluid

Ultimate performance of the annular displacement process is hydrostatic pressure replacement with the kill fluid as,

$$\Delta P_b = 0.052(\rho_{kf} - \rho_{af})h_a = 0.052 \Delta \rho h_a$$

As the fluid displacement may not always be complete, the most desirable KF should be one with largest density: $\rho_{kf} \rightarrow \text{Max}$

Buoyant slippage is the transport mechanism of the KF travelling downwards inside the column of AF. To make the process effective, gravity forces must significantly exceed viscous forces. The force ratio is represented by Archimedes number as,

$$Ar = \frac{g d^3 \rho_{af}(\rho_{kf} - \rho_{af})}{\mu_{af}^2}$$

Thus, maximum Ar requires KF providing maximum ratio: $\Delta \rho / \mu_{af}^2 \rightarrow \text{Max}$

LSU tests, discussed above, suggested that the heavy fluid (kill fluid, KF) candidate for a successful displacement should be immiscible with water based annular fluids (AF). Immiscibility is often described by the term called the partitioning or partition coefficient. Partition coefficient (logP) is a ratio of concentrations of a compound in two phases of a mixture of two immiscible liquids at equilibrium. High logP would mean low amount of KF dissolving in surrounding liquid (water) and high hydrophobia, shown as,

$$\log(P) = \log\left(\frac{[\text{solute}]_{\text{solution}}}{[\text{solute}]_{\text{water}}}\right)$$

Thus, theoretically, a KF would be immiscible with the water-based AF: $\log(P) \rightarrow \text{Max}$

After injection into well's annulus, KF is expected to break into droplets and start slipping downwards dependent on both annular and kill fluid properties. Theoretically, with no mixing, each KF particle (droplet) injected must move downwards by buoyant slippage. Assuming the injection rate constrained by the Rayleigh mechanism of the first and second wind-induced regime of the falling stream of droplets, discussed above (Figure 1.5), complete displacement time can be defined as,

$$t_d = \frac{h_a}{\vartheta_d} + \frac{V_a}{q} \quad (3.1)$$

where, t_d is total displacement time, h_a is annulus height, ϑ_d is droplet velocity, V_a is annular volume and q is injection rate.

Injection rate is the volume of kill fluid entering to the system per unit time. Assuming that KF disperses into identical spherical droplets immediately after issuing into AF, flow rate can be written as,

$$q = N V_d \quad (3.2)$$

where, N is the number of droplets entering into system per unit time and V_d is the droplet volume.

If the stream of spherical droplets forms a continuous rope having droplet size diameter, d , there is maximum number of droplets generated in unit time, $N_{\max} = \vartheta_d/d$, and flow rate is,

$$q = 0.52 \vartheta_d d^2 \quad (3.3)$$

and the displacement time is,

$$t_d = \frac{h_a}{\vartheta_d} \left(1 + 1.91 \frac{A_a}{d^2} \right) \quad (3.4)$$

where, A_a is annular cross-sectional area.

In buoyant slippage, droplet size defines slip velocity. The relationship, shown in Figure 3.1, was found by Abdelouahab and Gatignol ^[29]. As already explained in the literature review chapter, above, terminal velocity increases with increasing droplet diameter reading its

maximum value. For larger sizes of droplets, velocity would reduce until it becomes independent from droplet size.

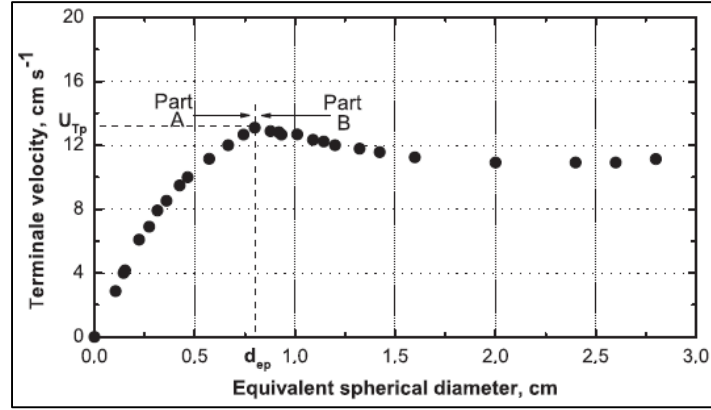


Figure 3.1: Terminal velocity vs. size of fluid droplets ^[28]

The authors proposed the following formula of velocity for Part A – velocity increase with droplet size as,

$$\vartheta_A = \vartheta_L / \left[1 + \left(\frac{82 m_p \mu_f}{\rho_f \alpha_p \vartheta_L d} \right)^2 \right]^{1/2} \quad (3.5)$$

where lift velocity, ϑ_L , is,

$$\vartheta_L = 2(\sigma g \Delta \rho / \rho_f^2)^{1/4} \quad (3.6)$$

and dimensionless fit factor, m_p , for peak velocity is,

$$m_p = \frac{\rho_f \vartheta_L}{82 \mu_f} d_p \sqrt{1 - \alpha_p^2} \quad (3.7)$$

and the ratio of velocities for peak velocity, α_p , is,

$$\alpha_p = 1 / \left[1 + \left(17.58 \frac{\mu_f \vartheta_L}{\sigma} \right)^{1/2} \right]^{1/2} \quad (3.8)$$

In order to compute maximum velocity from Equation 3.5 they proposed peak diameter formula as,

$$d_p = 1.311(\sigma / g \Delta \rho)^{1/2} \quad (3.9)$$

The authors also proposed velocity formula for Part B – velocity decrease with droplet size as,

$$\vartheta_B = \left[\frac{g \Delta \rho}{2 \alpha_p \rho_f} d + \frac{4 \alpha_p \sigma}{d \rho_f} \right]^{1/2} \quad (3.10)$$

In order to limit the size a maximum stable droplet diameter from Clift and Weber^[30] is used,

$$d_{\max} \approx 4(\sigma/g\Delta\rho)^{1/2} \quad (3.11)$$

where, σ is interfacial tension of fluids, $\Delta\rho$ is density difference between fluids, ρ_f is stagnant fluid density, μ_f is stagnant fluid viscosity and d is equivalent droplet diameter.

The above model is used to derive the minimum displacement time equation as,

$$t_{dA} = \frac{1}{60} \frac{h_a}{\vartheta_A} \left(1 + 1.91 \frac{A_a}{d^2} \right) \quad \text{for} \quad 0 < d < d_p \text{ (Part A)} \quad (3.12)$$

and,

$$t_{dB} = \frac{1}{60} \frac{h_a}{\vartheta_B} \left(1 + 1.91 \frac{A_a}{d^2} \right) \quad \text{for} \quad d_p < d < d_{\max} \text{ (Part B)} \quad (3.13)$$

As shown in Appendix-A, substituting explicit expressions for ϑ_A and ϑ_B gives two formulas for displacement time:

$$t_{dA} = \frac{h_a}{120 b} \sqrt{1 + \frac{a}{d^2}} \left(1 + 1.91 \frac{A_a}{d^2} \right) \quad \text{for } 0 < d < d_p$$

and,

$$t_{dB} = \frac{1}{60} \frac{h_a c \sqrt{d}}{\sqrt{e d^2 + f}} \left(1 + 1.91 \frac{A_a}{d^2} \right) \quad \text{for } d_p < d < d_{\max}$$

As proved in Appendix-A, the minimum displacement time is for the maximum droplet size, i.e. maximum terminal velocity. Abdelouahab and Gatignol^[29] stated the alpha peak value of 24 ppg bromoform as 0.871 and interfacial tension value as 40.6 dynes/cm. The same kill fluid displacing a 9 ppg fluid in a 3000-foot annulus (9 in – 7 in casings, $A_a=0.174$ sqft) is plotted in Figure 3.2.

The displacement time plot clearly indicates that increasing droplet size would reduce the droplets' travel time and the time needed to fill up the entire well annulus. For droplets larger than the peak-diameter droplet, the time would still reduce due to shortening of fill-up time with change of the travel time. As a result, feeding the system with the biggest droplet size would ultimately minimize the total time of displacement. Therefore, the maximum stable droplet size formula, Equation 3.12 ^[30], can be used to specify properties of the best immiscible kill fluid – the maximum ratio of interfacial tension, σ , to the KF/AF density difference, $\Delta\rho$.

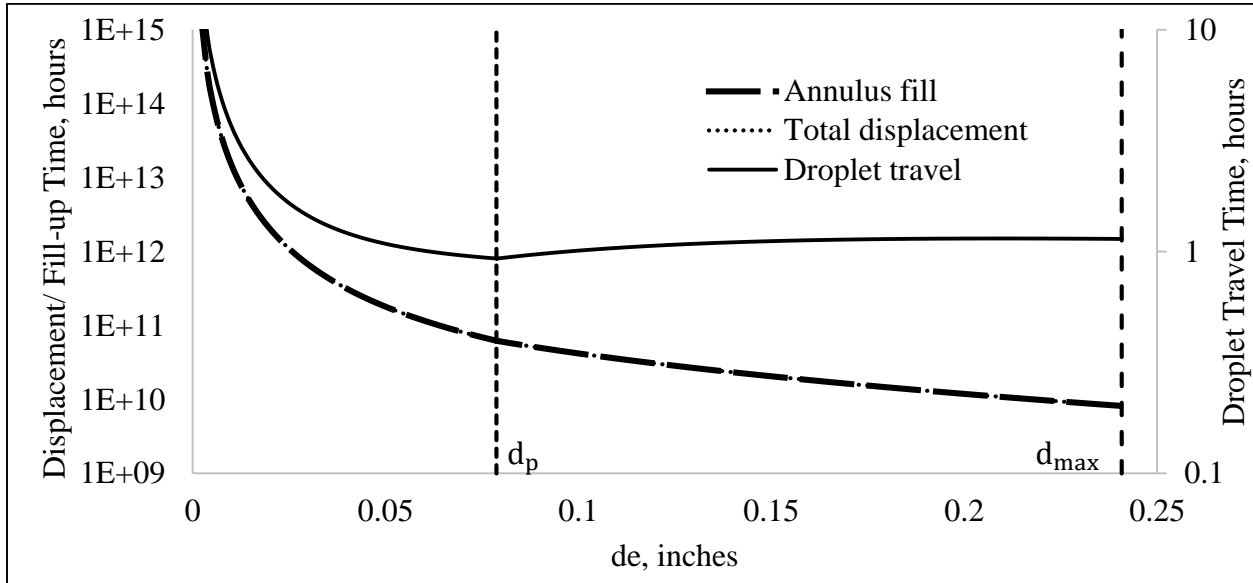


Figure 3.2: Example plot of displacement time and droplet traveling time changing with the droplet size

Table 3.1 summarizes kill fluid selection based on the above criteria. The analysis calls for low-viscosity of the annular fluid and high-density difference. However, since properties of the AF are given, KF should be designed specifically for a well with SCP. General specifications for KF require:

- Highest density of kill fluid;
- highest interfacial tension between the fluids; and,
- highest partitioning coefficient.

Table 3.1: Criteria and desired properties of kill fluid

Criteria	Property	Maximum/Minimum
----------	----------	-----------------

Pressure Replacement	$\Delta\rho = \rho_{kf} - \rho_{af}$	Maximum
Buoyancy	$\Delta\rho/\mu_{af}$	Maximum
Immiscibility	$\log(P)$	Maximum
Displacement time (Stable droplet size)	$\sigma/\Delta\rho$	Maximum

Fluids having the specified properties are available in the market; for instance, Abdelouahab and Gatignol ^[29] used bromoform, which is a derivative of bromine (Br), that has a specific gravity of 2.85 and is highly hydrophobic. However, these general properties are not sufficient for field use. Other specifications such as toxicity and corrosion rate (over 1 mm/year) make bromine a poor selection. Injecting a toxic and corrosive material in an annulus would result in failure of casings and might lead to environmental hazards. Another material called perchloroethylene, which is a kind of chlorocarbon, is a chemical being used for dry cleaning of fabrics. It appears to be less toxic and less corrosive as compared to bromine, while; its specific gravity can go up to 1.609. This liquid could be potentially used for remediating wells with low SCP, so, its applications would be limited.

3.3 Albemarle Brominated Organics

Albemarle Process Development Center – Bromine Research and Technology Group has developed fluids considering the selection requirements. They produced brominated organic liquids that have low viscosity since they are comprised of light atoms such as carbon, hydrogen, and oxygen and have significantly higher density since bromine is a heavy atom. The densities of their products can be adjusted between 11 to 25 ppg and the fluids are able to withstand up to at least 150 degrees Celsius. In addition, their partitioning coefficient values varies from 2 to 7, which makes the fluids highly hydrophobic. The chemical formula of the product is kept confidential by Albemarle Corporation due to marketing purposes.

The method Albemarle used for producing kill fluids with different densities was by blending three main components together; A, B and C with densities of 11.08 ppg, 24.7 ppg and 7.01 ppg, and viscosities of 4090 cP, 2 cP and 13 cP, respectively. Component B was mainly used for adding density to the blend and the two other components were used for dilution. Figure 3.3 shows the trend of viscosity with increasing density for the brominated organics produced with

components A and B. As can be seen, usage of component A for lowering densities results in dramatic viscosity increase. Therefore, low viscosity brominated organics were obtained by using component C.

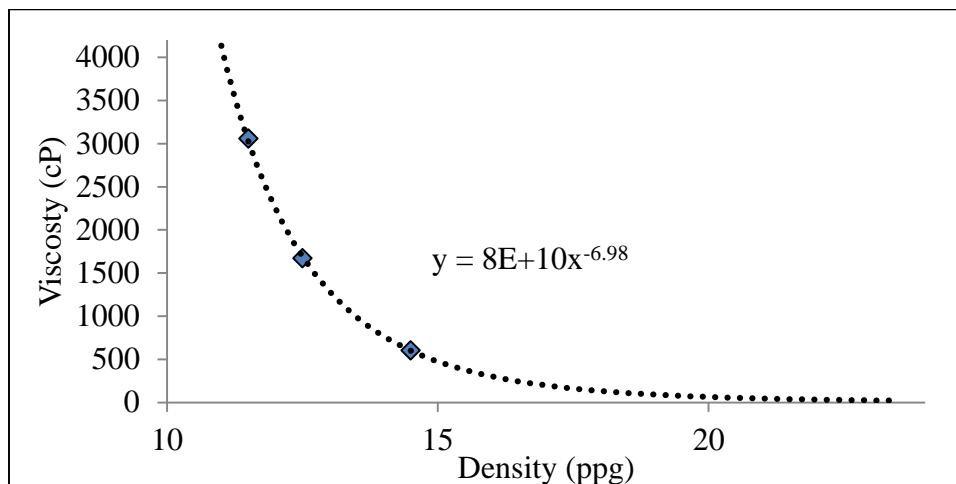


Figure 3.3: Viscosity versus density of brominated organics blended with components A and B

The brominated organics were chosen as the candidate kill fluids and compatibility tests have been conducted to evaluate their performance in water-based fluids.

3.4 Compatibility Testing of Brominated Organics

Compatibility of the KF and AF is a combination of properties specified in Table 3.1 that would result in gravity displacement. After selecting a hydrophobic KF, its performance should be tested in water before any further studies. To do this, a set of basic tests was conducted in LSU PETRLL and Albemarle labs.

3.4.1 Pilot Demo Test – 1

The first trial observation of brominated organics interacting with water was made by simply pouring 16 ppg organic solvent into a 4" ODx10 feet close-ended clear-PVC pipe filled with water to its $\frac{3}{4}$ height and a pressure gage attached to its bottom. A funnel with one-inch tip was installed on top of the pipe to direct the kill fluid flow into the pipe. Funnel's tip was 2 feet above the water level.

Procedure was to pour 2.5 gallons of kill fluid continuously by also keeping the same liquid level in the funnel. Therefore the injection rate would be more or less constant due to the

continual hydrostatic pressure exerting to the funnel's tip. Entire process of kill fluid settlement in water was videotaped and slipping times of droplets were recorded. After the system became static, settled kill fluid was recovered from the valve at the bottom.

First remark was the stream of kill fluid droplets hitting on the water surface and entrapping air onto their bodies. As these droplets traveled down, they parted to smaller bodies and attached air bubbles lifted up particularly the smaller droplets. Ultimately most of the droplets were able to become bubble-free, however the bottom sedimentation of kill fluid still included air in its structure. The air eventually migrated while carrying-over some kill fluid droplets upwards and delayed the static stabilization time of the system. As the water level increased the injection tip became submerged and eliminated the air entrapment. Slip velocity of a single droplet in water was then measured as around 43 feet per minute.

In summary, intrusion of the 3rd phase, air, slowed down the settling process so the submerged injection is required. During the settling process; the pressure value on the gage increased continuously and at the end; close to 100% of the kill fluid was recovered. No mixing with water was observed.

3.4.2 Pilot Demo Test – 2

In the light of the learning from the first demo test, a second test was designed and conducted to see the performance of the brominated organics with submerged injection and w/o trapped air during the injection. In addition to the same set-up and procedure, a 2 feet pipe with a 3/16" orifice was attached to the funnel to assure sub-surface injection of kill fluid.

As a result of submerged injection, stabilization time was significantly reduced. Organic droplets would continuously travel down without interacting with air bubbles. In front of the orifice, a 2 feet long dynamic jet was observed and at the end of the jet various sizes of droplets were formed. When jetting forces expired, this jet turned into a buoyant jet and formed droplets started to move downwards only under buoyant forces. During the injection process, the small droplets most of the time failed to travel downwards and were either suspended or lifted-up by the counter-current flow.

The velocity of a considerably big droplet being produced by the orifice was this time measured as around 60 feet per minute, 40% more than in the first test. Therefore, as a conclusion, if vertical injection is the case; air entrapment must be avoided by assuring a submerged kill fluid injection.

3.4.3 Weighted Fluid Column Test

A one-time compatibility test by using weighted annular fluid was performed in Albemarle PDC laboratories. The test was conducted in a vertical 3 feet glass pipe with 1.5” diameter. A 16 ppg brominated organic was dripped into the column of 14.2 ppg colorless calcium bromide solution. The slipping time was measured.

Observations indicated that the presence of a heavier stagnant medium slows down the droplets from slipping downwards, as already known from the literature. In addition, it was observed that low injection flow rate through a circular nozzle provides big droplets with uniform same size and these droplets can travel to the bottom without any interruption. The velocity of the droplets slipping in the kill solution was measured as 10-12 feet per minute, which is, considerably, lower than the velocity in water.

3.4.4 Bench-top Compatibility Tests

Previous compatibility tests involved only Newtonian fluids as the stagnant medium. To find out the performance of brominated organics in Non-Newtonian fluids, several bench-scale tests were performed in Albemarle PDC laboratories.

A custom made glass model, shown in Figure 3.4, was designed such that two glass pipes with diameters of 2” and 4” would be attached in another to form a 1” width of annular gap. Total length was 3 feet and the volumetric capacity was 1.5 gallons. The injection would take place in the annulus by using either a 0.25” glass funnel or nitrogen source feeding a 0.125” tygon tubing, and the annulus of the model would be drained from the valve at the bottom. In the tests, two kill fluids blended using components A and B are used, with densities of 15.4 ppg (orange) and 24.8 ppg (blue) and viscosities of 500 cP and 8 cP, respectively. And translucent annular fluids with a rheology character of Yield-Power-Law with high viscosity and 8.5 ppg density. Kill fluids were injected into the column by either pouring from a funnel or transferring pressure from the nitrogen bottle. The limited pressure source did not allow high flow rates for

the viscous kill fluid. Nevertheless, for the low viscosity organic three different flow rates could be obtained. In the tests, $\frac{3}{4}$ of the column (~ 1 gal) was filled with AF, and continuous submerged injection of KF was performed. Whole phenomenon was captured by a video camera.

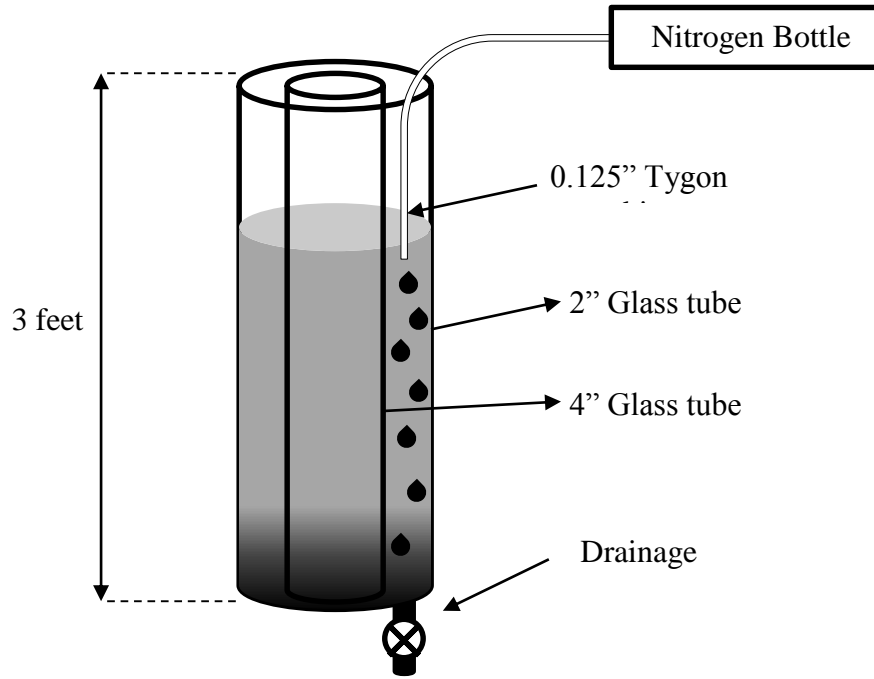


Figure 3.4: Bench-top physical model for compatibility tests

Results showed that when the injection rate is too high (Figure 3.5 - right picture), kill fluid disperses into the annular fluid and spreads throughout the AF column. However, when the rate is low (Figure 3.5 - left picture) uniform droplets form and settle down, reach the bottom and build-up. The phenomenon, as discussed above in the literature review chapter, is defined by the fragmentation modes directly influenced by the injection rate. Rayleigh mechanism, which causes big uniform droplets, is possible with low rates and enables an unconstrained transport of KF. Atomization regime causes mixture (due to dispersion) at the top and forms small KF droplets that fail to travel down but upwards. When Atomization is avoided a mixture zone forms at the KF/AF interface (at the bottom) due to disturbance that caused by the settling KF droplets. Formation of this zone begins at the very bottom and expands as the KF feed continues. Figure 3.6 shows the amount of mixture when the same amount of KF was injected in the same AF with different flow rates. For the lowest injection rate, mixture zone is comparably smaller than that with the highest.

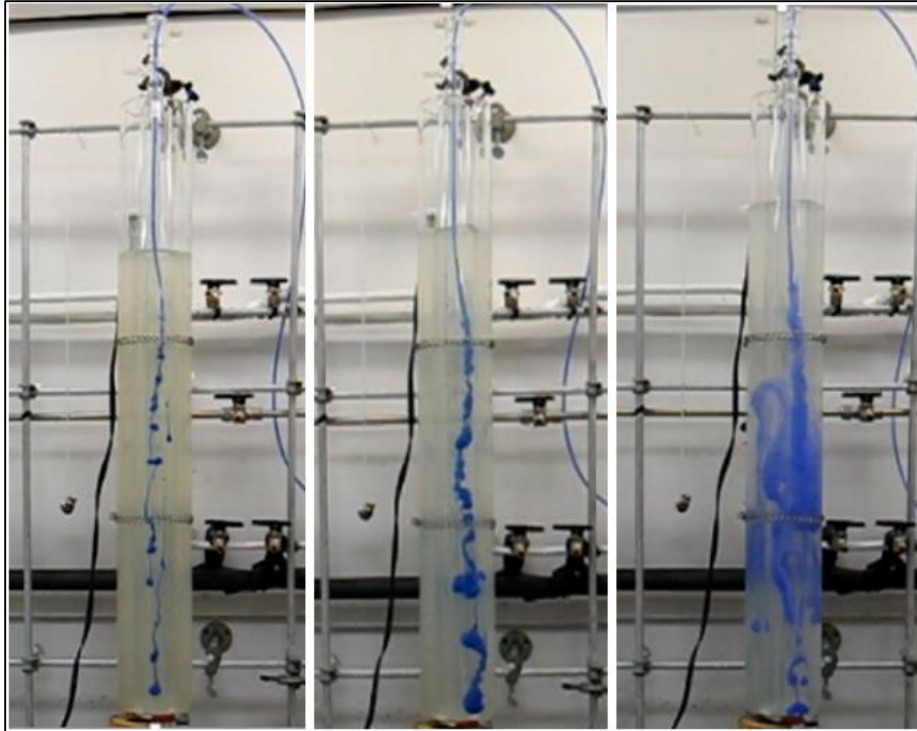


Figure 3.5: Bench-top compatibility tests; (0.11, 0.28, 0.57 gpm) Flow patterns vary from Rayleigh to Atomization.

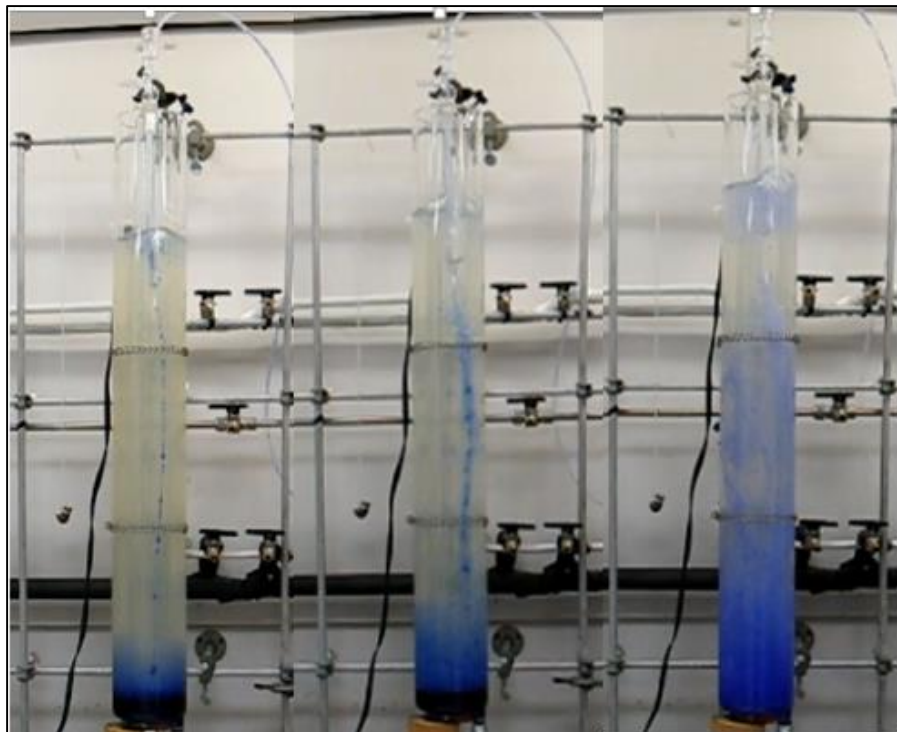


Figure 3.6: Snapshots of the tests when injection stopped. Mixture zone height increased with increasing injection rate.

In addition to forced injections (with controlled rate), few funnel experiments (free fluid discharge from funnel) were conducted by using different kill fluids. As seen in Figure 3.7, low viscosity-high density kill fluids showed different fragmentation modes (as already shown in Figure 1.5) and therefore caused various sizes of mixture zones; although, high viscosity- low density fluid performed a slow consistent slippage and generated no mixture zone. Unfortunately injection rate was limited for high viscosity fluid and its behavior under forced injection could not be observed.

In summary, kill fluid viscosity (not specified in Table 3.1) is an important property that controls dispersion and formation of mixture zone. Even though the heaviest fluid with low viscosity travels to the bottom much faster, generation of a mixture zone reduces the process performance. Instead of settling part of KF remains suspended. Thus, a fully compatible KF with high density should also feature elevated viscosity.

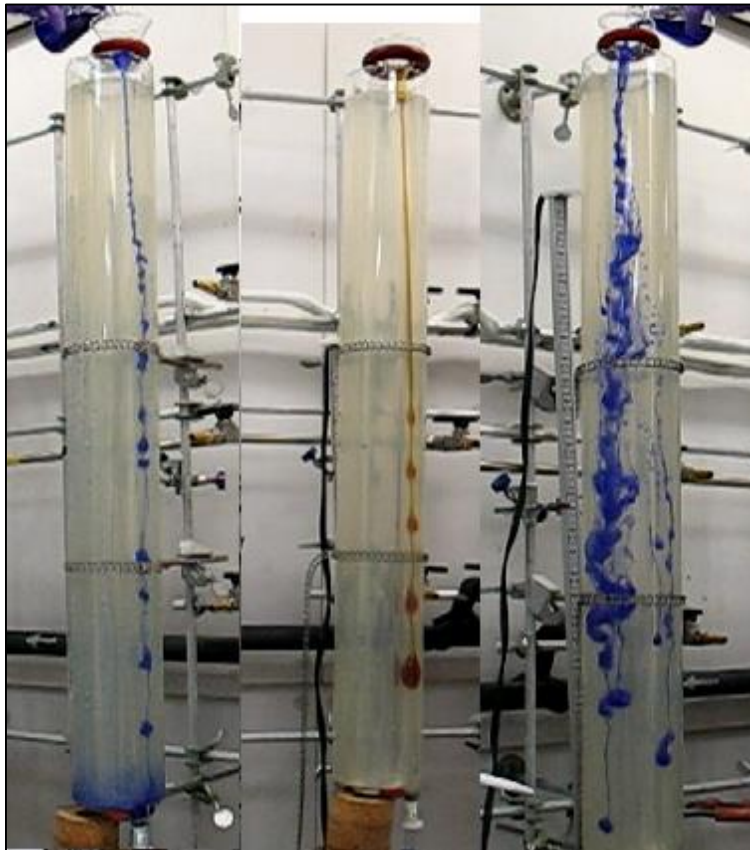


Figure 3.7: Poured kill fluids into Non-Newtonian AF generate different flow patterns. Left: Low viscosity kill-fluid with Rayleigh mechanism. Middle: High viscosity kill-fluid with First-Induced break-up. Right: Second-Induced Break-up ^[14].

3.5 Summary

Brominated organic fluids have been developed by Albemarle Corporation and tested for compatibility with water and synthetic clay suspensions. The demo tests with water mainly provided information about the injection method. Evidently, dumping the kill fluid above free AF surface results in air entrapment and slows down the settling process (For well applications, this might even cause taking the kill fluid back during the bleed-off cycles). To avoid this negative effect, submerged injection was conducted in all other tests.

Bench-top tests showed relation of droplet size being highly dependent on the injection rate. Highest rate caused partial dispersion of kill fluid in the annular fluids in small droplets and decreased settling of the kill fluid to the bottom.

Brominated organics provide flexibility in combinations of density, viscosity and interfacial tension. They are a promising kill fluid to be used in gravity displacement of annular fluid. However, operational parameters must carefully be designed.

CHAPTER 4: VISUALIZATION OF GRAVITY DISPLACEMENT

4.1 Objective

As discussed above, in the past, the bleed-and-lube technique for SCP removal by placing heavy fluid (KF) on the top of annular cement to kill gas migration has been tried and failed because the kill fluid did not effectively displaced the annular fluid column above the cement top. As the displacement requires gravity settling of the kill fluid in the lighter annular fluid, there was a need for a laboratory visualization model to study and understand the mechanism of the displacement process.

The first objective was to fabricate transparent laboratory scaled-down hydraulic analog of well's annulus. The second objective was to formulate clear synthetic-clay muds. The third objective was to conduct series of experiments with various kill fluids injected at the top and at the side of the annulus filled with different muds until maximum displacement occurred. The results involve videotapes, pressure records and measured volumes of the kill fluids. The measurements provide assessment of the process performance while the videos were used for geometrical description of the kill fluid plume change on its way down the annulus.

The following aspects of the displacement process are tested in this study:

- Comparison of the top with side injection in terms of fluid slippage and its consistency.
- Effect of the two fluids properties on fluid mixing and the slippage
- Comparison of immiscible and miscible injection
- Design of operational parameters for efficient injection of kill fluid

4.2 Methodology

4.2.1 Physical Model Design and Fabrication

Physical simulation of an annulus is a difficult task. Even though the design of circular pipes is alike to that of a well, they have significant disadvantages such as the visualization and disassembling practicality. A bench-top physical model, dubbed here “slot model”, has been designed by opening up the annulus to the sides and obtaining a rectangular geometry (Figure 4.1)

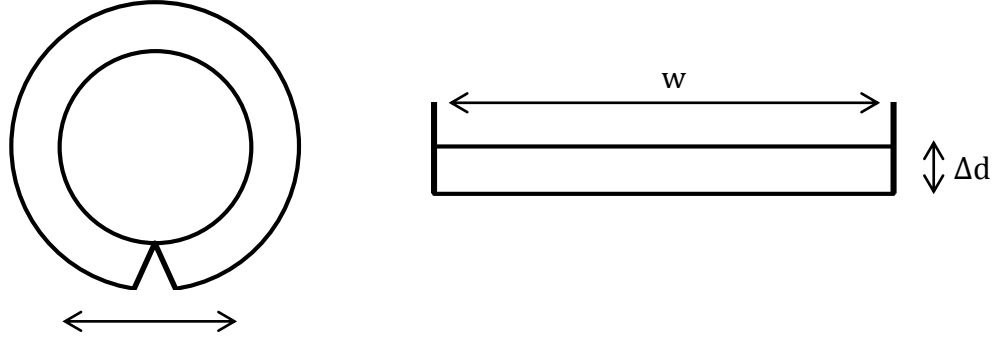


Figure 4.1: Well annulus (left) was cut from the red line; opened-up and converted into Slot model (right).

The easiest way of calculating the flow characteristics in a non-circular conduit is to compare it with a circular pipe, which is possible by calculating the shape's “equivalent diameter”^[66]. Langlinais et al. ^[67] used this approach to calculate the frictional pressure losses in a drill pipe annulus but the method has never been used for buoyant displacement studies. The concept has been employed to the slot model in order to maintain the hydraulic similarity of shapes, annulus and the slot.

Hydraulic radius, which is defined as the ratio of the shape's cross-sectional area to its wetting perimeter, is widely being used under the name of equivalent diameter ($d_e=4r_H$)^[68]. Equating the hydraulic radii of both shapes gives the following mathematical relationship.

$$r_{H_{\text{annulus}}} = r_{H_{\text{slot}}} = r_H \quad (4.1)$$

Considering,

$$r_H = \frac{w \Delta d}{2(w + \Delta d)}$$

Gives,

$$w = \frac{2 r_H \Delta d}{\Delta d - 2 r_H} \quad (4.2)$$

Figure 4.2 shows the plot of Equation 4.2. As it is shown, hydraulic diameter defines both the vertical and horizontal asymptotes. Sixty-two different combinations of casings are first considered and hydraulic radii of these combinations are calculated. To limit the population with the intermediate annuluses that generate SCP conductor casings, surface casings and relatively

small production casings are excluded, and 40 intermediate casings between 13 $\frac{3}{8}$ " and 5" are taken into consideration and hydraulic radii of each are calculated (Table 4.1).

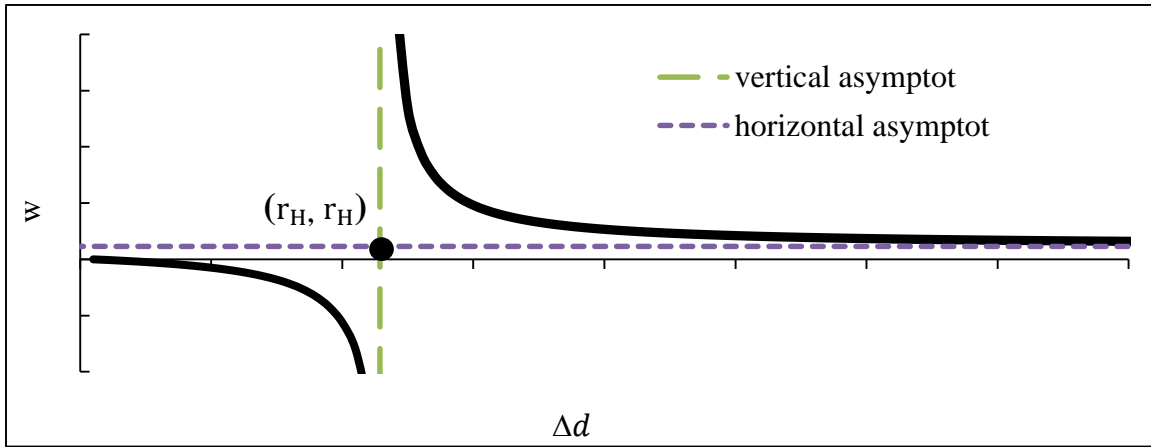


Figure 4.2: Dimensions plot for the slot model according to hydraulic radius theory

Statistical analysis of a population of 40 hydraulic radiuses gives right-skewed distribution and is shown in Figure 4.3. Statistical properties and results are also given in Table 4.2 and Table 4.3. Figure 4.4 shows the plots of the slot model width versus thickness for different central tendency measures of annuluses. The selected design was 1.3" thick and 20" wide slot that was later changed to 1.35" and 13.5", respectively, due to fabrication constraints.

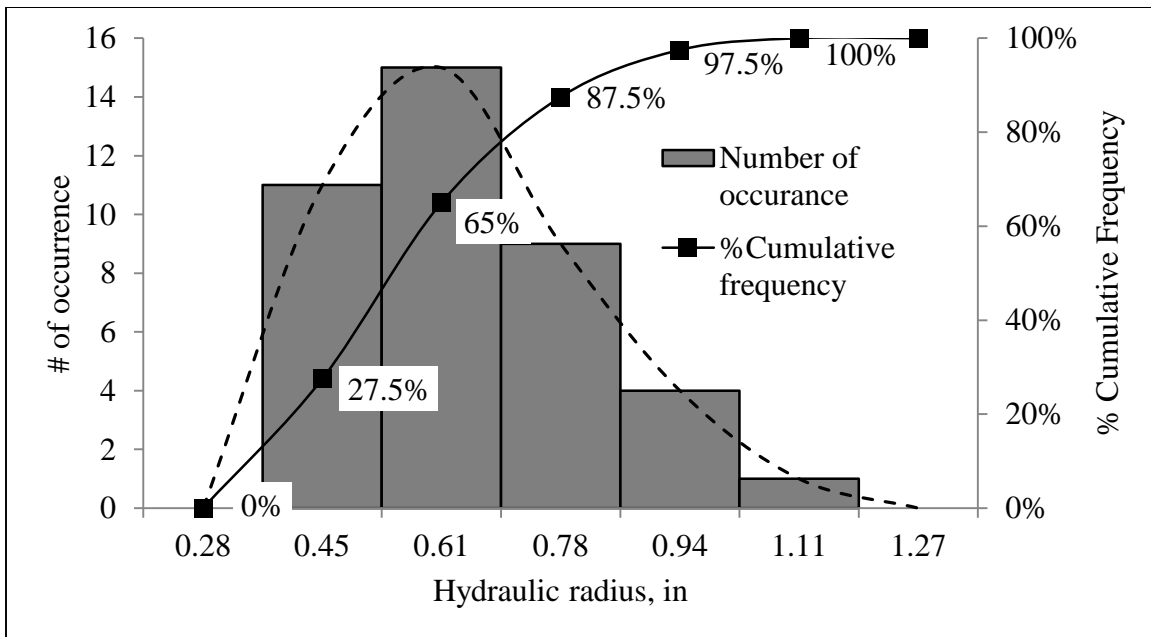


Figure 4.3: Statistical analysis of hydraulic radius of 40 intermediate casings

Table 4.1: Table of hydraulic radiuses for various casings and annular areas (OC= Outer casing, IC= Inner casing, ID= Inner diameter, OD= Outer diameter, NW= nominal weight [lb/ft.], CS= Cross-Section, r_h = Hydraulic Radius)

OC OD, in	OC NW in	OC Thickness in	OC ID in	OC Drift diameter in	Bit size in	Clearance in	IC OD in	CS Area sqin	Wetting Perimeter in	r_h in
13.375	48	0.33	12.715	12.559	12.25	0.1545	9.625	54.22	70.18	0.773
13.375	54.5	0.38	12.615	12.459	12.25	0.1045	9.625	52.23	69.87	0.748
			12.615	12.459	12.25	0.1045	8.625	66.56	66.73	0.998
13.375	61	0.43	12.515	12.359	12.25	0.0545	9.625	50.25	69.55	0.723
			12.515	12.359	12.25	0.0545	8.625	64.59	66.41	0.973
13.375	68	0.48	12.415	12.259	12.25	0.0045	9.625	48.30	69.24	0.698
			12.415	12.259	12.25	0.0045	8.625	62.63	66.10	0.948
13.375	72	0.514	12.347	12.191	11	0.5955	8.625	61.31	65.89	0.931
			12.347	12.191	11	0.5955	7.625	74.07	62.74	1.181
10.75	51	0.45	9.85	9.694	9.5	0.097	7	37.72	52.94	0.713
10.75	55	0.495	9.76	9.604	9.5	0.052	7	36.33	52.65	0.690
10.75	60.7	0.545	9.66	9.504	9.5	0.002	7	34.81	52.34	0.665
10.75	65.7	0.595	9.56	9.404	8.75	0.327	7	33.30	52.02	0.640
			9.56	9.404	8.75	0.327	6.625	37.31	50.85	0.734
9.625	32.3	0.312	9.001	8.845	8.75	0.0475	7	25.15	50.27	0.500
			9.001	8.845	8.75	0.0475	6.625	29.16	49.09	0.594
9.625	36	0.352	8.921	8.765	8.75	0.0075	7	24.02	50.02	0.480
			8.921	8.765	8.75	0.0075	6.625	28.03	48.84	0.574
9.625	40	0.395	8.835	8.679	8.625	0.027	7	22.82	49.75	0.459
			8.835	8.679	8.625	0.027	6.625	26.83	48.57	0.553
9.625	43.5	0.435	8.755	8.599	8.5	0.0495	6.625	25.73	48.32	0.533
			8.755	8.599	8.5	0.0495	6	31.93	46.35	0.689
9.625	47	0.472	8.681	8.525	8.5	0.0125	6.625	24.72	48.09	0.514
			8.681	8.525	8.5	0.0125	6	30.91	46.12	0.670
9.625	53.5	0.545	8.535	8.379	8.375	0.002	6	28.94	45.66	0.634
			8.535	8.379	8.375	0.002	5.5	33.45	44.09	0.759
8.625	24	0.264	8.097	7.972	7.875	0.0485	6	23.22	44.29	0.524
			8.097	7.972	7.875	0.0485	5.5	27.73	42.72	0.649
8.625	28	0.304	8.017	7.892	7.875	0.0085	6	22.21	44.04	0.504
			8.017	7.892	7.875	0.0085	5.5	26.72	42.46	0.629
8.625	32	0.352	7.921	7.796	6.75	0.523	5	29.64	40.59	0.730
8.625	36	0.4	7.825	7.7	6.75	0.475	5	28.46	40.29	0.706
8.625	40	0.45	7.725	7.6	6.75	0.425	5	27.23	39.98	0.681
8.625	44	0.5	7.625	7.5	6.75	0.375	5	26.03	39.66	0.656
8.625	49	0.557	7.511	7.386	6.75	0.318	5	24.67	39.30	0.628
7.625	24	0.3	7.025	6.9	6.75	0.075	5	19.12	37.78	0.506
7.625	26.4	0.328	6.969	6.844	6.75	0.047	5	18.51	37.60	0.492
7.625	29.7	0.375	6.875	6.75	6.75	0	5	17.49	37.31	0.469
7.625	33.7	0.43	6.765	6.64	6.5	0.07	5	16.31	36.96	0.441
7.625	39	0.5	6.625	6.5	6.5	0	5	14.84	36.52	0.406

Table 4.2: Statistical results of annulus hydraulic diameters

r_H	# of occurrence	Relative Frequency	%frequency	Cumulative Frequency	%Cumulative frequency
0.2 to 0.365	0	0.000	0.00 %	0.00	0.00%
0.365 to 0.53	11	0.275	27.50 %	11.00	27.50 %
0.53 to 0.695	15	0.375	37.50 %	26.00	65.00 %
0.695 to 0.86	9	0.225	22.50 %	35.00	87.50 %
0.86 to 1.025	4	0.100	10.00 %	39.00	97.50 %
1.025 to 1.19	1	0.025	2.50 %	40.00	100.00 %
1.19 to 1.355	0	0.000	0.00 %	40.00	100.00 %
Totals	40	1	100 %		

Table 4.3: Statistical properties of annulus hydraulic diameters

Count	40	# of classes	5	P90	0.82
Max Value	1.181	Class Width	0.165	P10	0.35
Min Value	0.459	Average	0.66		
Range	0.722	Median	0.653		

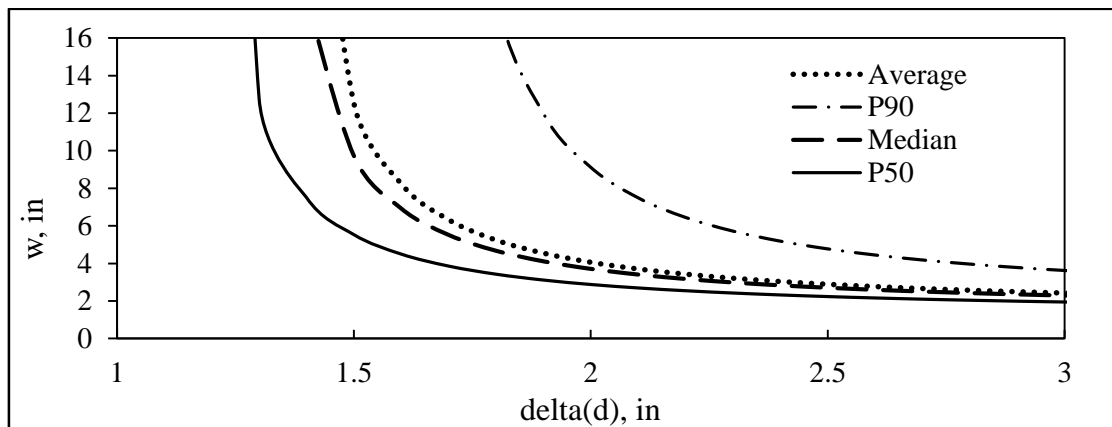


Figure 4.4: Slow model width vs. thickness plotted according to statistical results.

The model has been fabricated in LSU using one 0.75" thick glass for the front sight and a chemically resistant plastic plate for the back plate. The whole system was sealed with durable rubber and c-clamps. Injection could be conducted from nozzles with different sizes (0.125", 0.5", 0.6"), located at either at the top of the model or at the rear center point, below the top. Overflowing fluid could be collected from 1" holes drilled to the sides of the plastic plates one inch below the top that were connected to flexible hoses. A Teflon single cavity 1/2 HP motor pump is used for the injection and a pressure transducer is installed at the bottom drainage line to read the bottom pressure changes. Fluid displacement process in the model could be seen and

recorded with a video camera placed in front of the glass window. The volume of the model was designed as 2.8 gallons however due to plastic sealant rubber and clamping method the volume could be between 2.5 to 3 gallons. Schematics of the model is shown in Figure 4.5.

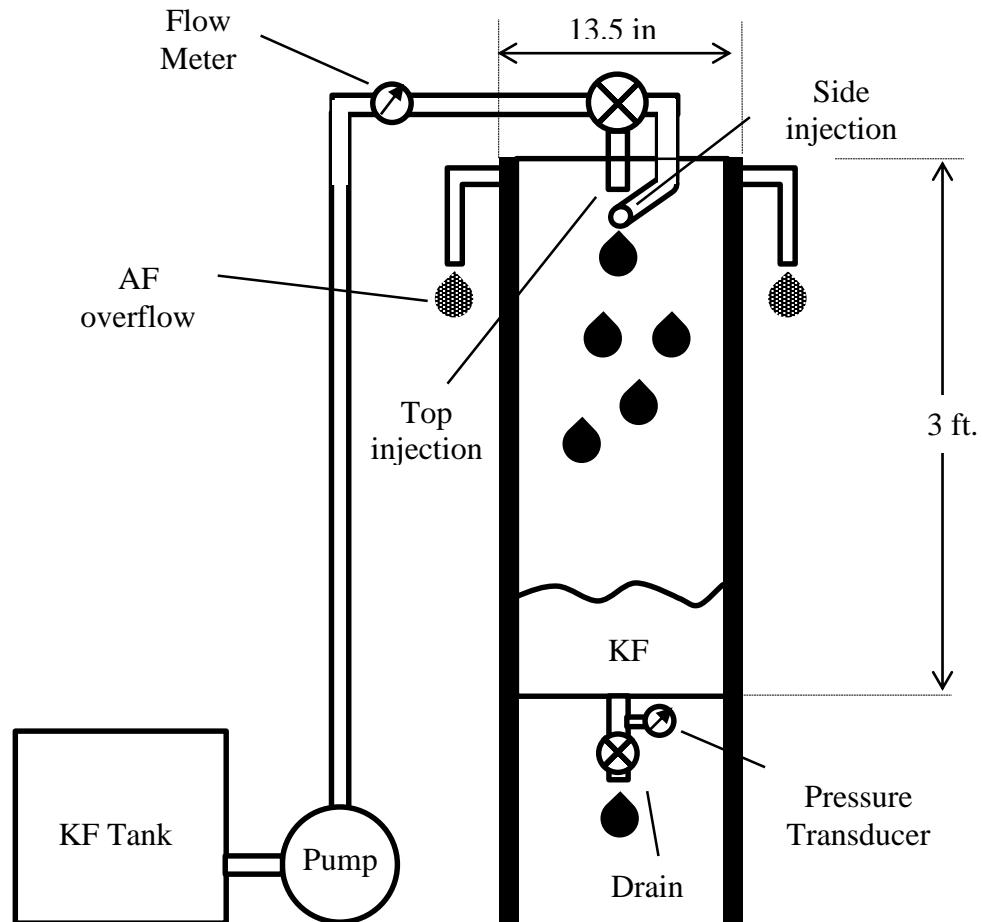


Figure 4.5: Slot physical model schematics

4.2.2 Fluids Properties

To conduct the displacement experiments, different kill fluids (KF) with various properties are used. Table 4.4 shows the kill fluids named according to their densities and viscosities. KF starting with #1 represents brominated organic fluids; #2 is weighted drilling mud and #3 shows heavy brine. Due to the available amount of KF1701, most of the experiments are conducted with it. Initial injection experiments with water as the annular fluids have been visually informing; however, according to characterization of annular fluid studies, fluid in a well

annulus – underneath the water layer – is expected to be a Non-Newtonian fluid that shows structural strength. Structural strength defined in this work as a combination of high rheology (viscosity) and tixotrophy (gel strength). For tixotrophy Laponite ® - a synthetic-based clay – is mixed with water, and for viscosity cellulose derivatives, PAC or Xantham Gum, are used. These fluids could also be weighted-up with Potassium Formate salt; however, this resulted in loss of structural strength.

Table 4.4: Kill fluid properties used in slot experiments

	Density, ppg	Viscosity, cP	Estimated IFT dyne/cm	Material
KF1201	11.95	14	30	Organic
KF1202	11.95	54	30	Organic
KF1203	11.95	94	30	Organic
KF1204	11.85	8	32	Organic
KF1401	13.9	11	30	Organic
KF1601	15.8	11	30	Organic
KF1402	14.1	25	30	Organic
KF1701	16.68	235	21.5	Organic
KF2012	12			Mud
KF2013	13.5			Mud
KF3011	11.25			Brine

Formulas of the translucent fluids is shown in Table 4.5, and rheology comparison of translucent fluids and un-weighted bentonite muds are in Figure 4.6. Higher Laponite concentrations gave higher gel strength values up to 30 lbf./100sqft. The hydration time of Laponite was tested as 5 days ^[45]. Thereby, fluids to be used for the slot experiments were mixed 3-5 fold greater than model capacity at least 5 days before the tests. Translucent fluids' rheology was computed (Table 4.6) from Fann-vg viscometer readings at 3 and 100 rpm using the following formulas for plastic viscosity,

$$\mu_{\text{Low Shear}} = \frac{300}{100 - 3} (\theta_{100} - \theta_3)$$

And for the yield point,

$$\tau_0 = \theta_3 - \mu_{\text{Low Shear}} \frac{3}{300}$$

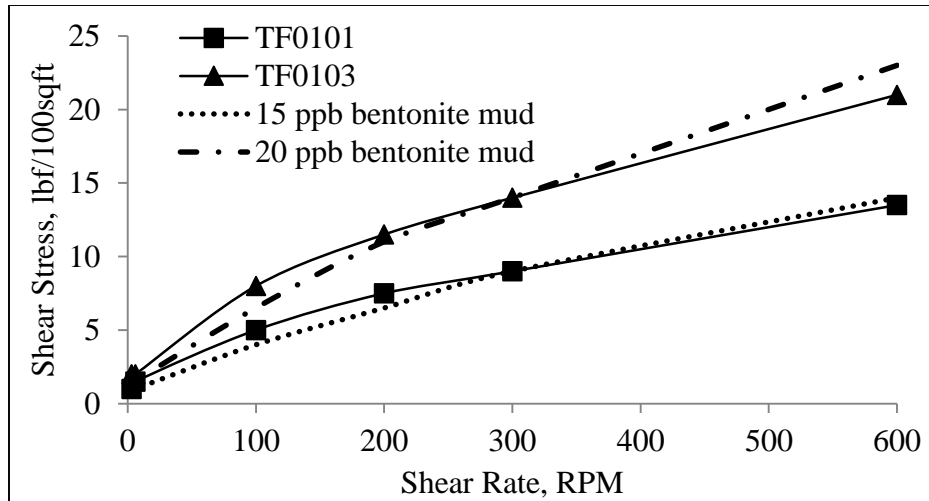


Figure 4.6: Comparison of two translucent fluids and un-weighted bentonite muds

Table 4.5: Prepared translucent fluid formulas for slot model experiments

Name	Grams of product per 350 mL water (lb/bbl.)		
	Laponite	Pac	Xantham Gum
TF0101	1.1	0.03	
TF0102			1.75
TF0103	1.65	0.06	0
TF0104			0.9
TF0105	2.5	0.1	
TF0107	2	1	
TF0108		0.02	
TF0205			1
TF0206	4	1	
TF0207	2	1	
TF0208			1

Table 4.6: Properties of generated translucent fluids for slot experiments

	TF0101	TF0102	TF0103	TF0104	TF0105	TF0107	TF0108	TF0205	TF0206	TF0207	TF0208
Density (ppg)	8.4	8.4	8.4	8.4	8.4	8.4	8.4	11	9.6	10	10
Low shear viscosity (cP)	12.4	24.7	18.6	17	24.7	40.2	21.7	26.3	29.4	15.5	15.5
Yield Point (lbf/100sqft)	0.9	9.8	1.8	3.8	10.8	6.6	0.8	2.2	2.7	1.9	0.9
10 min Gel (lbf/100sqft)	11	11	20	7	32	30	1.5	6	5	3	2

4.2.3 Experimental Procedure and Analysis

Experimental procedure consisted of five parts.

1. Prepare sample of TF and measure rheology and gel strength.
2. Fill up the slot model with TF from the top
3. Inject KF into the slot model from the top/side port using desired nozzle size and at the designed constant flow rate until bottom pressure stabilizes.
4. When bottom pressure does not increase for at least a minute (or no more kill fluid is available); stop injection
5. Videotape the whole experimental run

Visual record and pressure data were obtained during the experiments. In order to explain the phenomenon clearly, geometry of the process is evaluated. The impingement widths (W) and impingement heights (h) of each side injection run is measured. For the top injection droplet fragmentations are visually inspected and evaluated according to the study of Reitz ^[14], as already explain in Figure 1.5 in the literature review chapter of this work.

Beside the qualitative visual study of videos, quantitative inspection of bottom pressure is also evaluated. Recorded pressure data and injected KF volume are converted into dimensionless relationships of pressure replacement efficiency (E_p) and displacement ratio (R) defined as,

$$E_p = \frac{\Delta P}{\Delta P_u} = \frac{P - P_i}{P_u - P_i} \quad (4.3)$$

$$R = \frac{V_p}{V_s} \quad (4.4)$$

where, P is the bottom pressure, P_i is the initial bottom pressure when the model is filled with only AF, P_u is the ultimate bottom pressure when the model is filled with only KF, ΔP is the change in bottom pressure, ΔP_u is the pressure difference when AF is completely replaced with the KF, V_p is the volume of KF pumped into the model, and V_s is the slot model volume.

4.3 Results and discussion

A total of 59 experiments were conducted using various combinations of annular and kill fluids at different flow rates. For viscous kill fluids – particularly KF1701 and heavy muds –

flow rate was limited by the pump. The results are shown in Table 4.7; where, KF refers to kill fluid and TF refers to translucent fluid. In the table, nozzle sizes (d_n) and direction of injection are also stated. For the patterns; “GF” is gravity flow, Rayleigh is Rayleigh break-up regime and “Atom” stands for atomization regime^[69]. There were two above surface injections that are shown in the table with “as” addition. Flow rates are varied between 0.5 gpm to 5 gpm; however, due to the manual flow meter, these numbers may show +- 5% error.

Table 4.7: Table of results

No	KF	TF	q, gpm	side/top	d_n , in	W, in	h, in	pattern
1	1201	0101	2	side	0.5	3.32	2.6	GF
2	1201	0101	5	side	0.5	4.8	2.7	GF
3	1202	0103	0.5	side	0.5	0	0	Rayleigh
4	1202	0103	2	side	0.5	2.4	9.6	Rivulet
5	1202	0103	5	side	0.5	4.4	6.8	GF
6	1203	0101	0.75	side	0.5	0	2.7	Rayleigh
7	1203	0101	2	side	0.5	2.6	5.5	GF
8	1203	0101	5	side	0.5	3.4	5.5	GF
9	1401	0103	1	side	0.25	2	4	GF
10	1401	0103	2	side	0.25	4.1	4	GF
11	1401	0104	1	side	0.5	0	0	Rayleigh
12	1401	0104	2	side	0.5	2.36	3.5	GF
13	1401	0104	5	side	0.5	5.9	3.5	GF
14	1201	0101	1	top	0.5	0	2.7	Rayleigh
15	1201	0101	0.5	top	0.5	0	2.7	Rayleigh
16	1201	0101	5	top	0.5	0	4	Atom
17	1201	0102	2	top	0.5	0	2	Rayleigh
18	1201	0102	5	top	0.5	0	1	Atom
19	1202	0103	2	top	0.5	0	5.5	Induced
20	1203	0101	0.5	top	0.5	0	1.3	Rayleigh
21	1203	0101	5	top	0.5	0	5.8	Atom
22	1401	0103	1	top	0.25	0	4.6	Induced
23	1401	0104	1	top	0.5	0	4.6	Rayleigh
24	1401	0104	2	top	0.5	0	4.6	Induced
25	1401	0104	5	top	0.5	0	9	Atom
26	1204	0104	3	side	0.5	6.9	7.6	GF
27	1204	0104	3	top	0.6	0	10.7	Atom
28	1401	0104	3	side	0.5	5.17	7.65	GF
29	1402	0206	2	side	0.5	4.1	5.47	GF
30	1204	0107	2	side	0.4	8.7	11.9	GF
31	1204	0107	0.5	side	0.4	0	1	Rayleigh
32	1701	0102	2	side	0.6	0.7	11	Rivulet
33	1701	0104	2	side	0.6	3.2	10	GF
34	1701	0107	2	side	0.6	2.5	15.7	Rivulet
35	1701	0107	2	side	0.6	3	13	GF
36	1701	0107	0.5	side	0.6	0	4.3	Rayleigh

Table 4.7 continued

37	1701	0107	1.5	side	0.6	0.8	11.35	Rivulet
38	1701	0207	1.5	side	0.6	3.5	13.4	GF
39	1701	0208	1.5	side	0.6	3.13	13.45	GF
40	1701	0208	2	side	0.6	4	13.45	GF
41	1701	0107	5	side	1	3.4	15	GF
42	1701	0107	1.5	top	0.6	0	12.4	Induced
43	1701	0107	0.5	top	0.6	0	8.3	Rayleigh
44	1701	0107	1.5	top	0.125	0	0	Atom
45	1701	water	1.5	side	0.6	2.9	13.45	GF
46	1701	water	2	side	0.6	3.4	13.45	GF
47	1701	0107	1	side (as)	1	1.47		Rivulet
48	2013	0107	1	side	0.6	1.9	15.6	Rivulet
49	2013	0102	2	side	0.6	3.12	18.72	Rivulet
50	2013	0103	2	side	0.6	0	0	0
51	2013	0107	2	side	0.6	5.95	20.6	GF
52	2013	0107	4	side	0.6	7.04	20.6	GF
53	2013	0107	1	side	0.6	0.7	14	Rivulet
54	2013	0107	2	side	0.6	4	16	GF
55	2012	water	3	side	0.6	0	0	0
56	2013	B 8.6	2	side	0.6	4.9	9.75	GF
57	3011	B 8.6	1	side	0.6	2.6	10	Rivulet
58	3011	B 8.6	1	side (as)	0.6	2.4	10	Rivulet
59	1701	air	1.5	side	0.6	2.5	-	Rivulet

*B= bentonite mud

As the mechanism of miscible and immiscible displacement is completely different the results are analyzed separately for miscible displacement with brine and heavy mud, and immiscible displacement with brominated organics.

4.3.1 Observations – Miscible Displacement

Miscible displacement experiments with heavy mud as kill fluid were conducted with bentonite muds weighted up to 12 and 13.5 ppg with barite, using side injection port and 0.6” nozzle. Figure 4.7 shows the first and the most obvious observation; instant mixing of mud being injected into water. The rapid mixing occurs at the top and in about 6 seconds heavy mud spreads throughout the slot model homogeneously.

As shown in Figure 4.8, below, when the heavy mud is injected to Non-Newtonian fluid at 1 gpm rate, a rope of heavy mud forms with no mixing until the rope reaches the bottom. At the time the rope contacts the bottom it gets destabilized into mixture zone that builds upwards reaching promptly the overflow ports. However when injection rate is higher, destabilization of

heavy mud rope occurs earlier. As demonstrated in Figure 4.9, rope forms at the top but branches on its way down and mixes with the counter-current flowing translucent fluid.

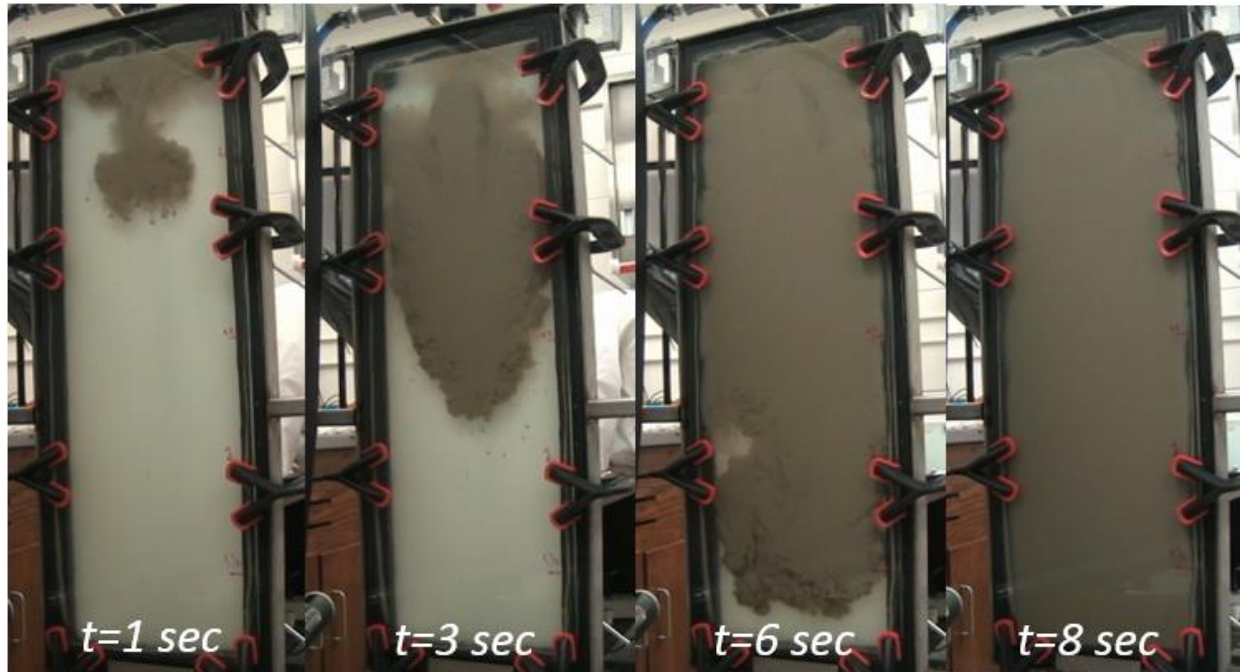


Figure 4.7: Injecting weighted mud KF2012 into water @~1 gpm (miscible displacement). Instant mixing occurs (Experiment #55).

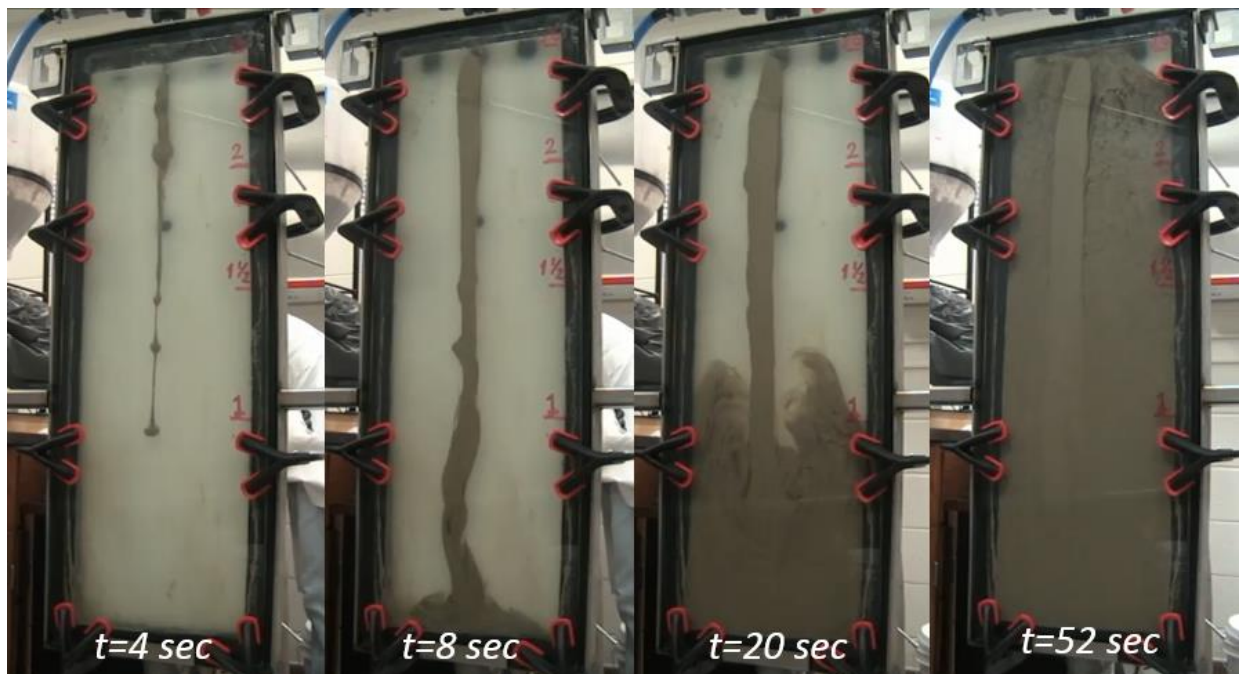


Figure 4.8: Injecting heavy mud KF2012 into Non-Newtonian TF0107 @~1 gpm (Experiment #53). Continuous rope transport and delayed mixing occur i.e. rope length = height of the model.

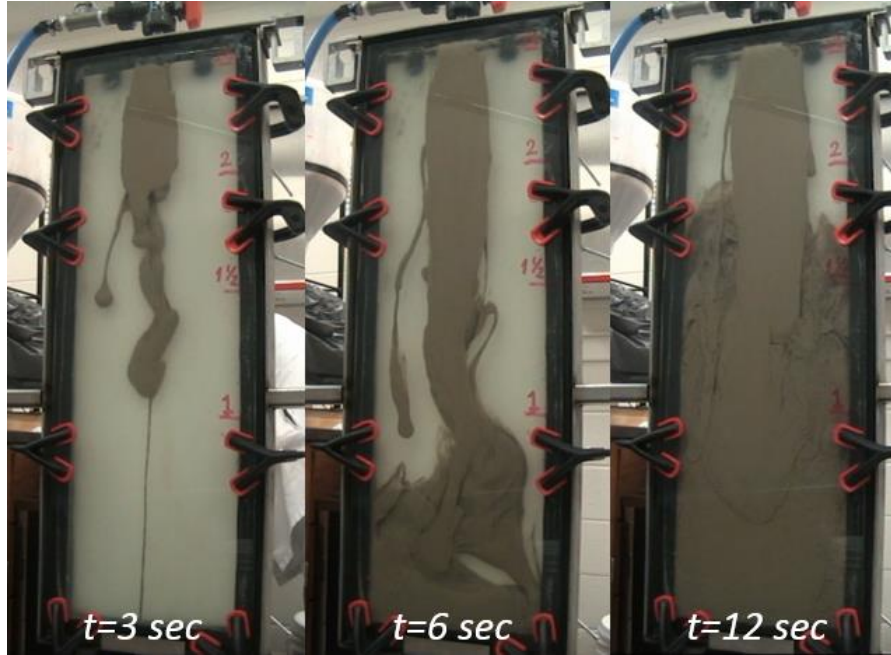


Figure 4.9: Injecting heavy mud KF2014 into Non-Newtonian TF0107 @~2 gpm (Experiment #51). Rope of KF destabilizes before reaching the bottom due to higher injection rate.

Figure 4.10 shows the pressure replacement efficiency plots of miscible displacements. Forty-five degree line is the perfect displacement line. The curve-linearity of each plot indicates increasing mixing of the two fluids while the initial slope value represents instant rate of loss of KF to overflow being 30% of the injection rate for heavy mud-water run. As one model volume of heavy mud is injected into water loss to overflow approaches to 65%. For heavy mud being injected into Non-Newtonian fluid, mixing is delayed and departure from perfect displacement line occurs after about 40% model volumes of model volume is injected. As injection continues, loss of heavy mud to overflow increases and loss approaches to 24% as one model volume has been injected. Heavy-mud KF experiment was conducted in a taller pilot column with no visualization but bottom pressure readings. When 1.6 model volumes (33 gallons) of heavy mud was injected, bottom pressure reached the complete displacement ($E_p=1$). Additional information about the run is shown in Appendix C.

As stated by Frigaard and Crawshaw ^[9], high yield stress of mud is required to provide cement plug slippage as an interface between two Bingham fluids (cement slurry and mud) in a closed pipe. The visual findings from the heavy mud miscible displacement experiments validate this statement. In addition, when the mud was pumped slow (Figure 4.8), the stability of the mud

stream did not break until it reaches the bottom; however, higher flow rates (Figure 4.9) showed formation of a slump. This phenomenon is explained by Alba et al. ^[70] as the exchange flow determined by the balance between yield stress and buoyant forces when the heavy fluid is presented into the system instantly.

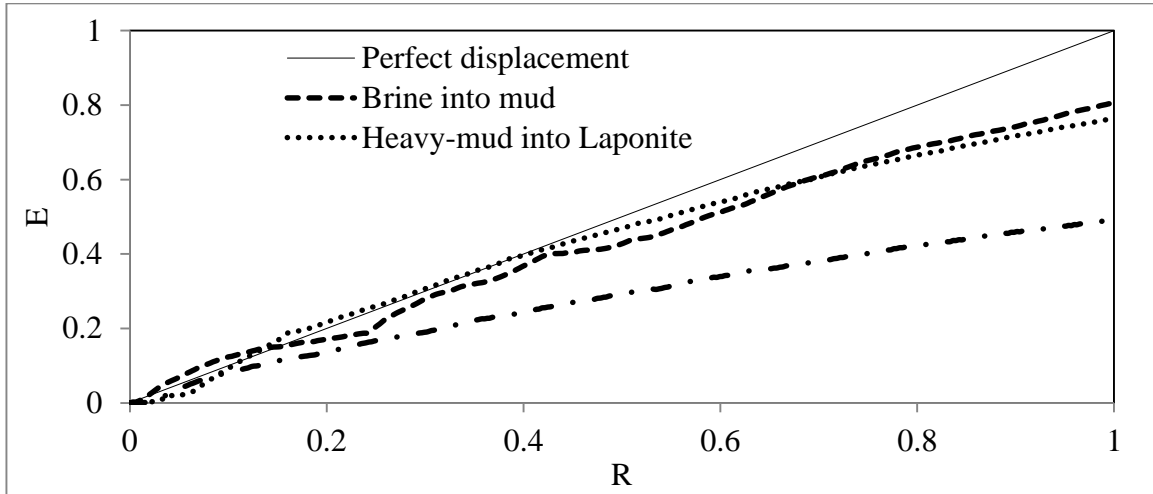


Figure 4.10: Dimensionless plots of miscible displacement @1 gpm. Miscible kill fluids give poor displacement of water or water-based Bingham fluid.

Addition series of miscible displacement experiments used heavy brine and water-based annular fluid. Published LSU tests with heavy brine kill fluids reported rapid flocculation of annular fluid being the reason for poor displacement^[8]. Unlike bentonite muds, Laponite clay suspensions show no significant flocculation when mixed with brine. Thereby, heavy brine miscible displacement experiments were conducted in un-weighted bentonite mud with poor visual inspection.

Injection of 11.25 ppg dyed (red) brine into 8.6 ppg bentonite mud at 1 gpm rate gives similar displacement performance to that for heavy mud KF and TF0107. Figure 4.11 shows the visual records of the injection process. Impinging brine slips down as a rope and displaces the mud (brown). After about 2.5 minutes the model – including the bottom section – becomes red. Visual inspections indicate that the falling rope of brine creates an envelope of flocculated mud that acts as a protective coating. The mechanism is demonstrated in Figure 4.14 more clearly. Similar to heavy mud KF displacement, once the rope reaches the bottom the “coated” rope gets destabilized and starts building up a mixture zone (MZ). As shown in Figure 4.10, plot of brine into mud shows a wavy increase due to overflowing slugs of flocculants.

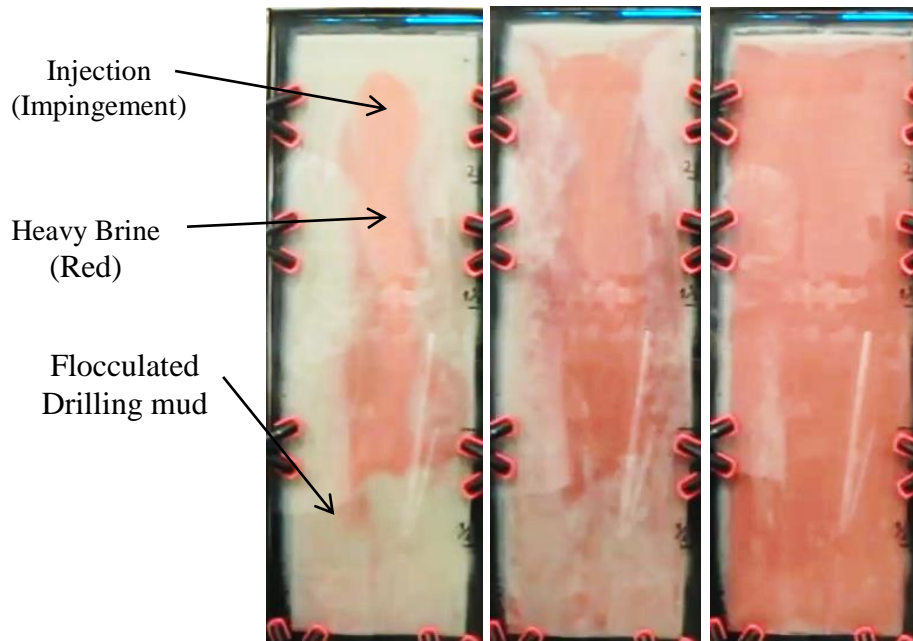


Figure 4.11: KF3011 (brine - red) into 8.6 ppg un-weighted mud (brown) with 1 gpm flow rate (Experiment #57). A flocculated mud coating covered the brine stream as it went down and displaced the clean mud.

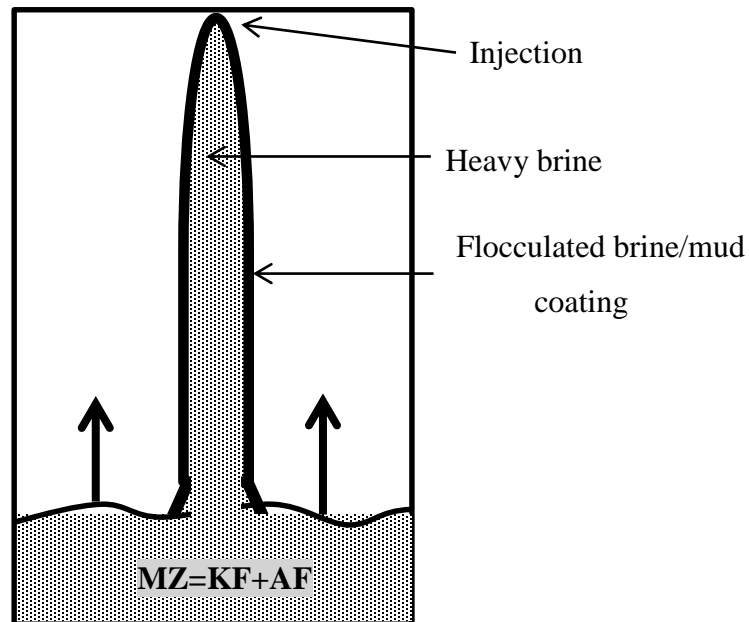


Figure 4.12: Mechanism of heavy brine slippage in mud

4.3.2 Observations – Immiscible Displacement

Hydrophobic fluids do not mix but may break-up while moving downwards under buoyant forces when injected into a lighter fluid. Therefore, the physics of immiscible displacement is

entirely different from miscible displacement. The geometry and rate of injection may control the initial consistency and integrity of the KF stream falling downwards. Also, fluid properties, such as density, interfacial tension and viscosity may affect the final shape and size of the fluid particles and, therefore, the slippage velocity and displacement rate. Nevertheless, the slot model experiments could only address the first issue – initial conditions of the displacement process– the model’s height is too small for studying the second issue.

Injection geometry effect:

Of the two geometries of KF injection conducted, vertical injection is supposed to produce initial laminar jet that would later destabilize into a droplets, shown in the right side of Figure 4.13. As the KF slippage continues, the droplets settle down at the bottom without mixing. However, small droplets show very slow or no settling as they get carried upwards by the displaced fluid and are mostly discharged in overflow.

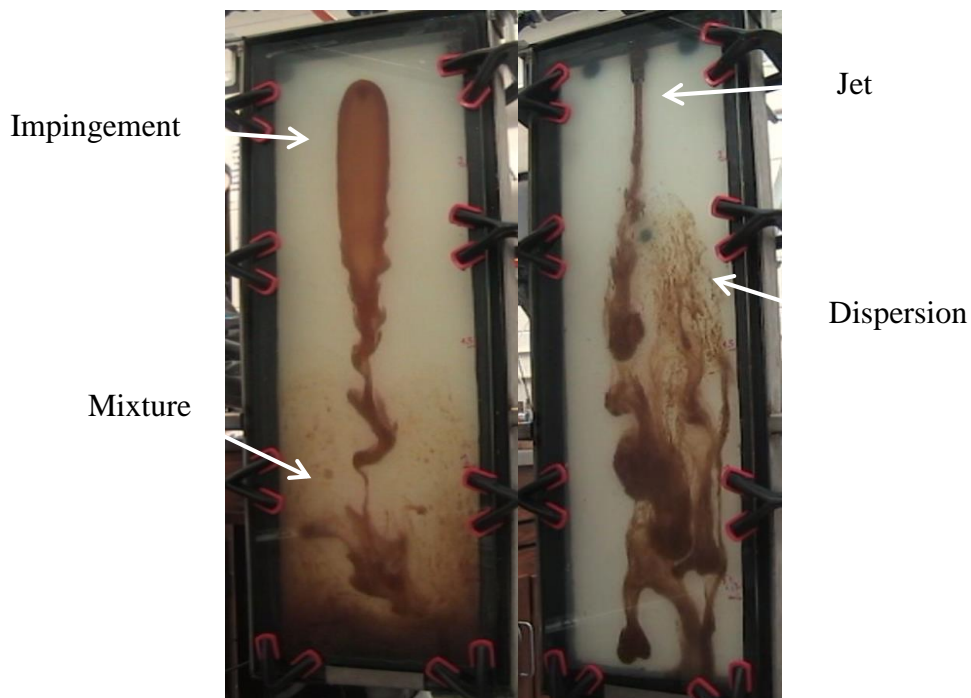


Figure 4.13: Heavy KF1701 displacing high-strength TF0107 (2 gpm) using side (left) and top (right) injection geometries

Side injection of KF forms an impingement zone on the glass plate. Size of this zone is much bigger than the top injection jet size so more KF volume may move downwards as a continuous stream. Eventually the stream breaks into KF fragments that settle to the bottom with no mixing

on lesser number of small fluid particles that could be carried upwards to the overflow. Higher injection rates demonstrate the difference in displacement physics for two injection geometries more clearly. As shown in Figure 4.14, although more than one model volume was pumped; dispersed KF droplets settle down when injection stops. Side injection, on the other hand, completely fills the model bottoms up and does not establish a settling region at the top (Figure 4.15). In summary, it appears that side injection is superior to top injection as the impingement stabilizes the KF shearing and increases the rate of buoyant slippage.

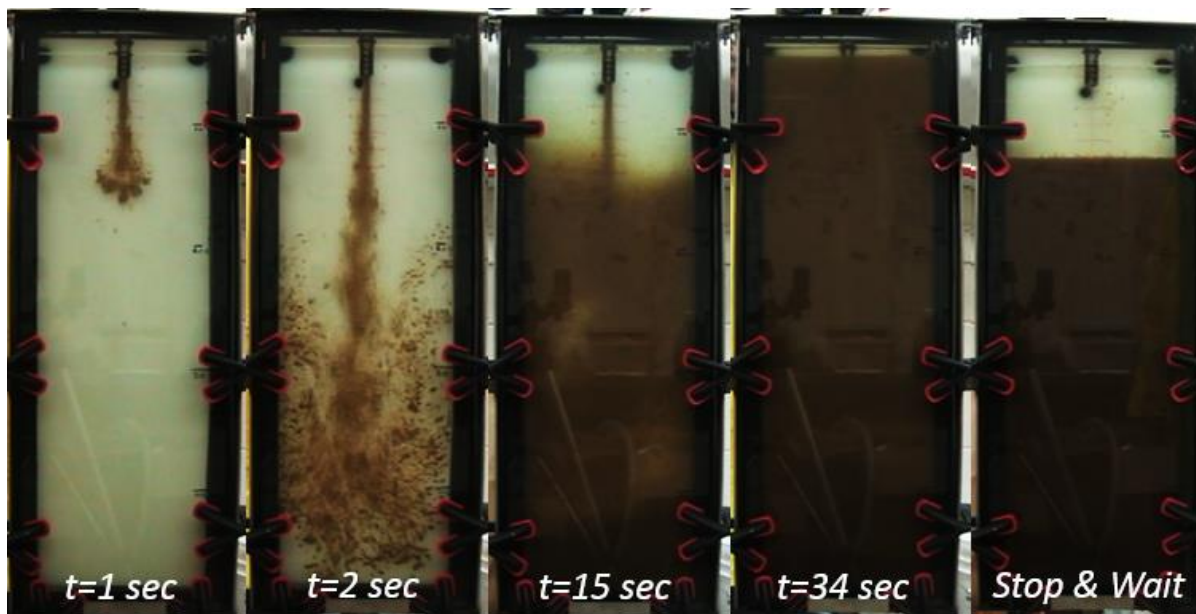


Figure 4.14: Top-injection of KF1203 into thin TF0101 at 5 gpm (Experiment #21). Fast injection “atomizes” KF into dispersed phase that eventually settles down with no stable mixture zone.

Density differential effect:

As stated by many (Archimedes, Stokes, Dedegil ^[26] etc.) density differential of heavy particle and stagnant media directly effects the slip velocity of the particle. The observations indicate that the slot model slower particles often get carried over by the counter-current flow and overflow. Figure 4.16 shows plots of immiscible kill fluids with different densities being injected into TF. All plots demonstrate extended condition of perfect displacement (linear trend) with mixing (non-linear top section). Plot 2 and 4 were run at the same injection rate but different densities of KF. It is clearly seen that performance of lighter KF is lower, as its departure from perfect displacement line is much sooner. The results show the beneficial effect

of using KF with maximum possible density. In addition, an increase in density differential (or KF viscosity) reduces the size of stable impingement zone thus enabling higher injection rates.

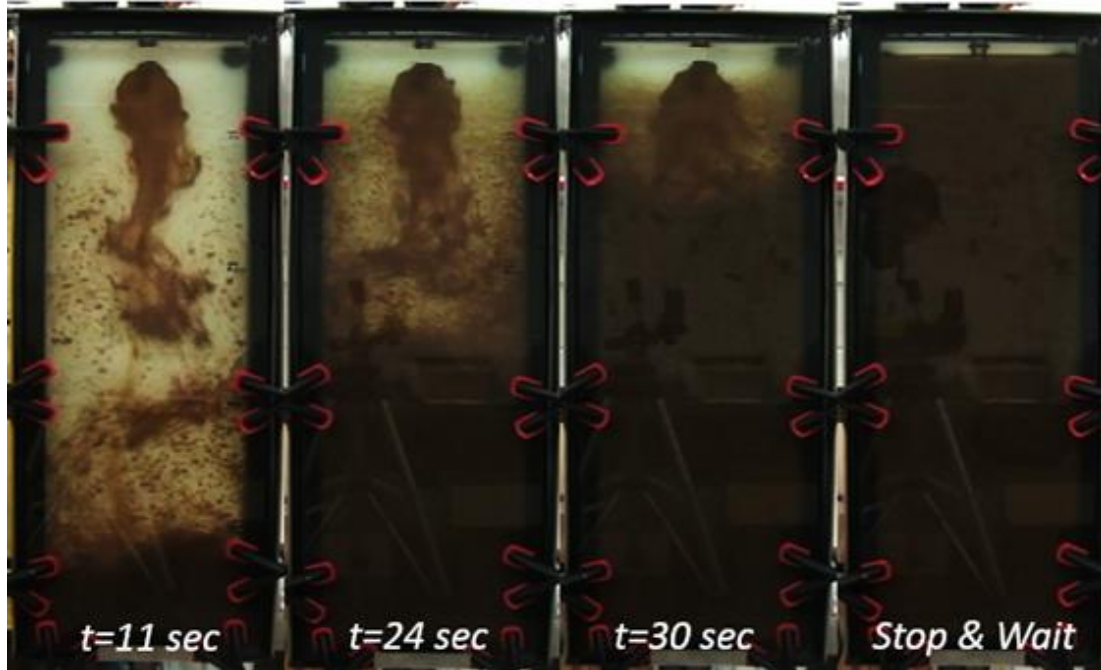


Figure 4.15: Side injection of KF1203 into thin TF0101 at 5 gpm (Experiment #8). Impingement absorbs the injection rate energy. Fluid droplets settle down by buoyancy. No stable mixture zone is observed.

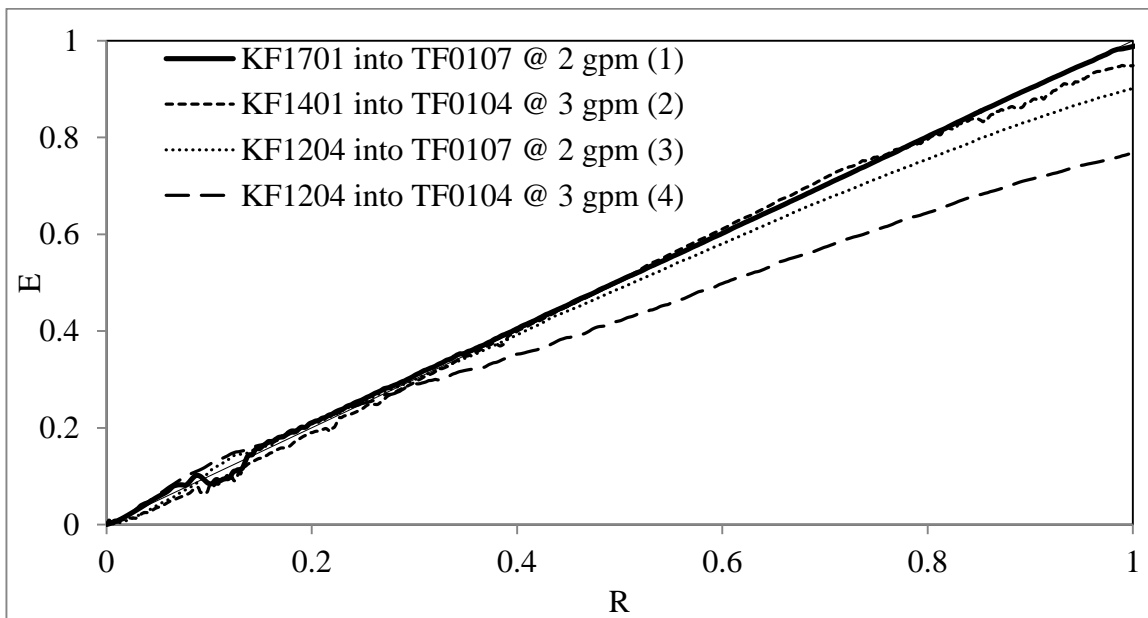


Figure 4.16: Dimensionless plots of immiscible displacement demonstrate beneficial effect of high density and detrimental effect of high injection rate on performance

Annular fluid strength effect:

In this section, annular fluid's viscosity and gels are considered together since both properties are mutually dependent. As can be seen from the comparison between 2 seconds snapshots of experiments #33 (Figure 4.17) and #32 (Figure 4.18), higher strength of annular fluid caused a slower transport of kill fluid thus enabling larger mixture zones. Moreover, higher viscosity of annular fluid caused more stable impingement zones (rivulet flow type of impingement), as the low viscosity caused unstable impingement zone (gravity flow) that caused spreading of KF throughout the model and could be more influenced by the counter-current flow.

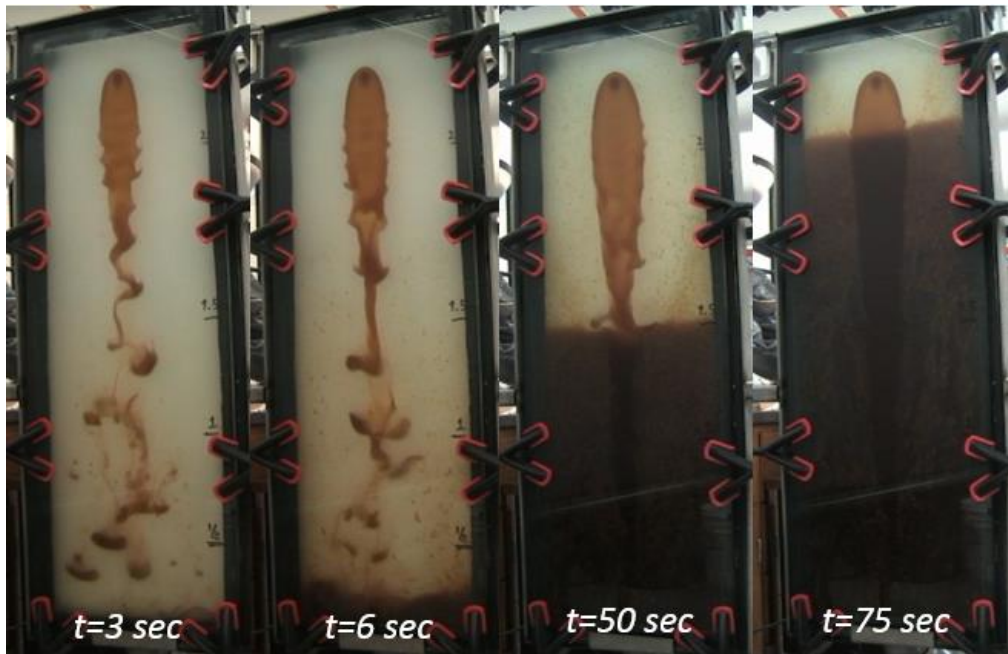


Figure 4.17: Side injection of KF1701 into low viscosity TF0104 at 2 gpm (Experiment #33). There is a sharp TF/KF interface – negligible mixture zone formed.

Injection rate effect:

For the top injection geometry and high rate, turbulent jetting generates dispersion (atomization) of exiting fluid ^[69] and returns to the overflow with no gravity settling. Reducing the injection rate allows formation of elongated buoyant jet that entrains annular fluid while breaking up into distribution of droplets. However, as the annular (displaced) fluid flows upwards it lifts small droplets thus creates mixture zone – shown in Figure 4.19. As also shown in Figure 4.20, only extremely low injection rates (0.5 to 1 gpm) would form Rayleigh fragments ^[14], and produce big and uniform droplets that are able to travel downwards and settle at the bottom with no mixing.

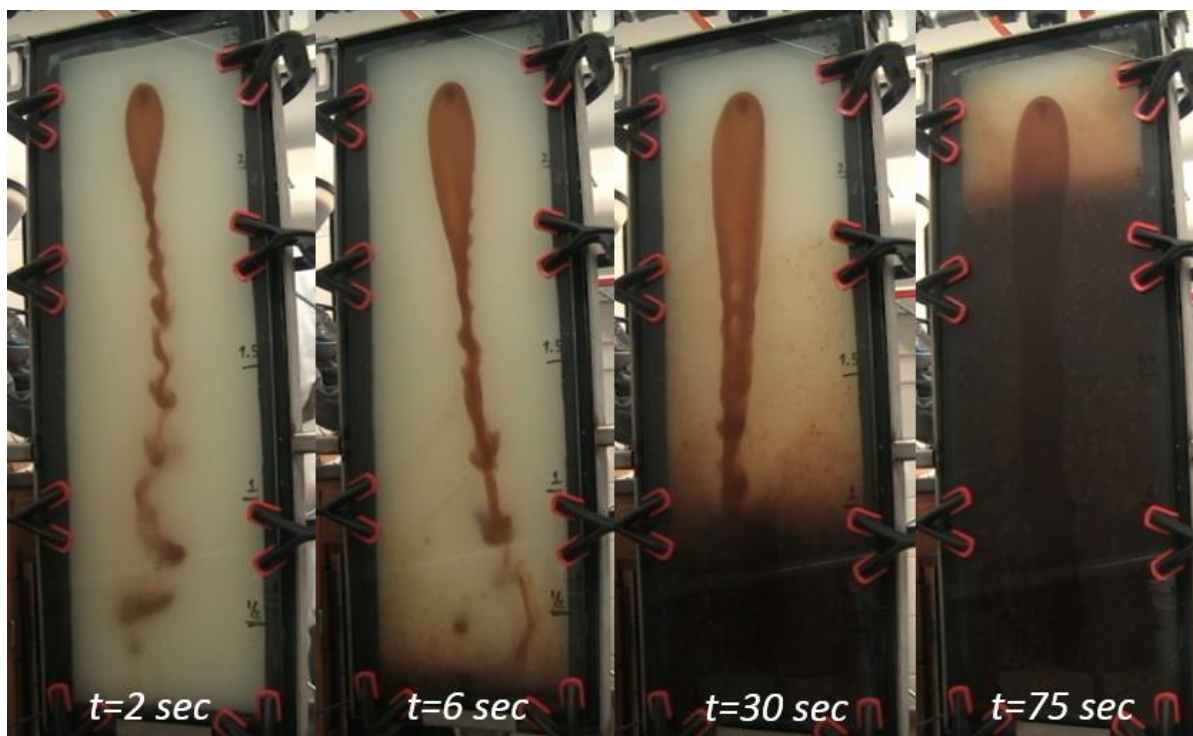


Figure 4.18: Side injection of KF1701 into high viscosity TF0102 at 2 gpm (Experiment #32). High strength of TF generated blurry AF/KF interface – mixture zone formed bottoms up.

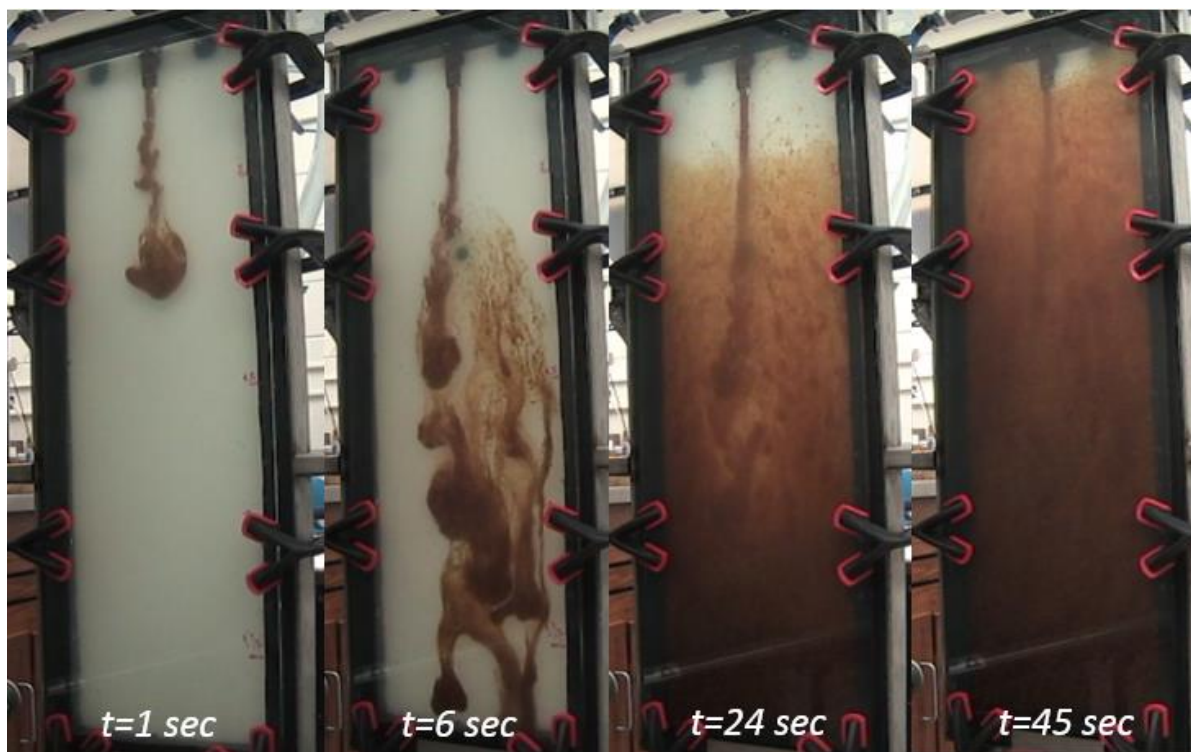


Figure 4.19: Top-injecting KF1701 into TF0107 at 1.5 gpm (Experiment #42). Despite low rate, dynamic jetting causes KF dispersion on its way downwards.

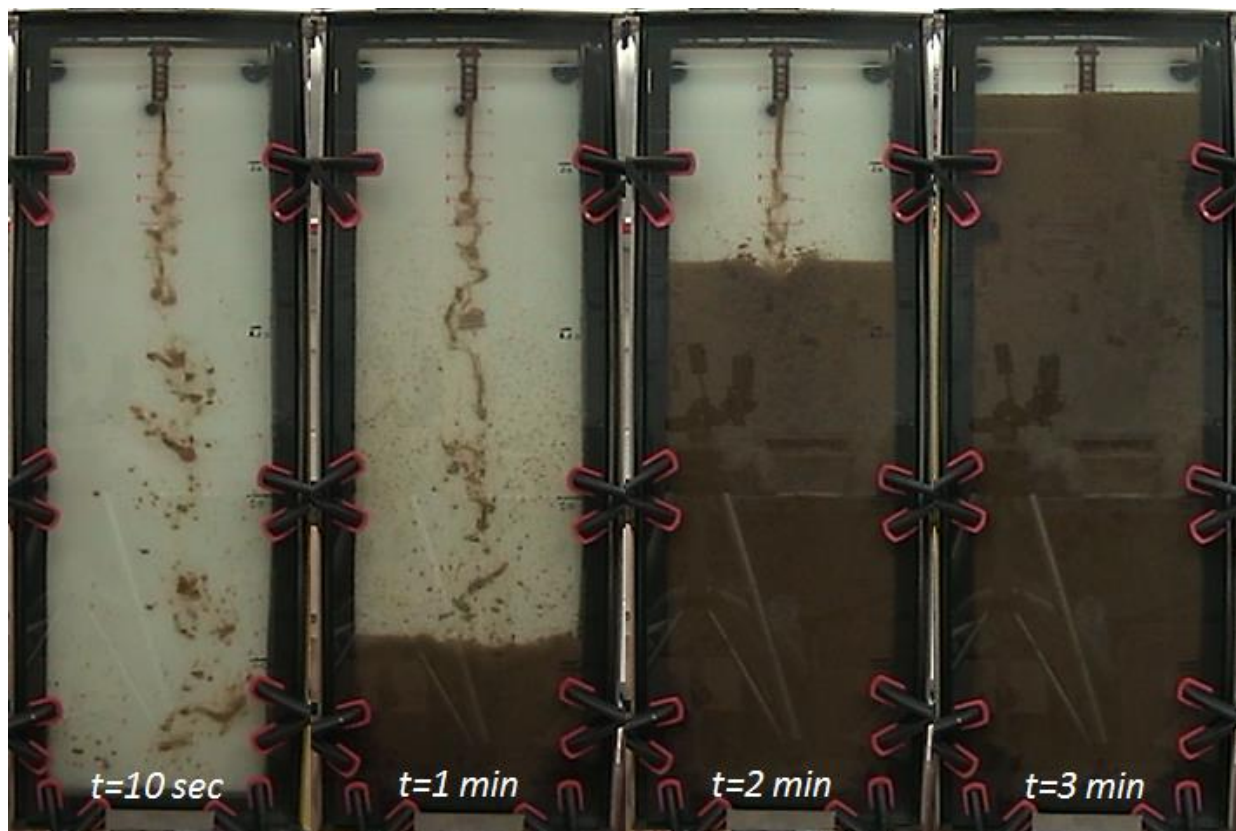


Figure 4.20: Top injection of KF1203 into thin TF0101 at 0.75 gpm (Experiment #6). Relatively large KF droplets form and settle down by buoyancy. A sharp KF/AF interface is observed

For the side injection geometry, energy of fluid stream dissipates in the inner wall's impingement where buoyant slippage begins. Stability of the impingement limits the injection rate as increasing flow rate results in large impingement for a given fluid. As shown in Figure 4.21, extremely slow rates allow a smooth transportation of KF to bottom and create a sharp KF/AF interface. Higher flow rates, as shown in Figure 4.22, impinges and cause more disturbance at the KF/AF interface thus resulting in mixture zone formation. Moreover, when rate is higher (or viscosity of KF is low) impingement regime changes from rivulet to gravity flow type and KF spreads mainly to the sides. Figure 4.23 demonstrates the unstable impingement. Generated droplets become more vulnerable to counter-current flow and discharge with AF.

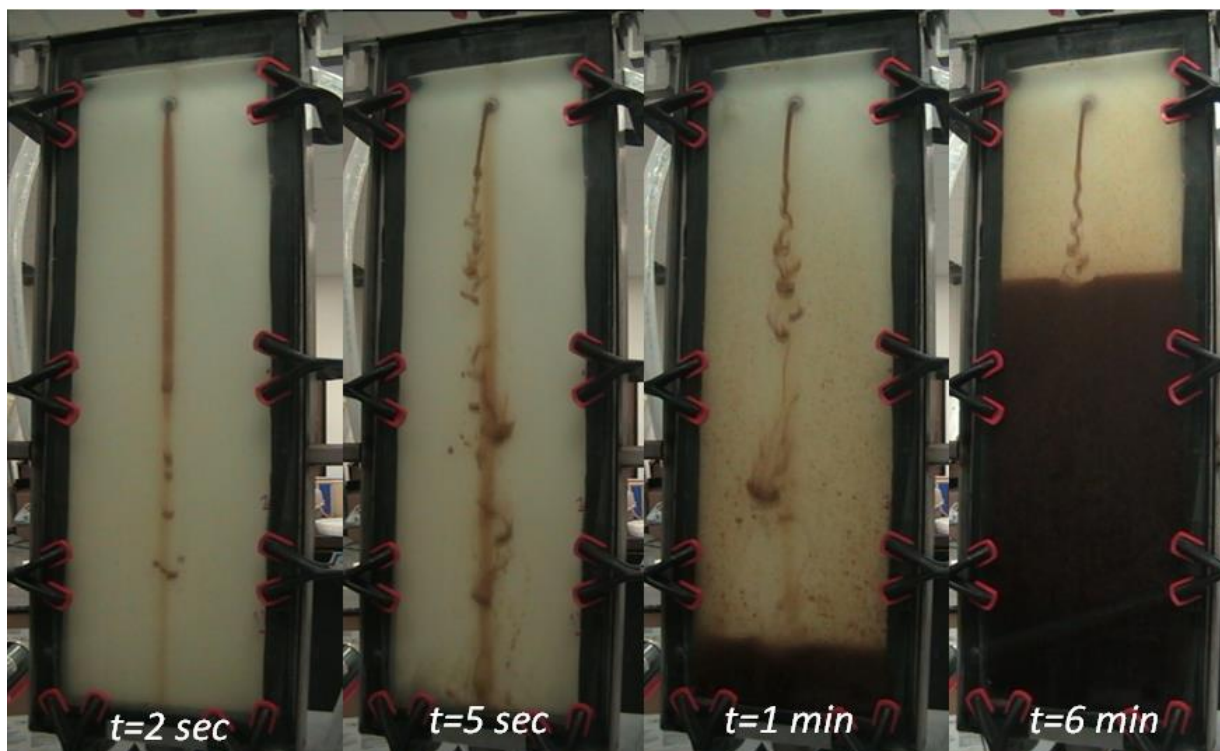


Figure 4.21: Side injection of KF1701 into TF0107 at low 0.5 gpm rate (Experiment #36) w/o impingement. Despite high GS of TF, no mixture zone develops.



Figure 4.22: Side injection of KF1701 into TF0107 at 2 gpm (Experiment #34). Higher flow rate creates a blurry interface between fluids.

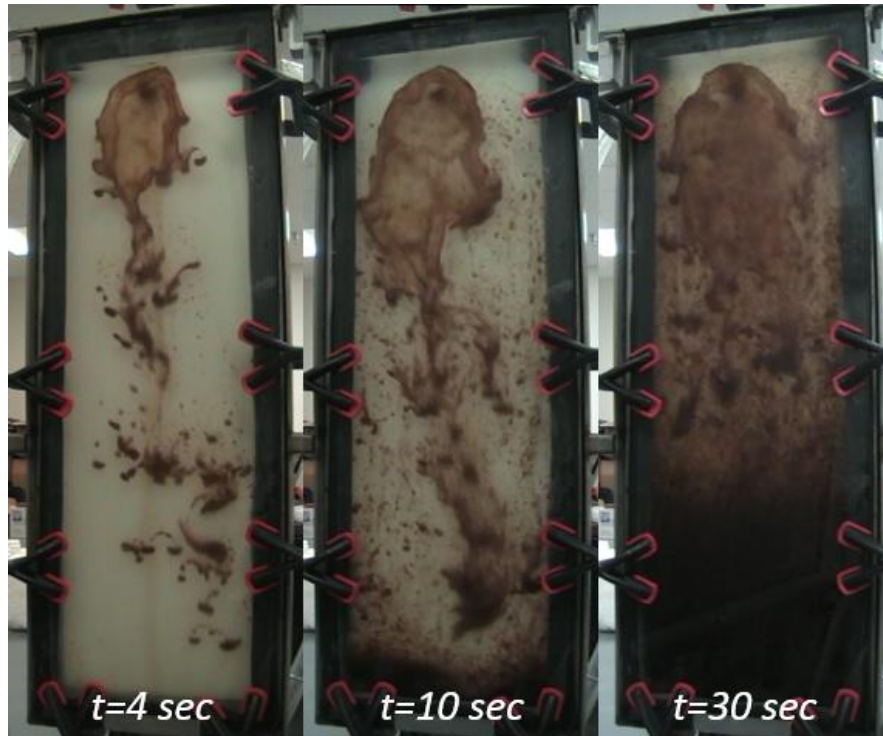


Figure 4.23: Side-injection of KF1204 into TF0107 at 2 gpm (Experiment #30) with large impingement. Low viscosity kill fluid brakes into droplets that are carried upwards by ascending TF- gravity settling with dispersion.

4.3.3 Relation to Field-Scale Applications

Results of the miscible displacement experiments above show that when the stagnant annular fluid has no strength the kill fluid (KF) mixes on contact with AF after injection. There is small (or none) buoyant slippage so fluid displacement in long columns is practically impossible. For structured AF (with some strength) some initial (rope-type) slippage occurs and mixing might be merely delayed.

As investigated in the “Characterization of Annular Fluid” chapter in this thesis (Chapter 2.4.2), drilling mud in a real well annulus produce water column at the top. This column with no structure would make it impossible for miscible KF to travel downwards. This may explain the failure of the early field trials of the Bleed-and-Lube technique with heavy muds ^[1].

Brominated organics, in the slot model experiments, rapidly settle in water with no mixing. They also travel through Non-Newtonian (structured) suspension after breaking into large number of particles (fragments) of various sizes. However, small particles may travel very slowly or become lifted upwards in the counter-current flow. Counter-current transport occurs

due to the upwards flow of annular fluid being displaced by the KF while moving downwards (In infinite stagnant fluid there is no counter-current flow). In real-wells transport depends on the annular area and distribution of KF particles. It is, therefore, critical to design KF injection such that initial fragmentation of the kill stream is prevented.

4.4 Maximum Injection Rate to Prevent Initial Dispersion

4.4.1 Side Injection

Side injection of heavy fluid into well's annulus results in impingement of the fluid stream on the inner casing wall. In the slot the front glass plate represents model inner casing. Large width of this impingement region would cause kill fluid to spread more in the annulus and result in a larger contact area of fluids; which would hamper the displacement process by carry over the kill fluid to overflow. Thus, control of the size of impingement is essential for finding limitations of the injection process.

As already explained in the literature review chapter, many researchers, mostly concerned about jetting liquid into ambient air, have studied impingement. However, jetting liquid into liquid has not been much studied.

For the liquid-to-air jetting Wilson et al. ^[71] relate the width of the impinged liquid film (W) to two dimensionless quantities, Eötvös Number and Reynolds number of impinging fluid. For the purpose of this study, we modify this approach by:

- Using difference of fluid densities instead of single fluid density (as air density $\cong 0$);
- Ignoring jet energy loss (and, therefore, distance) from jet exit to impingement surface.

With these modifications the impingement Eötvös number depends on properties of two liquids as,

$$Eo = \frac{\Delta \rho \, g \, W^2}{\sigma}$$

While Reynolds number depends on the injected (kill) fluid as,

$$Re = \frac{4 \, \dot{m}}{\mu_{kf} \, W} = \frac{4 \, \rho_{kf} \, q}{\mu_{kf} \, W}$$

Where, W is the impingement width in inches, $\Delta\rho$ is the density differential ($\rho_{kf} - \rho_{af}$) in ppg., σ is the interfacial tension in dynes/cm, \dot{m} is the mass flow rate in lb/min, q is the volumetric flow rate in gal/min and μ_{kf} is the kill fluid viscosity in cP.

Wilson et al. ^[71] defined group parameter, named here as β_1 – using our notation – becomes,

$$\beta_1 = \frac{g \mu_{kf}^4}{\rho_{kf} \sigma^3}$$

They also combined Eo and Re into another group parameter, β_2 , as,

$$\beta_2 = \frac{1}{16} Eo Re^2 = \frac{\Delta\rho g \dot{m}^2}{\sigma \mu_{kf}^2}$$

And they expressed Eötvös number in terms of the two groups as,

$$Eo = c_1^2 \beta_1^{0.25} \beta_2^{0.75}$$

Or,

$$\frac{\Delta\rho g W^2}{\sigma} = c_1^2 \left(\frac{g \mu_{kf}^4}{\rho_{kf} \sigma^3} \right)^{0.25} \left(\frac{\Delta\rho g \dot{m}^2}{\sigma \mu_{kf}^2} \right)^{0.75}$$

where, c_1 is the conversion factor and empirical constant.

Solving for W gives formula for impingement size,

$$W = c_1 \frac{\dot{m}^{0.75}}{\Delta\rho^{0.25} \mu_{kf}^{0.25} \sigma^{0.25}} \quad (4.5)$$

Equation 4.5 is a theoretical formula and needs to be validated. Therefore, the empirical size from the experiments (Table 4.7) is correlated with that predicted with Equation 4.3 for the constant “ c_1 ” value giving the linear regression slope equal to unity, as shown in Figure 4.24. The point marked with “x” is excluded from the correlation (Experiment #30). Triangular and diamond shaped data points represent rivulet and gravity-flow type impingements, respectively. In some runs, jet forces expired before KF reaching the wall and impingement width became very small or none. This low injection rate generated Rayleigh fragmentation mode and considered as rivulet type of impingement due to its desirability.

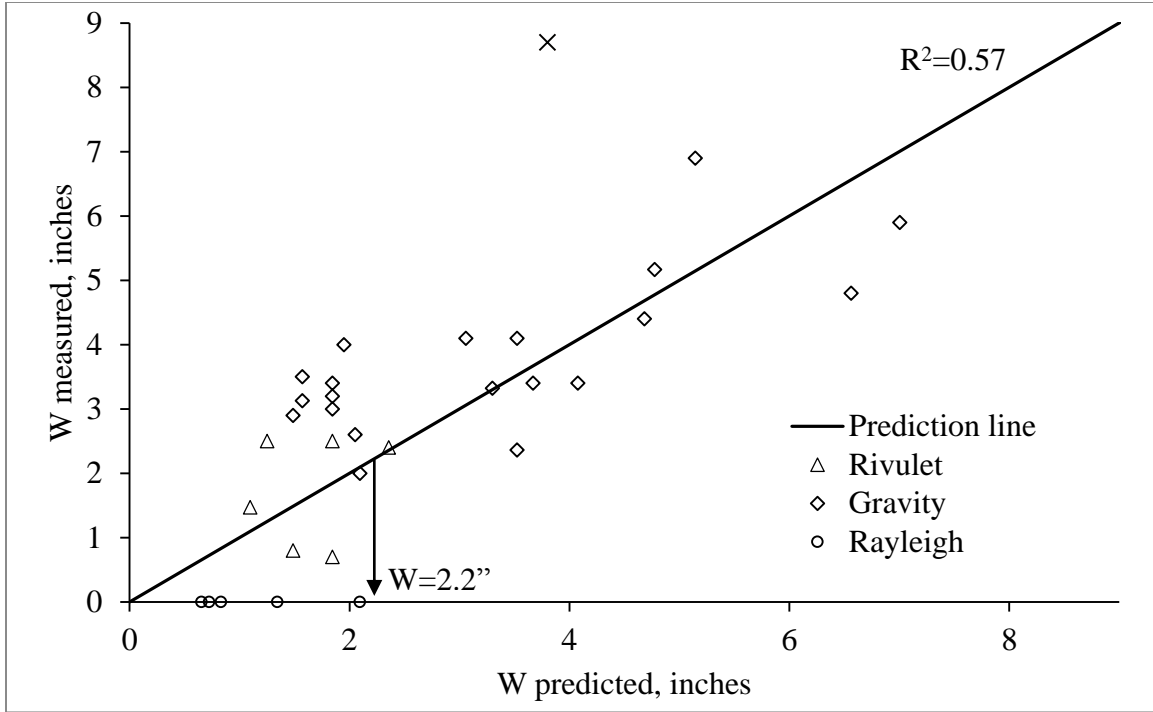


Figure 4.24: Impingement width actual vs prediction plot. Rivulet threshold is estimated as 2.2"

The unit slope regression line gives $a=1.904$. Therefore, the expression (Equation 4.5) becomes,

$$W = 1.904 \frac{\rho_{kf}^{0.75} q^{0.75}}{\Delta\rho^{0.25} \mu_{kf}^{0.25} \sigma^{0.25}} \quad (4.6)$$

The likely reason for poor correlation in Figure 4.24 is that the properties of kill fluids; listed in Table 4.4, are merely estimates (IFT). Also, measurements of flow rates were not precise. Nevertheless, the trend in Figure 4.24 is clear. The plot defines threshold between rivulet and gravity flow type of impingements for the width value, 2.2 inches. Substituting this number to Equation 4.6 and solving for the injection rate gives the formula for maximum injection rate as,

$$q_{cr-i} = 1.21 \frac{(\Delta\rho \mu_{kf} \sigma)^{\frac{1}{3}}}{\rho_{kf}} \quad (4.7)$$

Equation 4.7 represents the critical rate for impingement criteria. When the injection rate exceeds this value impingement zone loses its stability and KF droplets spread in the annulus.

4.4.2 Top Injection

Reitz ^[14] studied fragmentation modes of a liquid jet in air^[13]. He developed a plot of Ohnesorge number versus nozzle Reynolds number and defined the threshold conditions (Figure 1.5). (Ohnesorge number relates viscous forces to inertial and surface tension forces) In his experiments, the ambient fluid was air; however, in this case this fluid is liquid. A Modified Ohnesorge number, Z , that considers two liquids was proposed by Teng et al. ^[17]. They used the Z number for estimation of droplet sizes generated by a liquid spray emerging into an ambient fluid of different properties. Modified Ohnesorge number in field units is,

$$Z \equiv 0.018 (3\mu_{kf} + \mu_{af}) / (d_n \sigma \rho_{kf})^{\frac{1}{2}} \quad (4.8)$$

Using Z instead of Ohnesorge number in estimation of fragmentation modes is theoretically more accurate; since the effect of annular fluid on displacement process is significant. Figure 4.25, below, is similar to that in Figure 1.5 where Ohnesorge number is replaced with Modified Ohnesorge number. The transition line formulas in the plot are also modified.

The threshold between transition and atomization mode is,

$$Z = 948.7 \text{ Re}^{-1.25} \quad (4.9)$$

The threshold between Rayleigh Mechanism and transition is,

$$Z = 131.9 \text{ Re}^{-1.25} \quad (4.10)$$

As discussed earlier, atomization regime represents the flow pattern when the injected fluid disperses instantly just after it exits the nozzle. This phenomenon is obviously not wanted for gravity displacement because small droplets may form emulsion in the countercurrent flow shear and get lifted upwards. Transition do not atomize; but, generate various sizes of droplets (satellite droplets ^[15]) that may be also carried upwards by the displaced liquid. Therefore, flow rate must be designed such that the flow pattern of the kill fluid jet will always stay below atomization threshold line in Figure 4.25.

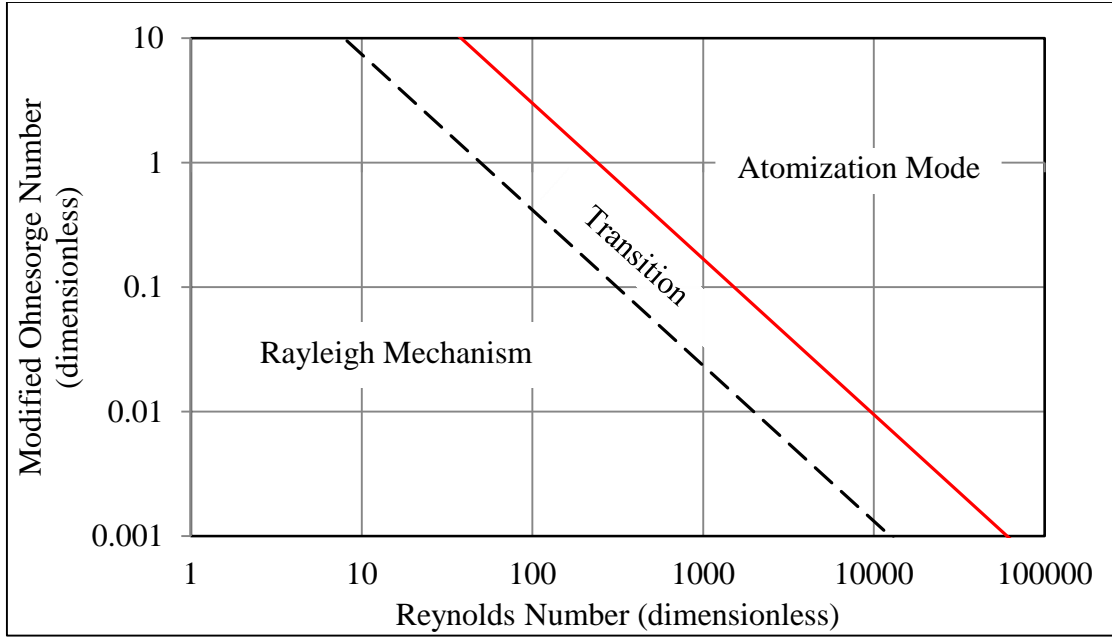


Figure 4.25: Fragmentation modes of a liquid jet in pressure atomization into an ambient fluid.

Reynolds number in field units is,

$$Re = 928 \rho_{kf} u d_n / \mu_{kf} \quad (4.11)$$

Where, ρ_{kf} is kill fluid density (ppg), μ_{kf} is kill fluid viscosity (cP), u is velocity of the jet (ft/sec), and d_n is nozzle diameter (inches).

Equation 4.10 in field units is,

$$Z = 131.9 \left(\frac{928 \rho_{kf} u d_n}{\mu_{kf}} \right)^{-1.25} \quad (4.12)$$

Velocity of kill fluid in the nozzle is,

$$u = q/A_n = \frac{4}{\pi} \frac{q}{d_n^2}$$

Or in fields units,

$$u \text{ [ft/s]} = 0.41 q/d_n^2 \quad (4.13)$$

Then, Equation 4.12 becomes,

$$Z = 0.078 \left(\frac{\rho_{kf} q}{\mu_{kf} d_n} \right)^{-1.25} \quad (4.14)$$

Equation 4.14 defines the modified Ohnesorge number where for offset of transition rate atomization regime starts forming. Solving for flow rate gives,

$$0.018 \frac{(3\mu_{kf} + \mu_{af})}{(d_n \sigma \rho_{kf})^{\frac{1}{2}}} = 0.078 \left(\frac{\rho_{kf} q}{\mu_{kf} d_n} \right)^{-1.25}$$

Or,

$$q_{cr-R} = 3.23 \frac{\mu_{kf} d_n^{1.4} \sigma^{0.4}}{\rho_{kf}^{0.6} (3\mu_{kf} + \mu_{af})^{0.8}} \quad (4.15)$$

Equation 4.15 defines critical flow rate to assure the Rayleigh mechanism of jetting. Similar derivation gives the critical flow rate defining the threshold for atomization,

$$q_{cr-A} = 15.76 \frac{\mu_{kf} d_n^{1.4} \sigma^{0.4}}{\rho_{kf}^{0.6} (3\mu_{kf} + \mu_{af})^{0.8}} \quad (4.16)$$

Atomization criteria can be applied to both top and side injection conditions to make sure that the dynamic forces do not generate the turbulent regime and gravity forces control the jet.

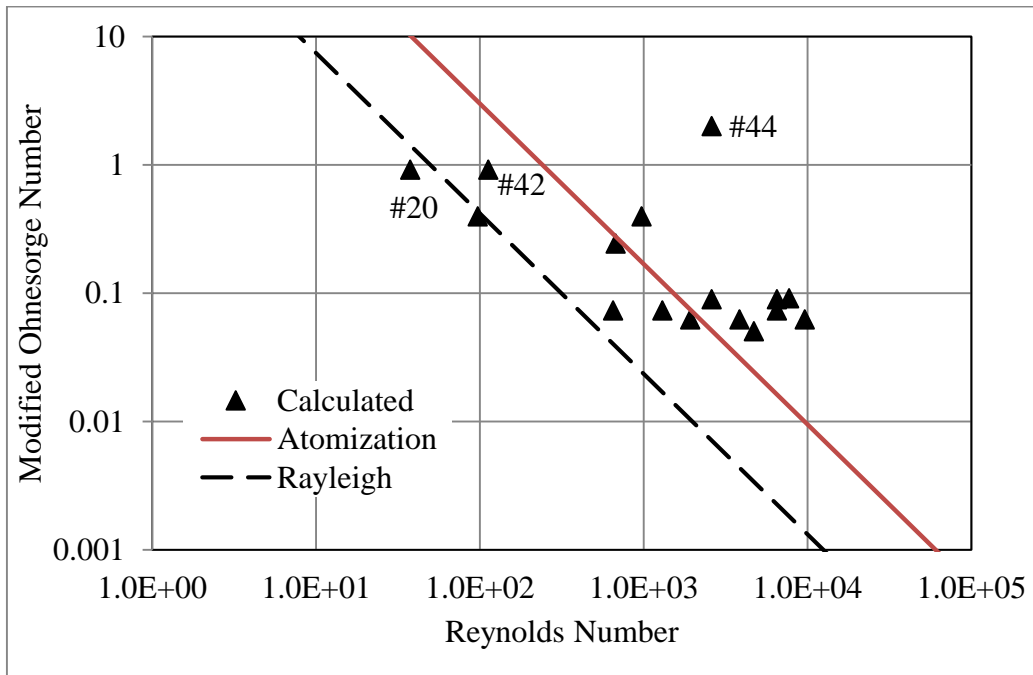


Figure 4.26: Matched flow pattern values for vertical injection

Conducted experiments are marked in Reynolds versus Modified Ohnesorge number and shown in Figure 4.26. The labeled data points are examples of three top jetting modes observed in our experiments. As shown in Figure 4.27, Rayleigh mechanism allows a continuous transport of KF to the bottom by maintaining uniform droplets, while atomization mode causes nozzle-front dispersion and result in inefficient transport.



Figure 4.27: Rayleigh mechanism (left), transition (middle) and atomization modes (left) from experiments #20, #42 and #44 respectively

As indicated by the power functions in Equation 4.13 and 4.15, the nozzle size has the most influence on the flow rate. Figure 4.28 illustrates this effect for fluid properties shown in Table 4.8. It follows from Figure 4.12 that the size of nozzle is an important operational parameter; nozzle increase from 0.5 in to 1.5 in may reduce the operational time five-fold. Figure 4.29 shows the change of critical flow rate (for atomization) with changing kill and annular fluid viscosities. The plot implies, again, that selecting kill fluid with viscosities above 25 cP would significantly reduce operational time.

Table 4.8: Fluid properties used in Figure 4.28 and Figure 4.29

Kill fluid viscosity	10 cP
Annular fluid viscosity	10 cP
Annular fluid density	9 ppg
Interfacial tension	30 dynes/cm

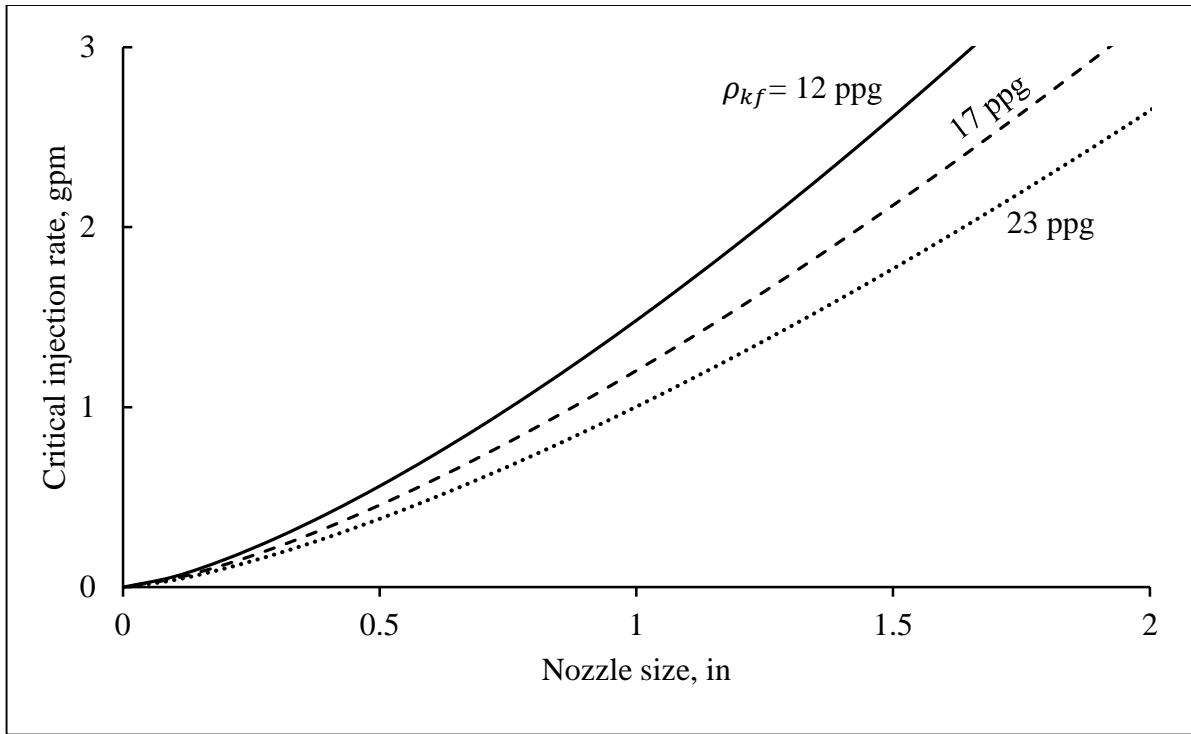


Figure 4.28: Critical injection (for atomization) can be increased several-fold with large nozzles

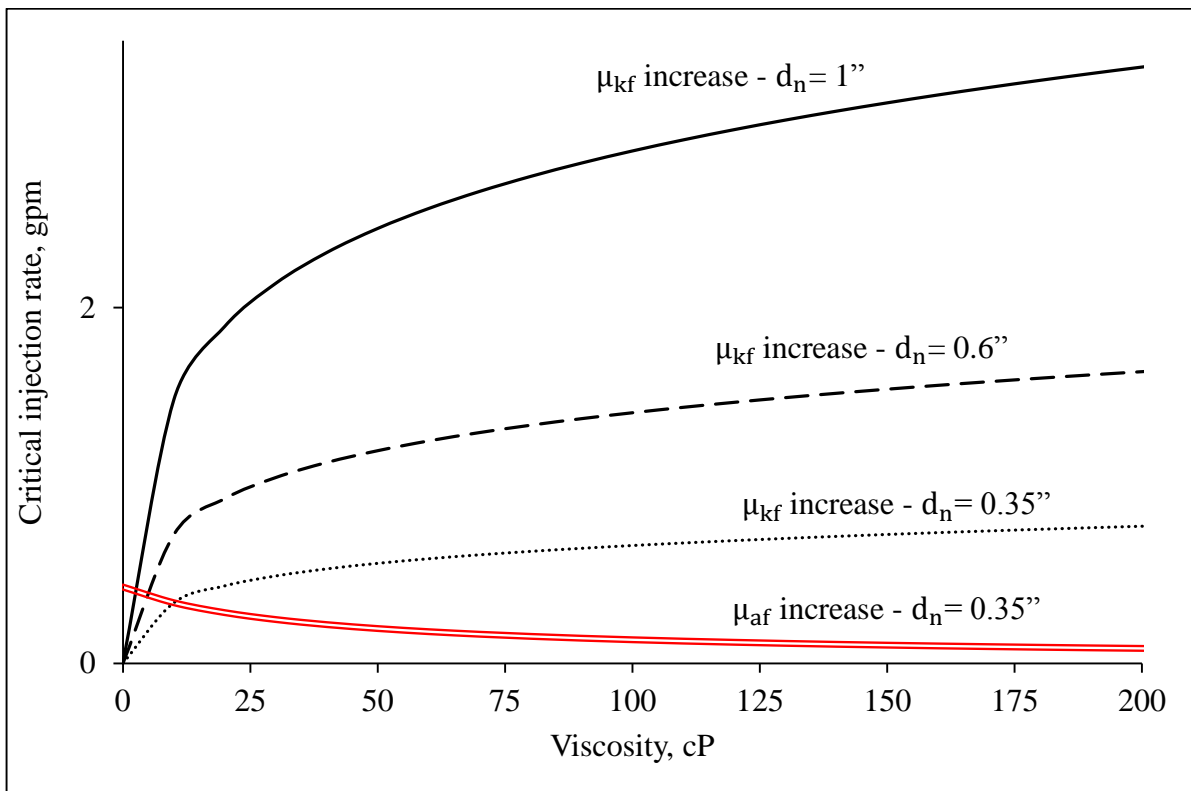


Figure 4.29: Critical injection rate (for atomization) can be increased for higher KF viscosities, and lower AF viscosities

CHAPTER 5: PILOT SCALE EXPERIMENTS

5.1 Objective

The slot-model experiments, above, provided useful insight of the kill fluid injection and the onset of buoyant slippage. However, small size of the model (a three-foot column) would not allow the process of downwards transport to stabilize – before reaching the model’s bottom. For example, spiral movement of the kill fluid stream (see Figure 1.3) did not establish any stable pattern prior to the settling. Moreover, the process of mixture zone buildup at the model’s bottom – on top of the settled kill fluid – was too short to fully develop. Therefore, a taller, pilot-scale model was built and used to study the followings:

- Investigate the pressure replacement and volumetric efficiencies for complete displacement of annular fluid in a pilot size set-up;
- study the individual effects of system and operational parameters on process efficiency;
- estimate the effect of gas migration during gravity displacement process; and,
- develop process design expressions for full-scale applications.

5.2 Methodology

5.2.1 Physical Model Design and Fabrication

Cyclic injection (Bleed-and-Lube) technique for gravity displacement method was tested at LSU using a clear PVC apparatus^[8]. The model system had been designed to imitate wellhead pressure cycles using a U-tube effect. However, the design also brought some disadvantages such as volumetric loss of kill fluid to inner pipe, and inability of injecting gas from the bottom. With the new model design, these effects have been eliminated. Moreover, much larger number of experiments with variety of fluids was designed to find the effects of various parameters on the displacement process performance.

A twenty-foot pilot physical model was manufactured at the Albemarle PDC facility by installing 6 in (6 5/8” OD) inside 8 in (8.329” ID) carbon steel pipes. Cross-sectional annular area was 0.14 square-feet and the entire annular volume was 20.5 gallons (Capacity= $A \times L = 1.05 \text{ gal/ft} \times 20 \text{ ft} = 20.5 \text{ gal}$). Four pressure transducers and manual gages were installed together in every 4 feet (3-11/12’) starting from 6” above the bottom (see Figure 5.1 and Figure 5.5). Gas breathers were

attached at the bottom of annulus and connected to facility air source that had a maximum pressure of 60 psi (see Figure 5.3). A 2-in overflow hole was drilled in the inner tubing at 1-in from the top. The tubing's bottom had an outlet for draining the overflowing fluid. A 4-in diameter glass viewer was placed at the very bottom of the inner pipe to observe the overflowing fluid. A 0.5-in valve was installed at the bottom to drain the column after each experiment run. A 0.5" OD (0.38" ID) injection port was welded at the top of annulus for top-injection of the annular fluid to fill-up the column. The same size port was installed at the outer pipe wall, 4' below the top for side-injecting the kill fluid (see Figure 5.4). The kill fluid was stored in a closed mixer tank (KF Tank) that was pressurized from the central gas source. For higher injection rates, a 50 HP downstream motor pump from KF tank was used. The KF tank weight was recorded by a scale so the KF mass was continuously measured in order to compute the flow rate. Schematics of the whole model is shown in Figure 5.5 in more details.



Figure 5.1: Pilot model

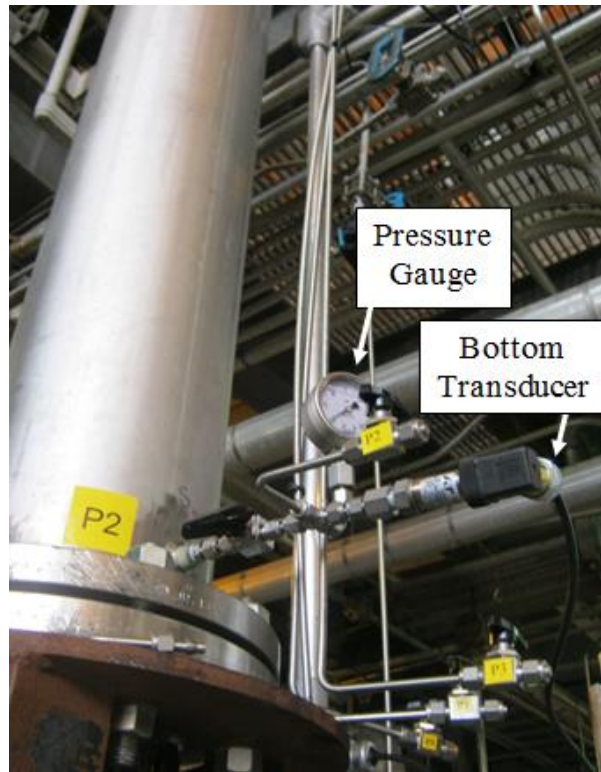


Figure 5.2: Bottom of outer casing with pressure instruments

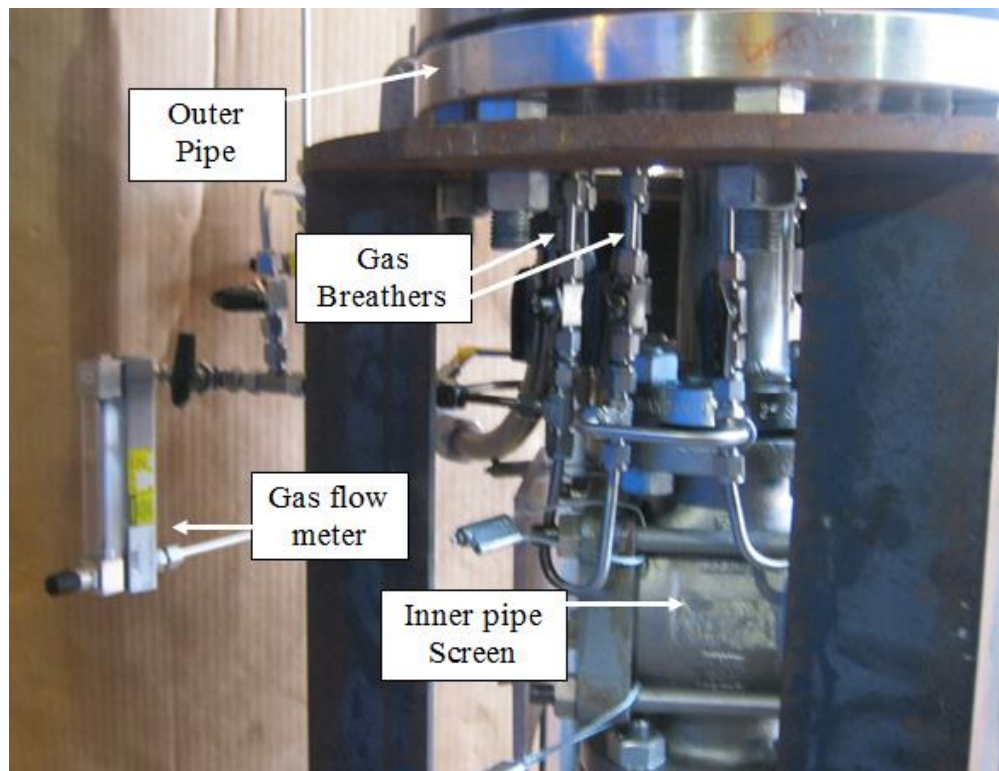


Figure 5.3: Gas injection installation below annular column's bottom with inner pipe drain viewer

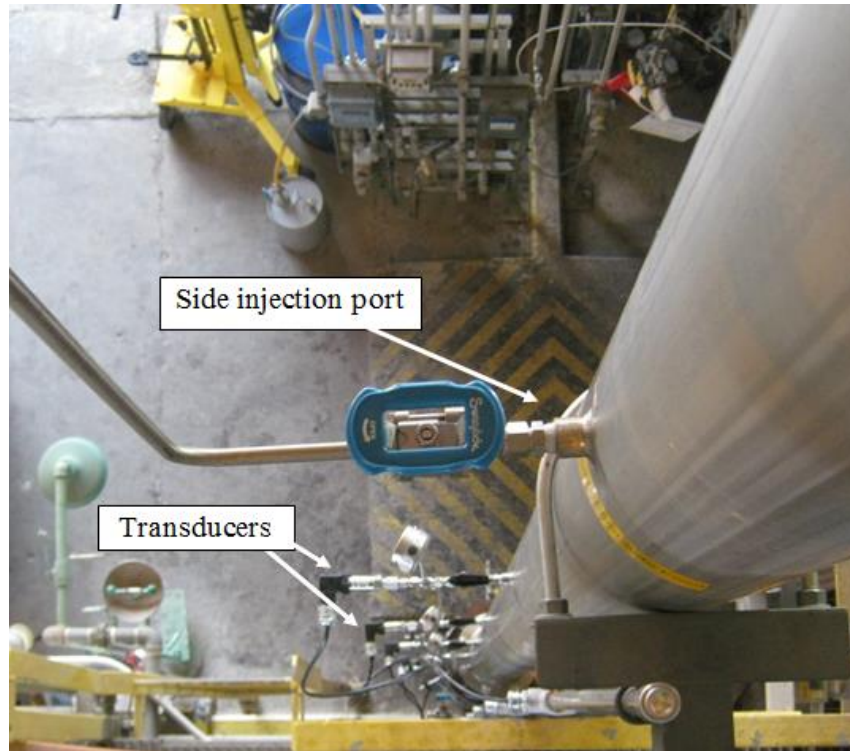


Figure 5.4: Top view down annular column showing spaced pressure transducers and KF side-injection port

5.2.2 Experimental Procedure

All experiments were run in ten steps listed below. Also, Figure 5.6 shows bottom pressure change at each step.

- 1) Transfer the kill fluid (KF) components to the KF tank and blend for at least 30 minutes to assure complete mixing. Record the initial mass of KF in the tank.
- 2) Agitate the annular fluid (AF) in the mud mixer and pump the fluid line into the annulus. Stop pumping when you see AF overflow in the glass viewer. Drain the viewer chamber to collect a 300 mL sample of the injected AF.
- 3) Leave the AF in annulus undisturbed for around 2 hours to develop structural (gel) strength.
- 4) Aerate the annular fluid by injecting gas from the breathers at maximum rate of 2 SCFM to simulate gas migration in a real well.
- 5) Pressurize the KF tank for the desired injection rate. For injecting viscous fluids, use the pump in addition to tank pressure.
- 6) Start kill fluid injection.

- 7) Record KF weight change in time.
- 8) Take samples of overflow every 5 gallons of KF injected.
- 9) After pumping all the KF in the tank close the injection valve and bleed off the gas pressure. Record the time.
- 10) Drain the fluid in annulus and collect samples.

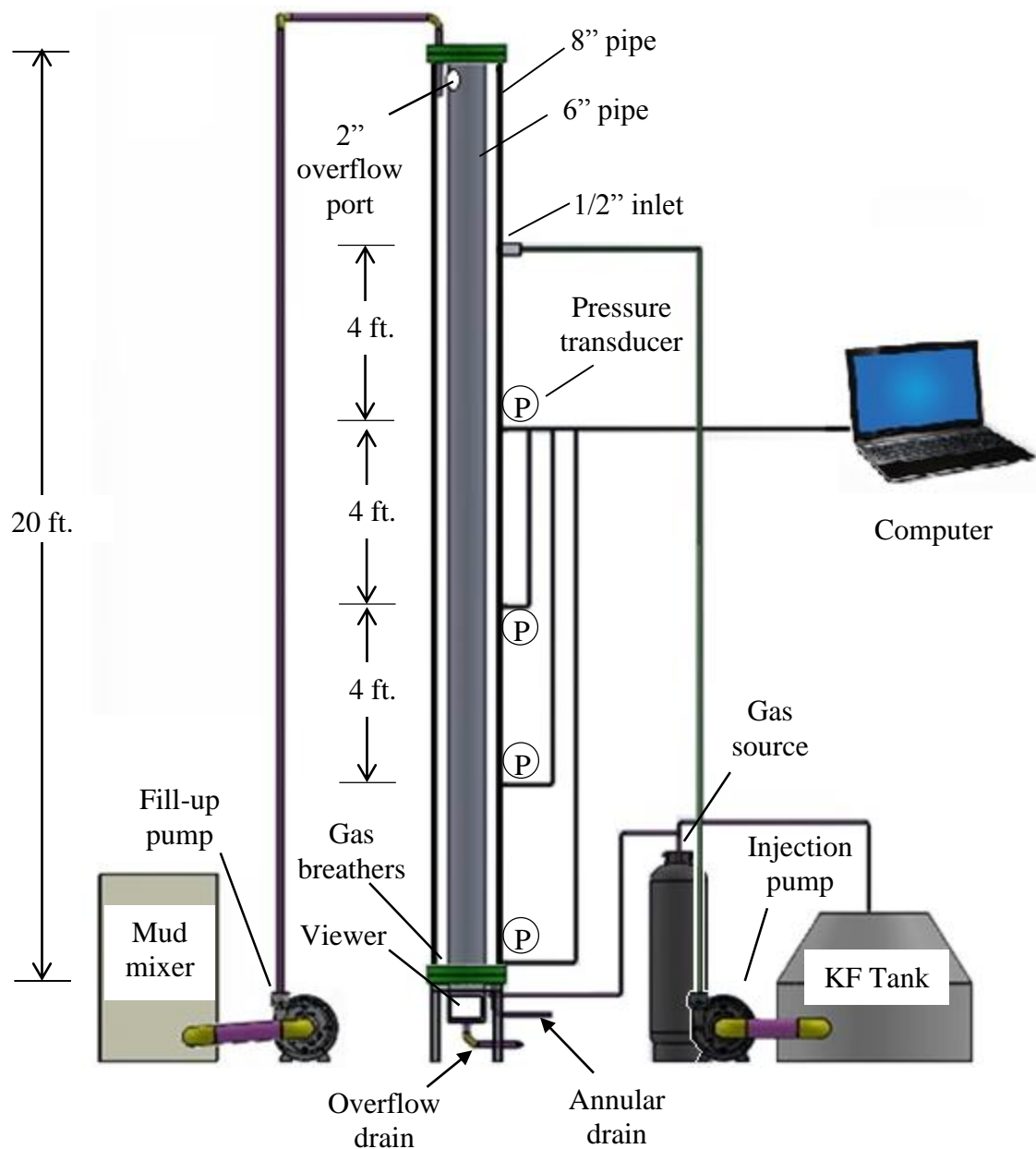


Figure 5.5: Pilot model schematics

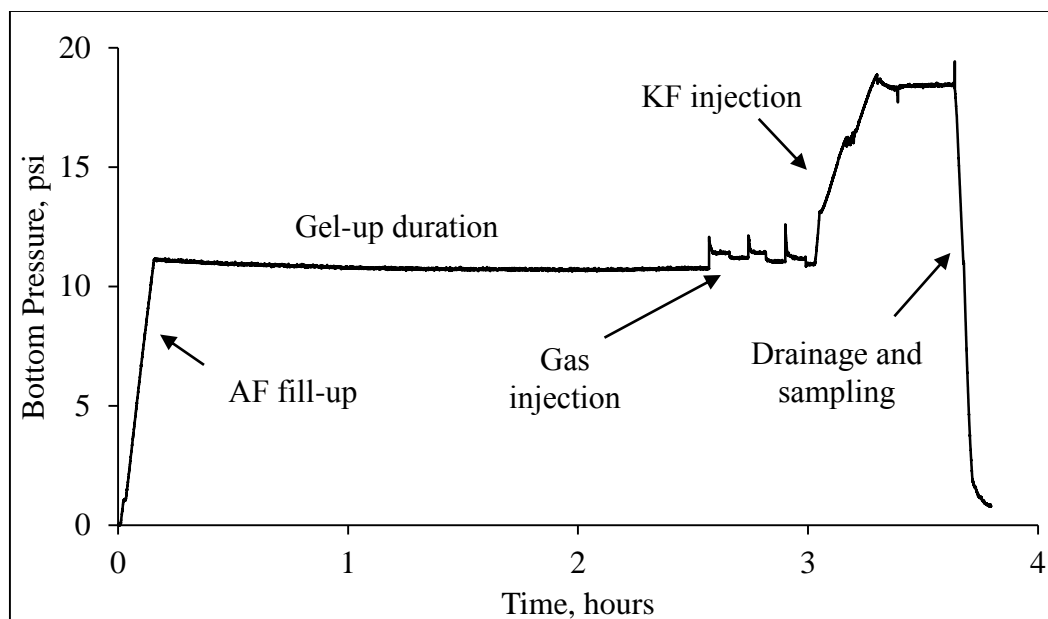


Figure 5.6: Bottom pressure change during experiment

Pressure measurements were obtained automatically from the pressure transducers and also manually from the pressure gages. The gages specified range of 30 psi and low accuracy and accuracy of the transducers was ± 0.015 psi. However, all the tested transducers except the one at the bottom had offsets of around 0.1 psi. Nevertheless, only the bottom transducer was used for the analysis so no corrections were required.

Flowmeter could not be installed on the injection line due to the safety regulations in Albemarle facility. Therefore, rate was calculated from the mass vs. time measurements. Therefore, error of the injection rate could only be detected and adjusted for after several minutes of injection. This method made it difficult to set a desired injection rate, particularly in the first five minutes of injection. Gas injection rate, on the other hand, could be fixed from a flowmeter installed on the gas line. After each experimental run, drained fluid samples from the annulus were tested for concentration of KF and AF. The samples in annulus were drained in different drums and weighted separately. If a sample density was smaller than density of KF, the sample was centrifuged to find volume fraction of each component.

5.2.3 Experimental Matrix

Annular fluid (AF) to be used in the pilot scale tests are mixed in a 20 barrel trip tank at LSU Petroleum Engineering Research & Technology Transfer Laboratory (PERTTL) by using

different concentrations of bentonite clay and Barite (barium sulfate) to obtain various structural strengths and densities. Structural strength is defined as a combination of fluid's resistance to shear and its gelation capability (rheology and tixotrophy). According to AF's density and structural strength level annular fluids are named starting with the letters "AF". Structural strength level varies dominantly with the drilling fluid's clay concentration. As concentration increases, AF shows higher rheology and higher gel strength. For instance the AF0901 fluid had 9 ppg density and properties the lowest level of structural strength. Annular fluid names, densities and structural strength are listed in Table 5.1.

When annular fluids with the same density were being mixed, initially the lowest concentration of bentonite was hydrated in the trip tank overnight. Then, barium sulfate was added to increase its density to desired value. After taking out some of this low strength (structural level 1) AF more bentonite is added to increase its structural strength and desired amount is again taken out after circulating the mud for an hour to attain homogeneity. The same process was repeated for all AF varieties. The fluids were collected in 30-gallon drums, labeled and shipped to Albemarle PDC. Samples from each batch of mixing were also collected for measurement.

Table 5.1: Table of annular fluids (AF) in pilot experiments

Name	Density ppg	Structural Strength Level	Bentonite concentration ppb
AF0901	9	1	13
AF0902	9	2	18
AF0903	9	3	25
AF1101	11	1	15
AF1102	11	2	20
AF1103	11	3	25
AF1301	13	1	15
AF1302	13	2	18
AF1303	13	3	22

Each kill fluid (KF) has been produced by blending two of three different components. As explained in selection kill fluid chapter in this work densities of these components were 11.08, 24.7 and 7.01 ppg and their viscosities were 4090 cP, 2 cP and 13 cP, respectively. Properties of

KF used in the pilot tests are listed in Table 4.3. The fluids code represent density and viscosity degree of the kill fluid. The blends heavier than 15 ppg were produced from the 11.08 ppg and 24.7 ppg components and their viscosities follow the trend shown in Figure 3.3. The KF having 12 ppg density was produced from the 24.7 ppg and 7.01 ppg components and the two blends (15.1 ppg and 14.91 ppg) were obtained by blending all three components (24.8 ppg, 11.08 ppg, and 7.01 ppg).

Table 5.2: Properties of annular fluids in pilot experiments

Fluid	ρ (ppg)	μ_p (cP)	τ_0 (lbf/100sqft)	$\tau_{g2hours}$ (lbf/100sqft)
AF0901	9	3.2	2.1	2.1
AF0902	9	10.6	4.2	13
AF0903	9	25.4	14.8	37
AF1101	11	9.5	4.2	5
AF1102	11	21.2	6.4	28
AF1103	11	55	58.3	73
AF1301	13	21.2	9.5	17
AF1302	13	30.8	30.8	32
AF1303	13	38	40.3	75

Table 5.3: Properties of kill fluids used in pilot experiments

	Density, ppg	Viscosity, cP	Estimated IFT, dynes/cm	Estimated log(P)
KF1204	11.8	8.0	32	3
KF1501	15.01	492.0	24	6
KF1502	14.91	12.0	28	3
KF1701	16.68	235.6	21.5	6.5
KF2001	19.6	76.4	29	2
KF2301	22.94	25.5	34	2.5

Table 5.4 shows the AF/KF combinations used in the experiments. Each run are named as “batch” and number. Batch refers to KF components mixed in the tank. This name has been selected to avoid confusion with the slot-model experiments. Since supply of brominated organic material was limited, most of the experiments were run with KF1701. Also, the maximum injection rate was limited at 6 gpm by the installation.

Table 5.4: Experimental matrix of pilot-scale experiments

AF KF	AF0901		AF0902		AF0903		AF1101		AF1102		AF1103		AF1301		AF1302		AF1303	
	Batch#	q, gpm	B#	q	B#	q	B#	q	B#	q	B#	q	B#	q	B#	q	B#	q
KF1204					27	1.0												
					28	6.0												
					29	4.3												
KF1501	20	1.2	21	1.2	11	1.1												
KF1502					30	0.8												
KF1701	4	1.2	5	1.4	2*	1.1	18	2.2	10	1.1	14	1.3	15	1.2	9	0.9	7	1.0
					3*	0.7	31	1.4	16	1.5	19	0.9						
					6	1.2												
KF2001	26	1.0	24	1.0	1*	1.2					12	1.2			33	1.1	8	1.3
					35	1.1					32	0.8					22	3.9
																	23	5.0
KF2301					17	1.3					13	1.1					25	1.3
AF1302					34	1.0												

* Concurrent displacement with gas migration

5.3 Results and Observations

A total of 34 immiscible displacement experiments have been run as shown in Table 5.5. In all experiments complete displacement was not achieved due limited volume of the kill fluid (Pressure replacement stopped when there was no more fluid in the KF tank). A few runs, such as Batch 31, shown in Figure 5.7, with 1.23 annular volumes of KF ($R_u=1.23$) resulted in almost complete displacement ($E_f=0.97$). Typically, as shown in the plot, the bottom pressure buildup was initially up to a departure point of the curved section that would asymptotically reach the ultimate pressure value, P_u .

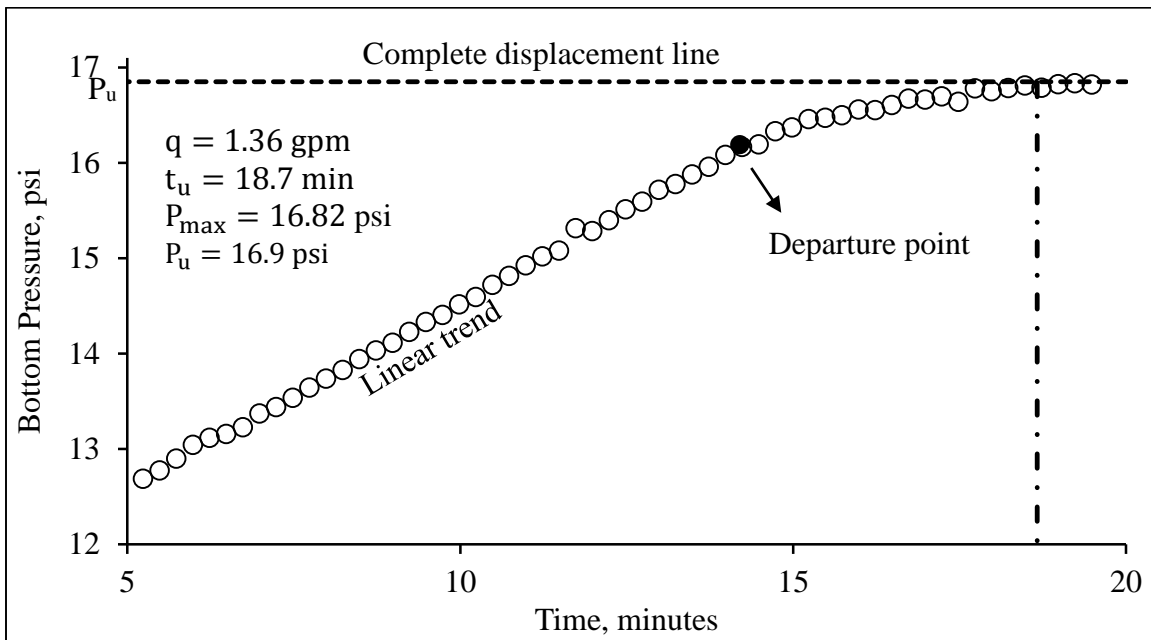


Figure 5.7: Pressure vs. time plot of Batch 31 run; P_{max} = maximum final pressure, P_u = ultimate pressure (complete displacement)

Figure 5.8 demonstrates two examples of unfinished displacement due to KF volume shortage. The Batch 6 run used only 0.83 annular volumes of KF and did not show any deviation from linear trend. The Batch 23 run, on the other hand, showed a curvature forming after 1.4 minutes of injection and did reach the complete displacement line despite injecting 1.79 volumes of KF.

As explained in more details in the experimental procedure, KF injection rates are obtained without use of a flowmeter. Therefore, as also shown in Figure 5.8 (Batch 6 run), the initial rate was high before it got under control after minutes of injection. These operational problems

caused multiple flow rates and generated more than one linear trends in the pressure vs time plots. Averaged flow rates, batch numbers and their corresponding fluid properties are shown in the results, Table 5.5. In the table, R_f column shows the final displacement ratio when available volume of KF was injected, and E_f column shows the final pressure replacement efficiencies.

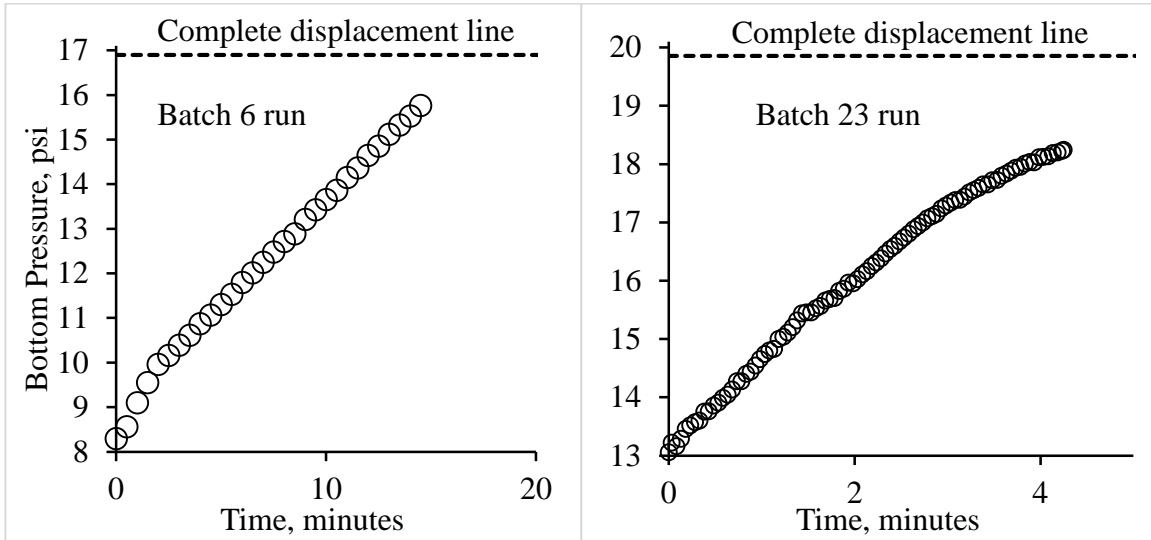


Figure 5.8: Pressure vs. time plots of Batch 6 and Batch 23 runs demonstrate unfinished displacements due shortage of KF

Fluid samples collected from the overflow and the annulus indicated presence of a mixture zone on top of the settled clean kill fluid column. This zone had distributed density with depth – shown in Figure 5.9. Density measurements for minus values of depth are obtained from the overflow, and positive values are taken from annular drain samples. The general shapes of density trends are not the same but their curvatures are different.

During an actual bleed-and-lube operation, the pressure bleed-off cycle may induce additional gas migration. In order to simulate such a scenario (in the Batch 1, 2 and 3 runs) injection of KF was conducted concurrently with gas injection. Figure 5.10 shows a comparison of the pressure vs. time plots of the Batch 1 run and Batch 35 run.

The Batch 1 plot shows early curvature indicating loss of KF to overflow resulting from flotation effect. As the plot's curvature continues, it indicates an asymptote pressure value below that for complete displacement. The phenomenon represents an “incomplete displacement” of annular fluid and is indeed not a desirable performance of the displacement process.

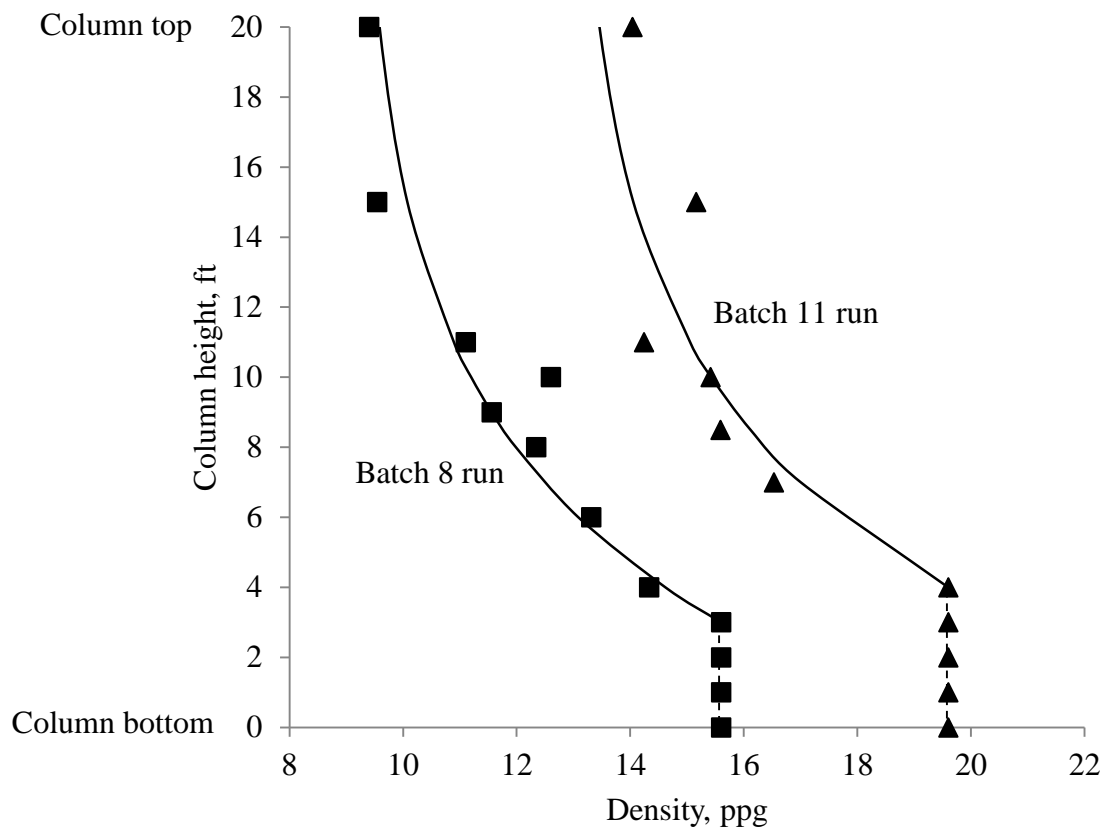


Figure 5.9: Depth of mixture zone above top of clean KF

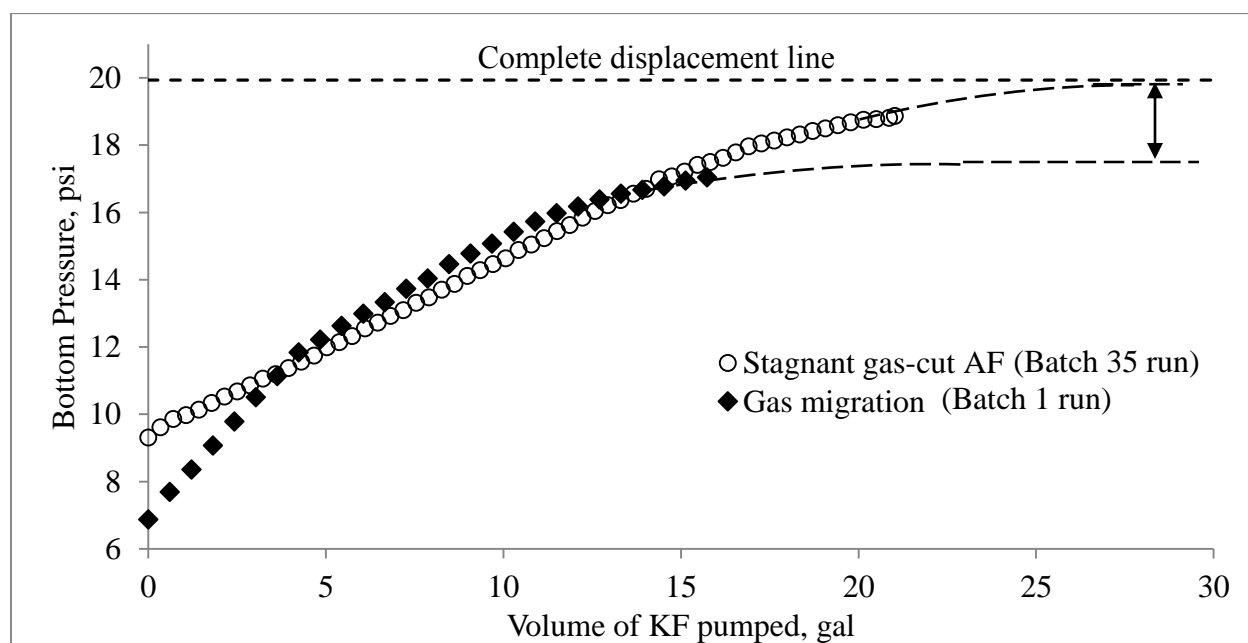


Figure 5.10: Comparison plots of pressure buildup with (Batch 1 run) and without concurrent gas migration (Batch 35 run)

Table 5.5: Immiscible displacement test results* and analysis

Batch	ρ_{kf} ppg	μ_{kf} cP	ρ_{af} ppg	μ_{af} cP	τ_0 lbf/100sqft	τ_g lbf/100sqft	q gpm	\bar{q} gpm	a ft	t_L min	t_u min	E_L	R_f	E_f	R_u
4	16.68	236	8.90	3.18	2.12	2	1.2	1.2	0.85	15.50	17.65	0.92	0.97	0.97	1.04
5	16.68	236	9.00	10.60	4.24	11	1.4	1.4	4.33	13.50	17.79	0.88	0.96	0.92	1.18
6	16.68	236	9.00	25.44	14.84	25	1.2	1.2	1.00	14.00	17.80	0.84	0.84	0.83	1.06
7	16.68	236	12.90	39.22	32.96	71	1.0	1.2	8.36	6.72	23.96	0.51	0.96	0.67	1.41
8	19.60	76	13.01	36.04	31.80	71	1.3	1.3	11.75	7.72	22.78	0.50	0.99	0.88	1.45
9	16.68	236	13.10	28.62	27.56	28	0.9	1.0	3.38	13.72	24.30	0.66	1.02	0.94	1.22
10	16.68	236	10.90	22.79	16.96	25	1.1	1.1	3.28	16.97	23.15	0.83	1.04	0.93	1.21
11	15.60	376	9.11	27.56	27.56	35	1.1	1.1	1	0.00	23.11	1.00	0.98	0.77	1.22
12	19.60	76	11.10	51.94	78.44	69	1.2	1.4	4.13	7.72	18.12	0.52	0.98	0.86	1.26
13	22.94	25	11.00	63.60	74.20	69	1.1	1.2	4.61	11.22	21.40	0.65	0.96	0.95	1.21
14	16.85	219	11.00	60.42	62.54	69	1.3	1.3	8.11	7.48	21.30	0.48	0.99	0.70	1.36
15	16.68	236	13.20	21.20	9.54	16	1.2	1.2	9.31	12.23	22.68	0.73	1.00	0.89	1.36
16	16.68	236	11.00	25.44	20.14	25	1.5	1.5	8.48	12.23	17.72	0.87	1.04	0.89	1.26
17	22.68	28	9.00	29.15	26.50	35	1.3	1.3	4.76	10.73	20.18	0.65	0.87	0.85	1.24
18	16.68	236	10.90	12.72	7.42	5	2.2	2.2	13.93	4.38	13.82	0.50	0.93	0.70	1.46
19	16.68	236	11.00	55.12	69.96	69	0.9	1.0	4.70	19.32	25.69	0.88	1.06	0.97	1.25
20	15.01	492	8.86	6.36	1.06	2	1.2	1.2	1.35	14.32	19.52	0.78	1.01	0.91	1.09
21	15.01	492	8.93	13.78	7.42	12	1.2	1.2	1	0.00	19.43	1.00	1.01	0.93	1.12
22	19.60	76	13.00	36.04	26.50	71	3.9	3.8	11.35	3.98	8.30	0.62	1.04	0.88	1.52
23	19.35	84	13.00	33.92	31.80	71	5.0	5.0	20.09	1.43	7.33	0.35	1.04	0.79	1.79
24	19.60	76	8.90	11.66	8.48	12	1.0	1.0	2.35	17.32	22.17	0.86	1.04	0.92	1.11
25	22.52	29	12.85	39.16	29.68	71	1.3	1.4	5.57	6.65	18.90	0.46	1.04	0.86	1.30
26	19.60	76	8.80	3.18	3.18	2	1.0	1.0	1.21	17.73	21.22	0.88	1.04	0.96	1.08
27	11.80	8	9.10	27.56	20.14	35	1.0	1.0	1.53	19.00	21.02	0.96	0.99	0.95	1.07
28	11.92	8	9.00	28.62	23.32	35	6.0	6.0	11.91	2.82	5.22	0.69	1.04	0.82	1.53
29	11.92	8	9.10	27.56	34.98	35	4.3	4.3	7.45	1.82	6.74	0.34	1.02	0.94	1.41
30	14.91	12	9.00	28.62	29.68	35	0.8	1.0	2.60	16.73	24.01	0.80	1.03	0.92	1.20
31	16.68	236	11.00	11.66	6.36	5	1.4	1.4	4.85	13.73	18.66	0.85	1.29	0.98	1.23
32	19.60	76	11.10	68.90	84.80	69	0.8	1.1	1.80	17.65	22.15	0.88	1.03	0.93	1.15
33	19.60	76	13.00	29.68	37.10	35	1.1	1.1	10.10	10.00	25.02	0.57	1.03	0.90	1.39
35	19.68	74	9.10	28.62	37.10	35	1.1	1.0	6.63	13.32	23.87	0.72		0.90	1.22

*No runs with gas migration (Batch 1, 2, and 3)

5.4 Analysis of Pilot Testing Results

5.4.1 Process Performance Measures

The main objective of the pilot testing was to test the performance of gravity displacement process by measuring the hydrostatic pressure change at the bottom of the fluid column. The ultimate goal of the process is to increase the bottom pressure by displacing the annular fluid; in a reasonable time. Thus, bottom pressure versus time data from the experiments are used for calculating the performance measures: pressure replacement efficiency (E_p) and volumetric efficiency (E_v) or displacement ratio defined as,

Pressure replacement efficiency:

$$E_p = \frac{\Delta P}{\Delta P_u} = \frac{P - P_{af}}{P_u - P_{af}} \quad (5.1)$$

Volumetric efficiency:

$$E_v = \frac{1}{R} = \frac{V_a}{V_p} \quad (5.2)$$

Displacement ratio:

$$R = \frac{V_p}{V_a} \quad (5.3)$$

where, ΔP is bottom pressure change, ΔP_u is ultimate bottom pressure difference, P is bottom pressure, P_{af} is bottom pressure when the column is filled with only AF, P_u is bottom pressure when the column is filled with only KF, V_a is the volume of annulus (20.5 gal) and V_p is the volume of KF pumped into the column.

The end of a fully successful ideal displacement process is when the pressure replacement and volumetric efficiencies are both equal one. Obviously, as already observed from the experiments, more than one annular volume of kill fluid is required to reach 100% pressure replacement efficiency. (Therefore, inverse of E_v , volume displacement ratio (R), is used for computations.) End of the displacement process is defined as the time when the pressure replacement efficiency is either one, or its value becomes constant and cannot be increased anymore.

5.4.2 Pressure Replacement Model

As most of displacement runs were unfinished due to KF volume shortage, pressure buildup plots must be extrapolated to determine the end of displacement process. Moreover, the extrapolation model must have physical sense. Figure 5.11 shows fluid zones in the annulus during displacement process. During the process, a mixture zone develops above the KF top and expands. At the time the mixture zone (MZ) reaches the overflow port ($t = t_L$, and $z_{af} = 0$), the overflow density (ρ_{of}) starts increasing from the annular fluid density up to the kill fluid density when the clean KF comes to the top ($z_{kf} = 0$). The moment when KF column reaches the overflow port indicates the ultimate time of displacement (t_u).

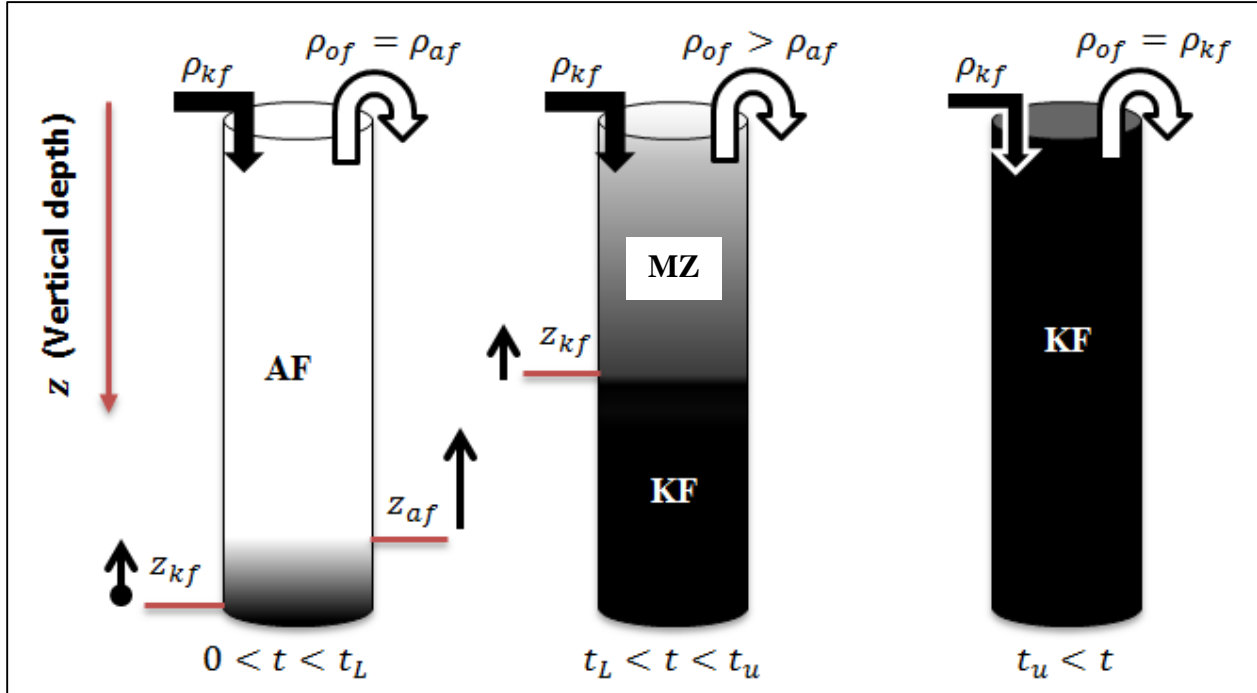


Figure 5.11: Fluid zones distribution in annulus: kill fluid (KF), mixture zone (MZ) and annular fluid (AF)

In most of the experiments displacement stopped when the mixture zone was already overflowing. In order to extrapolate the process duration mixture zone density must be related to density change in overflow. Exponential distribution of mixture zone density, shown in Figure 5.9, has been fitted with exponential function and the plots in Figure 5.12 demonstrate good match.

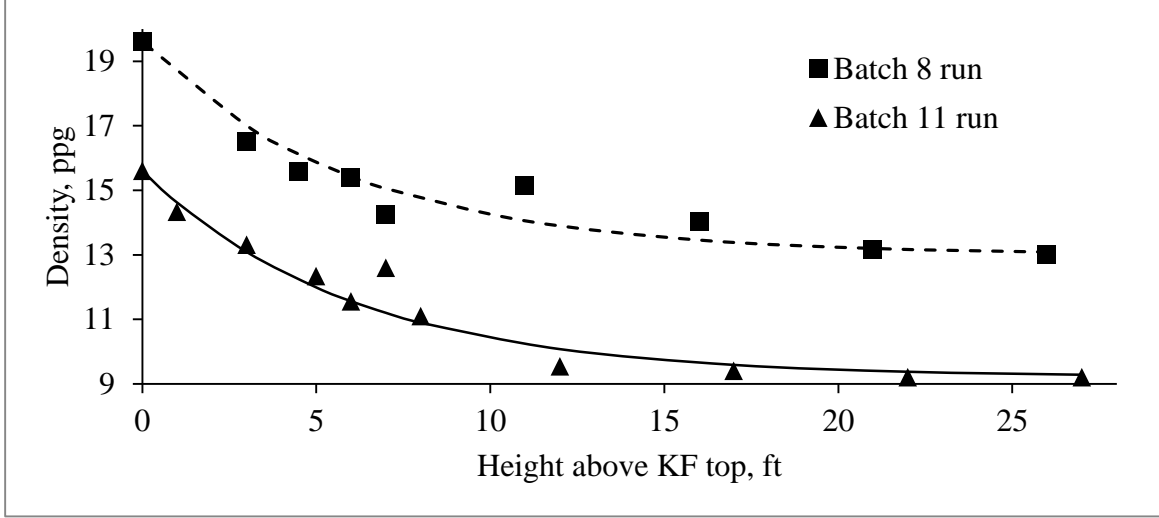


Figure 5.12: Exponential fit of mixture zone density with exponent (6) shows good match

Thus, density distribution in the annulus at any time,

$$\rho_a(z) = \rho_{af} \quad \text{for } 0 < z < z_{af} \quad (5.4)$$

$$\rho_a(z) = \rho_{af} + (\rho_{kf} - \rho_{af}) \exp\left(-\frac{z_{kf} - z}{a}\right) \quad \text{for } z_{af} < z < z_{kf} \quad (5.5)$$

$$\rho_a(z) = \rho_{kf} \quad \text{for } z_{kf} < z \quad (5.6)$$

where, z = depth below top of annulus

z_{af} = depth of AF section

z_{kf} = depth of clean KF section top

Since, function 5.5; asymptotically approaches annular fluid density,

$$\lim_{z \rightarrow \infty} \rho_{af} + (\rho_{kf} - \rho_{af}) \exp\left(-\frac{z_{kf} - z}{a}\right) \cong \rho_{af}$$

depth of AF section, z_{af} , is defined by setting small value, TOL, as $TOL = [\rho_a(z_{af}) - \rho_{af}] \ll 1$.

In general, length of the mixture zone, increases with time but the overflow density, ρ_{of} , remains constant ($\rho_{of} = \rho_{af}$) until the top of mixture zone comes to the overflow port so,

$$\text{for } 0 < t < t_L \quad \rho_{of} = \rho_{af} \quad (5.7)$$

where: t_L = end of linear trend

Later, no change in the mixture zone composition is assumed. With this assumption, travel distance of each point in the mixture zone becomes linear function of time,

$$z(t) = -\frac{q}{A}t$$

Where, q is injection rate and A is annular capacity.

As the mixture zone passes the overflow port, its length decreases at linear velocity, $dz/dt = -q/A$ and, concurrently the overflow density increases from ρ_{af} to ρ_{kf} . The ultimate time, t_u , is when the clean kill fluid top reaches the overflow port, and $z_{kf} = 0$.

Thus, the overflow density change vs. time (Equation 5.5) is,

$$\rho_{of}(t) = \rho_{af} + (\rho_{kf} - \rho_{af}) \exp\left(-\frac{q}{A} \frac{(t_u - t)}{a}\right) \quad \text{for } 0 < t < t_L \quad (5.8)$$

Overflow density change during the Batch 12 displacement run is shown in Figure 5.13. Before and after mixture zone is displaced, annular fluid and kill fluid start flowing out. This brings two discontinuity points: the time when clean annular fluid finishes and mixture zone starts overflowing (t_L), and the time when mixture zone finishes and clean kill fluid starts overflowing (t_u). Figure 5.13 shows these points and fit functions on measured overflowing density data.

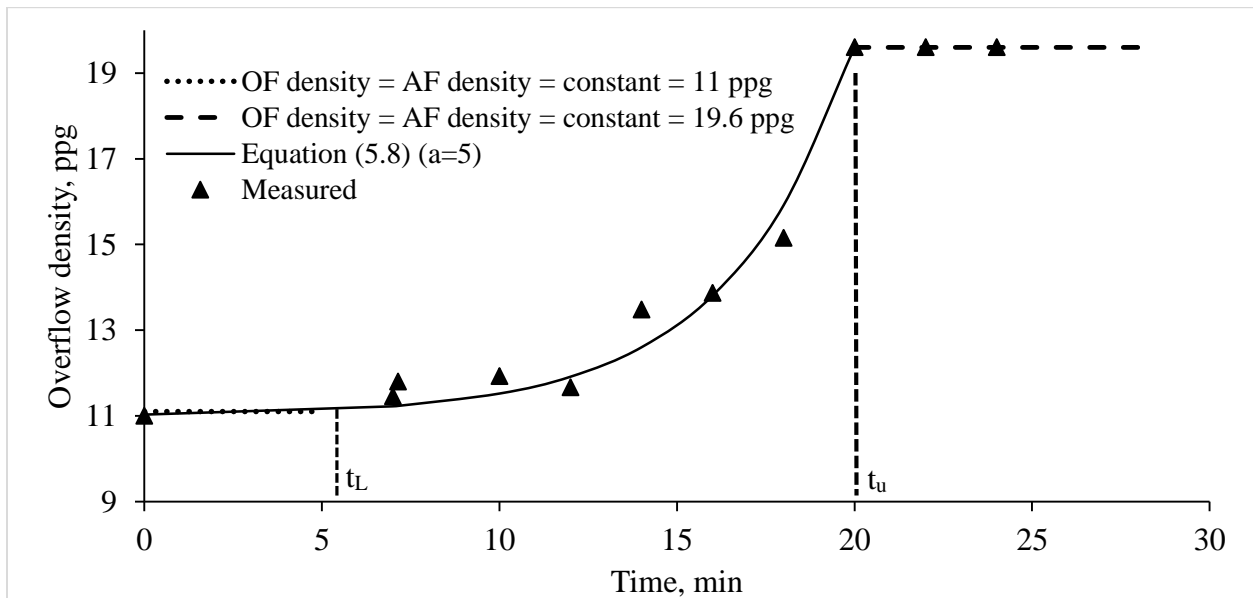


Figure 5.13: Overflowing density change during Batch12 experimental data

As shown in Appendix B, overflow density change is mathematically related to the change of fluid mass in the annular column using two assumptions: (1) Constant-rate injection of KF; and (2) Constant composition of mixture zone during the zone discharge.

During displacement of clean annular fluid, the annulus mass is,

$$m_a(t) = m_{af} + q (\rho_{kf} - \rho_{af}) t \quad (5.9)$$

During charge of mixture zone, the annular mass is,

$$m_a(t) = m_{af} + q (\rho_{kf} - \rho_{af}) t - aA(\rho_{kf} - \rho_{af}) \exp\left(-\frac{q}{Aa}t_u\right) \left[\exp\left(\frac{q}{Aa}t\right) - 1 \right] \quad (5.10)$$

At the end of mixture zone discharge, the annular mass is constant and equal to the mass of kill fluid, m_{kf} . Where, m_{af} and m_{kf} represent annular fluid mass full of annular and kill fluids, respectively.

After converting fluid mass to hydrostatic bottom pressure, mathematical model of the pressure replacement process is developed as follows.

For displacement of annular fluid stage,

$$P_{ba}(t) = P_{af} + 0.052 \frac{q}{A} \Delta\rho t \quad \text{for} \quad \begin{matrix} 0 \leq t \leq t_L \\ 0 \leq P \leq P_L \end{matrix} \quad (5.11)$$

For change of mixture zone stage,

$$P_{ba}(t) = P_L + \frac{0.052 q \Delta\rho}{A} (t - t_L) - 0.052 a \Delta\rho \exp\left(-\frac{q}{Aa}(t_u - t_L)\right) \left[\exp\left(\frac{q}{Aa}(t - t_L)\right) - 1 \right] \quad (5.12)$$

for $t_L \leq t < t_u$ and $P_L \leq P < P_e$.

After the mixture zone discharge, ultimate pressure, P_u , is reached: $P_u = 0.052 \rho_{kf} V_a/A$

Note, that Equation 5.12 for $t=t_u$ relates (typically unknown) mixture zone parameter “a” to the measured values of t_L and t_u , as,

$$P_u = P_L + 0.052\Delta\rho \left[\frac{q}{A}(t_u - t_L) - a + a \exp\left(-\frac{q}{Aa}(t_u - t_L)\right) \right] \quad (5.13)$$

In dimensionless formulation, using the process performance measures, E_p and R – defined above, the pressure replacement model (Appendix B) becomes as follows.

For displacement of annular fluid (linear pressure increase), $0 \leq R \leq R_L$ and $0 \leq E_p \leq E_{pL}$;

$$E_p(R) = R = \frac{V_p}{V_a} = \frac{qt}{h_a A}$$

For mixture zone discharge stage, $R_L \leq R \leq R_u$ or $E_{pL} \leq E_p \leq 1$;

$$E_p(R) = R - \frac{a}{h_a} \exp\left(-\frac{h_a}{a}(R_u - R_L)\right) \left[\exp\left(\frac{h_a}{a}(R - R_L)\right) - 1 \right] \quad (5.14)$$

After the mixture zone discharge ($R \geq R_u$),

$$E_p(R) = 1$$

Note that for ultimate displacement ratio, Equation 5.14 equals unity and relates the (typically) unknown mixture zone parameter “a” to the measured values of R_L and R_u from the tests, as,

$$E(R_u) = 1 = R_u - \frac{a}{h_a} \exp\left(-\frac{h_a}{a}(R_u - R_L)\right) \left[\exp\left(\frac{h_a}{a}(R_u - R_L)\right) - 1 \right]$$

Solving for R_L gives,

$$R_L = \frac{a}{h_a} \ln\left(1 - \frac{h_a}{a}(R_u - 1)\right) + R_u \quad (5.15)$$

5.4.3 Algorithm of Analysis of Unfinished Runs

As discussed, above, most of the runs were unfinished due to KF shortage. In order to extrapolate the incomplete pressure build-up data obtained from these runs Equation 5.13 was used. The two unknown parameters, a and t_u , were determined by assuming complete ultimate displacement. The computation procedure was as follows:

1. Verify the slope of initial straight line by using Equation 5.11, q and Δp data.
2. Estimate time of departure from the straight line.
3. Plot Equation 5.12 on the data points, starting from assigned t_L and P_L values.
4. With the known ultimate pressure, solve Equation 5.13 to find an expression between t_u and a .
5. By changing t_u in the expression found in step 4, try different a values and find the best curve that matches the measured data points according to the method of least squares.
6. If it is not a good match, repeat the algorithm starting from step 2 with a different estimation of t_L .

An example extrapolation is depicted in Figure 5.14 and also demonstrated in Figure 5.15 and Figure 5.16. For different values of t_u and a , various extrapolations can be obtained, but only one of them gives the best fit with the highest R^2 value.

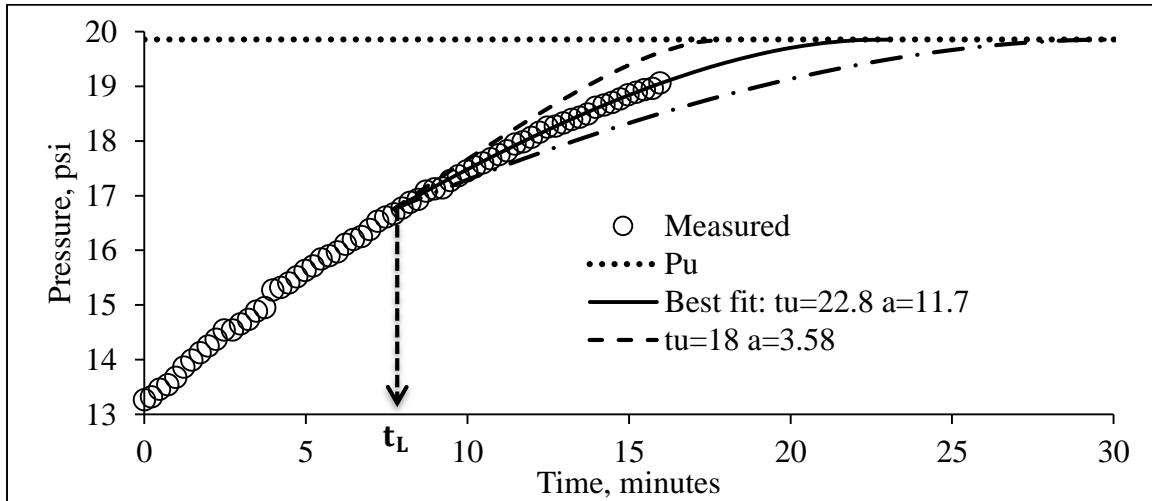


Figure 5.14: Example plot for extrapolating measurements to estimate ultimate time

Using the above algorithm all incomplete pressure build-up vs. time plots were extrapolated to determine t_u and a . The values are shown in Table 5.5.

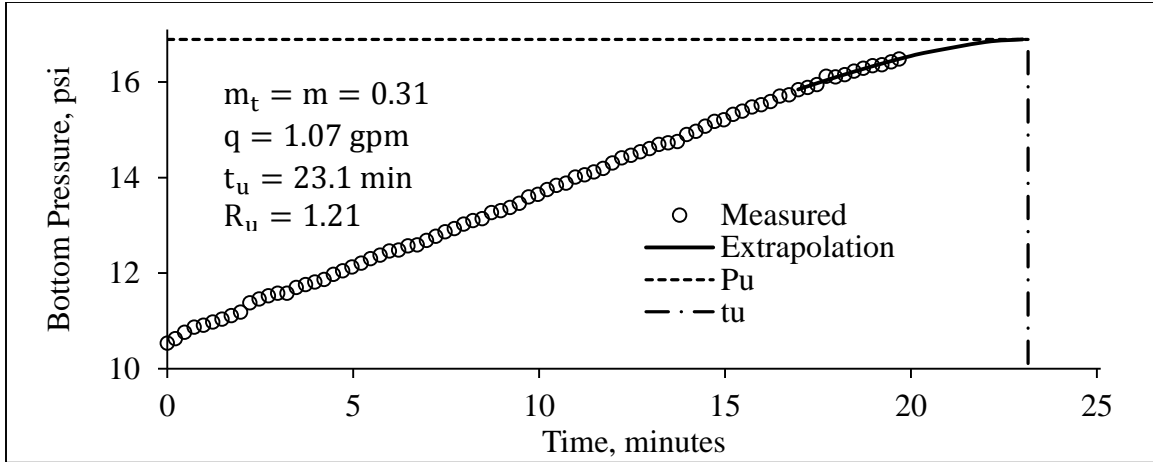


Figure 5.15: Extrapolation of pressure buildup for Batch 10 run

5.5 Empirical Correlations

5.5.1 Trend Analysis

Figure 5.17 shows the change in performance parameters with increasing density of annular fluid, and consequently due to structural strength h , occurred as a result of higher barite concentrations. For all three runs flow rate was around the same value and the volumes of injected kill fluid were similar. According to the plot, as the density of annular fluid increases, departure from linear pressure build-up occurs earlier. Therefore, mixture zone overflow starts much sooner for heavier annular fluids, as also can be understood from the increase in exponential coefficient. Accordingly, maximum obtainable efficiency for one annular volume injection reduces significantly as the density goes up.

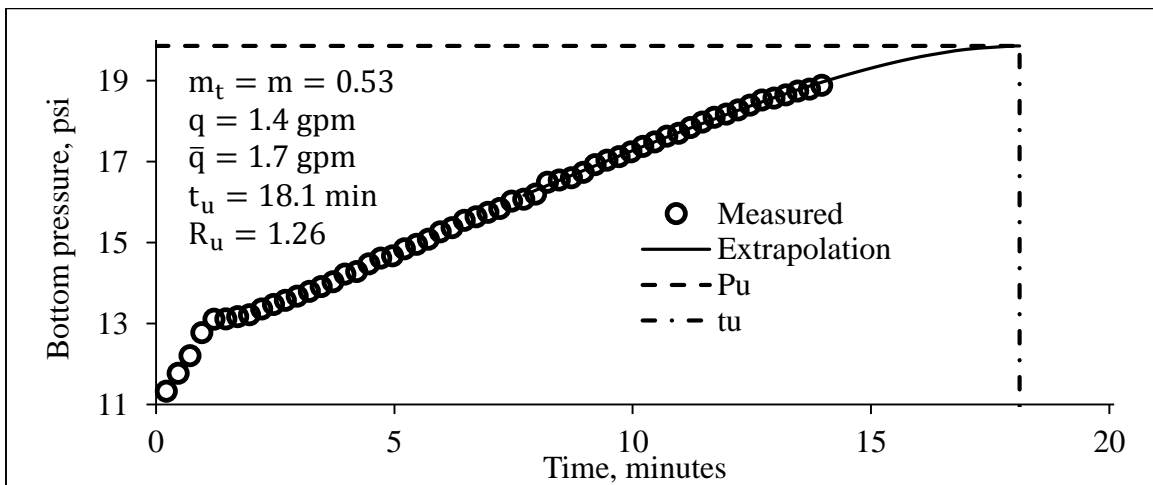


Figure 5.16: Extrapolation of pressure buildup for Batch 12 run

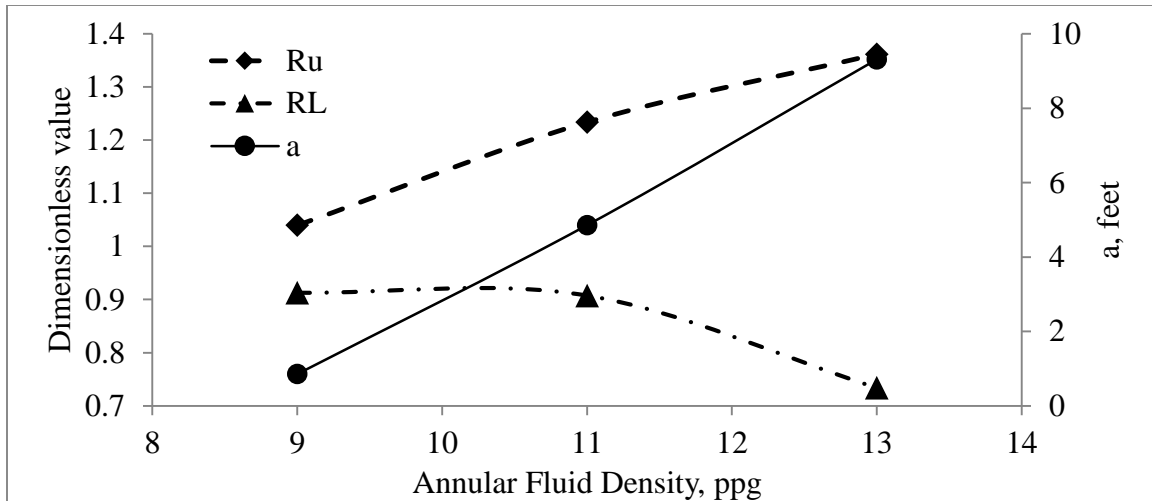


Figure 5.17: Change in dimensionless values and exponential coefficient with increasing annular fluid density. Batches 4, 31 and 15 runs show the effectiveness of the process when lighter and low structural strength AF is present

Shown in Figure 5.18 are the trends of performance change with increasing injection rate. The most obvious result of faster injection is the ultimate displacement ratio, which increases to ~1.5 with increasing flow rate. In other words, about 1.5 times more kill fluid provides a complete displacement when injecting with 6 gpm than injecting with 1 gpm. The process inefficiency increase results from the change of mixture zone coefficient “a” that determines the mixture zone size. It should also be noted that pressure replacement efficiency, E_p , was equal unity in all experiments for the range of injection rates applied.

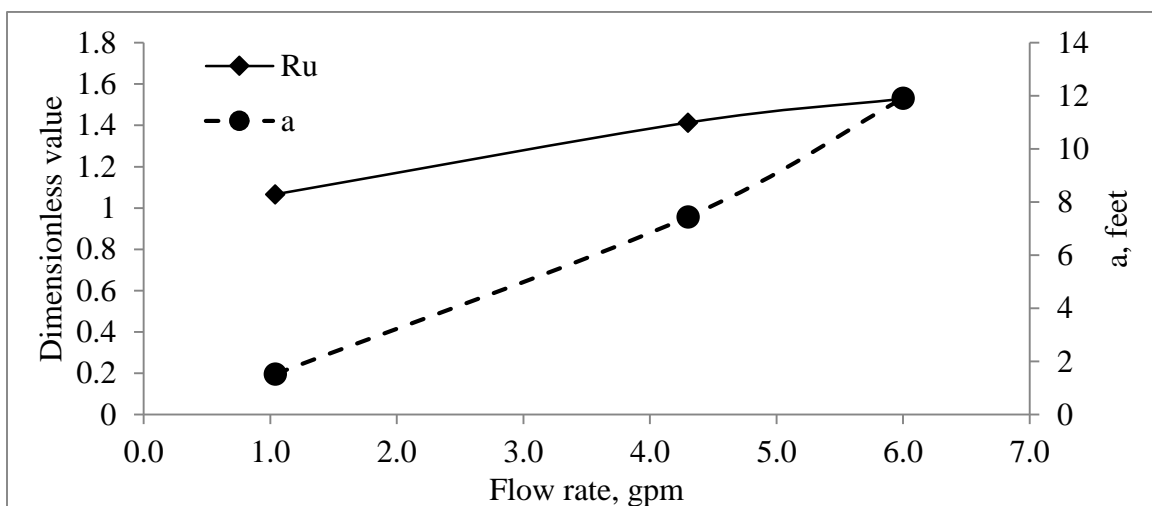


Figure 5.18: Change in dimensionless values and exponential coefficient with increasing flow rate. KF1204 injections into AF0903 with different rates (Batches 27, 28 and 29) show increasing mixture zone height and more losses to overflow with increasing rate

5.5.2 Volume Displacement Ratio Correlation

Qualitative results indicate that R_u is strongly dependent on flow rate. Beside this operational parameter, system parameters - properties of kill and annular fluids - also affect the process performance. The variables that might have influence on R_u are listed in Table 5.6. The variables are correlated with R_u .

Table 5.6: Variables that might control displacement process

Symbol	Description	Unit
ρ_{kf}	Kill fluid density	ppg
ρ_{af}	Annular fluid density	ppg
μ_{kf}	Kill fluid apparent viscosity	cP
μ_{af}	Annular fluid plastic viscosity	cP
τ_0	Annular fluid yield point	lbf/100sqft
τ_g	Annular fluid 2 hour gel strength	lbf/100sqft
q	Flow rate	gpm

Figure 5.19 is the scatterplot of variables and shows their inter-dependence. The most obvious relationship can be seen between kill fluid density and viscosity. This dependence results from the blending method of brominated organics. As the density of the fluid increases its viscosity generally reduces. In addition, annular fluid viscosity, yield point and gel strength showed clear interdependence – an expected relationship between rheology and tixotrophy of water based-based drilling muds. Because of interdependence, only one variable from each interdependent group is considered in correlations.

Two experiments, Batch 6 and Batch 27 runs, had been run with insufficient amount of kill fluid and their extrapolations were not reliable. Thus, the two runs are eliminated from the correlations.

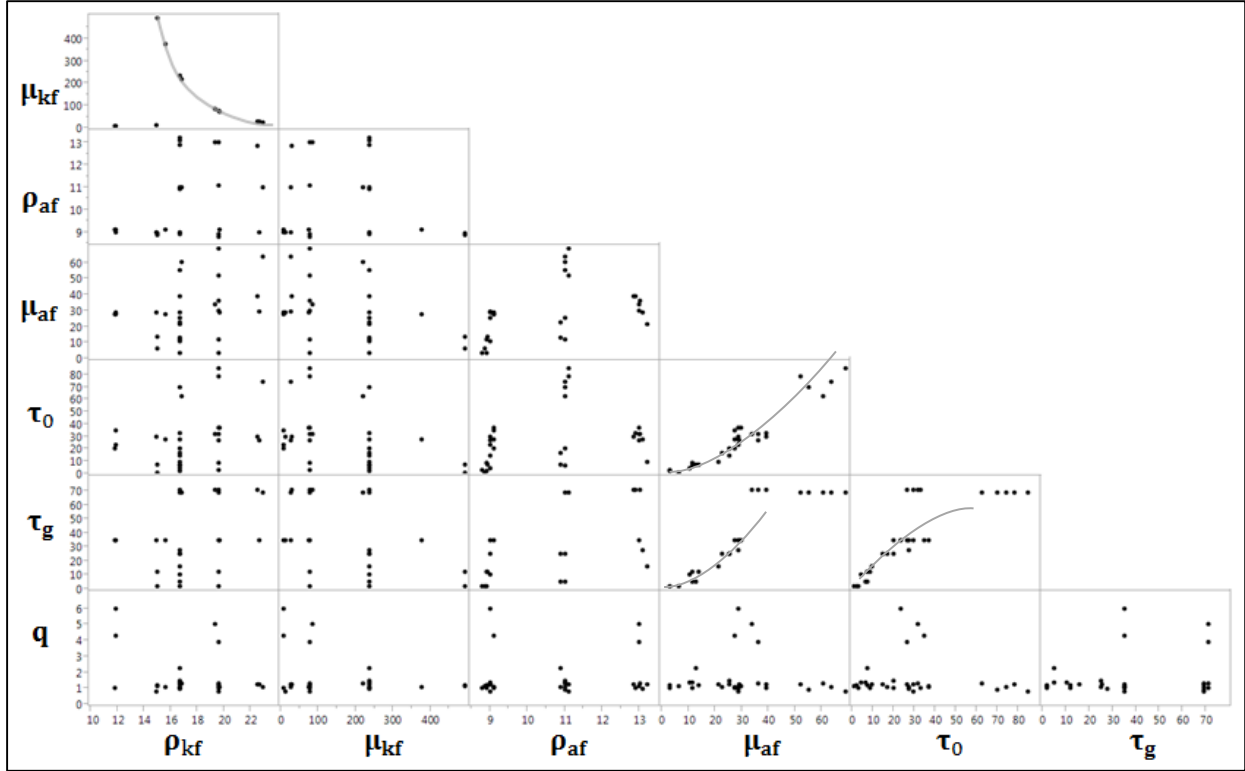


Figure 5.19: Scatter plot of experimental variables

By using all the variables that may affect the displacement process (variables in Table 5.6) a prediction expression with a coefficient of determination (R^2) of 0.896 is first obtained. Parameter estimates is shown under initial prediction column in Table 5.7 and leverage plots are drawn in Figure 5.20. In the initial prediction despite the high R^2 value, t-Ratio values – which represent the ratio of estimate over estimate standard error – of several parameters are found as quite low. A significant variable generally should have an absolute t-ratio value greater than 2. Leverage plots in Figure 5.20 also show the insignificance of several parameters. Leverage plots are used for seeing which points might be exerting influence on the hypothesis test for the variable. In other words, a leverage plot for an effect shows the impact of adding this effect to the model, given the other effects already in the predictive model. In the plots, distance between the points to fit line (red) gives the error when the variable is in the predicted model; and the distance between the point and horizontal line (blue) gives the error when the variable is removed from the model. The cloud-like plots confirm the annular fluid properties interdependence, which causes a collinearity problem so that only one variable should be considered in the correlation.

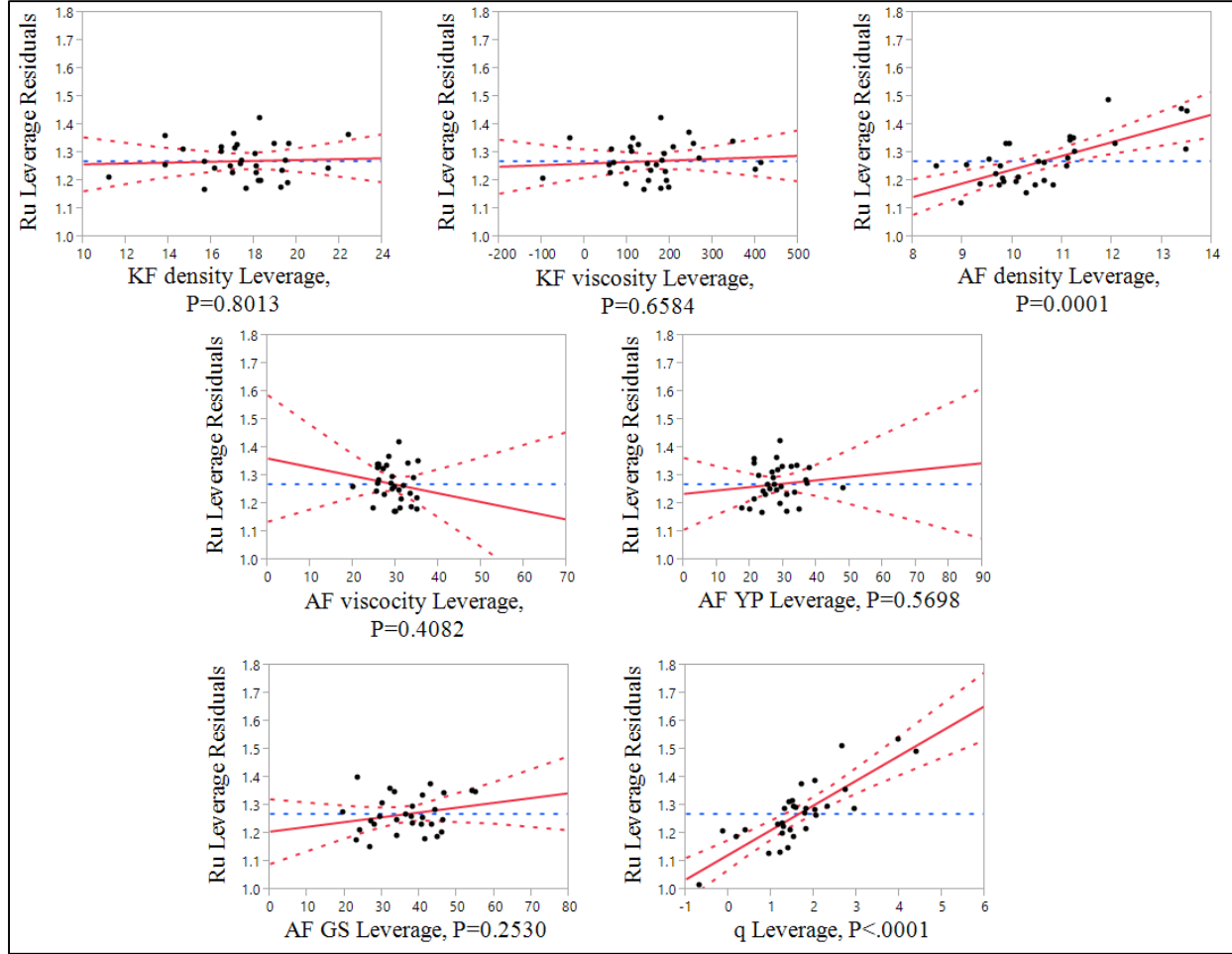


Figure 5.20: Leverage plots of R_u residuals vs. all the variables

Table 5.7: Summary and parameter estimates of the fits

	Initial Prediction			Final Prediction		
R^2	0.896			0.878		
R^2 adj	0.86			0.857		
Root Mean Square Error	0.020			0.021		
Mean of Response	0.104			0.104		
Data Count	29			29		
Term	Estimate	Std. Error	t Ratio	Estimate	Std. Error	t Ratio
Intercept	-0.3781	0.0826	-4.58	-0.3759	0.0794	-4.74
$\log_{10} \rho_{af}$	0.3062	0.0790	3.87	0.3771	0.0685	5.51
$\log_{10} \mu_{kf}$	0.0181	0.01	1.81	-	-	-
$\log_{10} \tau_0$	0.0164	0.0278	0.59	0.0187	0.00904	2.07
$\log_{10} q$	0.1882	0.0208	9.04	0.1719	0.01832	9.38
$\log_{10} \rho_{kf}$	0.0485	0.0614	0.79	0.0351	0.0597	0.59
$\log_{10} \tau_g$	0.0074	0.0292	0.25	-	-	-
$\log_{10} \mu_{af}$	0.0091	0.0465	0.19	-	-	-

By eliminating the insignificant parameters one by one, the best expression for R_u is obtained by using only annular fluid density, and yield point, kill fluid viscosity (or density) and injection rate. Statistical analysis is shown in Table 5.7 - final prediction column. Figure 5.21 shows the prediction plot and Equation 5.16 is the predicted expression and gives an R^2 value of 0.878. Excluded points are also shown in the prediction plot with the cross shapes. In the figure, the red solid line is the 45° line and represents the goodness of the fit. The red dashed lines give the 95% confidence interval and blue dashed line is the mean value of actual displacement ratios.

Predicted Expression for displacement ratio:

$$R_u = 10^{-0.376} \rho_{af}^{0.377} \rho_{kf}^{0.035} \tau_0^{0.019} q^{0.1719} \quad (5.16)$$

Figure 5.22 shows the prediction profiler of variables. In this figure, X-axis shows the variables, and the red numbers indicates their current values. Y-axis gives the corresponding R_u value and red numbers show the corresponding R_u for the current values of the variables. Black lines give the changing R_u when that particular variable is being changed while the others remain constant. Based on the figure and Equation 5.16, the most significant variable is flow rate, and second dominant variable is annular fluid density. Kill fluid density and annular fluid yield point have some effect on R_u but not significant.

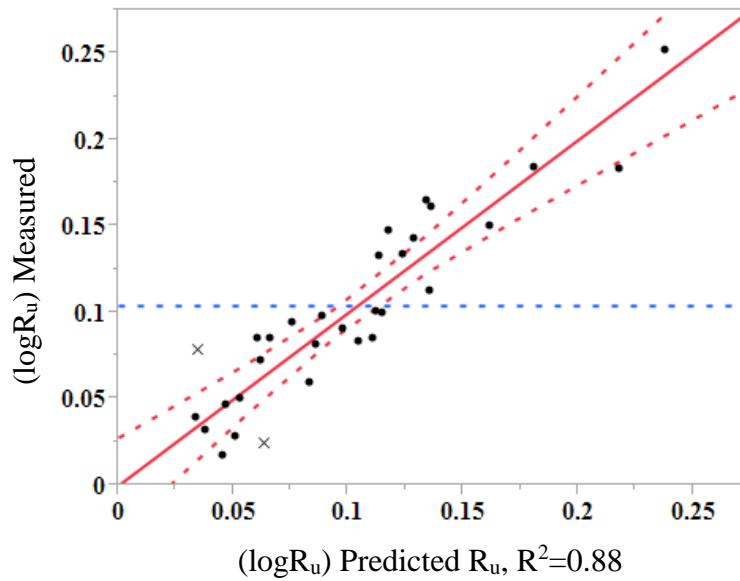


Figure 5.21: $\log R_u$ actual versus $\log R_u$ predicted with correlation in Equation 5.16 (Properties are shown in Table 5.7)

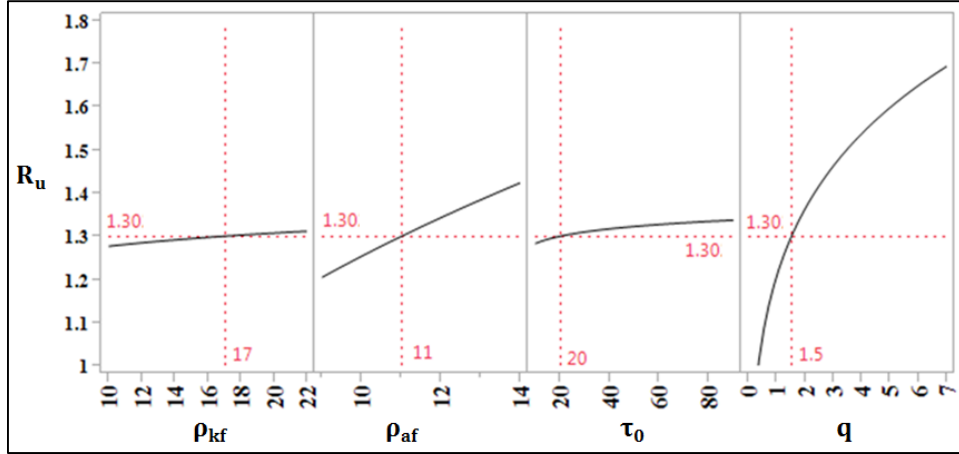


Figure 5.22: Profiler plot of variables

The obtained equation makes physical sense except the increasing R_u with increasing kill fluid density. This unexpected outcome is caused from the fact that higher density fluids were tested with annular fluids that had higher structural strengths. Consequently, expression indicated that increasing kill fluid density results in higher displacement ratio. The yield point profiler also supports this relation. As yield goes up, kill fluid to be pumped also increases. Besides, as expected increasing annular fluid density requires more kill fluid to be pumped. Similarly, if the process is desired to be completed as quickly as possible more kill fluid will be needed.

5.5.3 Mixture zone Size Correlation

As explained earlier, bottom pressure increase starts linear, and as the mixture zone forms and starts being displaced by the kill fluid; deviates from linearity. Predicting mixture zone characteristics would be useful for up-scaling the process to an actual-well annulus. Not all the results from the pilot experiments could be used for this prediction; because, the mixture zone was not formed during all the runs. In addition, due to the operational errors constant flow rate could not be established for several experiments. Thereby, t_L values misrepresent the mixture zone overflowing durations. Nevertheless, density distribution in any mixture zone can be predicted with known mixture zone density distribution exponential coefficient. Size of the mixture zone is solely controlled by the coefficient (a) that is correlated with linear regression. The correlation in Equation 5.17 has a R^2 value of 0.79 (Table 5.8). The correlation has been developed by following the same variable elimination method resulting in three significant: AF density, AF viscosity and flow rate (Table 5.9). Correlation is shown in Figure 5.23, measured

data is scattered through around the prediction line; therefore, using experimental data – when available – instead of the correlation is recommended.

$$a = 10^{-1.61} \rho_{af}^{1.55} \mu_{af}^{0.45} q^{0.66} \quad (5.17)$$

Table 5.8: Summary of fit for predicting exponential coefficient

R^2	0.79
R^2 adjusted	0.76
Root Mean Square Error	0.16
Mean of Response	0.704
Data Count	25

Table 5.9: Parameter estimates calculated for predicting exponential coefficient

Term	Estimate	Std. Error	t Ratio
Intercept	-1.606	0.5123	-3.13
$\log_{10} \rho_{af}$	1.5525	0.5600	2.77
$\log_{10} q$	0.6619	0.1394	4.75
$\log_{10} \mu_{af}$	0.4461	0.1122	3.98

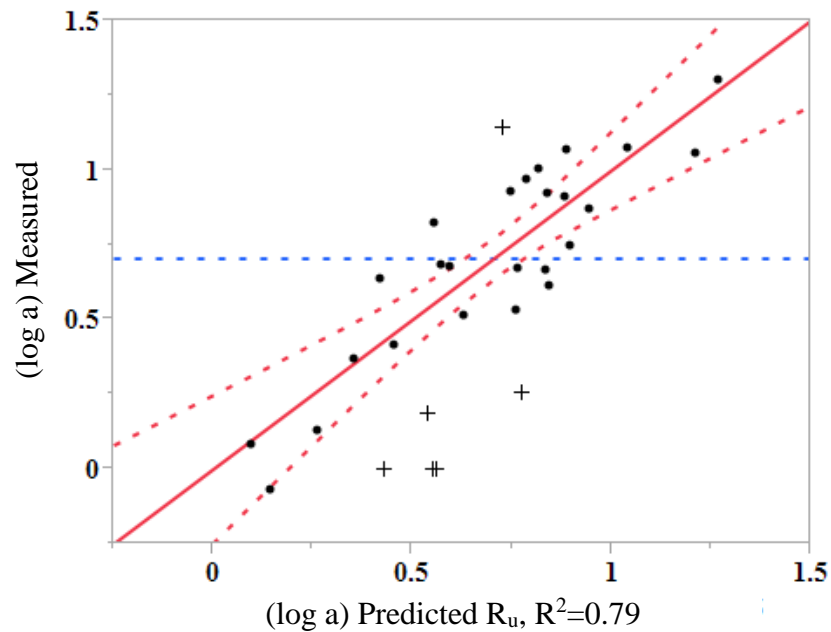


Figure 5.23: Prediction plot of mixture zone exponential coefficient

The plot in Figure 5.24 shows the change in exponential coefficient with increasing flow rate and annular fluid viscosity. As can be seen, faster injection rates and higher viscosities result in greater coefficients, which indicate a larger mixture zone.

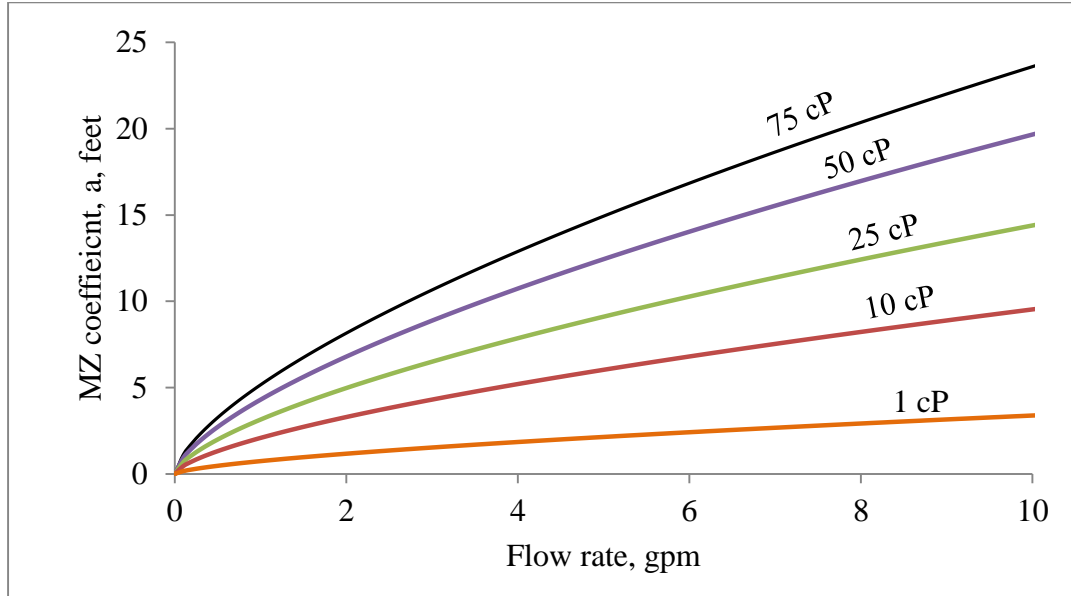


Figure 5.24: Mixture zone coefficient vs. flow rate for different AF viscosities for AF density 12 ppg

5.5.4 Use of Correlations for Design

Using the empirical model, described above, for predicting performance of the displacement process in 20-foot pilot to the field-length annulus. The upscaling is limited by the following assumptions:

1. Well-head pressure stays constant during the displacement process so there is no new gas entry to the fluid column.
2. Injection rate is constant.
3. Injection rate does not exceed its maximum value.
4. Scaling factor for the process performance is the ratio of fluid column length in the pilot model and the well annulus.

The third assumption implies a designed rate of kill fluid that would not cause initial dispersion (q_{cr-i}) as described in chapter 4.4 and would not exceed the rate of buoyant settling (q_{cr-T}) defined in the following chapter.

The fourth assumption entails hydraulic similarity of steady-state counter-current buoyant slippage in the pilot model and a full-scale annulus. The assumption awaits further experimental verification.

Under the light of the learnings from the experiments, process design models can be employed for any up-scaling attempt.

For a designed injection rate necessary volume of kill fluid to be used in displacement operation can be found from Equation 5.45 (remembering: $R_u = V_{\text{pumped}}/V_{\text{annulus}}$).

$$R_u = 10^{-0.376} \rho_{af}^{0.377} \rho_{kf}^{0.035} \tau_0^{0.019} q^{0.1719} \quad (5.16)$$

A similar modification gives the time needed for complete displacement.

Considering the R_u definition,

$$R_u = \frac{1}{E_v} = \frac{V_p}{V_a} = \frac{qt_u}{V_a}$$

time needed for complete displacement is,

$$t_u [\text{hours}] = 7.01 * 10^{-3} \rho_{af}^{0.377} \rho_{kf}^{0.035} \tau_0^{0.019} q^{-0.8281} V_a \quad (5.18)$$

Pressure replacement efficiency can be estimated by using the fourth assumption to define scaling factor, k , as,

$$k = \frac{h_{\text{annulus}}}{h_{\text{pilot}}}$$

Thus, dimensionless pressure replacement versus displacement ratio equations (Equation 5.14) can be rewritten as,

$$\text{For,} \quad 0 \leq R \leq R_L \quad E_p(R) = R$$

$$\text{and for,} \quad R_L \leq R \leq R_u \quad (\text{or } E_{pL} \leq E_p \leq 1)$$

$$E_p(R) = R - \frac{ka}{h_a} \exp\left(-\frac{h_a}{ka}(R_u - R_L)\right) \left[\exp\left(\frac{h_a}{ka}(R - R_L)\right) - 1 \right] \quad (5.19)$$

Since for $R \geq R_u$ $E_p(R) \equiv 1$

it is possible to back calculate R_L as,

$$R_L = R_u + \frac{ka}{h_a} \ln\left(1 - \frac{h_a}{ka}(R_u - 1)\right) \quad (5.20)$$

After estimating the values of “ R_u ” and “ a ” from the correlations, the above equations can be used for predicting a dimensionless plot for any length of well annulus. An example upscaling design is presented by using the values in Table 5.10. Dimensionless trends are plotted by using the critical injection rates and shown in Figure 5.25.

Table 5.10: Parameters used for upscaling example

Outer casing size, in	9-5/8” (9.001” ID)	AF density, ppg	9
Inner casing size, in	7” (7” OD)	AF viscosity, cP	10
Annular capacity, gal/ft	1.31	Yield point, lbf/100sqft	2
Annulus height, ft	4000	KF density, ppg	17
Annular volume, gal	5225	KF viscosity, cP	20
k	205.3	Interfacial tension, dynes/cm	22
q_{cr-i} , gpm	1.1	q_{cr-A} , gpm	2.5
q_{cr-T} , gpm	10.7		

To learn the bottom pressure at any particular moment; time can be converted into displacement ratio. Then, pressure replacement efficiency can be either read from the plot or calculated from the equations and converted to bottom pressure value. The example plot is shown in Figure 5.26. The example demonstrates the effect of injection rate that may not always be designed at maximum. At high rates, more KF is needed but the operation time is shorter. Thus, the KF cost should be balanced with the well-site hourly cost.

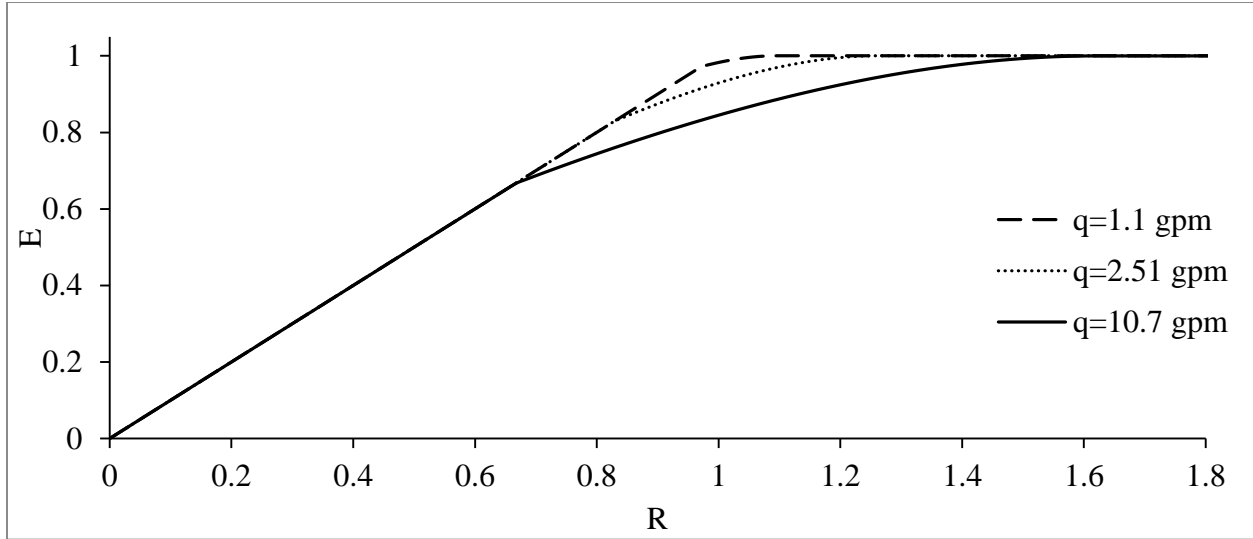


Figure 5.25: Example upscaled dimensionless displacement process at various flow rates. Increasing rate results in early deviation from 45 degree line.

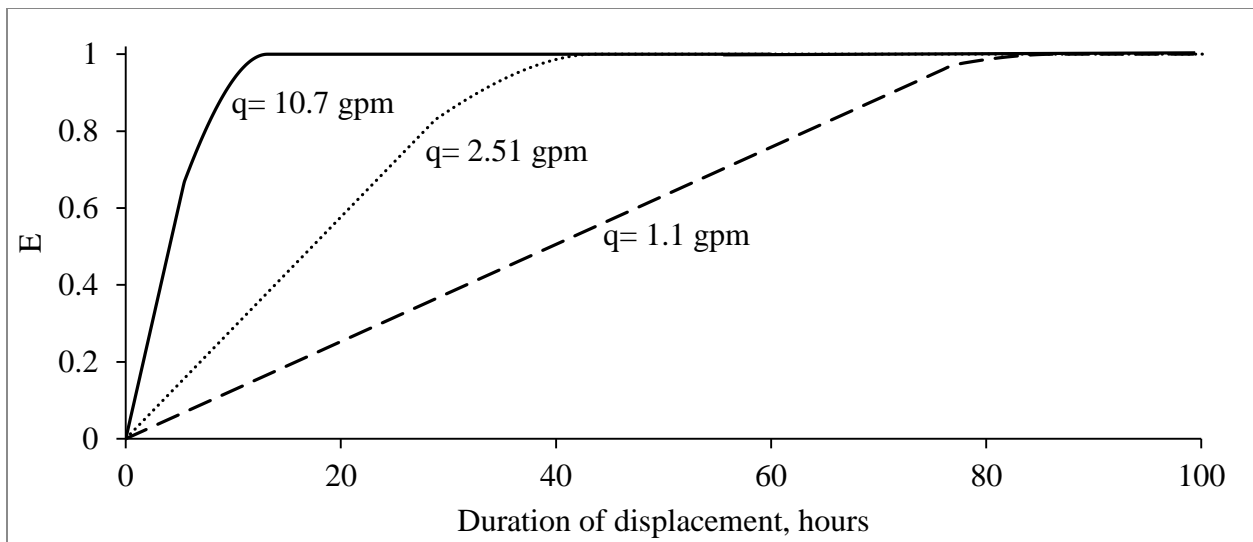


Figure 5.26: Duration of displacement of three different critical rates for upscaling example

5.6 Maximum Injection Rate for Buoyant Settling

Results of the slot and pilot model experiments have shown that excessive KF injection rate reduces efficiency of displacement by: (1) causing KF dispersion at the injection port, and (2) increasing the counter-current flow rate and the KF reversal effect. The latter effect requires finding a maximum value of KF injection rate for efficient buoyant transport of this fluid downwards.

The efficient buoyant transport occurs when the system is fed with kill fluid (KF) not faster than the previously-injected KF travels downwards. Assuming that KF does not form a rope but breaks-up into droplets, transport rate of the KF can be predicted using the droplet slip velocity theory. Transport velocity (ϑ_T) of a concentrated fluid column is slower than the velocity of a single droplet (ϑ_d) thus can be represented as multiplication of droplet velocity by a correction factor, $\epsilon \leq 1$, as,

$$\vartheta_T = \epsilon \vartheta_d \quad (5.21)$$

Dedegil ^[26] developed an equation that represents the velocity of a solid particle in non-Newtonian media.

$$\vartheta_p = \sqrt{\frac{2}{C_D \rho_f} \left(\frac{2}{3} (\rho - \rho_f) d g - \pi \tau_0 \right)}$$

that to be used for droplet velocity, in field units is,

$$\vartheta_d = \sqrt{\frac{0.27}{C_D \rho_{af}} (13.23 \Delta \rho d - \tau_0)} \quad (5.22)$$

Where, ϑ_d is velocity of a single droplet in ft/sec, C_D is drag coefficient acting on slipping droplet, ρ_{af} is annular fluid density in ppg, $\Delta \rho$ is density differential between droplet and stagnant fluid in ppg, τ_0 is yield stress of stagnant fluid in lbf/100sqft and d is equivalent droplet diameter in inches.

Bozzano and Dente ^[31] developed drag coefficient equations for liquid droplets at terminal velocities dependent upon values of the asymptotic friction function (f_∞) as follows:

$$f_\infty = 0.9 \frac{Eo^{\frac{1}{2}}}{1.4 \left(1 + 30 Mo^{\frac{1}{6}} \right) + Eo^{\frac{3}{2}}} \quad (5.23)$$

For $f_\infty < 0.45$,

$$C_D = \frac{48}{Re} \frac{\sqrt{1 + 0.25 Re}}{1 + \sqrt{1 + 0.25 Re}} \frac{3/2 + \mu_{af}/\mu_{kf}}{1 + \mu_{af}/\mu_{kf}} \frac{1 + 12 Mo^{\frac{1}{3}}}{1 + 36 Mo^{\frac{1}{3}}} + 0.45 \quad (5.24)$$

For $f_\infty \geq 0.45$,

$$C_D = \frac{48}{Re} \frac{\sqrt{1 + 0.25 Re}}{1 + \sqrt{1 + 0.25 Re}} \frac{3/2 + \mu_{af}/\mu_{kf}}{1 + \mu_{af}/\mu_{kf}} \frac{1 + 12 Mo^{\frac{1}{3}}}{1 + 36 Mo^{\frac{1}{3}}} + 0.9 \frac{Eo^{\frac{1}{2}}}{1.4 \left(1 + 30 Mo^{\frac{1}{6}}\right) + Eo^{\frac{3}{2}}} \quad (5.25)$$

Where, dimensionless Morton (Mo) Number and Eötvös Number (Eo) are,

$$Mo = \frac{\Delta \rho g \mu_{af}^4}{\rho_{af}^2 \sigma^3}$$

$$Eo = \frac{\Delta \rho g d^2}{\sigma}$$

or in field units,

$$Mo = 8.2 \cdot 10^{-5} \frac{\Delta \rho \mu_{af}^4}{\rho_{af}^2 \sigma^3}$$

$$Eo = 23.6 \frac{\Delta \rho d^2}{\sigma}$$

and particle Reynolds number to calculate drag coefficient is,

$$Re = 928 \frac{\rho_{af} \vartheta_p d}{\mu_{af}}$$

There are several studies addressing the effect of geometrical restriction on terminal velocity of particles (Richardson and Zaki ^[72], Di Felice ^[73], Kaneda ^[74], Koch and Sangani ^[75], Koch and Hill ^[76], all qtd. in Multiphase Flow Handbook ^[13]). Wen and Wu ^[77] presented a correction for the effect of particle concentration in a contained system as,

$$C_D = C_{D0} (1 - C)^{-3.7} \quad (5.26)$$

where, C_{D0} is drag coefficient of a single particle and C is particles' concentration in the system.

Wen and Wu ^[77] included the effects of relative Reynolds number in the expression for the terminal velocity of a single particle. Thus, their correlation for the effect of concentration became independent of the Reynolds number and, therefore, is represented with the constant

value, -3.7. The correlation is widely used in fluidization systems ^[13] and also practical for computer coding, so, it is selected for this study.

All the above equations include size (diameter) of fluid droplets. For eliminating the droplet diameter (d), maximum stable diameter of a droplet traveling in a stagnant media developed by Clift and Weber ^[30] can be used. Maximum stable droplet diameter in field units is,

$$d_{\max} \approx 0.14 (\sigma/\Delta\rho)^{1/2} \quad (5.27)$$

Substituting d_{\max} and particle velocity to Reynolds number gives,

$$\text{Re} = 130 \frac{\rho_{\text{af}} \vartheta_p}{\mu_{\text{af}}} \sqrt{\frac{\sigma}{\Delta\rho}} \quad (5.28)$$

Eötvös number for maximum droplet size becomes constant as,

$$\text{Eo} = 23.6 \frac{\Delta\rho}{\sigma} \left(0.14 \left(\frac{\sigma}{\Delta\rho} \right)^{1/2} \right)^2 = 0.46$$

Also, substituting maximum stable droplet diameter and including concentration correction into particle velocity formula (Equation 5.22) gives the transport velocity as,

$$\vartheta_T = \sqrt{\frac{0.27}{C_D \rho_{\text{af}}} (1.85 \sqrt{\sigma \Delta\rho} - \tau_0)} \quad (5.29)$$

Above equation assumes that the maximum stable droplet diameter will be achieved and maintained as the kill fluid stream travels downwards. By substituting Equation 5.29 (after writing corrected drag coefficient in place, $C_D = C_{D0}(1 - C)^{-3.7}$) and Equation 5.22 we can define the correction factor as,

$$\epsilon = \sqrt{3.7(1 - C)^{3.7} \frac{1.85 \sqrt{\sigma \Delta\rho} - \tau_0}{13.23 \Delta\rho d - \tau_0}}$$

In steady-state transport, concentration can be defined using material balance of KF in a unit-length volume of annulus. For constant feed rate into the unit volume, if the transport velocity is

too slow, KF concentration would increase. On the other hand, when velocity is high, concentration may become negligibly small. Thus, concentration of KF in the annular fluid column is,

$$C = \frac{q}{60 A \vartheta_T} \quad (5.30)$$

The formula relates flow rate (injection rate) to transport velocity and kill fluid concentration as,

$$q_c = 60 A \vartheta_T C \quad (5.31)$$

Equation 5.31 implies that, for a given injection rate, q_c , when transport velocity is small, concentration becomes high that, in turn (considering Equation 5.29), further reduces transport velocity causing chain-reaction that would stop the displacement process. By substituting Equation 5.29 and to 5.31 equilibrium injection rate can be defined resulting in KF concentration, C , as,

$$q_c = 31.18 A C \sqrt{\frac{(1 - C)^{3.7}}{C_{D0} \rho_{af}} (1.85 \sqrt{\sigma \Delta \rho} - \tau_0)} \quad (5.32)$$

Equation 5.32 directly relates injection rate with fluid concentration. In order to determine relationship between injection rate and transport velocity the following trial-and-error procedure is used.

1. Guess an initial value of ϑ_T .
2. Calculate asymptotic friction factor from Equation 5.23.
3. Calculate Reynolds Number from Equation 5.28.
4. Calculate uncorrected drag coefficient from Equation 5.24 or 5.25.
5. Find concentration from Equation 5.30.
6. Correct drag coefficient for concentration from Equation 5.26.
7. Find new transport velocity from Equation 5.29.
8. Repeat steps 1 through 6 until matching the two values of transport velocity.
9. Find the corresponding flow rate from Equation 5.31.

The above algorithm has been coded in Matlab as shown in Appendix D. Results from example calculations are plotted in Figure 5.27. The top-left plot in Figure 5.27 depicts the effect

of concentration on transport velocity. For the lowest concentration, maximum transport velocity can be reached. When concentration is too high, transportation velocity approaches zero value. Interestingly, the plots of injection rate vs. concentration (top right) and vs. transport velocity (bottom left) have maximum. The maximum value represents the only combination of the rate, velocity and concentration that makes the rate of KF settling equal to injection rate- the condition for steady-state settling. Thus, the maximum flow rate is the desired critical flow rate (q_{cr-T}) and is analytically calculated below.

First derivative of corresponding flow rate formula is,

$$\frac{dq_c}{dC} = \frac{d}{dC} \left[60AC \sqrt{\frac{0.27 (1 - C)^{3.7}}{C_{D0}\rho_{af}} (1.85 \sqrt{\sigma \Delta\rho} - \tau_0)} \right] \quad (5.33)$$

After defining constant, G, as,

$$G = \sqrt{\frac{0.27}{C_{D0}\rho_{af}} (1.85 \sqrt{\sigma \Delta\rho} - \tau_0)} \quad (5.34)$$

and differentiation, equation for maximum q_c can be written as,

$$\frac{dq_c}{dC} = 60 AG \left[\sqrt{(1 - C)^{3.7}} + \frac{-3.7 (1 - C)^{2.7}}{2 \sqrt{(1 - C)^{3.7}}} C \right] = 0 \quad (5.35)$$

having only one root,

$$C = 0.35$$

Substituting the $C=0.35$ value into Equation 5.32 gives a closed formula for injection rate,

$$q_{cr-T} = q_c(C = 0.35) = 4.92 A \sqrt{\frac{(1.85 \sqrt{\sigma \Delta\rho} - \tau_0)}{C_{D0}\rho_{af}}} \quad (5.36)$$

It must be emphasized, here, that validity of the critical rate formula (Equation 5.46) is limited by validity of two empirical correlations: (1) maximum stable droplet size, Equation 5.27, and (2) corrected drag coefficient, Equation 5.26. Nevertheless, the formula gives useful estimation for designing the displacement process.

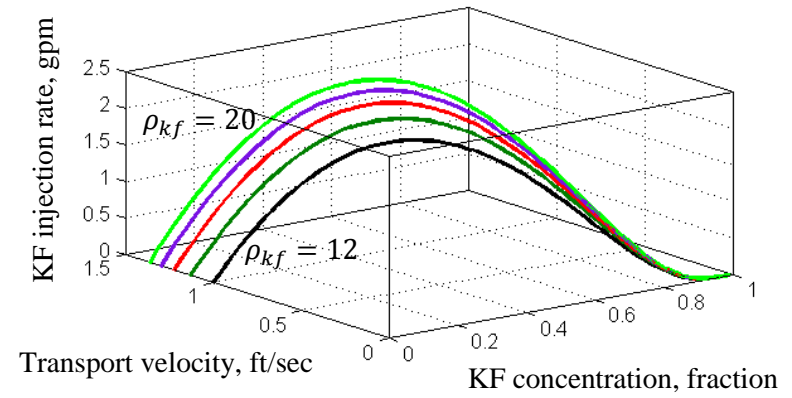
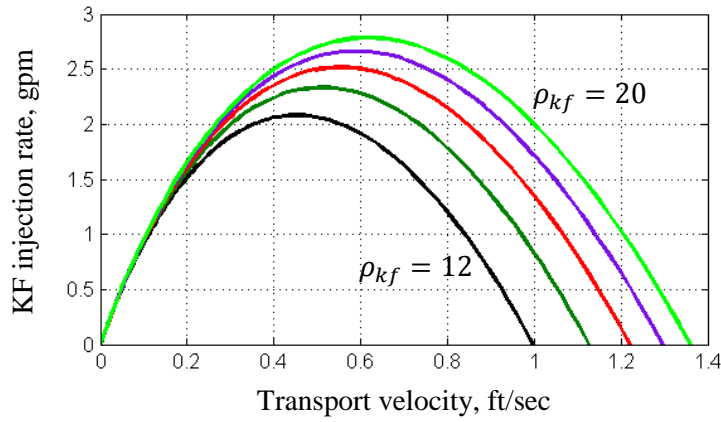
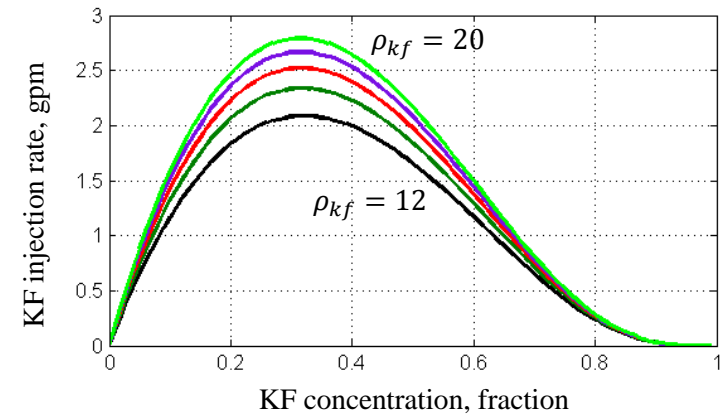
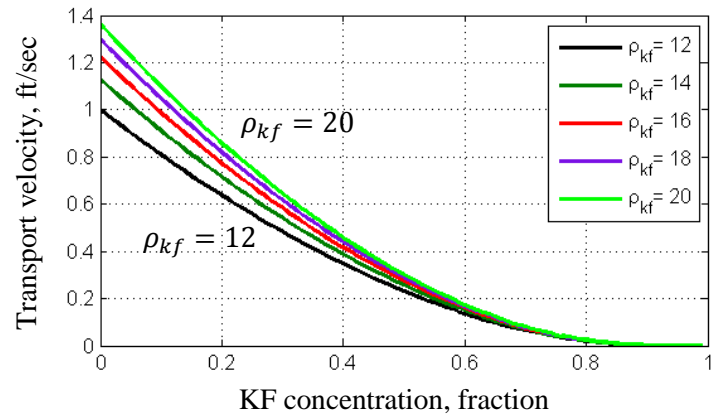


Figure 5.27: KF injection rate design plots ($\tau_0 = 2$ lbf/100sqft, $\rho_{af} = 8.6$ ppg, $\mu_{kf} = 8$ cP, $\mu_{af} = 5$ cP, $\sigma = 30$ dyne/cm and $A = 0.24$ gal/ft)

CHAPTER 6: FULL SCALE TEST

As demonstrated in pilot-scale testing, above; brominated organics would completely displace Non-Newtonian fluids and increase the bottom pressure. However, effectiveness of the displacement process remains unknown for fluid column longer than 20-foot. Moreover, the process performance may be also affected by surface pressure at the casing head. A single full-size test was conducted with the following objectives:

- Investigate efficiency of the displacement process under surface pressure (SCP);
- verify performance of displacement in long fluid column; and,
- test validity of the up-scaling model.

6.1 Methodology

6.1.1 Well installation

For the test, Well #1 in the LSU Petroleum Engineering Research & Technology Transfer Laboratory was designated. Schematics of the well can be seen in Figure 6.1. A 2-7/8" (ID=2.441") tubing was installed in 5-1/2" and 10-3/4" intermediate casings. The tubing was 2750' and had 16 barrels volumetric capacity (0.24 gal/ft.). A gas injection valve was installed at 2717' depth, and two pressure transducers were attached to 1650' and 2728' feet depths. A check valve that allowed one-way flow from annulus into tubing was connected to the bottom of the tubing. Considering the kill fluid removal problem from the 2-7/8" - 5-1/2" annulus, the displacement would take place in the 2-7/8" tubing. For top-injection of fluid injection a 0.5" (ID=0.375") diameter 60-ft long micro-tubing with an elbow on its end was installed at the wellhead. Well #4 was used as a source of natural gas to transfer pressure into the annulus. A 2" flow-line was also attached to the wellhead to receive the overflowing fluid. A conductivity-meter on the flow-line would measure composition of the overflow stream. A pressure-temperature transducer at the flow-line was connected to an auto-choke to regulate the pressure. The flow-line discharged to a mud-gas separator. In addition, a sampling port was assembled between the transducers and the wellhead to be able to obtain samples and visually inspect the overflowing fluid. Injection would be provided by a positive displacement chemical resistant pump that was able to reach up to 900 psi and 9-90 gallons per hour. Steel high-pressure tubing was connected to the wellhead from the pump and a totalizer/flow meter was installed to be able

to read the flow rate and the volume of fluid injected for each batch. Schematics of the full-scale installation can be seen in Figure 6.2 and a picture of the surface well installation is shown in Figure 6.3.

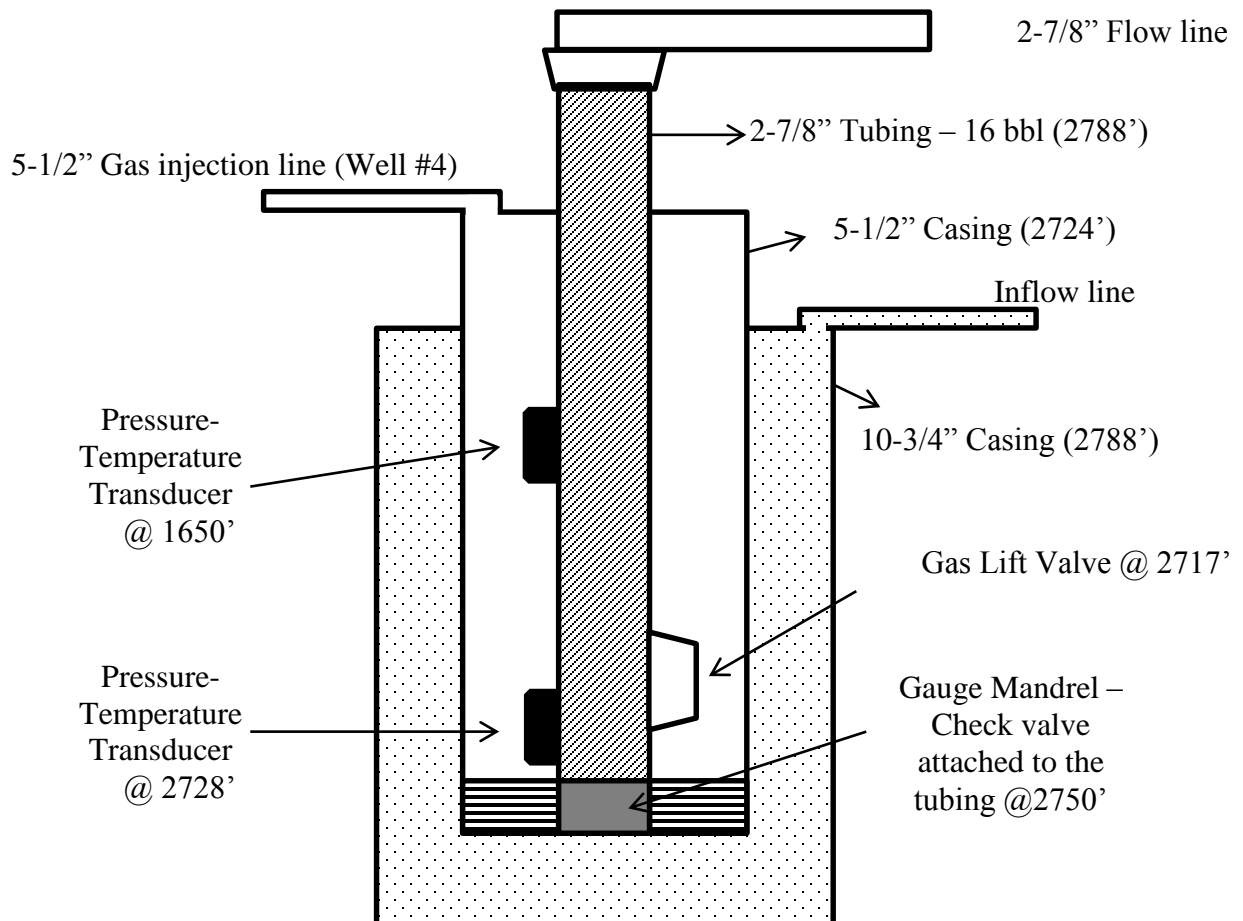


Figure 6.1: Well#1 schematics

A 11.85 ppg low-viscosity (8 cP) kill fluid was used to enable efficient cleaning after the test. The displaced (annular) fluid (AF) was slightly weighted bentonite drilling mud having 8.6 ppg density. Properties of both fluids can be seen in Table 6.1. A total of 32 barrels of kill fluid was blended at the facility using three of 550 gallons capacity totes. A 20-barrel trip tank was used to prepare the annular fluid. The mixed mud was stored and hydrated in the tank for a week.

Table 6.1: Properties of the kill and annular fluids

	Kill Fluid	Annular Fluid
Type	Brominated Organic Blend	Water-Based Mud
Density, ppg	11.85	8.6
Viscosity, cP	8	5
Yield Point , lbf/100sqft	-	2

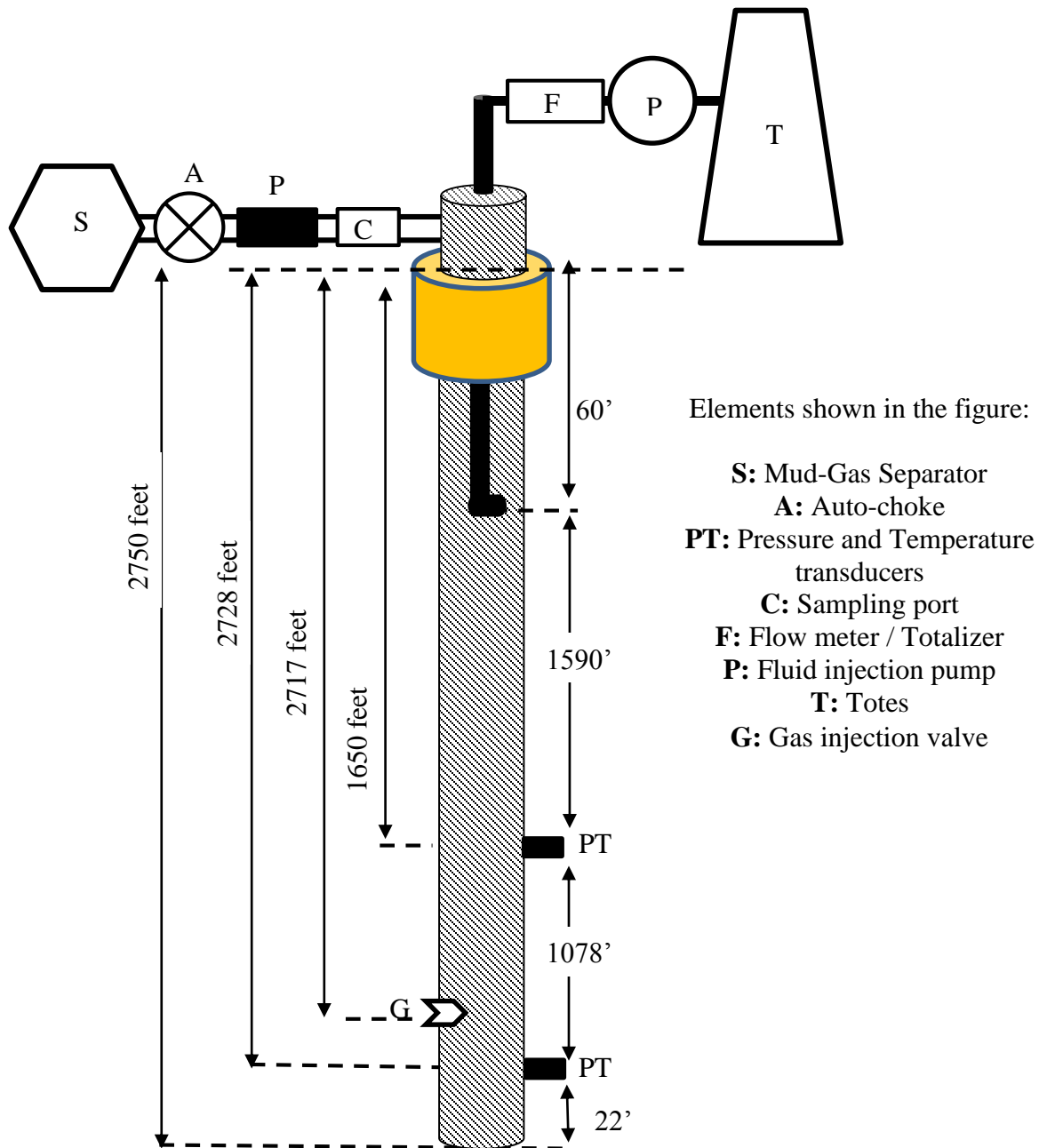


Figure 6.2: Full-scale test – well installation

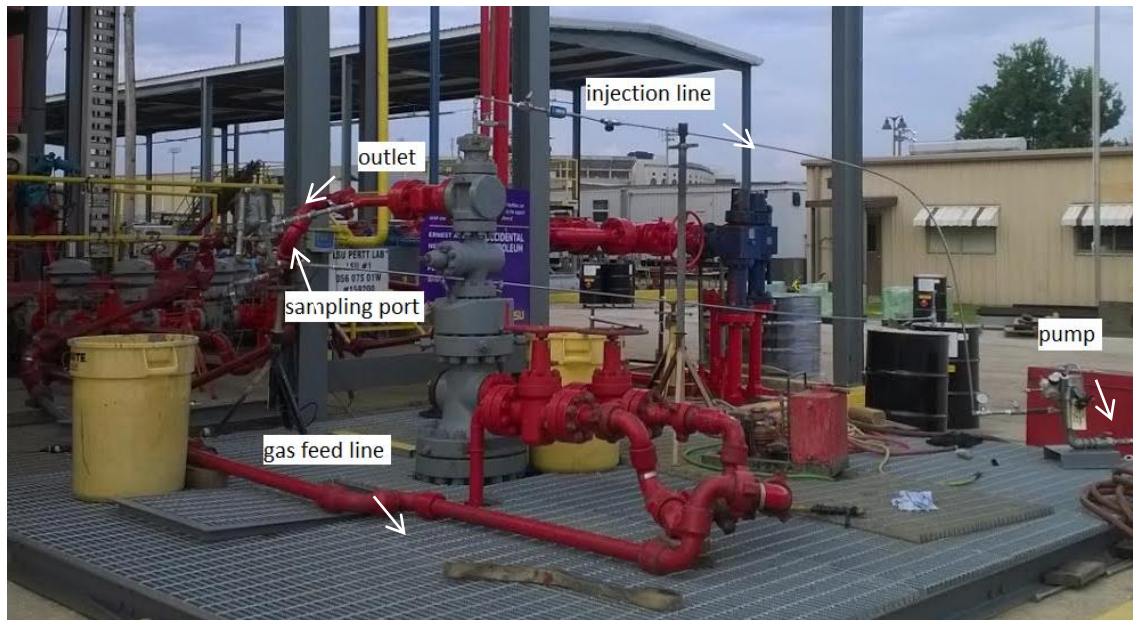


Figure 6.3: Picture of well installation

6.1.2 Testing Procedure

- 1) Fill the tubing 15.5 barrels of the mud by leaving 57 feet space at the top in order to create a gas cap and to obtain submerged kill fluid injection
- 2) Close all the valves; trap the mud in the tubing and keep it undisturbed (no gas injection) for two hours for it to gain structural strength.
- 3) Set auto-choke to 2000 psi and inject gas through the gas lift valve.
- 4) Control wellhead pressure during gas migration to achieve its final value 350 psi.
- 5) Start injecting kill fluid while checking the pressure readings.
- 6) Collect fluid samples every 30 minutes to make sure that the AF is being displaced. If KF is present in samples, reduce flow rate.
- 7) Keep the bottom pressure constant by bleeding-off the choke pressure by 50 psi if the bottom pressure increases by 50 psi (do not drop below the initial bottom pressure).
- 8) Stop injection process when top pressure becomes zero or KF supply finishes – whichever comes first.

Figure 6.4 shows the planned pressure history of the full-scale test. Step 1 represents the AF fill up in the pipe. Step 2 is the 4-hr stagnant mud gelation. Step 3 and 4 represent gas injection and migration that would be controlled by the auto-choke to prevent excessive pressure buildup. At the end of this process, the wellhead pressure would be set at 350 psi. Step 5 is the kill fluid

injection. The choke would be adjusted in increments to keep the bottom pressure (lower P-T transducer) constant.

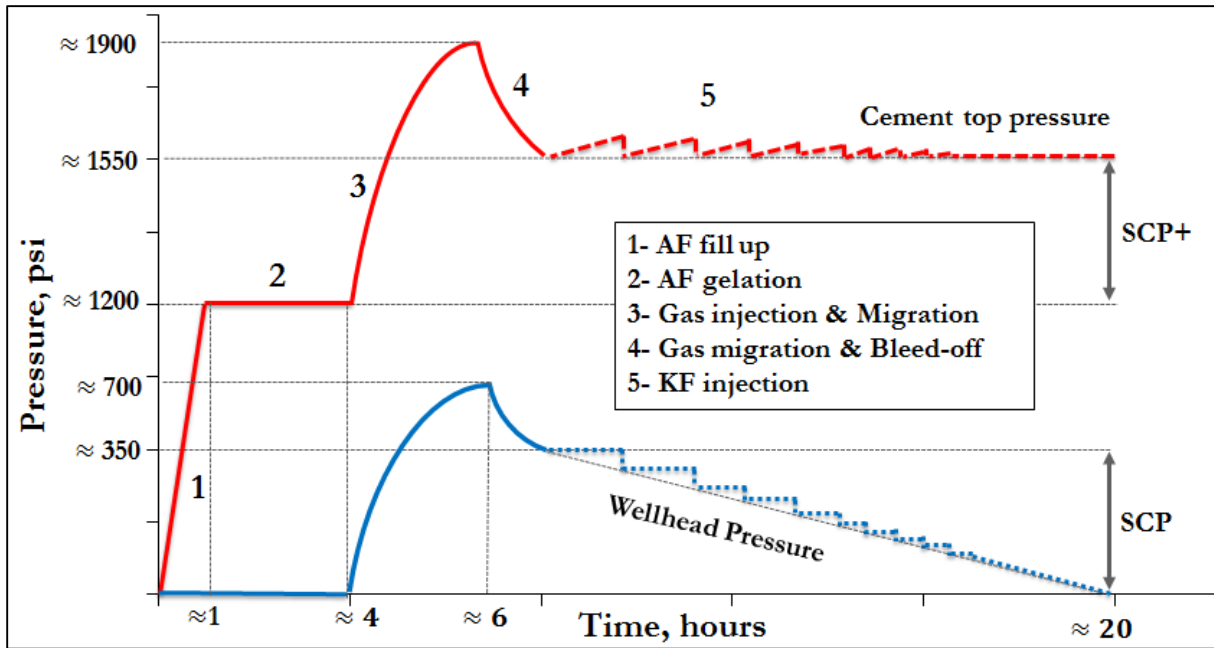


Figure 6.4: Planned pressure change during test

6.1.3 Injection rate design

As learned from the previous tests, studied above, the efficiency of the displacement process strongly depends on the injection rate. The rate was designed using data from earlier experiments and theoretical considerations.

Experimental Considerations

The same kill fluid was used in the pilot-scale experiments, above, with a slightly thicker mud as the annular fluids. All three runs with the same KF in the pilot tests (batches 27, 28 and 29) showed high volumetric and pressure replacement efficiencies. The difference was the annular vs. pipe geometry in the full-scale test. The pilot had a 1.05 gal/ft annular capacity and the well has; 23% of the pilot: 0.24 gal/ft. pipe capacity. In order to obtain the similar performance, relationship between the rate and the annular capacity are assumed to be proportional. This assumption neglects the effect of geometrical effects such as the whirling flow of heavy fluid through a lighter fluid, as stated in the study of Calvert et al. ^[11]. Table 6.2 below shows the flow rate conversion from the pilot tests to the full-scale test by multiplying the actual rate by 0.23, ratio of capacities.

Table 6.2: Injection rate conversion from pilot-scale for full scale test*

Batch #	Injection Rate, gpm	Converted rate, gpm
27	1	0.23
28	4.3	1
29	6	1.4

*Flow area criterion

In addition to the flow area, slip velocity of KF needs to be estimated and used for injection rate conversion. A 4-foot 2.5" (2.323" ID) clear PVC pipe (0.23 gal/ft) pipe (similar size to 2-7/8" tubing) was used for the conversion. One third of the pipe was filled with the kill fluid, the rest is completed with Non-Newtonian translucent fluid (TF0103) and both sides of the pipe were closed. Then, the pipe was flipped to have KF on top of AF and displacement process was timed (Figure 6.5).

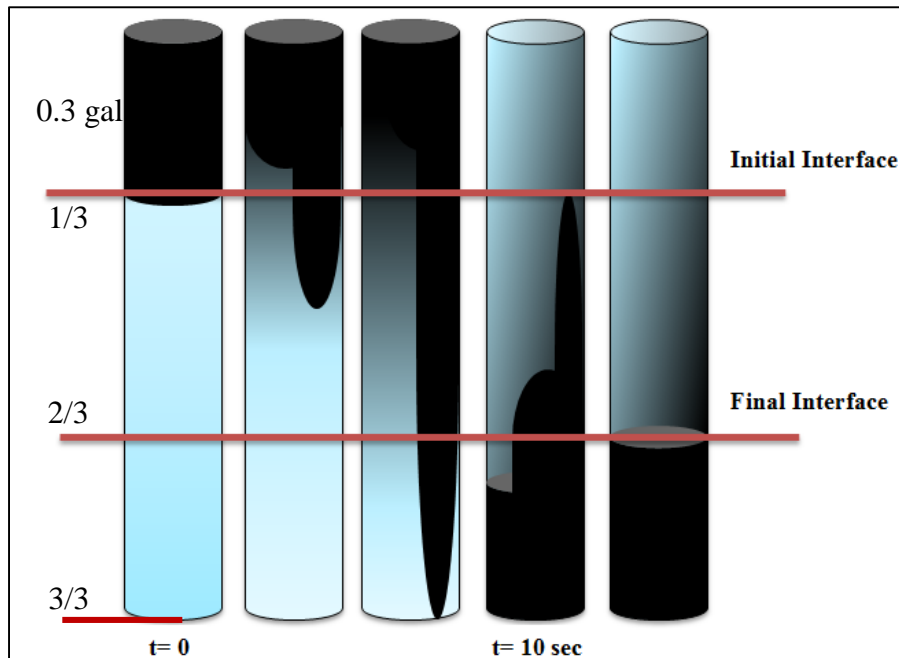


Figure 6.5: Flip-flop test for injection design. KF is in black, Translucent Fluid is in light color.

By the time the pipe is flipped; KF/TF interface broke and a plume of kill fluid started to slip down. Translucent fluid interfering into initial kill fluid section parted kill fluid into droplets, and these droplets started to slip down much slower. Nevertheless, the stagnant fluid occupied the kill fluid's initial place completely in after about 10 seconds. In other words, kill fluid evacuated its top location in 10 seconds, sketched in Figure 6.5. Therefore, the rate of KF slippage is estimated as, $q = 60 \cdot 0.3 \text{ gal}/10 \text{ sec} = 1.8 \text{ gpm}$

Theoretical Considerations

Table 6.3 below is generated based on the maximum injection rate criteria above (Chapter 4.4 and 5.6). Other estimations are also included for comparison. Beside these performance limitations, time factor must also be considered. By employing Equation 5.47, necessary times to displace 16 barrels of annular fluid with different flow rates are calculated and presented in Figure 6.6. Considering the importance of atomization criteria and trying to keep the operation time below about 12 hours; flow rate has been designed as between 1 and 2 gpm. The process would start with 1.5 gpm and overflowing fluid would be visually inspected simultaneously. If a high content of kill fluid overflows, injection rate would be dropped to 1 gpm or a lower value.

Table 6.3: Injection rate design based on different criterion

Symbol	Design Criteria	Source	Calculated Value, gpm
q_{cr-i}	Impingement Width	Equation 4.7	0.71
q_{cr-A}	Atomization	Equation 4.16	1.96
q_{cr-T}	Transport velocity	Figure 5.42	2.1
$q(R_u = 1)$	Best performance	Equation 5.46	0.77
q_{pilot}	Pilot scale exp.	Table 6.2	1.4
q_f	Flip-flop test	Equation 6.1	1.8

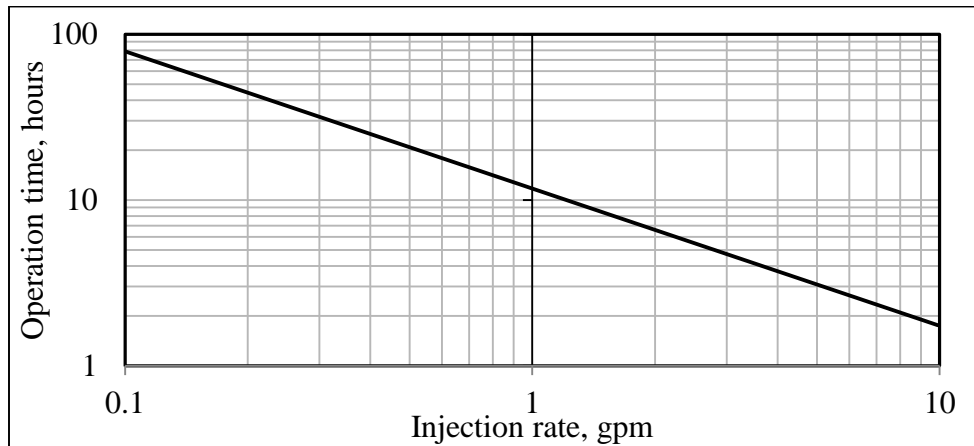


Figure 6.6: Corresponding operation durations for injection rates based on Equation 5.46

6.2 Results and Observations

As shown in Figure 6.7, the test did not proceed as planned due to some minor and major problems. Injection was interrupted frequently by the leaks in the feed line and malfunction of the pump. Moreover, the most important problem was the failure of the auto choke after 2.5

hours of KF injection. The choke failure caused complete decompression of the wellhead. As a result, shown in Figure 6.7, injection rate increased rapidly from 0.4 to 1.8 gpm. After the pressure was lost, choke was reset to 350 psi again and pressure at the surface. Pressure data and overflow samples were the only source to estimate the process in the well. Results obtained from the pressure readings and from the samples taken during and after the test are explained in details below.

6.2.1 Pressure data

Figure 6.7 is the recorded lower tubing pressure (LTP), upper tubing pressure (UTP) and choke pressure (CP) during the test. Comparing with Figure 6.4 reveals that the first four steps went on as planned. However, at the onset of kill fluid injection the choke failed resulting in wellhead decompression – Step 5. The reason for choke failure is not clear – it might have been caused by the choke reaction to rapid pressure increase due to filling up the top tubing with incompressible kill fluid. During Step 6 the choke pressure was slowly rebuilt and somewhat stabilized with reducing tendency resulting from poor choke performance. Also, each time a sample was taken from the wellhead, the choke pressure would drop. As the downhole pressure follows the pattern of surface pressure, the difference between the two pressures (i.e. hydrostatic pressure) – shown in Figure 6.8 would better represent displacement process performance.

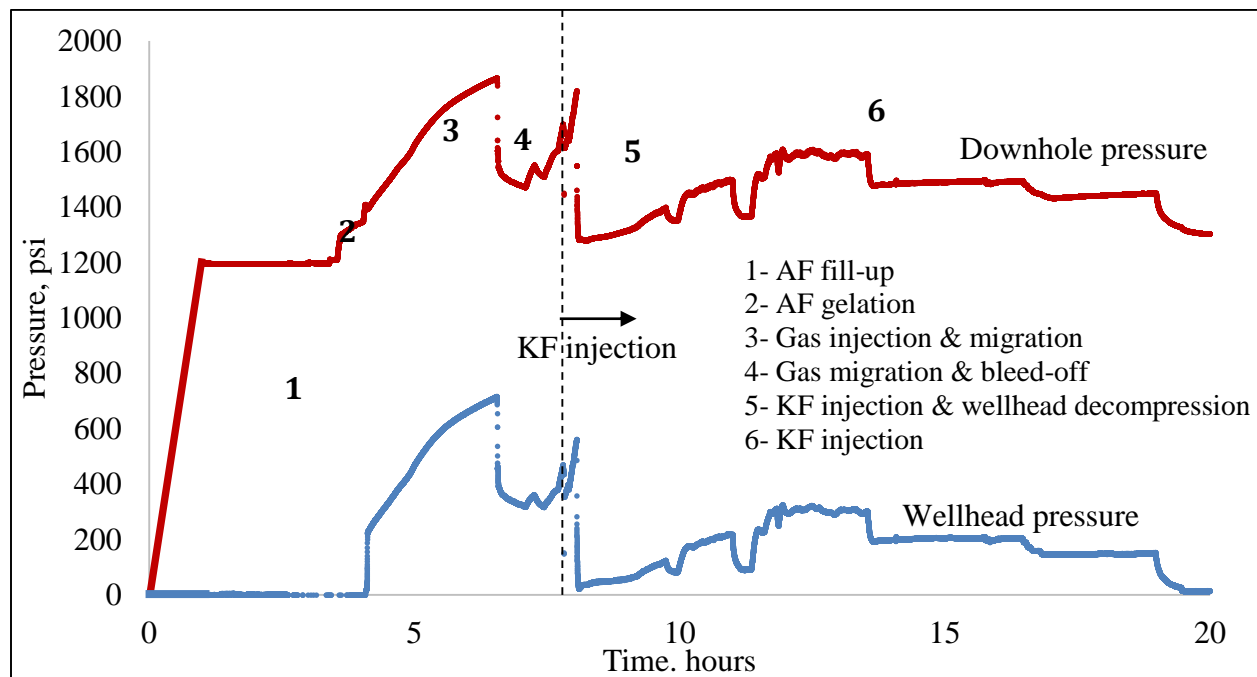


Figure 6.7: Top and bottom pressure change

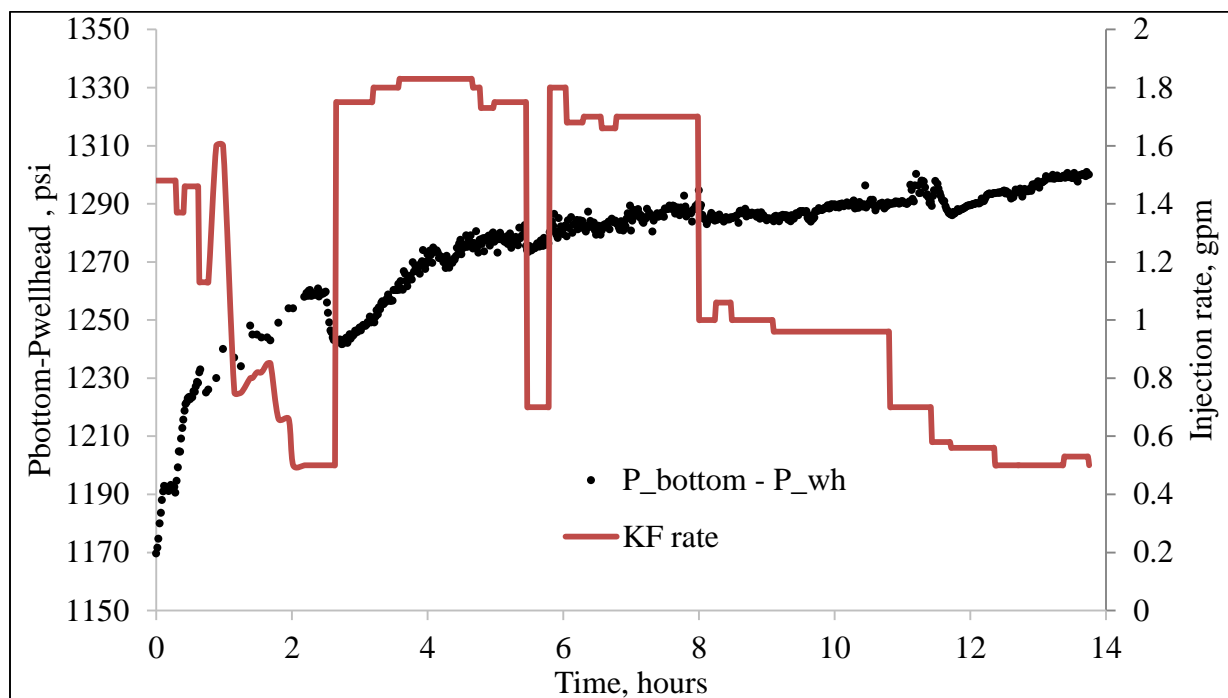


Figure 6.8: Change of hydrostatic pressure and KF injection rate

6.2.2 Sampling

Five overflow fluid samples were taken during the injection and several more were extracted during the cleanup. Pictures of the overflow samples are shown in Figure 6.9 with descriptions given in Table 6.4. All of the overflow samples, except sample #3, contained high content of the kill fluid. Due to the sample collection method, the first two samples (#1 and #2) represent the fluid settled in the sampling port. Thus, the samples do not represent the overflowing fluid. The third sample (#3) was taken after bleeding about 250 mL of the overflow that may have caused wellhead depressurization. The sample had high content of mud (Figure 6.10).

The jars shown in Figure 6.11 are received during the cleanup and represent the sections of remained fluid in the well. Number 1 corresponds to the top section and number 10 is the heavy mud used for displacing the fluid in the pipe after the test. Samples 3, 4 and 5 clearly demonstrate the presence of KF section somewhere in the middle of the fluid column that has not settle to the bottom. The watery samples (7, 8, and 9) contain water from the tubing bottom above the check valve and below the gas lift valve. As all these samples were taken after 4 days, they cannot be considered an exact representation of fluid column.

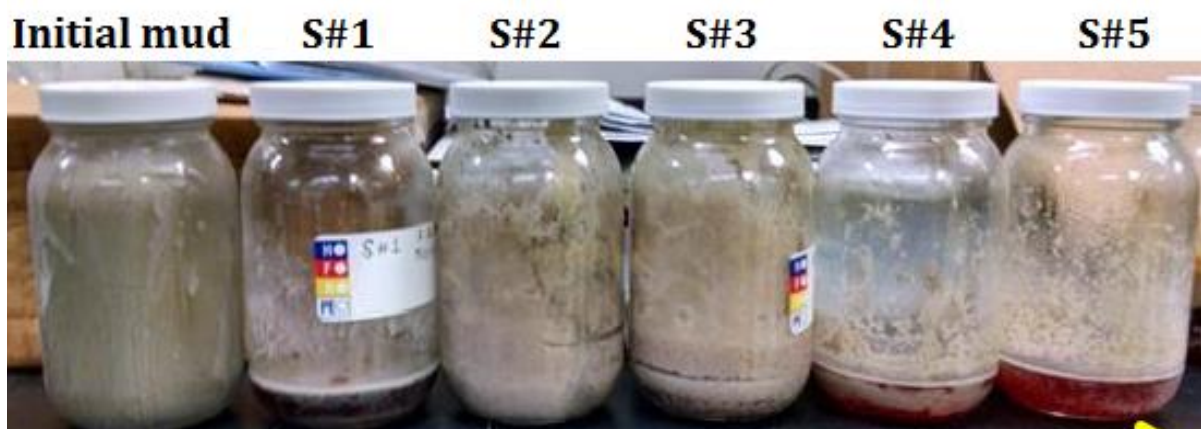


Figure 6.9: Taken samples during KF injection (Sample numbers are chronological). Kill fluid color is red. All samples, except S#3, show high KF content.

Table 6.4: Description of overflow samples

Sample #	Time taken, hours	Remarks
1	1	High KF%
2	1.5	High KF%
3	2.5	Lower KF%
4	4	High KF%
5	4.5	High KF%



Figure 6.10: Overflow sample #3 taken after 2.5 hours of injection.

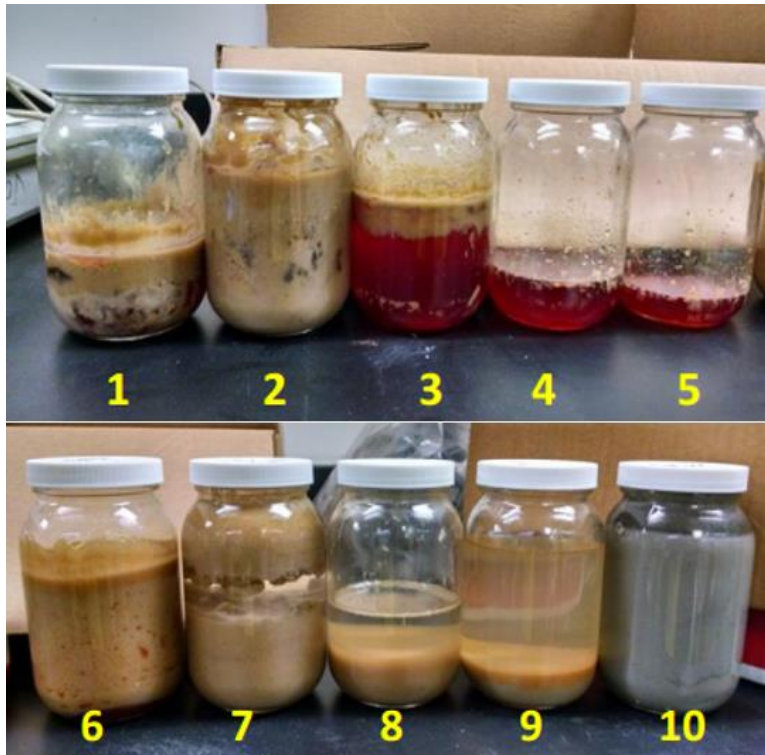


Figure 6.11: Samples taken during cleanup. Number 1 represent top of tubing and number 10 is the heavy displacing (cleaning) mud.

6.3 Analysis

Figure 6.12 shows fluid density change in the tubing during KF injection. The bottom fluid section density is calculated from pressure difference between the two transducers (Initial density of gas cut mud is ~8.5 ppg). The density of top section and total density in the tubing result from the choke pressure and the transducer readings (Initial density is smaller than the mud density during the top gas cap fill up). Patterns of the top and bottom sections density change are quite different. Despite increasing density of the top section, the bottom section density stays generally constant for about 2.6 hours. This means that the kill fluid traveled 1590' of pipe section in about that time. Accordingly, transport velocity is calculated as 0.17 ft/sec. (The transport model, developed in chapter 5, gives 0.2 ft/sec for 1.5 gpm rate). After 2.6 hours, the bottom section density started to raise as the kill fluid entered the section (However, the increase did not exceed 9 ppg. After 9 hours were elapsed, despite the increase in upper section; lower section density stayed constant indicating no more kill fluid settling to the bottom).

According to density measurements, only 10% of injected KF retained in the well and 90% of it is lost to overflow. Only 2% of the injected KF was able to reach to the bottom section.

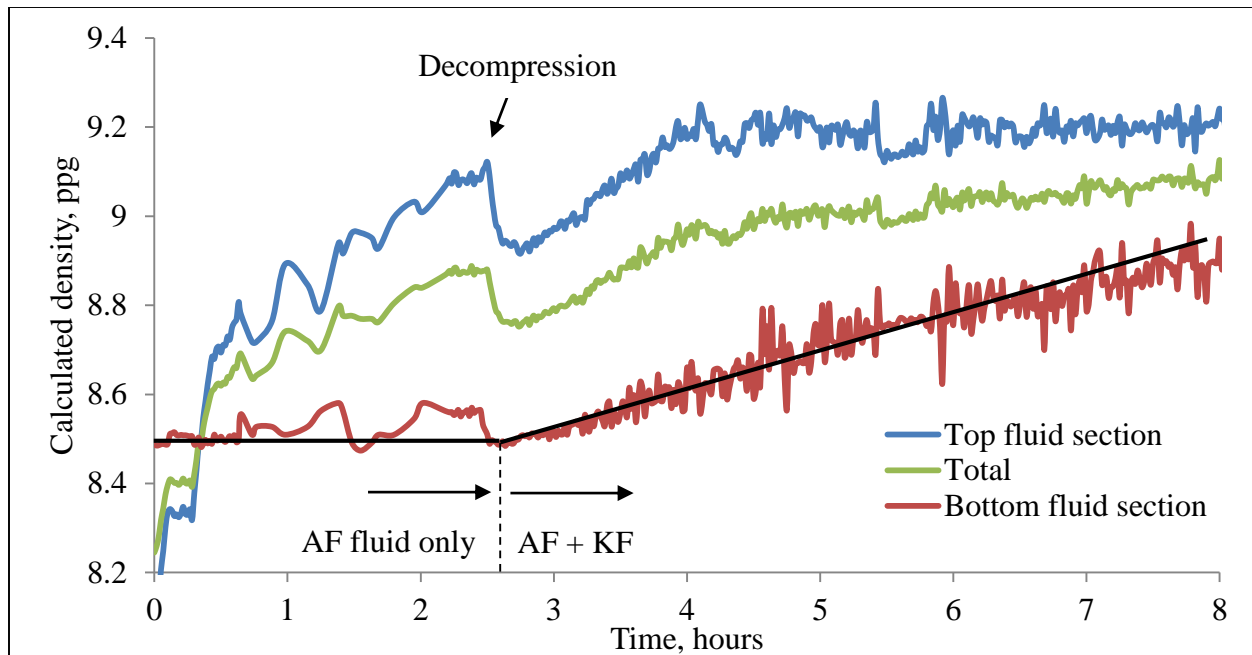


Figure 6.12: Density change in top and bottom well sections

In the full-scale test design, a 350-psi SCP was to be removed by fluid displacement. However, due to the failure of the choke SCP could not be established for the entire test. Theoretical remediation of wellhead pressure is shown in Figure 6.13. The dotted lines represent perfect pressure replacement efficiency and reduction of SCP. The solid lines represent actual performance. The show that 150 psi out of 350 psi of SCP was removed. The displacement process was efficient for 2.5 hours; later, the process deteriorated and reached efficiency plateau at around 30%. As shown in Figure 6.8, reducing injection rate could not enhance KF settling any further. Apparently, the tubing section below the KF injection exit was plugged with a KF/AF emulsion that would not allow KF slippage.

During the test only part of injected KF was retained in the well while another part was getting lost in the overflow. The retained part contributed to hydrostatic pressure buildup. This, analysis of the pressure buildup rate could determine the fraction of KF retained and lost at any time of displacement process. A pressure buildup rate analysis, presented in Figure 6.14, considers four stages of the pressure-time record and the corresponding values of injection rate – as shown in Equation 6.1 – the pressure buildup rate analysis is summarized in Table 6.5. It clearly shows progressive deterioration of the displacement process in terms of reduced KF retainment and increased density of the overflow.

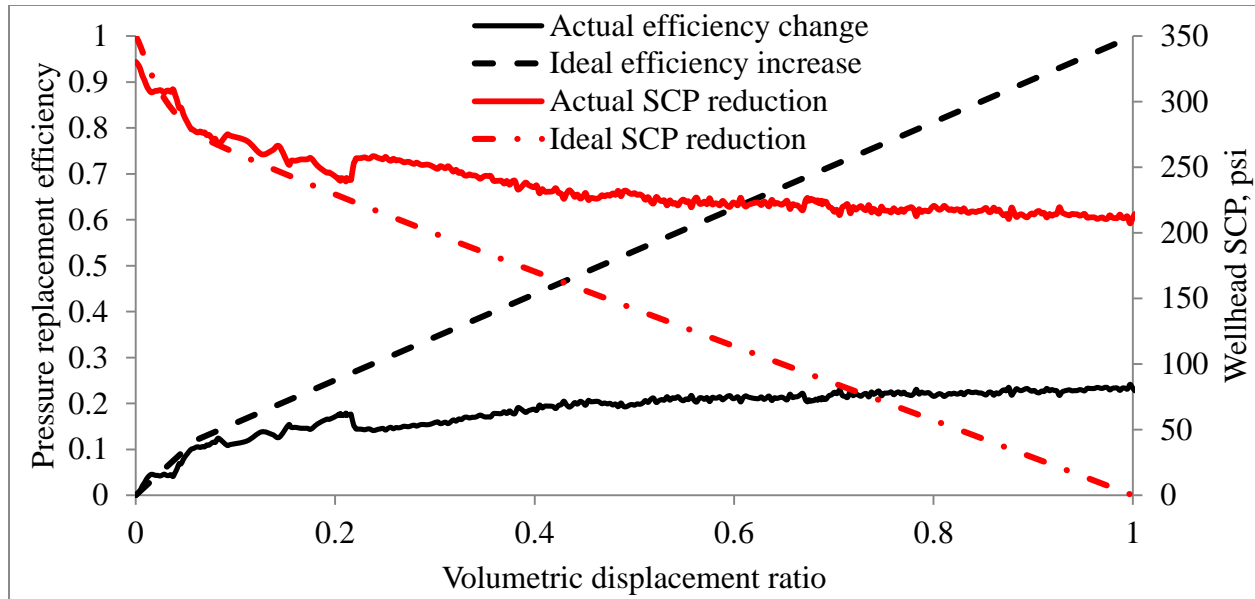


Figure 6.13: Actual and ideal change in E_p and SCP

$$\text{KF retained, \%} = 0.3205 \frac{m A}{\Delta \rho q_{\text{inj}}} \quad (6.1)$$

Where:

m – Pressure buildup rate, psi/hr

A – tubing capacity, gal/ft

$\Delta \rho$ – Density difference of KF and AF, ppg

q_{inj} – KF injection rate, gpm

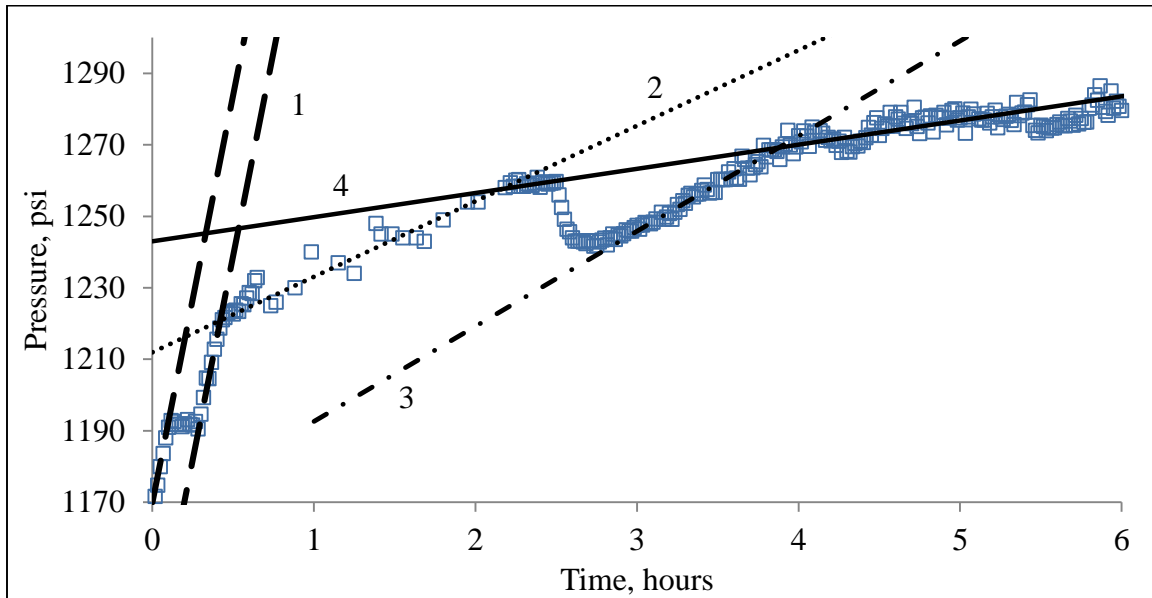


Figure 6.14: Hydrostatic pressure buildup rate analysis

Table 6.5: Slopes of straight lines in Figure 6.14 and corresponding overflow densities

Stage	1*	2	3	4
Slope, psi/hr	228	21.13	26.62	6.76
Average flow rate measured	1.48	0.83	1.8	1.78
Overflow density, ppg	0	9.9	10.7	11.6
KF retained in well, %	100 %	60 %	35 %	8 %

*Gas cap fillup

The analysis emphasizes importance of maintaining stable injection rate. Rapid fluctuations of the flow rate could cause dispersion of KF forming emulsified mixture that would slow down the KF settling. As the process continued, the incoming KF would build an emulsified mixture column at the KF exit – causing bridge-over of buoyant slippage. To demonstrate the bridge-over effect a small size experiment was run in the lab by using the same two fluids. Figure 6.15 shows the generated emulsified mixture after pumping 2.75 gallons of kill fluid into 2.25 gallons of mud with 4 gpm rate through a 0.4” nozzle. Only about 1 gallon of clean kill fluid settled under 1.5 gallons of emulsion. Density of the emulsion was similar to that observed in the pilot-scale tests. Although the emulsified mixture had no structural strengths it was completely stable with no further separation after 6 days. Moreover, settling of fresh KF through the emulsified mixture- although possible – was much slower than through the clean mud.

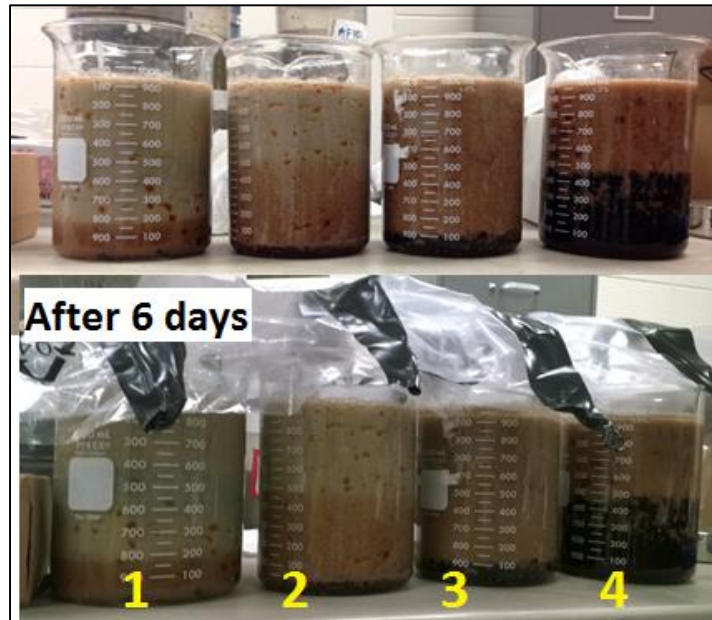


Figure 6.15: Pictures of samples from laboratory generated emulsion. #1 represents the highest and #4 represents the lowest portions of the mixture zone. No further separation occurred in 6 days (bottom samples).

6.4 Bridge-over of Buoyant Slippage

As discussed above, excessive or unstable injection might cause the bridge-over effect. Another reason to be considered is fluctuation of pressure causing trapped gas expansion and migration resulting in the flotation effect. The effects are explained below in more details.

6.4.1 Effect of Pump Pulsation

The pneumatic positive displacement pump used for KF injection generates pressure pulses that result in fluctuation of flow rate. The flow-meter reading gave the average flow rate; but the pump discharge pressure gauge fluctuated wildly.

Figure 6.16 shows the pump strokes per minute versus flow rate published in the pump manual. Pulse frequency values from this figure were used for calculations. The stroking behavior of the pump was modeled as a sinusoidal cyclic function, so the average flow rate is the function's integral divided by time.

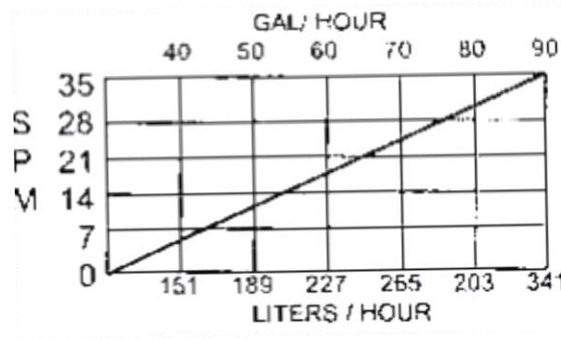


Figure 6.16: Pump strokes per minute versus flow rate [Manual of Morgan Products Pump, Model 5500DS-TR2-SR2S]

The pump discharge flow-rate fluctuation is described as,

$$q(t) = \frac{q_{\max}}{2} \sin(2\pi ft) + \frac{q_{\max}}{2} \quad (6.2)$$

Integrating Equation 6.2, is,

$$\int_0^t q \, dt = \int_0^t \left(\frac{q_{\max}}{2} \sin(2\pi ft) + \frac{q_{\max}}{2} \right) dt$$

gives,

$$q t = \frac{-q_{\max}}{4\pi f} \cos(2\pi f t) + \frac{q_{\max} t}{2} + \frac{q_{\max}}{4\pi f} \quad (6.3)$$

then the average flow rate becomes,

$$q = \frac{q_{\max}}{2t} \left[t + \frac{1 - \cos(2\pi f t)}{2\pi f} \right] \quad (6.4)$$

so, the maximum flow rate is,

$$q_{\max} = 2qt / \left(t + \frac{1 - \cos(2\pi f t)}{2\pi f} \right) \quad (6.5)$$

In order to demonstrate dynamics of the pulsation effect on the injection rate, 0.83 gpm is assigned as the average flow-rate during the initial injection with the wellhead pressurized and 1.8 gpm value is assigned after the wellhead's decompression. Figure 6.17 shows the injection rate pulsation and the pulse frequency. The dashed line marks the maximum rate (atomization) threshold. It is clear that after decompression the average flow rate increased and the flow rate; periodically exceeded its maximum value. Consequently, KF dispersed into small droplets forming the emulsified mixture and resulting in bridge-over of buoyant slippage.

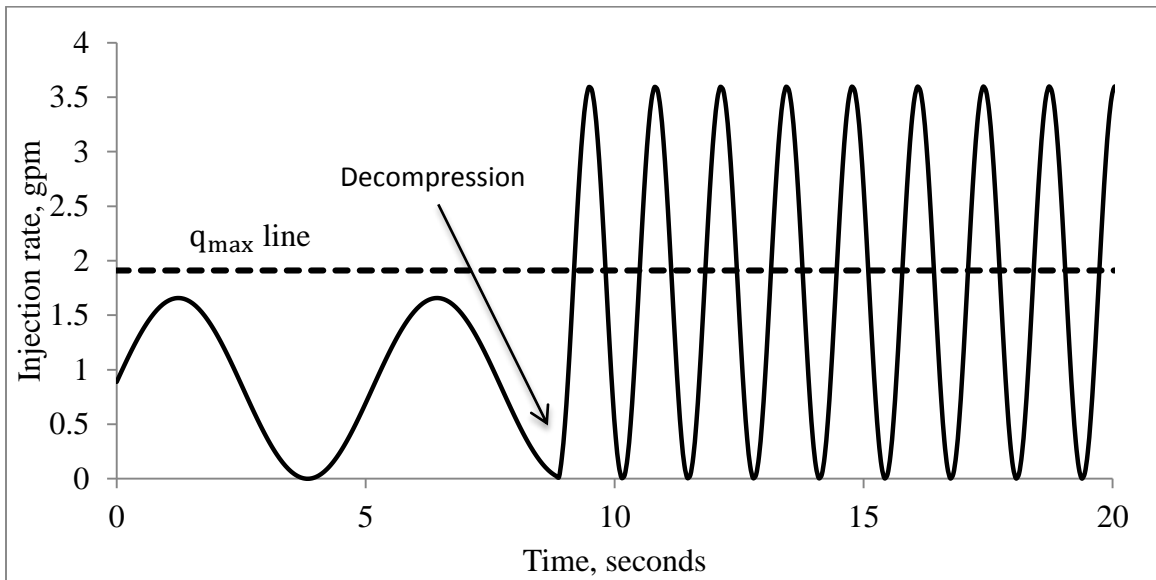


Figure 6.17: Feed pump pulsation after wellhead decompression brings injection rate above its limit

6.4.2 Effect of Gas Flotation

Yield point and wellhead compression cause gas entrapment in the mud. Releasing the well-head pressure would reduce the pressure on top of trapped gas bubbles and allow them to expand. Expanding gas bubbles would; (1) decrease the density of the fluid column, (2) start migrating upwards. The similar phenomenon was actually tested in the pilot scale experiments. As already shown in Figure 5.10; KF injection during gas migration results in poor displacement. From the very beginning of the full scale test, as the kill fluid is injected and well-head pressure increases the auto choke bled out gas; thus, a continuous but small gas expansion was present. Nevertheless, failure of the auto choke caused decompression of the wellhead and resulted in a drastic gas expansion, which ultimately contributed to formation of the emulsified mixture column around the KF discharge point (bottom end of the micro-tubing).

CHAPTER 7: CONCLUSIONS

The objective of this study has been to understand the properties and to investigate the success of gravity displacement of annular fluid, by a heavier fluid, to kill SCP. The following conclusions are drawn:

- Characterization of annular fluid experiments in Chapter 2 show that; in an annulus until SCP occurs, annular fluid clears out from its weighting agents and becomes a low density – low rheology Non-Newtonian drilling mud.
- A good portion of sagged barite occupies the bottom section of the annulus. This portion is very difficult to displace due to its high density and high rheology.
- Gravity displacement of annular fluid is possible with immiscible kill fluids that have the highest density, partitioning coefficient and interfacial tension, based on the minimum displacement time criteria, studied in Chapter 3.
- Visualization of miscible displacement experiments showed the instantaneous mixing of heavy mud and heavy brine kill fluids right after they are injected into water. As the annular fluid in a real-well annulus consists of water at the top, displacement becomes impossible by using these kill fluid. When Non-Newtonian annular fluid is present, mixing of both fluids delays but still occurs as the miscible kill fluid reaches the bottom.
- Visualization experiments, documented in Chapter 4, illustrated the effect of injection geometry on the kill fluid injection process. Side (horizontal) injection is superior to top (vertical) injection due to advantageous effect of dissipation of jetting energy on the casing wall, which allows higher injection rates.
- For the side injection, visual inspections indicate that a narrow impinging width (rivulet type) is required for a continuous downward movement and minimum loss of kill fluid to overflow. For given fluids, recommended injection rate for rivulet type of impingement is developed and presented in the study.
- Vertical injection should precisely be limited since dispersion may easily occur; thus, displacement worth nothing. Threshold injection rates for different type of fragmentation modes are studied and given as injection rate limitations in the study. If vertical injection through flexible tubing is desired, with given nozzle size and fluids properties, developed limitations can be used for injection rate design.

- Pilot scale experiments in Chapter 5 indicated the formation and structure of a mixture zone that builds bottoms up and expands during ongoing displacement process, and has an exponential density distribution. Based on the experimental measurements, a pressure replacement model is developed that predicts the pressure change on top of cement in an annulus.
- The pressure replacement model is converted into dimensionless numbers by using process measures to be used for upscaling. Correlations obtained from the experimental data can be employed for up-scaling designs and process predictions.
- Full scale test (Chapter 6) shows that when an emulsion of KF/AF forms, bridge-over occurs and displacement process may stop. The emulsion may be formed by high injection rate (dispersion) and/or due to concurrent movement of gas bubbles (flotation) and kill fluid droplets.

CHAPTER 8: RECOMMENDATIONS

- For a better estimation of displacement time, transport velocity model might be improved. Experiments that would help for model validation could be run.
- Although the well had a different geometry; the full-scale test was designed based on the correlations obtained from the pilot tests. For a better design, displacement process in different geometries might be better studied.
- Beside the pipe and slot geometry, experiments in a transparent pilot physical annulus are recommended to see the motion of slipping kill fluid. KF might be following a downwards whirl motion and the droplet model could be incorrect in an annular geometry. Seeing the phenomenon would improve or disprove study in this thesis.
- In addition to water-based annular fluids, performance of immiscible buoyant displacement in oil and synthetic based annular fluids could be tested.
- The effect of brominated organics on the environment could be evaluated for any well-size process design. Economic and environmental concerns could be compared.
- Over time, any mud column creates a free-water layer on its top. Injecting miscible kill fluids into this column might be mixing with this free-water and not displacing the annular fluid below it. Methods for improving this method might be investigated. Before injecting miscible heavy fluid into the column, light but high rheology mud could initially be injected to improve Non-Newtonian character of annular fluid. Then injecting heavy kill fluid could achieve a rope transport due to high yield-stresses of both fluids. All these could be experimentally and theoretically studied.

REFERENCES

- [1]Bourgoyne, A.T., S.L. Scott, and W. Manowski. *A review of Sustained Casing Pressure Occuring on the OCS*. 2000. Web. December 19, 2014.
- [2]Hopman, P. *Webinar on Wellbore Integrity*. 2013, Society of Petroleum Engineers.
- [3]Kinik, K. 2012. Risk of Well Integrity Failure Due Sustained Casing Pressure. Louisiana State University, M.S. Thesis.
- [4]Wojtanowicz, A.K., S. Nishikawa, and X. Rong. *Diagnosis and Remediation of Sustained Casing Pressure in Wells*. Final Report. Baton Rouge (LA): LSU, 2001. Web. December 19, 2014.
- [5]Milanovic, D. and L. Smith. 2006. A Case History of Sustainable Annulus Pressure in Sour Wells - Prevention, Evaluation and Remediation. SPE-97597-MS proceedings of the SPE ATW HPHT Sour Well Design, The Woodlands, TX. May 17-19, 2005.
- [6]Carpenter, R.B., M.E. Gonzalez, V. Granberry, and T.E. Becker. 2004. Remediating Sustained Casing Pressure by Forming a Downhole Annular Seal with Low-Melt-Point Eutectic Metal. SPE-87198-MS proceedings of the IADC/SPE Drilling Conference, Dallas, TX. March 2-4, 2004.
- [7]Nishikawa, S., A.K. Wojtanowicz, and J.R. Smith. 2001. Experimental Assessment of the Bleed-and-Lube Method for Removal of Sustained Casing Pressure. PETSOC-2001-041 proceedings of the Petroleum Society's Canadian International Petroleum Conference, Calgary, Alberta, Canada. June 12-13, 2001.
- [8]Nishikawa, S. 1999. Mechanism of Gas Migration After Cement Placement and Control of Sustained Casing Pressure. Louisiana State University, M.S. Thesis.
- [9]Frigaard, I.A. and J.P. Crawshaw. 1999. Preventing buoyancy-driven flows of two Bingham fluids in a closed pipe – Fluid rheology design for oilfield plug cementing. *Journal of Engineering Mathematics* 36(4): p. 327-348.
- [10]Crawshaw, J.P. and I. Frigaard. 1999. Cement Plugs: Stability and Failure by Buoyancy-Driven Mechanism. SPE-56959-MS proceedings of the Offshore Europe Conference, Aberdeen, Scotland. Sept 7-9, 1999.
- [11]Calvert, D.G., J.F. Heathman, and J.E. Griffith. 1995. Plug Cementing: Horizontal to Vertical Conditions. SPE-30514-MS proceedings of the SPE Annual Technical Conference and Exhibition, Dallas, Texas. Oct. 22-25, 1995.

- [12]Ohnesorge, W. 1936. Formation of drops by nozzles and the breakup of liquid jets. *Z. Angew. Math. Mech.* 16: p. 355-358.
- [13]*Multiphase Flow Handbook*. ed. C.T. Crowe. 2006.
- [14]Reitz, R.D. 1978. Mechanism of Breakup of Round Liquid Jets. Princeton University, Ph.D. Dissertation.
- [15]Ramalingam, S., M.D. Cloeter, B. Smith, S.C. Garrick, and W. Liu. 2013. Experimental Investigation of Viscous Liquid Jet Transitions. proceedings of the 25th Annual Conference on Liquid Atomization and Spray Systems, Pittsburgh, PA. May 2013.
- [16]Tyler, E. 1933. Instability of liquid jets. *Phil. Mag.* 16: p. 504-518.
- [17]Teng, H., C.M. Kinoshita, and S.M. Masutani. 1995. Prediction of droplet size from the breakup of cylindrical liquid jets. *International Journal of Multiphase Flow* 21(1): p. 129-136.
- [18]Rayleigh, L. 1878. On the instability of jets. *Lond. Math. Soc. Proc.* 10: p. 4-18.
- [19]Miranda, J.M. and J.B.L.M. Campos. 1999. Impinging jets confined by a conical wall: Laminar flow predictions. *AIChE Journal* 45(11): p. 2273-2285.
- [20]Storr, G.J. and M. Behnia. 2000. Comparisons between experiment and numerical simulation using a free surface technique of free-falling liquid jets. *Experimental Thermal and Fluid Science* 22(1-2): p. 79-91.
- [21]Morison, K.R. and R.J. Thorpe. 2002. Liquid Distribution from Cleaning-in-Place Sprayballs. *Food and Bioproducts Processing* 80(4): p. 270-275.
- [22]Wilson, K.C., R.R. Horsley, T. Kealy, J.A. Reizes, and M. Horsley. 2003. Direct prediction of fall velocities in non-Newtonian materials. *International Journal of Mineral Processing* 71(1-4): p. 17-30.
- [23]Wang, T., J.F. Davidson, and D.I. Wilson. 2013. Effect of surfactant on flow patterns and draining films created by a static horizontal liquid jet impinging on a vertical surface at low flow rates. *Chemical Engineering Science* 88(0): p. 79-94.
- [24]Nusselt, W. 1916. Oberflächen kondensation des Wasserdampfes. *Zeitschrift Verein Deutscher ingenieure* 60: p. 569-575.
- [25]Bourgoyne, A.T., M.E. Chenevert, K.K. Millheim, and F.S. Young. *Applied Drilling Engineering*. SPE Textbook. Vol. 2. 1984.

- [26]Dedegil, M.Y. 1987. Drag Coefficient and Settling Velocity of Particles in Non-Newtonian Suspensions. *Journal of Fluids Engineering* 109(3): p. 319-323.
- [27]Valentik, L. and R.L. Whitmore. 1965. The Terminal Velocity of spheres in Bingham Plastics. *Brit. J. Appl. Phys.* 16: p. 1197-1203.
- [28]Krishna, P.M., D. Venkateswarlu, and G.S.R. Narasimhamurty. 1959. Fall of Liquid Drops in Water. Terminal Velocities. *Journal of Chemical & Engineering Data* 4(4): p. 336-340.
- [29]Abdelouahab, M. and R. Gatignol. 2011. A new approach for computation of drop terminal velocity in stagnant medium. *Chemical Engineering Science* 66(8): p. 1523-1535.
- [30]Clift, R. and J.R.G.a.M.E. Weber. *Bubbles, Drops and Particles*. 1978, Academic Press, INC.
- [31]Bozzano, G. and M. Dente. 2009. Single Bubble and Drop Motion Modeling. proceedings of the AIDIC Conference Series, 2009.
- [32]Gordon, C., S. Lewis, and P. Tonmukayakul. 2008. Rheological Properties of Cement Spacer: Mixture Effects. AADE-08-DF-HO-09 proceedings of the AADE Fluids Conference and Exhibition, Houston, TX. April 8-9, 2008.
- [33]Erge, O., M.E. Ozbayoglu, S.Z. Miska, M. Yu, N. Takach, A. Saasen, and R. May. 2014. Effect of Drillstring Deflection and Rotary Speed on Annular Frictional Pressure Losses. *Journal of Energy Resources Technology-Transactions of the Asme* 136(042909-1).
- [34]Griffin, T.J. and W.L. Crowe. 1977. Water-Base Spacer Increases Success Ratio Of Cement Jobs In Illinois Basin. SPE-6489-MS proceedings of the SPE/AIME Midwest Gas Storage and Production Symposium, Indianapolis, Indiana. April 13-15, 1977.
- [35]Nelson, E.B. *Well Cementing*. 1990: Schlumberger Educational Services.
- [36]Griffin, T.J. and L.K. Moran. Spacer Composition and Method of Use. U.S. Patent. 4,083,407. Feb. 7, 1977. Print.
- [37]Erge, O., E.M. Ozbayoglu, S.Z. Miska, M. Yu, N. Takach, A. Saasen, and R. May. 2014. The Effects of Drillstring Eccentricity, Rotation, and Buckling Configurations on Annular Frictional Pressure Losses While Circulating Yield Power Law Fluids. SPE-167950-MS proceedings of the IADC/SPE Drilling Conference and Exhibition, Fort Worth, TX. March 4-6, 2014.

- [38]Brice, J.W., Jr. and B.C. Holmes. 1964. Engineered Casing Cementing Programs Using Turbulent Flow Techniques. SPE-742-PA proceedings of the SPE Annual Gas Meeting, New Orleans, Louisiana. Oct. 6-9, 1963.
- [39]Beirute, R.M. 1976. All Purpose Cement-Mud Spacer. SPE-5691-MS proceedings of the Society of Petroleum Engineers of AIME Symposium on Formation Damage Control, Houston, Tx. Jan 29-30, 1976.
- [40]Benge, G. 1990. Field Study of Offshore Cement-Spacer Mixing. *SPE Drilling Engineering* SPE-19864-PA.
- [41]Shah, S.N., N.H. Shanker, and C.C. Ogugbue. 2010. Future Challenges of Drilling Fluids and Their Rheological Measurements. AADE-10-DF-HO-41 proceedings of the AADE Fluids Conference and Exhibition, Houston, TX. April 6-7, 2010.
- [42]Ehrhorn, C. and A. Saasen. 1996. Barite Sag in Drilling Fluids. 4(Annual Transactions of the Nordic Rheology Society).
- [43]Parvizinia, A., R.M. Ahmed, and S.O. Osisanya. 2011. Experimental Study on the Phenomenon of Barite Sag. IPTC-14944-MS proceedings of the IPT Conference, Bangkok, Thailand. Feb 7-9, 2014.
- [44]Makinde, F.A., A.D. Adejumo, C.T. Ako, and V.E. Efeovbokhan. 2011. Modelling the Effects of Temperature and Aging Time on the Rheological Properties of Drilling Fluids. *Petroleum & Coal* 53: p. 167-182.
- [45]Erge, O. 2013. Effect of Free Drillstring Rotation on Frictional Pressure Losses. University of Tulsa, M.S. Thesis.
- [46]Zamora, M. 2009. Mechanisms, Measurement And Mitigation Of Barite Sag. OMC-2009-105 presented at the Offshore Mediterranean Conference, Ravenna, Italy. Mar 25-27, 2009.
- [47]Scott, P.D., M. Zamora, and C. Aldea. 2004. Barite-Sag Management: Challenges, Strategies, Opportunities. SPE-87136-MS proceedings of the IADC/SPE Drilling Conference, Dallas, TX. Mar 2-4, 2004.
- [48]Paslay, P., U.B.R. Sathuvalli, and M.L. Payne. 2007. A Phenomenological Approach to Analysis of Barite Sag in Drilling Muds. SPE-110404-MS proceedings of the SPE Annual Technical Conference and Exhibition, Anaheim, CA. Nov 11-14, 2007.
- [49]Wagle, V., S. Maghrabi, and D. Kulkarni. 2013. Formulating Sag-Resistant, Low-Gravity Solids-Free Invert Emulsion Fluids. SPE-164200-MS proceedings of the SPE Middle East Oil and Gas Show and Conference, Manama, Bahrain. March 10-13, 2013.

- [50]Baldock, T.E., M.R. Tomkins, P. Nielsen, and M.G. Hughes. 2004. Settling velocity of sediments at high concentrations. *Coastal Engineering* 51(1): p. 91-100.
- [51]Boycott, A.E. 1920. Sedimentation of Blood Corpuscles. *Nature* 104: p. 532.
- [52]Hanson, P.M., T.K. Trigg, Jr., G. Rachal, and M. Zamora. 1990. Investigation of Barite "Sag" in Weighted Drilling Fluids in Highly Deviated Wells. SPE-20423-MS proceedings of the SPE 65th Annual Technical Conference and Exhibition, New Orleans, LA. Sept 23-26, 1990.
- [53]Saasen, A., D. Liu, and C.D. Marken. 1995. Prediction of Barite Sag Potential of Drilling Fluids From Rheological Measurements. SPE-29410-MS proceedings of the SPE/IADC Drilling Conference, Amsterdam, The Netherlands. Feb 28-Mar 2, 1995.
- [54]Skalle, P., K.R. Backe, S. Lyomov, and J. Svven. 1999. Barite Segregation In Inclined Boreholes. *Journal of Canadian Petroleum Technology* PETSOC-97-76 38(13): p. 97-76.
- [55]Moran, L.K. and K.O. Lindstrom. 1990. Cement Spacer Fluid Solids Settling. SPE-19936-MS proceedings of the IADC/SPE Drilling Conference, Houston, TX. Feb 27-Mar 2, 1990.
- [56]Wojtanowicz, A.K., S.D. Field, and Z. Krilov. 1989. Statistical Assessment and Sampling of Drilling-Fluid Reserve. *SPE Drilling Engineering* SPE-17245-PA: p. 162-170.
- [57]Suckling, T.P., C. Lam, S.A. Jefferis, and C.J. Pantling. 2011. Evaluation of Causes of Bleeding of Free Water From Bentonite Slurry. proceedings of the 36th Annual Conference on Deep Foundations, Boston, Massachusetts.
- [58]Bol, G.M. 1986. Bentonite Quality and Quality-Evaluation Methods. SPE-13454-PA proceedings of the IADC/SPE Drilling Conference, New Orleans. Aug, 1985.
- [59]Abshire, L., S. Hekelaar, and P.C. Desai. 2013. Offshore Plug & Abandonment: Challenges and Technical Solutions. OTC23906 proceedings of the Offshore Tehnology Conference, Houston, TX. May 6-9, 2013.
- [60]Hayden, R., C. Russell, A. Vereide, P. Babasick, P. Shaposhnikov, and D. May. 2011. Case Studies in Evaluation of Cement with Wireline Logs in a Deep Water Environment. proceedings of the SPWLA 52nd Annual Logging Symposium, Colorado Springs, CO. May 14-18, 2011.
- [61]Shaposhnikov, P. and D. Findlater. 2013. Advanced Techniques in Integrated Cement Evaluation. proceedings of the SPWLA 54th Annual Logging Symposium, New Orleans, LA. June 22-26, 2013.

- [62]Schlumberger "Isolation Scanner Brochure". 2011.
- [63]Shaposhnikov, P. 2014. Current and New Developments in the Cement Evaluation Technologies. presented at the Well Integrity & Asset Digitalization Conference, Houston, TX. April 15-16, 2014.
- [64]Amani, M., M. Al-Jubouri, and A. Shadravan. 2012. Comparative Study of Using Oil-Based Mud Versus Water-Based Mud in HPHT Fields. *Advances in Petroleum Exploration and Development* 4(2): p. 18-27.
- [65]Wojtanowicz, A.K. and J. Yawen Ye. 1998. Environmental Control of Drilling Mud Discharge Through Dewatering in Cold Weather Climates: Effect of Ambient Temperature. *Canadian Petroleum Technology* 37(5): p. 35-40.
- [66]Anifowoshe, O.L. and S.O. Osisanya. 2012. The Effect of Equivalent Diameter Definitions on Frictional Pressure Loss Estimation in an Annulus with Pipe Rotation. SPE-151176-MS proceedings of the SPE Deepwater and Completions Conference and Exhibition, Galveston, Texas. June 20-21, 2012.
- [67]Langlinais, J.P., A.T. Bourgoyne, Jr., and W.R. Holden. 1983. Frictional Pressure Losses for the Flow of Drilling Mud and Mud/Gas Mixtures. SPE-11993-MS proceedings of the SPE 58th Annual Technical Conference and Exhibition, San Francisco, CA. Oct 5-8, 1983.
- [68]Munson, B.R., D.F. Young, T.H. Okiishi, and W.W. Huebsch. *Fundamentals of Fluid Mechanics*. 6 ed. 2009.
- [69]Lin, S.P. and R.D. Reitz. 1998. Drop and Spray Formation from a Liquid Jet. *Annual Review of Fluid Mechanics* 30(1): p. 85-105.
- [70]Alba, K., S.M. Taghavi, J.R. de Bruyn, and I.A. Frigaard. 2013. Incomplete fluid–fluid displacement of yield-stress fluids. Part 2: Highly inclined pipes. *Journal of Non-Newtonian Fluid Mechanics* 201(0): p. 80-93.
- [71]Wilson, D.I., B.L. Le, H.D.A. Dao, K.Y. Lai, K.R. Morison, and J.F. Davidson. 2012. Surface flow and drainage films created by horizontal impinging liquid jets. *Chemical Engineering Science* 68(1): p. 449-460.
- [72]Richardson, J.F. and W.N. Zaki. 1954. The fall velocities of spheres in viscous fluids. *Trans. Inst. Chem. Eng.* 32: p. 35-41.
- [73]Di Felice, R. 1994. The voidage function for fluid-particle interaction systems. *International Journal of Multiphase Flow* 20: p. 153-162.

- [74] Kaneda, Y. 1986. The drag on a sparse random array of fixed spheres in flow at small but finite Reynolds number. *Journal of Fluid Mechanics* 167: p. 455-463.
- [75] Koch, D.L. and A.S. Sangani. 1999. Particle pressure and marginal stability limits for a homogenous monodisperse gas fluidized bed: kinetic theory and numerical calculations. *Journal of Fluid Mechanics* 400: p. 229-263.
- [76] Koch, D.L. and R.J. Hill. 2001. Inertial effects in suspension and porous media flows. *Annual Review of Fluid Mechanics* 33: p. 619-647.
- [77] Wen, C.Y. and Y.H. Wu. 1966. Mechanics of fluidization. *Chem. Eng. Prog. Symp. Ser.* 62: p. 100-125.

APPENDIX A: SELECTION OF KILL FLUID DERIVATION

Rearranging Equation 3.5 by substituting Equations 3.6, 3.7 and 3.8 gives,

$$\vartheta_A = \frac{2(\sigma g \Delta \rho / \rho_f^2)^{1/4}}{\left[1 + \left(\frac{82 \left(\frac{\rho_f \vartheta_L}{82 \mu_f} d_p \sqrt{1 - \alpha_p^2} \right) \mu_f}{\rho_f \alpha_{pm} \vartheta_L d} \right)^2 \right]^{1/2}}$$

Or,

$$\vartheta_A = 2 \left\{ \frac{\sqrt{\sigma g \Delta \rho}}{\rho_f} \middle/ \left[1 + \left(\frac{d_p \sqrt{1 - \alpha_p^2}}{\alpha_{pm} d} \right)^2 \right] \right\}^{1/2} \quad (A.1)$$

Using peak diameter (Equation 3.10) in place gives,

$$\vartheta_A = 2 \left\{ \frac{\sqrt{\sigma g \Delta \rho}}{\rho_f} \middle/ \left[1 + \left(\frac{1.311}{\alpha_{pm}} \sqrt{\frac{\sigma(1 - \alpha_p^2)}{g \Delta \rho}} \right)^2 \frac{1}{d^2} \right] \right\}^{1/2} \quad (A.2)$$

Grouping the parameters as,

$$a = \left(\frac{1.311}{\alpha_{pm}} \sqrt{\frac{\sigma(1 - \alpha_p^2)}{g \Delta \rho}} \right)^2$$

$$b = (\sqrt{\sigma g \Delta \rho} / \rho_f)^{1/2}$$

so, Equation A.2 becomes,

$$\vartheta_A = \frac{2b}{\sqrt{1 + \frac{a}{d^2}}} \quad (A.3)$$

Substituting Equation A.3 into 3.13 gives the displacement time as,

$$t_{dA} = \frac{h_a}{120 b} \sqrt{1 + \frac{a}{d^2}} \left(1 + 1.91 \frac{A_a}{d^2} \right)$$

Or,

$$t_{dA} = \frac{h_a}{120 b} \left(\frac{\sqrt{d^2 + a}}{d} + 1.91 A_a \frac{\sqrt{d^2 + a}}{d^3} \right) \quad (A.4)$$

Equation A.4 represents the displacement time for the droplet sizes generated below the peak diameter. Same derivation is employed for Part B. Rearranging Equation 3.11 gives,

$$\vartheta_B = \frac{1}{\sqrt{2} \alpha_{pm} \rho_f} \left[\frac{g \Delta \rho d^2 + 8 \alpha_{pm}^2 \sigma}{d} \right]^{1/2} \quad (A.5)$$

Grouping the parameters as,

$$c = \sqrt{2} \alpha_{pm} \rho_f \quad e = g \Delta \rho \quad f = 8 \alpha_{pm}^2 \sigma$$

Equation A.5 becomes,

$$\vartheta_B = \frac{1}{c} \left[\frac{e d^2 + f}{d} \right]^{1/2} \quad (A.6)$$

Substituting Equation A.6 to 3.14 gives the displacement time for Part B as,

$$t_{dB} = \frac{1}{60} \frac{h_a c \sqrt{d}}{\sqrt{e d^2 + f}} \left(1 + 1.91 \frac{A_a}{d^2} \right)$$

Or,

$$t_{dB} = \frac{h_a c}{60} \left(\frac{\sqrt{d}}{\sqrt{e d^2 + f}} + 1.91 A_a \frac{d^{-3/2}}{\sqrt{e d^2 + f}} \right) \quad (A.7)$$

In order to minimize displacement time, the roots of the derivatives of functions A.4 and A.7 should be found.

$$\frac{dt_{dA}}{dt} = 0 \quad \frac{dt_{dB}}{dt} = 0$$

Taking derivative of Equation A.4:

$$t'_{dA} = \frac{h_a}{120 b} \left[\frac{1}{\sqrt{d^2 + a}} - \frac{\sqrt{d^2 + a}}{d^2} + 1.91 A_a \left(\frac{1}{d^2 \sqrt{d^2 + a}} - \frac{3\sqrt{d^2 + a}}{d^4} \right) \right]$$

Yields,

$$\frac{d^2(a + 3.82A_a) + 5.73 A_a a}{d^4 \sqrt{d^2 + a}} = 0$$

$$d^2(a + 3.82A_a) + 5.73 A_a a = 0 \quad \text{Gives,} \quad d = \sqrt{-\frac{5.73A_a a}{a+3.82A_a}}$$

Where, $A_a > 0$ and $a > 0$.

Thus,

$$1/d^4 = 0 \quad \text{Gives,} \quad d = \mp\infty$$

$$1/\sqrt{d^2 + a} = 0 \quad \text{Gives,} \quad d = \mp\infty$$

Above derivations mean that for Part A has no real roots for maximum or minimum displacement time.

Taking derivative of Equation 3.21:

$$t'_{dB} = \frac{h_a c}{60 (e d^2 + f)} \left(\frac{\sqrt{d} \sqrt{e d^2 + f}}{2 d} - \frac{e d^2 \sqrt{d}}{\sqrt{e d^2 + f}} - \frac{3 * 1.91 A_a \sqrt{e d^2 + f}}{2 d^2 \sqrt{d}} - \frac{1.91 A_a e}{\sqrt{d} \sqrt{e d^2 + f}} \right)$$

Since $ed^2 + f > 0$,

$$\frac{(e d^2 + f)(0.5 d^2 - 2.865 A_a) - e(d^4 + 1.91A_a)}{d^{\frac{5}{2}} \sqrt{e d^2 + f}} = 0$$

Since $d > 0$,

$$(e d^2 + f)(0.5 d^2 - 2.865 A_a) - e(d^4 + 1.91A_a) = 0$$

Or,

$$0.5 e d^4 + (2.865 A_a e - 0.5 f)d^2 + (2.865 A_a f + 1.91 A_a e) = 0$$

It can be proved that for most practical values of A_a , e and f , the expression $(2.865 A_a e - 0.5 f) > 0$, so the LHS > 0 and the equation has no roots.

Calculating delta as,

$$\Delta = (2.865 A_a e - 0.5 f)^2 - 4 * 0.5 e (2.865 A_a f + 1.91 A_a e)$$

Or,

$$\Delta = 4.38 A_a^2 e^2 - 8.595 A_a e f + 0.25 f^2$$

So the roots are of variable (d^2) are,

$$d^2 = \frac{-(2.865 A_a e - 0.5 f) \mp \sqrt{4.38 A_a^2 e^2 - 8.595 A_a e f + 0.25 f^2}}{e}$$

or the “d” roots are,

$$d_1 = \sqrt{\frac{-(2.865 A_a e - 0.5 f) + \sqrt{4.38 A_a^2 e^2 - 8.595 A_a e f + 0.25 f^2}}{e}}$$

$$d_2 = \sqrt{\frac{-(2.865 A_a e - 0.5 f) - \sqrt{4.38 A_a^2 e^2 - 8.595 A_a e f + 0.25 f^2}}{e}}$$

$$d_3 = -\sqrt{\frac{-(2.865 A_a e - 0.5 f) + \sqrt{4.38 A_a^2 e^2 - 8.595 A_a e f + 0.25 f^2}}{e}}$$

$$d_4 = -\sqrt{\frac{-(2.865 A_a e - 0.5 f) - \sqrt{4.38 A_a^2 e^2 - 8.595 A_a e f + 0.25 f^2}}{e}}$$

Since the droplet size must be positive, d_3 and d_4 are not real. The other two roots, d_1 and d_2 , are also imaginary as shown by the following example.

Considering,

$$e = g \Delta p = 981 \frac{\text{cm}}{\text{s}^2} * 1.8 \frac{\text{gr}}{\text{cm}^3} = 1736$$

$$f = 8 \alpha_{pm}^2 \sigma = 8 * 0.871^2 * 40.6 \frac{\text{dyn}}{\text{cm}} = 283$$

$$A = 130 \text{ cm}^2$$

Thus roots become,

$$d_1 = 10 \sqrt{-1} \quad \text{and} \quad d_2 = 25 \sqrt{-1}$$

In conclusion, the displacement time function in regions A and B have no minimum value and are monotonically decreasing, so the minimum time $t_{d_{\text{minimum}}} = t_d(d_{\text{max}})$

APPENDIX B: PRESSURE REPLACEMENT MODEL DERIVATION

Displacement process involves injection of kill fluid and overflow of displaced fluid, and can mathematically be derived from material balance equation.

$$m_a(t) = m_{af} + m_{in}(t) - m_{of}(t) \quad (B.1)$$

Where, m_a is changing mass in annulus, m_{af} is mass of annular fluid initially in annulus, m_{in} is mass injected into annulus and m_{of} is mass displaced (overflowed).

Injection rate and density of kill fluid does not change in time.

$$m_{in}(t) = \int_0^t q(t) \rho(t) dt = q \rho_{kf} t \quad (B.2)$$

If both fluids inside the annulus are incompressible, outflow rate should be equal to injection rate. The outflowing fluid mass can be represented in three separate sections: displacement of clean annular fluid, displacement of mixture zone and displacement of clean kill fluid.

Displacement of clean annular fluid:

$$m_{of_{AF}}(t) = q \int_0^t \rho_{af} dt = q \rho_{af} t \quad \text{for } 0 < t < t_L \quad (B.3)$$

Displacement of mixture:

$$m_{of_{mixture}}(t) = q \int_0^t \rho_{of}(t) dt \quad \text{for } t_L < t < t_u \quad (B.4)$$

Displacement of kill fluid:

$$m_{of_{KF}}(t) = q \int_0^t \rho_{kf} dt = q \rho_{kf} t \quad \text{for } t_u < t \quad (B.5)$$

Substituting Equation 5.8 to Equation B.4 gives,

$$m_{\text{of mixture}}(t) = q \int_0^t \left[\rho_{\text{af}} + (\rho_{\text{kf}} - \rho_{\text{af}}) \exp\left(-\frac{q}{Aa} t_u\right) \exp\left(\frac{q}{Aa} t\right) \right] dt$$

Considering,

$$\int_0^t \exp\left(\frac{q}{Aa} t\right) dt = \frac{aA}{q} \left[\exp\left(\frac{q}{Aa} t\right) - 1 \right]$$

Equation B.4 becomes,

$$m_{\text{out mixture}}(t) = q\rho_{\text{af}}t + aA(\rho_{\text{kf}} - \rho_{\text{af}}) \exp\left(-\frac{q}{Aa} t_u\right) \left[\exp\left(\frac{q}{Aa} t\right) - 1 \right] \quad (\text{B.6})$$

Thus, mass balance in the annulus (Equation B.1) for all three sections become,

During displacement of clean annular fluid, the annulus mass is,

$$m_a(t) = m_{\text{af}} + q (\rho_{\text{kf}} - \rho_{\text{af}}) t \quad (\text{B.7})$$

During charge of mixture zone, the annular mass is,

$$m_a(t) = m_{\text{af}} + q (\rho_{\text{kf}} - \rho_{\text{af}}) t - aA(\rho_{\text{kf}} - \rho_{\text{af}}) \exp\left(-\frac{q}{Aa} t_u\right) \left[\exp\left(\frac{q}{Aa} t\right) - 1 \right] \quad (\text{B.8})$$

At the end of mixture zone discharge, the annular mass is constant and equal to the mass of KF, $m_a(t) = m_{\text{kf}} = \text{constant}$. Where, m_{af} and m_{kf} represent annular fluid mass full of annular and kill fluids, respectively.

In order to derive the mass balance equations to represent pressure build-up; a few assumptions must be made:

- The minor losses of small kill fluid particles to counter-current flow are negligible.
- From the moment when mixture appears in the overflow, vertical density distribution above the top of clean kill fluid in annulus remains unchanged.
- The top of clean kill fluid section will always reach the overflow port and complete displacement will always be established by pumping necessary amount of kill fluid.

Using pressure data obtained from the bottom transducer is possible by converting mass balance principle to pressure difference equation. Pressure at the bottom of annulus is related to fluid weight as,

$$P_{ba} = mgh = \frac{V_a \rho g}{A} = \frac{m_a}{A} g$$

Or, in field units,

$$P_{ba} = 0.052 \frac{m_a}{A} \quad (B.9)$$

Substituting Equation 5.20 to mass balance equations gives the pressure increase functions. Density differential is grouped as $\Delta\rho = \rho_{kf} - \rho_{af}$.

After converting fluid mass to hydrostatic bottom pressure, mathematical model of the pressure replacement process is developed as follows.

For displacement of annular fluid:

$$P_{ba}(t) = P_{af} + 0.052 \frac{q}{A} \Delta\rho t \quad \text{for} \quad \begin{array}{l} 0 \leq t \leq t_L \\ 0 \leq P \leq P_L \end{array} \quad (B.10)$$

For discharge of mixture zone, stage,

$$P_{ba}(t) = P_L + \frac{0.052 q \Delta\rho}{A} (t - t_L) - 0.052 a \Delta\rho \exp\left(-\frac{q}{Aa} (t_u - t_L)\right) \left[\exp\left(\frac{q}{Aa} (t - t_L)\right) - 1 \right] \quad (B.11)$$

for $t_L \leq t < t_u$ and $P_L \leq P < P_e$.

After the mixture zone discharge, ultimate pressure, P_u , is reached.

Where,

P_{ba} – Bottom pressure, psi

P_{af} – Initial pressure in annulus, psi

P_L – Pressure when linear increase ends

q – Injection rate, gpm

t – Time, min

t_L – Time when linear increase ends, min

a – Exponential coefficient, ft

A – Annular capacity, gal/ft

$\Delta\rho$ – Density difference of fluids, ppg

t_u – Ultimate time: end of displacement, min

P_u – Ultimate pressure t_u , psi

Equation B.10 gives P_{af} when $t=0$ and Equation B.11 gives P_L when $t=t_L$. Based on the single complete run, (Batch 31 shown in Figure 5.7), all the experiments are assumed as they would reach to the complete displacement line. Thus, Equation B.11 should give the ultimate pressure when the complete displacement is established and ultimate time of displacement has elapsed.

Hydrostatic pressure at the bottom when annular column is filled with only kill fluid is,

$$P_u = 0.052 \frac{V_a}{A} \rho_{kf} \quad (B.12)$$

Plugging t_u into Equation B.11 gives,

$$P_u = P_{ba}(t_u) = P_L + \frac{0.052}{A} q \Delta\rho (t_u - t_L) - 0.052 a \Delta\rho \exp\left(-\frac{q}{Aa}(t_u - t_L)\right) \left[\exp\left(\frac{q}{Aa}(t_u - t_L)\right) - 1 \right]$$

Note that Equation B.11 for $t=t_u$ relates (typically unknown) mixture zone parameter “a” to the measured values of t_L and t_u , as,

$$P_u = P_L + 0.052 \Delta\rho \left[\frac{q}{A} (t_u - t_L) - a + a \exp\left(-\frac{q}{Aa}(t_u - t_L)\right) \right] \quad (B.13)$$

Equation B.13 above represents the relationship between two unknowns; ultimate time of displacement and mixture zone density distribution coefficient (exponential coefficient). When all the other variables are known, the equation can be solved iteratively to find t_u .

Pressure replacement is transformed into dimensionless forms by using performance measures.

Considering,

$$P_u - P_{af} = 0.052 (\rho_{kf} - \rho_{af}) h_a \quad (B.14)$$

Pressure replacement efficiency becomes,

$$E_p = \frac{P_{ba} - P_{af}}{P_u - P_{af}} = \frac{P_{ba} - P_{af}}{0.052 \Delta \rho h_a} \quad (B.15)$$

Also displacement ratio yields,

$$R = \frac{qt}{V_a} = \frac{qt}{h_a A} \quad (B.16)$$

Thus,

$$h_a = \frac{qt}{R A} \quad (B.17)$$

Rearranging Equation B.10, substituting Equation B.17, and dividing by Equation B.14 gives,

$$\frac{P_{ba} - P_{af}}{P_u - P_{af}} = \frac{0.052 \Delta \rho \frac{qt}{A}}{0.052 (\rho_{kf} - \rho_{af}) h_a}$$

Considering Equations B.15 and B.16; above formula becomes,

$$E_p = R$$

Substituting Equation B.10 to B.12 when $t=t_L$ gives,

$$P_{ba} - P_{af} = 0.052 \Delta \rho \left\{ \frac{q}{A} t - a \exp \left(-\frac{q}{Aa} (t_u - t_L) \right) \left[\exp \left(\frac{q}{Aa} (t - t_L) \right) - 1 \right] \right\}$$

Dividing sides by B.14 and substituting Equations B.15 and B.16 gives,

$$E_p = R - \frac{a}{h_a} \exp \left(-\frac{h_a}{a} (R_u - R_L) \right) \left[\exp \left(\frac{h_a}{a} (R - R_L) \right) - 1 \right]$$

As learned from the slot model experiments and also mentioned in chapter 5.3 , a minor kill fluid loss during the injection is inevitable. Similar suggestion applies to ultimate displacement rate and pressure replacement efficiency. If the entire annular column is displaced with kill fluid, final efficiency should give one; however, in fact, some kill fluid may be trapped in the annular

fluid column and 100% efficiency cannot be established. Nevertheless, neither the minor losses nor the trapped fluid is considered in the pressure build-up model.

In dimensionless formulation, using the process performance measures, E_p and R – defined above, the pressure replacement model becomes as follows.

For displacement of annular fluid (linear pressure increase), $0 \leq R \leq R_L$ and $0 \leq E_p \leq E_{pL}$;

$$E_p(R) = R = \frac{V_p}{V_a} = \frac{qt}{h_a A}$$

For mixture zone discharge stage, $R_L \leq R \leq R_u$ or $E_{pL} \leq E_p \leq 1$;

$$E_p(R) = R - \frac{a}{h_a} \exp\left(-\frac{h_a}{a}(R_u - R_L)\right) \left[\exp\left(\frac{h_a}{a}(R - R_L)\right) - 1 \right] \quad (B.18)$$

After the mixture zone discharge ($R \geq R_u$),

$$E_p(R) = 1$$

Note that for ultimate displacement ratio, Equation 5.14 equals unity and relates the (typically) unknown mixture zone parameter “a” to the measured values of R_L and R_u from the tests, as,

$$E(R_u) = 1 = R_u - \frac{a}{h_a} \exp\left(-\frac{h_a}{a}(R_u - R_L)\right) \left[\exp\left(\frac{h_a}{a}(R_u - R_L)\right) - 1 \right]$$

Solving for R_L gives,

$$R_L = \frac{a}{h_a} \ln\left(1 - \frac{h_a}{a}(R_u - 1)\right) + R_u \quad (B.19)$$

APPENDIX C: PILOT-SCALE MISCIBLE DISPLACEMENT RUN

According to slot model experiments, when AF is water displacement is almost impossible. However, when a viscous but low density AF is present, a rope transport of heavy-mud KF is possible. To observe the phenomenon in a longer column, similar experiment was conducted in the 20-foot pilot model. AF0903 and AF1303 (notations and properties are given in pilot scale chapter) were used as the AF and KF, respectively. Flow rate was about 1 gpm and 45.4 gallons of heavy mud was injected into the model for the test.

After pumping about 33 gallons of heavy mud ($t_u = 33$ min, $R_u = 1.6$), bottom pressure approached to the complete displacement line ($E_p \approx 1$) - shown in Figure C.1. Bottom pressure increased almost linearly for about 15 minutes and then the overflow density started to increase, which indicated the mixture zone.

This single heavy-mud displacement run validates the statements in the visualization chapter. Heavy-mud KF – when injected into a viscous AF – is able to travel downwards with little mixing. But – once the bottom is reached – mixing starts and complete displacement is delayed despite the low injection rate. In conclusion, even if the fluid in the annulus is viscous (which is not expected considering the characterization of AF experiments), efficiency of the miscible displacement in thousands of feet annulus is still indefinite.

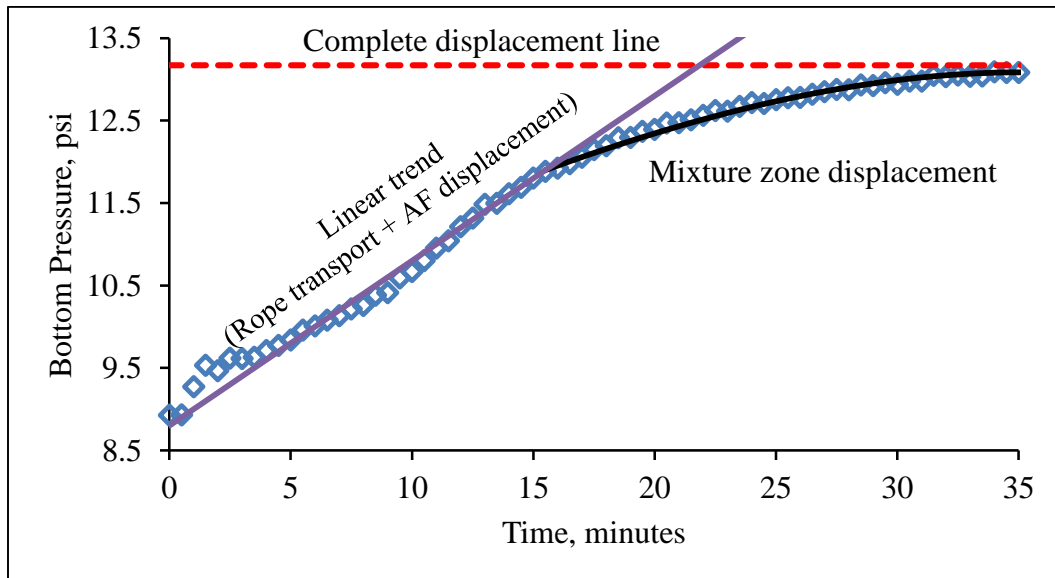


Figure C.1: Pressure plot of heavy mud kill fluid displacement. (Batch#34)

APPENDIX D: SOFTWARE SCRIPTS

- Injection rate design function (Matlab)

```
function [vt, Re, Cd, qmax]= FlowRate(yp, denkf, denaf, visaf, viskf, ift, a, C)
%Density difference
dendiff=denkf-denaf;
% Viscosity ratio
visr=visaf/viskf;
% Eotvos number
Eo=0.46;
% Morton number
Mo=8.2/10^5*dendiff*visaf^4/denaf^2/ift^3;
% Variables dependent on C
numC=length(C);
vt=zeros(numC,1);
Re=zeros(numC,1);
Cd=zeros(numC,1);
qmax=zeros(numC,1);
% Grouped constants
Refix=130*denaf/visaf*sqrt(ift/dendiff);
Cdfix1=48*(3/2+visr)/(1+visr)*(1+12*Mo^(1/3))/(1+36*Mo^(1/3));
Cdfix2=0.9*Eo^(1/2)/(1.4*(1+30*Mo^(1/6))+Eo^(3/2));
vtfix=sqrt(0.27/denaf*(1.87*sqrt(ift*dendiff)-1.01*yp));
% Iteration
tol=10^-10;
maxiter=1000;
for i=1:numC
    vtest=0.5;
    errvt=1;
    iter=0;
    while errvt>tol && iter<=maxiter
        iter=iter+1;
        Recal=Refix*vtest;
        if Cdfix2<0.45
            Cdcal=((Cdfix1/Recal)*sqrt(1+0.25*Recal)/(1+sqrt(1+0.25*Recal))+0.45)*(1-C(i,1))^(-3.7);
        else
            Cdcal=((Cdfix1/Recal)*sqrt(1+0.25*Recal)/(1+sqrt(1+0.25*Recal))+Cdfix2)*(1-C(i,1))^(-3.7);
        end
        vtcals=vtfix*sqrt(1/Cdcal);
        errvt=abs(vtest-vtcals)/vtest*100;
        vtest=vtcals;
    end

    vt(i,1)=vtcals;
    Re(i,1)=Recal;
    Cd(i,1)=Cdcal;
    qmax(i,1)=60*a*vt(i,1)*C(i,1);
end
```

- Plotting function (Matlab)

```

clear all
clc
%Input Data
%Yield point (lbf/100sqft)
yp=2;
%Kill and Annular Fluid Densities (ppg)
denkf=(12:2:20)';
denaf=8.6;
%Kill and Annular Fluid Viscosities (cP)
viskf=8;
visaf=5;
%Interfacial Tension (dynes/cm)
ift=30;
%Annular capacity (gal/ft)
a=0.24;
%Concentration from 0.01 to 0.99
C=(0:0.01:0.99)';
%Variables dependent on concentration
numC=length(C);
numden=length(denkf);
vt=zeros(numC, numden);
Re=zeros(numC, numden);
Cd=zeros(numC, numden);
qmax=zeros(numC, numden);
%Plotting function
for i=1:numden
    [vt(:,i), Re(:,i), Cd(:,i), qmax(:,i)]= FlowRate(yp, denkf(i,1), denaf, visaf, viskf, ift, a, C);
end
ColorMatrix=[0 0 0;...
    0 0.498039215803146 0;...
    1 0 0;...
    0.47843137383461 0.062745101749897 0.894117653369904;...
    0 1 0];
figure
subplot(2,2,1)
hold on;
for i=1:numden
    plot(C, vt(:,i), 'LineWidth', 2, 'Color', ColorMatrix(i,:))
end
hold off;
grid on; box on;
xlabel('KF Concentration', 'FontWeight', 'bold', 'FontSize', 10)
ylabel('Transport Velocity, ft/sec', 'FontWeight', 'bold', 'FontSize', 10)
legend('\rho_{kf}= 12', '\rho_{kf}= 14', '\rho_{kf}= 16', '\rho_{kf}= 18', '\rho_{kf}= 20')
subplot(2,2,2)
hold on;
for i=1:numden
    plot(C, qmax(:,i), 'LineWidth', 2, 'Color', ColorMatrix(i,:))
end

```

```

hold off;
grid on; box on;
ylabel('Corresponding Flow Rate, gpm', 'FontWeight', 'bold', 'FontSize', 10)
xlabel('KF Concentration', 'FontWeight', 'bold', 'FontSize', 10)
subplot(2,2,3)
hold on;
for i=1:numden
    plot(vt(:,i), qmax(:,i), 'LineWidth', 2, 'Color', ColorMatrix(i,:))
end
hold off;
grid on; box on;
ylabel('Corresponding Flow Rate, gpm', 'FontWeight', 'bold', 'FontSize', 10)
xlabel('Transport Velocity, ft/sec', 'FontWeight', 'bold', 'FontSize', 10)
subplot(2,2,4)
axis([0 1 0 1.5 0 2.5])
hold on;
for i=1:numden
    plot3(C, vt(:,i), qmax(:,i), 'LineWidth', 2, 'Color', ColorMatrix(i,:))
end
hold off;
grid on; box on;
xlabel('KF Concentration', 'FontWeight', 'bold', 'FontSize', 10)
ylabel('Transport Velocity, ft/sec', 'FontWeight', 'bold', 'FontSize', 10)
zlabel('Corresponding Flow Rate, gpm', 'FontWeight', 'bold', 'FontSize', 10)

```

- Displacement Ratio Fit model – For empirical correlation (JMP)

Fit Model(

```

    Y( :log10Ru ),
    Effects( :log10q, :log10KF_dens, :log10AF_dens, :log10AF_yp ),
    Personality( Standard Least Squares ),
    Emphasis( Effect Leverage ),
    Run(
        :log10Ru << {Lack of Fit( 0 ), Show Prediction Expression( 1 ),
        Plot Actual by Predicted( 1 ), Plot Regression( 0 ),
        Plot Residual by Predicted( 1 ), Plot Effect Leverage( 1 )}
    )

```

);

)

Mixture zone exponential Coefficient Fit model (JMP)

Fit Model(

```

    Y( :log10a ),
    Effects( :log10AF_dens, :log10AF_visc, :log10q ),
    Personality( Standard Least Squares ),
    Emphasis( Effect Leverage ),
    Run(
        :log10a << {Lack of Fit( 0 ), Show Prediction Expression( 1 ),
        Sorted Estimates( 1 ), Plot Actual by Predicted( 1 ), Plot Regression( 0 ),
        Plot Residual by Predicted( 1 ), Plot Effect Leverage( 1 )}
    )

```

);

VITA

Efecan Demirci was born in Istanbul, Turkey in 1988. He received his Bachelor of Science degree in Petroleum and Natural Gas Engineering from Istanbul Technical University. During his undergraduate studies he taught mathematics to high school students for a living. After his graduation in 2010 he started working for Viking International Company as a coiled tubing engineer, participated in various well stimulation operations in Turkey and Iraq, and also played role in importing coiled tubing technology to Turkey and translating the technology to Turkish Language. He later got qualified for the scholarship of National Turkish Petroleum Corporation (TPAO) to study abroad for his masters. In 2011, he proceeded to Middle East Technical University and pursued his International Welding Engineering diploma. Then in January 2012, he started his graduate studies at Louisiana State University. A year later, he started to work on a joint industry R&D project investigating the viability of immiscible buoyant kill technology on remediation of sustained casing pressure in a well annulus.